UNIVERSITÄT PADERBORN
Die Universität der Informationsgesellschaft

Advanced optical analysis of ferroelectric domain structures

Towards nonlinear-optical devices in $LiNbO_3$ and $KTiOPO_4$

Der Fakultät für Naturwissenschaften der Universität Paderborn zur Erlangung des akademischen Grades eines Doktors der Naturwissenschaften (Dr. rer. nat.) vorgelegte

Dissertation

von

Peter Walter Martin Mackwitz

First supervisor: Prof. Dr. Artur Zrenner

Second supervisor: Prof. Dr. Christine Silberhorn

Department Physik

Universität Paderborn

Februar 2023

Abstract

In the field of integrated optics, the development of new quantum optical devices occupies a prominent position. For the utilization of various nonlinear effects, ferroelectric materials are used in which the principle of quasi-phase matching based on periodic domain inversion is exploited. Material-specific process parameters are of fundamental importance for the fabrication of tailored functional structures. This is precisely where the present work comes in, with a focus here on analytics. Thus, the optical methods of nonlinear analysis and Raman spectroscopy were successfully applied as noninvasive methods in the context of this dissertation, and ferroelectric domain structures in potassium titanyl phosphate and volume crystals or thin film systems on insulators in lithium niobate were investigated based on these methods. The questions regarding physical fundamentals and device development were clarified in close cooperation with the technology side.

For a clear interpretation of the results and the underlying physics, a fundamental understanding of the occurring measurement signatures is necessary. Thus, within the framework of this work, via an experimental-theoretical approach it was possible to elucidate the contrast mechanisms for nonlinear microscopy, which is based on an analysis of the nonlinear polarization linked to the electric field distribution generated in the focal plane. On the part of Raman spectroscopy, structure-sensitive vibrational modes for the material system potassium titanyl phosphate or waveguide structures in it were fully verified. This was done by exploiting the various mode parameters of intensity, full width at half maximum and relative Raman shift. In this context, the depth-profile respectively -homogeneity of domains or possibly occurring stress gradients were studied, whereby the vibration analysis was flanked by the detection of the locally varying nonlinear susceptibility.

The characterization of waveguides as well as periodically poled structures in different material systems focused on questions concerning domain-inversion and -dynamics. With respect to a combined technological/analytical approach, domain structures fabricated by means of different process parameters were systematically investigated. This includes, among others, periodically poled rubidium waveguide structures in potassium titanyl phosphate and domain structures in lithium niobate. The feedback loop with the device fabrication side thus resulted in optimized quantum optical devices, such as a module for counter-propagating parametric down-conversion. A key component of this work was the investigation of domain inversion in thin film lithium niobate. In particular, X-cut was applied, which is relatively insensitive to chemical wet etching, making the non-invasive analytical techniques used here almost unavailable for imaging the ferroelectric structure. In this context, the process-specific parameters for the poling process in thin-film lithium niobate could be evaluated and modified poling methods derived.

Overall, with the utilized analytical methods the fundamental physical issues such as the contrast mechanisms or the poling dynamics could be clarified. The resulting direct process control for different material systems thus enabled the realization of nonlinear optical components with poling lengths below the micron-range.

Kurzfassung

Im Bereich der integrierten Optik nimmt die Entwicklung neuer quantenoptischer Bauelemente eine herausragende Stellung ein. Für die Ausnutzung diverser nichtlinearer Effekte werden hierbei ferroelektrische Materialien verwendet, bei denen das Prinzip der Quasi-Phasenanpassung basierend auf der periodischen Domäneninversion ausgenutzt wird. Für die Herstellung maßgeschneiderter funktionaler Strukturen sind materialspezifische Prozessparameter von grundlegender Bedeutung. Gerade hier setzt die vorliegende Arbeit an, wobei hier der Schwerpunkt im Bereich der Analytik liegt. So wurden im Rahmen dieser Dissertation die optischen Verfahren der nichtlinearen Analyse und der Raman-Spektroskopie als nichtinvasive Methoden erfolgreich eingesetzt und darauf basierend ferroelektrische Domänenstrukturen in Kaliumtitanylphosphat und Volumenkristalle bzw. Dünnschichtsysteme auf Isolatoren in Lithiumniobat untersucht. Die Fragestellungen hinsichtlich physikalischer Grundlagen und der Bauelemententwicklung wurden dabei in enger Kooperation mit der Technologieseite geklärt.

Für eine eindeutige Interpretation der Ergebnisse und der darunterliegenden Physik ist ein grundlegendes Verständnis der auftretenden Mess-Signaturen notwendig. So konnten im Rahmen dieser Arbeit durch einen experimentell-theoretischen Ansatz die Kontrastmechanismen für die nichtlineare Mikroskopie aufgeklärt werden, welcher auf einer Analyse der nichtlinearen Polarisation verknüpft mit der in der Fokalebene erzeugten elektrischen Feldverteilung basiert. Seitens der Raman-Spektroskopie wurden struktursensitive Schwingungsmoden für das Materialsystem Kaliumtitanylphosphat bzw. Wellenleiterstrukturen in diesem vollständig verifiziert. Dies geschah unter Ausnutzung der verschiedenen Modenparameter Intensität, Halbwertsbreite und relativer Raman-Verschiebung. In diesem Kontext wurden Tiefenverlauf bzw. -homogenität von Domänen bzw. eventuell auftretende Spannungsgradienten studiert, wobei die Schwingungsanalyse durch die Erfassung der örtlich variierenden nichtlinearen Suszeptibilität flankiert wurde.
Bei der Charakterisierung von Wellenleitern als auch periodisch gepolten Strukturen in unterschiedlichen Materialsystemen lag der Fokus bei Fragenstellungen hinsichtlich Domänen-Inversion und –Dynamik. Hinsichtlich eines kombinierten technologisch/analytischen Ansatzes wurden Domänenstrukturen, welche mittels unterschiedlicher Prozess-Parameter hergestellt wurden, systematisch untersucht. Dies umfasst u.a. periodisch gepolte Rubidium-Wellenleiterstrukturen in Kaliumtitanylphosphat und Domänenstrukturen in Lithiumniobat. Aus der Feedback-Schleife mit dem Bereich der Bauelementherstellung ergaben sich somit optimierte quantenoptische Bauelemente, wie beispielsweise ein Modul für die gegenläufige parametrische Fluoreszenz. Ein zentraler Bestandteil dieser Arbeit war die Untersuchung der Domäneninversion in Dünnschicht-Lithiumniobat-Filmen. Dabei fand vor allem der X-Schnitt Anwendung, welcher gegenüber chemischem Nassätzen relativ unempfindlich ist, sodass zur Abbildung der ferroelektrischen Struktur die hier eingesetzten nichtinvasiven Analyseverfahren nahezu alternativlos sind. In diesem Zusammenhang konnten die prozessspezifischen Parameter für den Polungsprozess in Dünnschicht-Lithiumniobat evaluiert werden und modifizierte Polungsverfahren abgeleitet werden.

Insgesamt erfolgte durch die eingesetzten analytischen Verfahren eine Klärung fundamentaler physikalischer Sachverhalte wie beispielsweise der vorliegenden Kontrastmechanismen oder der Polungsdynamik. Die daraus resultierende direkte Prozesskontrolle für verschiedene Materialsysteme ermöglichte somit die Realisierung nichtlinearer optischer Bauelemente mit Polungslängen unterhalb des µm-Bereichs.

Table of Contents

1 Preface

The combination of integrated optics and microelectronics opened up the novel research fields of optoelectronics and photonics. Here, a widespread amount of applications like opto-electronic couplers, ferroelectric storages, optical filters and modulators [1]–[3] have been developed utilizing the various possibilities to exploit linear as well as nonlinear properties and effects of light. Dating back to the 1960s the term integrated optics has been established for the unification of optical effects with integrated circuits and its miniaturization [4], [5]. The latter advanced tremendously throughout the progress within the semiconductor industry whereas the optics gained significance by the emerging research of nonlinear optical effects like second harmonic generation (SHG) with the invention of the laser in that time and in the following decades by the utilization of those effects for quantum optics [6].

Experiments within quantum optics are commonly designed to investigate the nature of single photons, their detection, entanglement [7] or heralded states. This fundamental research on the aforementioned issues is projected to form the platform of secure and tap-proof quantum communication and shall supersede classical encryption technologies. The basic requirement for those research fields is the provisioning of single photons and their appropriate sources. One very important single photon source is represented by the effect of parametric down conversion (PDC) also discovered in the late 1960s [8], [9] and applied by Mandel et al. in the 1980s [10]. Here, a pump photon is split up into an idler and signal photon, which can have different polarization states among themselves. The application of this quantum optical effect in turn requires certain precisely tailored devices and hence the understanding of further nonlinear optical effects. Reasonable PDC efficiencies in the range of 4 photons per 10^6 [11] for co-propagating PDC are achieved in periodically poled waveguide structures in ferroelectric materials like $LiNbO_3$ (LN) or $KTiOPO_4$ (KTP) for instance. This forward directed PDC unfortunately features high bandwidths and requires elaborated spatial filtering which diminishes the intensity. To circumvent these drawbacks counter-propagating PDC devices became an alternative. They come up with a high modal purity as narrowband single photon sources but the technological requirements for 1^{st} order processes within those sources are ultra-short poling period which represents a big challenge for the fabrication and a proper analytics. Amongst other issues this is going to be investigated and tackled within this work.

The choice of the material platform for integrated optical devices is crucial for the exploitation of the particular quantum optical effects. Hence, fundamental studies of different materials are indispensable. In LN such devices have been fabricated for several decades [12] and the material became a workhorse for frequency conversion processes especially in the telecommunication sector. The material features a wide transparency range and high exploitable elasto-optic, piezo-electric and especially nonlinear optical coefficients. As a widespread and well understood material system in terms of poling techniques and waveguide fabrication it is a promising platform for the realization of ultra-short poling periods. Furthermore, LN is likely to be a basis for ridge waveguides. Common waveguides in LN fabricated via titanium in-diffusion offer advantages like low attenuation or the guidance of both TE- and TM-polarization but also limitations due to the comparatively low refractive index change here [13].

Besides bulk LN thin film lithium niobate respectively lithium niobate on insulator (LNOI) has drawn attention within the community of integrated optics in the recent years. In contrast to the bulk counterpart, it comes up with an increased nonlinear efficiency, a higher mode confinement and the precise control of the refractive index and dispersion [14]–[17]. Thus, its role within integrated optics becomes very important. The efficiency enhancement arises from the miniaturized waveguide cross-sections and thus a higher refractive index difference compared to the bulk material arises [18]. This is accompanied with much smaller bending radii [17]. Domain engineering in terms of poling techniques and lithography issues are not elaborated as in bulk LN which presents one of the crucial challenges regarding this novel material platform.
Besides the LN platform(s) KTP serves as another platform for integrated nonlinear optical devices since similarly a broad transparency range and high nonlinear optical coefficients lead to a utilization for conversion processes and quantum optical experiments [15], [19], [20]. Low propagation losses for type-II photon pair sources are likely to be fabricated in this material [21], [22]. Furthermore, KTP offers a high damage threshold and several more advantages in terms of fabrication treatment [23] especially the lower coercive field strength [24] and that it is very insensitive to photo refraction. However, KTP unfortunately features a high ionic conductivity due to its crystallographic structure which can turn out as a challenge for domain engineering.

Tailored nonlinear devices are designed to fulfill the condition for quasi phase-matching (QPM) for the particular frequency conversion processes since birefringence phase-matching comes up with drawbacks like the lacking addressability of the strongest nonlinear tensor element d_{33}. Those devices are characterized by various parameters like their period length and duty cycle. Hence, the design of a sufficient domain grating is the first step towards a nonlinear optical device with high conversion efficiencies. The domain inversion in ferroelectrics is nowadays commonly conducted via the application of an external electric field. Further methods like stacked GaAs plates or a domain pattern directly obtained via the melt within the Czochralski method are also used [25]–[27]. In order to provide samples with a homogeneous domain pattern the e-field is applied in one or multiple certain pulses. The duration of those pulses and the shape of its envelope are precise parameters which have to be determined. Overall, the efficiency of functional structures depends on the quality of the transferred ferroelectric domain structure. A quite established method especially to reveal the periodic domain pattern is chemical wet etching, but on the one hand this method is invasive and on the other hand not applicable onto every crystal face due to the dependency on the etching rate. Another technique to study the domain structure utilizes the piezo force microscopy (PFM), which is limited to the surface and in case of depth discrimination also invasive. Therefore, structure sensitive methods allowing for a non-invasive 3-dimensional analysis with high spatial resolution like Imaging Raman-Spectroscopy or Nonlinear Microscopy have to be applied.

One part of this thesis deals with the fundamental analysis of occurring contrast mechanisms with respect to the applied analysis methods. Here Raman spectroscopy is utilized characterize the vibrational fingerprints, which refers on the one hand to the stoichiometry and on the other hand to structure-sensitive vibrational modes. The applied SH characterization considers the nonlinear light matter interaction and the occurrence of nonlinear contrast in the tightly focusing regime. The other part of this thesis is connected to the inspection of the ferroelectric domain structure and the determination of the important process parameters for different material platforms (structures in: KTP, LN, LNOI) via the aforementioned visualization methods.

Structure of the thesis:

As the first chapter the physical fundamentals related to the topics of the work are explicated. This relates to the second-harmonic generation in nonlinear media as it is the basis for SH microscopy as well as the concept of phase-matching to provide the link to periodically poled structures in this context. Further nonlinear processes like PDC and a brief outline of wave guiding physics are presented since this is also part of the investigated devices. Besides this the physics of ferroelectric domains and the process of domain inversion are discussed. The fundamental characteristics of both material platforms (KTP and LN) are also given in this chapter.

Subsequently chapter three deals with the methodology and experimental realization of the applied characterization techniques utilized in this work. These are linear confocal microscopy (pre-characterization), µ-Raman spectroscopy and the nonlinear microscopy. Furthermore, the relevant systems parameters (e.g. spatial and/or spectral resolution) are given and specific system extensions are considered. Last but not least for each method an example for application is presented.

The main part of the thesis is to be found within the next two chapters (four & five). First it starts with a fundamental explanation of the theoretical concept of the nonlinear contrast mechanism substantiated with an experimental validation of the model by unpoled pristine bulk and periodically poled material results for LN and KTP. This is followed by a general analysis of the vibrational properties of these materials including comprehensive mode assignments and the investigation of structure sensitive phonon modes. In chapter five the functional structures in tailored nonlinear devices within the different material platforms are examined.

The last chapter summarizes the main contents and results of the present doctoral thesis and additionally provides an outlook for further developments.

2 Fundamentals

The investigation of functional structures in quantum devices for nonlinear applications demands a thorough understanding of the underlying physics in particular the light-matter interaction as a basis for nonlinear optics as well as the principles of wave-guiding in different media, which is the essential basis for nonlinear optical devices as studied in this work. For this, SHG and further nonlinear processes like PDC are discussed in detail. Connected to nonlinear devices the concept of quasi phase-matching is explained. Furthermore the properties of ferroelectric materials, aspects of domain inversion and the physics of waveguides are discussed.

2.1 Nonlinear Optics

Since the invention of the laser in 1960 by Maiman [28] a sufficient intense light source is available representing the starting point of nonlinear optics, where the optical properties of matter under the influence of intense radiation are going to be changed. In order to understand the nonlinear light-matter interaction one has to start with the induced nonlinear polarization as a material inherent trait. Based on the polarization $\vec{P}(t)$ the electromagnetic field can obtain newly induced components.

Nonlinear polarization:

Commonly the polarization $\vec{P}(t)$ of a certain material is defined as the dipole moment per unit volume. Beyond this, it is contingent on an additionally applied electric field $\vec{E}(t)$ as for the case of nonlinear optical phenomena. This results in that $\vec{P}(t)$ is technically a response function either for the time-domain or for the frequency-domain. In order to quantify how a driving external electric field influences the polarization $\vec{P}(t)$ the expansion within the time-domain is useful [29]:

$$\vec{P}(t) = \vec{P}^{(1)}(t) + \vec{P}^{(2)}(t) + \vec{P}^{(3)}(t) + \cdots + \vec{P}^{(n)}(t) + \cdots \tag{2.1}$$

For the time-interval dt' the incremental polarization contribution is given the following:

$$d\vec{P}^{(1)}(t) = \epsilon_0 F^{(1)}(t : t')\, \vec{E}(t')\, dt' \tag{2.2}$$

Here, $F^{(1)}(t : t')$ represents the first order time-domain response tensor which links the electric field and the polarization at t'. For the overall polarization, it follows:

$$\vec{P}^{(1)}(t) = \epsilon_0 \int_{-\infty}^{t} F^{(1)}(t : t')\, \vec{E}(t')\, dt' \tag{2.3}$$

Taking into account that only the time delay instead of an absolute value is the important factor one can rewrite the response tensor:

$$F^{(1)}(t:t') \equiv G^{(1)}(t-t') \tag{2.4}$$

Under consideration of the causality principle $\left(\underline{G}^{(1)}(t-t') = \underline{G}^{(1)}(\tau') = \underline{G}^{(1)}(t,\tau)\right)$ the linear respectively first-order polarization is given by:

$$\vec{P}^{(1)}(t) = \epsilon_0 \int \underline{G}^{(1)}(t,\tau) \cdot \vec{E}(\tau)\, d\tau \tag{2.5}$$

For a higher order polarization an analogous method has to be performed including two electric fields $\vec{E}(t_1')$ and $\vec{E}(t_2')$. The quantification of the polarization depending on the electric field requires a transition from time- to frequency-domain via a Fourier transformation:

$$\vec{E}(t) = \frac{1}{2\pi} \int \vec{E}(\omega) \cdot e^{i\omega t}\, d\omega \tag{2.6a}$$

$$\vec{E}(\omega) = \frac{1}{2\pi} \int \vec{E}(\tau) \cdot e^{i\omega\tau}\, d\tau \tag{2.6b}$$

This can be utilized with equation (2.5) to reshape the response function:

$$\vec{P}^{(1)}(t) = \epsilon_0 \int_{-\infty}^{\infty} \underline{G}^{(1)}(t-\tau) \cdot \vec{E}(\tau)\, d\tau = \epsilon_0 \int_{-\infty}^{\infty} \underline{G}^{(1)}(\tau) \frac{1}{2\pi}\, \vec{E}(\omega) e^{-i\omega(t-\tau)} d\omega\, d\tau$$

$$= \epsilon_0 \int_{-\infty}^{\infty} \frac{1}{2\pi} \underbrace{\int_{-\infty}^{\infty} \underline{G}^{(1)}(\tau) e^{i\omega(t-\tau)} d\tau}_{\chi^{(1)}}\, \vec{E}(\omega) e^{-i\omega(t-\tau)} d\omega \tag{2.7}$$

The evaluation of the integral $\int_{-\infty}^{\infty} d\tau\, G^{(1)}(\tau) e^{i\omega\tau}$ yields the first order susceptibility $\chi^{(1)}(-\omega_d : \omega)$. Since the electric field $\left(\vec{E}(\omega)\right)^* = \vec{E}(-\omega)$ and the polarization are real quantities and with (2.3) it follows that the response function is also real. This implies that it holds $\left\{\underline{\chi}^{(1)}(-\omega_0 : \omega)\right\}^* = \underline{\chi}^{(1)}(\omega_0^* : -\omega^*)$.

The linear polarization then yields: $\vec{P}^{(1)}(\omega) = \epsilon_0 \underline{\chi}^{(1)}(-\omega_0, \omega)\vec{E}(\omega)$ (2.8)

For the description of higher order nonlinear processes like second-harmonic generation the susceptibility has to be extended to the second-order:

$$\vec{P}^{(2)}(t) = \epsilon_0 \iiint_{-\infty}^{\infty} \underline{G}^{(2)}(\tau_1, \tau_2)\, \vec{E}(\omega_1)\vec{E}(\omega_2) e^{-i\{\omega_1(t-\tau_1)+\omega_2(t-\tau_2)\}}\, d\omega_1 d\omega_2 d\tau_1 d\tau_2 \quad (2.9)$$

With the restriction $\omega_0 = \omega_1 \pm \omega_2$ the second-order susceptibility then reads:

$$\underline{\chi}^{(2)}(-\omega_0 : \omega_1, \omega_2) = \iint_{-\infty}^{\infty} d\tau_1 d\tau_2\, \underline{G}^{(2)}(\tau_1, \tau_2) e^{i\{\omega_1\tau_1+\omega_2\tau_2\}} \quad (2.10)$$

The polarization for this is finally given in equation (2.12):

$$\vec{P}^{(2)}(t) = \frac{\epsilon_0}{4\pi^2} \int\int \underline{\chi}^{(2)}(-\omega_0 : \omega_1, \omega_2) \cdot \vec{E}(\omega_1) \cdot \vec{E}(\omega_2) e^{-i\omega_0 t} d\omega_1 d\omega_2 \quad (2.11)$$

Generally, the polarization can be expressed as a n^{th}-order polarization with a susceptibility of a general order (n). Obviously the polarization is represented as a series of the externally applied field:

$$\vec{P}(t) = \epsilon_0 \left[\chi^{(1)}\vec{E}(t) + \chi^{(2)}\vec{E}^2(t) + \chi^{(3)}\vec{E}^3(t) + \cdots\right] \quad (2.12)$$

An estimate of the numerical value of $\chi^{(2)}$ can be given via the relation $\chi^{(2)} = \chi^{(1)}/E_{at}$ [30]. Here, E_{at} represents the atomic field strength, which is used in this context because when electromagnetic radiation passes through matter, the electric field of this radiation leads to a periodic shift of the electric charges of the atoms with the frequency of the radiation.

The value of the atomic field strength then yields $E_{at} = e/4\pi\epsilon_0 a_0^2 \approx 5{,}14 \cdot 10^{11}$ V/m. With this for the second-order susceptibility follows:

$$\chi^{(2)} = \chi^{(1)}/E_{at} \approx 1{,}94 \cdot 10^{-12}\ \text{m/V} \quad (2.13)$$

Here, the first-order susceptibility is set as one.

Nonlinear wave equation:

The quantitative description of second-harmonic generation requires not only the fundamental understanding of how the polarization is connected with the second-order susceptibility but also the depiction how electromagnetic waves do interact with nonlinear media. Here, the Maxwell's equations are fundamental for the description of the light propagation of electromagnetic waves.

If a non-magnetic material without free (no charge densities, $\vec{\rho} = 0$) or moving charge carriers (no current density, $\vec{j} = 0$) is assumed [31], the result is the Maxwell's equations as follows with $\vec{B} = \mu_0 \vec{H}$:

$$\nabla \times \vec{E} = -\frac{\partial \vec{B}}{\partial t}, \qquad \nabla \times \vec{H} = -\frac{\partial \vec{D}}{\partial t} + \vec{j}, \qquad \nabla \times \vec{D} = \rho, \qquad \nabla \times \vec{B} = 0 \tag{2.14}$$

The polarization $\vec{P}(t)$ is introduced to the Maxwell's equations via the dependence of the electric displacement field $\vec{D} = \epsilon_0 \vec{E} + \vec{P} = \epsilon_0 (1 + \chi^{(1)}) \vec{E}$ to it:

$$\begin{aligned} \Rightarrow \quad \nabla \times \left(\nabla \times \vec{E}\right) = \nabla \times \left(-\frac{\partial \vec{B}}{\partial t}\right) = -\frac{\partial}{\partial t}\left(\nabla \times \vec{B}\right) = -\frac{\partial}{\partial t}\left(\mu_0 \frac{\partial \vec{D}}{\partial t}\right) = -\mu_0 \frac{\partial^2 \vec{D}}{\partial t^2} \\ = -\underbrace{\mu_0 \epsilon_0}_{\frac{1}{c^2}} \frac{\partial^2 \vec{E}}{\partial t^2} - \underbrace{\mu_0}_{\frac{1}{\epsilon_0 c^2}} \frac{\partial^2 \vec{P}}{\partial t^2} \end{aligned} \tag{2.15}$$

$$\Rightarrow \quad \nabla \times \left(\nabla \times \vec{E}\right) + \frac{1}{c^2} \frac{\partial^2 \vec{E}}{\partial t^2} = -\frac{1}{\epsilon_0 c^2} \frac{\partial^2 \vec{P}}{\partial t^2} \tag{2.16}$$

Reshaping the first term of the left-hand side of equation (2.16) from $\nabla \times \nabla \times \vec{E}$ into $\nabla \cdot \left(\nabla \cdot \vec{E}\right) - \nabla^2 \vec{E}$ and referring to the prerequisites introduced above it also holds that $\nabla \vec{D} = 0, \nabla \vec{E} = 0$ as a simple transversal plane wave is assumed in an isotropic medium. Hence, the differential operator on $\vec{E}$ vanishes and one obtains the following wave equation:

$$\nabla^2 \vec{E} - \frac{1}{c^2} \frac{\partial^2 \vec{E}}{\partial t^2} = \frac{1}{\epsilon_0 c^2} \frac{\partial^2 \vec{P}}{\partial t^2} \tag{2.17}$$

In the context of equation (2.15) the dependence of the electric displacement field has been explicated. For the case of nonlinear optics this can be extended for the nonlinear polarization $\vec{D} = \underbrace{\epsilon_0 \vec{E} + \vec{P}^{(1)}}_{\vec{D}^{(1)}} + \vec{P}^{(NL)}$. Furthermore the nonlinear treatment also requires to account for each frequency fractions resulting in $\underline{\epsilon}^{(1)}(\omega_i) = n(\omega_i)^2$. The nonlinear wave equation is then independent of any constant polarization part:

$$\nabla^2 \vec{E} - \frac{1}{\epsilon_0 c^2} \frac{\partial^2 \vec{D}^{(1)}}{\partial t^2} = \frac{1}{\epsilon_0 c^2} \frac{\partial^2 \vec{P}^{(NL)}}{\partial t^2} \;\Rightarrow\; \nabla^2 \vec{E}_i - \frac{n(\omega_i)^2}{c^2} \frac{\partial^2}{\partial t^2} \vec{E}_i = \frac{1}{\epsilon_0 c^2} \frac{\partial^2}{\partial t^2} \vec{P}_i^{(NL)} \tag{2.18}$$

Based on the nonlinear wave equation the arising of second-harmonic generation in an anisotropic media can be derived in the next section.

2.1.1 Second-harmonic generation

Qualitatively the second-harmonic light-matter interaction is the consequence of the periodical displacement of electric charges with the frequency ω_0 caused by a strong electro-magnetic field. Hence those dipoles emit an own electro-magnetic radiation. In case of small intensities of the excitation light this displacement is negligible small and therefore the process behaves like a harmonic oscillator. Intense external excitation fields force the dipole displacement to act in a non-linear potential ($2\omega_0$ for SHG or $3\omega_0$ for THG).

For a quantitative description the induced nonlinear polarization of a second-harmonic process is described by a plane wave (only consideration of the real part; hence the absolute amplitude value has to be treated bisected). The amplitude of the second-harmonic light is denoted as $A_3 = E_{2\omega_0}$ and the corresponding frequency as $\omega_3 = 2\omega_0$ with a wave vector $k_3 = n_3\omega_3/c$. Therefore, in the picture of a plane wave the electric field of a generated second-harmonic light is written as:

$$\mathrm{E_3(z,t)} = \mathrm{A_3}(z)e^{i(k_3 z-\omega_3 t)} + c.c. \tag{2.19}$$

To find an expression for the nonlinear intensity $I_3(z)$ the nonlinear wave equation (2.18) has to be considered again. Centrally for the nonlinear polarization $\vec{P}_i^{(NL)}$ which yields $P_3(z,t) = P_3(\omega)e^{-i\omega t}$ and with the later introduced relation $P_i(\omega_n + \omega_m) = \epsilon_0 \sum_{jk} \sum_{nm} 2d_{ijk}E_j(\omega_n)E_k(\omega_m)$ and equation (2.19) it follows:

$$P_3(z,t) = 4\epsilon_0 d_{eff} A_1(z)A_2(z)e^{i([k_1+k_2]z-\omega_3 t)} \tag{2.20}$$

Equation (2.18) requires a second derivative of $P_3(z,t)$ and also for $E_3(z,t)$:

$$\frac{\partial^2}{\partial t^2}P_3(z,t) = -4\omega_3^2\epsilon_0 d_{eff} A_1(z)A_2(z)e^{i([k_1+k_2]z-\omega_3 t)} \tag{2.21}$$

$$\frac{\partial^2}{\partial z^2}E_3(z,t) = \left[\frac{\partial^2}{\partial z^2}A_3(z) + 2ik_3\frac{\partial}{\partial z}A_3(z) - k_3^2 A_3(z)\right]e^{i(k_3 z-\omega_3 t)} + c.c. \tag{2.22}$$

From [27] for example one can take advantage of the slowly varying envelope approximation (SVEA) $\left|\frac{\partial^2}{\partial z^2}A_3(z)\right| \ll \left|k_3\frac{\partial}{\partial z}A_3(z)\right|$ and the equation (2.22) can be reduced to:

$$\frac{\partial^2}{\partial z^2}E_3(z,t) = \left[2ik_3\frac{\partial}{\partial z}A_3(z) - k_3^2 A_3(z)\right]e^{i(k_3 z-\omega_3 t)} + c.c. \tag{2.23}$$

In the same manner the further derivative yields:

$$\frac{\partial^2}{\partial t^2}E_3(z,t) = -\omega_3^2 A_3(z)e^{i(k_3 z-\omega_3 t)} + c.c. \tag{2.24}$$

In terms of the specific amplitudes, the nonlinear wave equation can be written as follows (note: for reasons of a clear arrangement, several mathematical intermediate steps of inserting and canceling out have been spared out and the relation $k_3 = n_3\omega_3/c$ is used):

$$2ik_3\frac{\partial}{\partial z}A_3(z) = -\frac{4\omega_3^2 d_{eff}}{c^2}A_1(z)A_2(z)e^{i([k_1+k_2-k_3]z)} \tag{2.25}$$

Equation (2.25) is called a coupled amplitude equation. Besides the connection of the amplitudes this equation also yields the term for the phase-mismatch $\Delta k = k_1 + k_2 - k_3$ in the exponent.

The intensity expression is obtained via an integration of the left part of equation (2.25). Rearranged it gives:

$$A_3(L) = \frac{2i\omega_3^2 d_{eff}}{k_3 c^2}A_1A_2\int_0^L e^{i\Delta kz}\,dz = \frac{2i\omega_3^2 d_{eff}}{k_3 c^2}A_1A_2\left(\frac{e^{i\Delta kL}-1}{i\Delta k}\right) \tag{2.26}$$

The amplitude and intensity are connected via the time-averaged Poynting vector. The relation is given by $I_p = 2n_p\epsilon_0 c|A_p|^2$ and it follows for I_3:

$$I_3 = I_{2\omega} = \frac{8n_3\epsilon_0\omega_3^4 d_{eff}^2}{k_3^2 c^3}|A_1|^2|A_2|^2\left|\frac{e^{i\Delta kL}-1}{i\Delta k}\right|^2 = \frac{2\omega_3^2}{\epsilon_0 n_1 n_2 n_3 c^2}d_{eff}^2 L^2 sinc^2\left(\frac{\Delta kL}{2}\right) \tag{2.27}$$

With this final equation the nonlinear second-harmonic intensity is quantitatively described. Its form is characterized by the $sinc^2$-function and yields its maximum at $\Delta k = 0$ as seen in Figure 2.1.

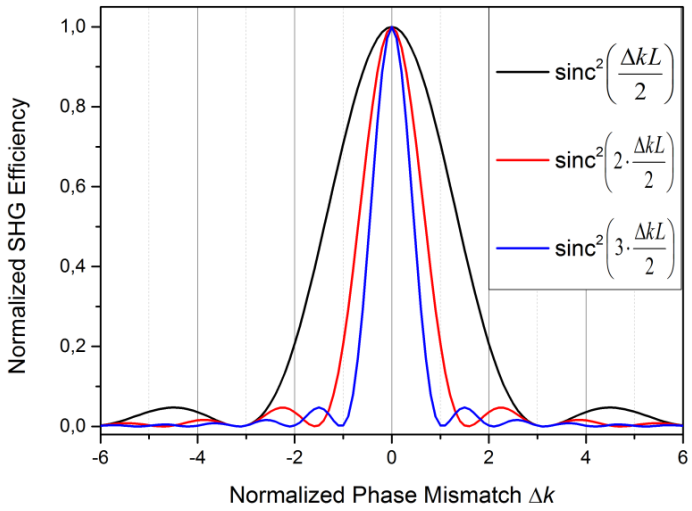

Figure 2.1: *Normalized SH intensity as a function of the phase mismatch Δk the pump power.*

Symmetry considerations and nonlinear coefficient:

In the following quantitative description of the SHG process only the characteristics of the propagating second-harmonic wave has to be taken into account (period poling length or the field distribution within the focal plane (see section 4.1) and the nature of the nonlinear tensor of the respective material are neglected in this consideration). With the two frequencies ω_n and ω_m at hand P_i^2 looks as follows:

$$P_i^2(\omega_n + \omega_m) = \epsilon_0 \sum_{jk} \sum_{(nm)} \chi_{ijk}^{(2)}(-[\omega_n + \omega_m], \omega_n, \omega_m) E_j(\omega_n) \cdot E_k(\omega_m) \tag{2.28}$$

From this general formula for a process with three involved waves one finds six positive as well as six negative tensors for the second-order susceptibility $\chi_{ijk}^{(2)}$ including 27 elements enabling for 324 ways for such an interaction process under the proposition that the conservation of energy is not violated. For this formula it is likely to use the Kleinman's symmetry allowing for the permutation of the indices when constant frequencies are considered i.e. far from resonances. This requires that all the parts of equation (2.28) are real and provide a permutation symmetry:

$$\chi_{jki}^{(2)}(-\omega_3, \omega_1, \omega_2) = \chi_{kij}^{(2)}(-\omega_3, \omega_1, \omega_2) \tag{2.29}$$

This special symmetry is valid for transparent and loss-free media with a vanishing wavelength dispersion but nevertheless the directional dispersion is still prevailing [32] and a contracted notation yields [33]:

$$d_{ijk} = \frac{1}{2} \chi_{ijk}^{(2)} \tag{2.30}$$

Therefore, the polarization is given by:

$$P_i(\omega_n + \omega_m) = \epsilon_0 \sum_{jk} \sum_{nm} 2 d_{ijk} E_j(\omega_n) E_k(\omega_m) \tag{2.31}$$

Using symmetric *j* and *k*, one gets a 3x6 matrix with several independent elements results. One of the 32 crystal classes governs the amount of the independent elements.

$$-P^{(2)}(t) = \epsilon_0 \chi^{(2)} \big(-E(t)\big)^2 = \epsilon_0 \chi^{(2)} \big(E(t)\big)^2 = P^{(2)}(t) \tag{2.32}$$

For a material with a centro-symmetric crystallographic structure the change of the sign of the applied external field causes a change of the sign of the induced polarization, cf. equation (2.32). In the centro-symmetric case this is only fulfilled if $P(t) = 0$ so that $\chi^{(2)}$ vanishes. Hence, the second-harmonic process requires a non-inversion symmetry.

The polarization as stated in equation (2.31) is dependent on the two fields E_j and E_k. Here, the Voigt notation [34] is very useful because it allows to combine the last two indices of the nonlinear coefficient d_{ijk} to one with the following set of coordinates: $xx = 1,\ yy = 2, zz = 3, zy = yz = 4, zx = xz = 5, yx = xy = 6$. The tensor for SHG then turns out to be:

$$\begin{pmatrix} P_x(2\omega) \\ P_y(2\omega) \\ P_z(2\omega) \end{pmatrix} = 2\epsilon_0 \begin{bmatrix} d_{11} & d_{12} & d_{13} & d_{14} & d_{15} & d_{16} \\ d_{21} & d_{22} & d_{23} & d_{24} & d_{25} & d_{26} \\ d_{31} & d_{32} & d_{33} & d_{34} & d_{35} & d_{36} \end{bmatrix} \cdot \begin{pmatrix} E_x^2(\omega) \\ E_y^2(\omega) \\ E_z^2(\omega) \\ 2E_z(\omega)E_y(\omega) \\ 2E_z(\omega)E_x(\omega) \\ 2E_x(\omega)E_y(\omega) \end{pmatrix} \tag{2.33}$$

With the Kleinman's symmetry a contracted nonlinear tensor with 10 independent elements (marked blue in formula (2.34) arises:

$$d_{il} = \begin{bmatrix} d_{11} & d_{12} & d_{13} & d_{14} & d_{15} & d_{16} \\ d_{16} & d_{22} & d_{23} & d_{24} & d_{14} & d_{12} \\ d_{15} & d_{24} & d_{33} & d_{23} & d_{13} & d_{14} \end{bmatrix} \tag{2.34}$$

In case of SHG here the d_{26}-element is set to be $d_{26} = d_{12} = d_{122} = d_{212}$ and the d_{25}-element is $d_{25} = d_{14} = d_{123} = d_{213}$. KTP stems from the point group *mm2* with the space group *Pna2₁* [35] and is hence C_{2v} symmetric whereas LN features a C_{3v} symmetry [36]. The both tensors of these materials are given by:

$$d_{KTP} = \begin{bmatrix} 0 & 0 & 0 & 0 & d_{15} & 0 \\ 0 & 0 & 0 & d_{24} & 0 & 0 \\ d_{31} & d_{32} & d_{33} & 0 & 0 & 0 \end{bmatrix} \tag{2.35a}$$

$$d_{LN} = \begin{bmatrix} 0 & 0 & 0 & 0 & d_{31} & -d_{22} \\ -d_{22} & d_{22} & 0 & d_{31} & 0 & 0 \\ d_{31} & d_{31} & d_{33} & 0 & 0 & 0 \end{bmatrix} \tag{2.35b}$$

Based on these tensor elements the spatial partitioned nonlinear polarization can be calculated. Both materials feature d_{33} as their largest tensor element [37], [38]. All tensor element values for both materials are listed in subchapter 2.3.

2.1.2 Aspects of phase-matching

In the last section the generation of a second-harmonic of a certain fundamental wave has quantitatively been considered but without taking into account the phase relationship of such two waves which is crucial for the SHG efficiency for any application or devices. Due to dispersion in the particular material both waves feature different phase velocities leading to a divergence of the fundamental waves, i.e. the excitation laser light, and the driven harmonic wave. As a consequence the waves do not have a constant phase relation and will rather destructively than constructive interfere on average.

From equation (2.27) this becomes obvious - the intensity of the generated SH wave oscillates with the squared sinc and does not increase steadily. This increase is limited to a small range around the ideal point $\Delta k = 0$. Outside of this region destructive interference takes place. This range is equivalent with the period of this oscillation for a finite phase-mismatch along the excitation axis for a SHG process and called the coherence length [31]:

$$l_c = \frac{\pi}{\Delta k} \tag{2.36}$$

The Δk – also called the phase-mismatch - in this equation is crucial for this consideration as it determines that for each $\Delta k \neq 0$ a phase displacement between both waves is apparent. The phase-matching condition for a SHG process is given as [31]:

$$n(\omega_1) = n(2\omega_1) \tag{2.37}$$

Hence, for a perfect (SHG) conversion process $\Delta k = k_3 - k_2 - k_1 = k_{2\omega_1} - 2k_{\omega_1} = 0$ needs to be achieved to obtain a quadratically growing SHG intensity. To overcome this issue several techniques can be utilized aiming that for a given propagation direction the phase velocities of both waves are identical.

The two most prominent techniques birefringent phase-matching (BPM) as well as quasi phase-matching (QPM) will be described in a more precise manner whereas other phase-matching techniques like *modal-dispersion phase-matching*, *Cerenkov-type phase-matching* [39] or *anomalous-dispersion phase-matching* shall only be mentioned at this point.

Birefringent phase-matching in uniaxial and biaxial crystals:

The refractive index is not only wavelength dependent as it holds for dispersion in general but can also be dependent on the polarization of the incident light. Crystals with one or more distinguished optical axis feature this behavior which is then called birefringence. In crystals with an optical axis (i.e. the refractive index is axially symmetric), a plane is defined by this and the direction of propagation of the light. With this prerequisite one can distinguish between light polarized parallel and orthogonal to this plane. The latter one is governed by the ordinary refractive index n_0 whereas the parallel polarized light is determined by the extraordinary refractive index n_{eo}. In order to utilize the birefringence for phase-matching the two waves have to be polarized contrarily, i.e. $\beta_\perp(\omega) = \beta_\parallel(2\omega)$. The exact type of index dependence of the SH beam is determined by whether the particular crystal is positive ($n_{eo} > n_o$) or negative ($n_{eo} < n_o$). Hence, one has to differentiate between two types of phase-matching.

Type I phase-matching in both kinds of crystals with equally polarized fundamental waves and Type II phase-matching with contrarily polarized driving fields. For the first type the relevance of equation (2.37) becomes obvious because with a period of $2l_c$ the SH amplitude performs the sine-like behavior mentioned above resulting in destructive interference as the phase velocity is different. An overview of the various types of birefringent phase-matching is given in Table 1.

Type	Positive crystal	Negative crystal
I	$eo(\omega)eo(\omega) \rightarrow o(2\omega)$	$o(\omega)o(\omega) \rightarrow eo(2\omega)$
II	$eo(\omega)o(\omega) \rightarrow o(2\omega)$	$o(\omega)eo(\omega) \rightarrow eo(2\omega)$

Table 1: *The different types of birefringent phase-matching in uniaxial crystals.*

Those different types of birefringent phase-matching are also to be classified in terms of a critical and noncritical manner. For an orthogonal incidence ($\theta = 90°$) regarding the axis of the nonlinear tensor and a certain temperature tuning the phase-matching is noncritical whereas for angles unlike 90° it is referred to as critical phase-matching. Besides uniaxial crystals birefringent phase-matching can also be utilized in biaxial crystals which represent a more complex case due to the ambiguous determination of the two waves. Figure 2.2 illustrates the phase-matching type I via an index ellipsoid in which the harmonic (2ω) is polarized extraordinary (phase propagation along ellipsoidal planes with constant phase relation) and its fundamental wave exhibits the ordinary polarization (phase propagation along surface of a sphere). The phase adjustment angle to the optical axis is in the intersection of the refractive index ellipse of the extraordinary polarized ray of the harmonic and the refractive index circle of the ordinary polarized ray.

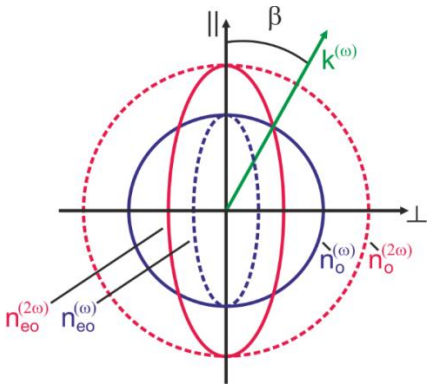

Figure 2.2: *Index ellipsoid to demonstrate the behavior of ordinary and extraordinary indices for birefringence and SHG taken from* [40].

This kind of phase-matching on the one hand provides the most efficient SHG intensity exploitation, c.f. Figure 2.3, but is on the other hand restricted in terms of unsuitable phase-matching temperatures as well as angles [41], the barely addressing of lower nonlinear coefficients [41] and a Poynting-vector walk-off [31]. The highest nonlinear tensor element d_{33} cannot be addressed because for this all relevant waves feature the same polarization. Moreover the entire spectral range is not covered for this technique. Those drawbacks lead to the alternative technique quasi phase-matching.

Quasi phase-matching:

A more elaborate but lavish way to achieve a very efficient phase-matching regime is the quasi phase-matching technique proposed in the 1960's by Armstrong et al. [42], [43] followed by the practical realization [44] in the next decades. The aforementioned sine-like behavior of the second-harmonic amplitude because of unequal phase velocities and thus a phase displacement is resolved within this technique via a special treatment of the material properties, i.e. the spatial tailoring of the nonlinear tensor.

In contrast to birefringent phase-matching this additional material treatment comprises a periodic modulation of the tensor with a doubled period of the coherence length l_c. The technological implementation of this periodic modulation respectively periodic polarization reversal is referred to as periodic poling of the investigated materials in this work within the subchapters of chapter 2.2.2.

According to the dependence of the SHG intensity on the sinc-function (2.38) the intensity only increases up to the length $L = \frac{\Delta kL}{2} = \frac{\pi}{\Delta k}$ for an unmodified material and decreases in the range of $\frac{\pi}{\Delta k} < L < \frac{2\pi}{\Delta k}$:

$$I_3 = I_{2\omega} \propto L^2 sinc^2\left(\frac{\Delta kL}{2}\right) = \left(\frac{2}{\Delta k}\right)^2 \sin^2\left(\frac{\Delta kL}{2}\right) \tag{2.38}$$

This case is illustrated in Figure 2.3 with the blue curve indicating no phase-matching. The approach of QPM is to reverse the value of the effective nonlinear tensor d_{eff} into $-d_{eff}$ after the coherence length l_c. Therefore, the SHG amplitude is enhanced instead of decreased, as the former oscillation would lead to.

The comparison in Figure 2.3 between a QPM amplitude slope (green) and a BPM one (red) shows the lowered increase of a QPM amplitude but with QPM one is able to obtain a huge amount of advantages as most prominently the d_{33} addressing, widespread wavelength regime and different interaction possibilities. Beyond this the Poynting vector's direction holds for all involved waves, hence no walk-off is at hand and the QPM technique is applicable to isotropic as well as anisotropic materials.

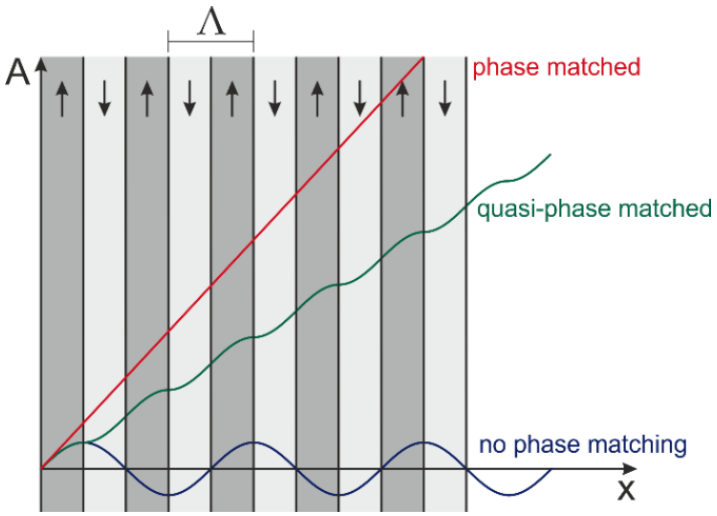

Figure 2.3: *Progression of the particular amplitudes of a second harmonic signal in a quasi-phase matched regime, for ideal phase matching and without phase matching.*

The coupled modes diverge at the l_c to the phase difference of π, c.f. coupled wave equation (2.25). For the case of QPM l_c stops at one particular point – the domain boundary – and with the inverted internal polarization an additional phase difference of π is added and the modes are cophasal again and the nonlinear amplitude is enhanced up to $L = \frac{2\pi}{\Delta k}$. This coherence length is then given by [45]:

$$l_c = \frac{2\pi}{\Delta k} = \frac{\lambda}{2(n^{2\omega_1} - n^{\omega_1})} \tag{2.39}$$

Reaching this length the enhancing process is reset and recurs leading to the characteristic staircase-like enhancement slope portrayed in Figure 2.3. It should be noted that the respective amplitude is oscillating with half of the respective intensity's frequency. In order calculate any desired period length to utilize the advantage of the widespread wavelength window and design a particular periodically poled structure one has to consider the spatial dependence of the nonlinear tensor in terms of a Fourier series:

$$d(z) = d_{eff} \cdot \operatorname{sign}\left[\cos\left(\frac{2\pi z}{\Lambda}\right)\right] = d_{eff} \cdot \sum_{m=-\infty}^{\infty} G_m \cdot e^{ik_m z} \tag{2.40}$$

This equation features the characteristic vector for the desired periodic grating $k = \frac{2\pi n}{\lambda}$, whereas the Fourier coefficient is defined as $G_m = \frac{2}{\pi m}\sin(\pi m D)$ including the duty-cycle $D = \frac{l_p}{\Lambda}$ for a length l_p with a positive nonlinear coefficient. Taking into account a 50:50 duty-cycle like in Figure 2.3 the maximum of the increased amplitude is achieved which also holds for the effective nonlinear tensor $d_{eff} = \frac{2}{\pi m} d$ [39], [46]. From the coupled amplitude equation (2.25) one can now derive an expression for the SHG amplitude with the aforementioned prerequisites (note: C comprises the negligible rest of eq. (2.25)):

$$\frac{d}{dz} A_3(z) = C \cdot e^{-i\Delta k_{QPM} z} \qquad \text{with} \quad \Delta k_{QPM} = \Delta k - k_m \tag{2.41}$$

The amplitude is obtained via integration along the direction of propagation and at the point $z = L$ and the following relation holds:

$$\int_0^L e^{-i\Delta k_{QPM} z}\, dz = 2 \cdot \frac{e^{\frac{-i\Delta k_{QPM} \cdot L}{2}}}{\Delta k_{QPM}} \cdot \sin\left(\frac{\Delta k_{QPM}}{2} \cdot L\right) \tag{2.42}$$

$$A_3(L) = C \cdot L \cdot e^{\frac{-i\Delta k_{QPM} \cdot L}{2}} \cdot \operatorname{sinc}\left(\frac{\Delta k_{QPM}}{2} \cdot L\right) \tag{2.43}$$

The purpose of the QPM mechanism is reached at $\Delta k_{QPM} = 0$ and the amplitude is only dependent on the length L. This condition is fulfilled for the following equation regarding the wave vectors:

$$\Delta k_{QPM} = k_{2\omega} - 2k_{\omega} - \frac{2\pi}{\Lambda} = 0 \tag{2.44}$$

The expression for the domain grating period is calculated by using the expressions for the two wave vectors $k_{2\omega} = \frac{2\pi n(2\omega)}{\lambda_{2\omega}}$ and $k_{\omega} = \frac{2\pi n(\omega)}{\lambda_{\omega}}$. For any given material the Sellmeier equation can be used to calculate the desired period length. In the upcoming subsections the respective equations and corresponding coefficients are stated for the materials investigated in this work. Using [46] the final formula for the grating period is given as:

$$\Lambda = \frac{\pi}{\Delta k} = \frac{\lambda_{\omega_1}}{2\left(n_{\omega_3} - n_{\omega_1}\right)} \tag{2.45}$$

In general it has to be noticed that the QPM mechanism is also dependent on external influences like temperature and thus an alteration of the material extensions. Furthermore the refractive index is also affected from this [47], [48]. Several prominent materials like Potassium titanyl phosphate (KTP) for QPM via periodic poling unfortunately feature a low damage threshold. Hence, BPM is still applied in more resilient materials like β-Barium borate or Lithium triborate [31].

The Sellmeier equation mentioned above is dependent on different crystal classes. As to be seen in the section dealing with the respective material characteristics the Sellmeier equation of KTP is for example given via [49]. This material is a positive biaxial crystal, thus all three Cartesian directions have to be accounted for resulting in three distinguished refractive indices $n_z > n_y > n_x$.
In turn Lithium niobate features a hexagonal crystal structure and is hence uniaxial. The corresponding Sellmeier equation can be taken from [48]. The differentiation between an ordinary and extraordinary ray is here as crucial as it is for the calculation of BPM.

All the derivation for the final equation (2.47) holds in general for domain periods in bulk crystals. In this work not only periodically poled bulk crystals are investigated but also waveguide structures in bulk and thin film crystals. For those advanced material platforms the calculation is more elaborate and may lead to a correction of the pump wavelength for example because waveguide structures can impose a certain shift of the wavelength. This issue can be overcome via methods of perturbation theory like the Wentzel–Kramers–Brillouin approximation (WKB) [50], the Hocker and Burns' numerical method [51], FEM [52], [53] or a kind of brute force method to obtain the refractive index via each mode.

2.1.3 Further nonlinear processes

Besides second-harmonic generation, the field of nonlinear optics features a widespread palette of effects of second as well as higher order that are the basis for single photon emission or numerous frequency conversion devices. Here, a brief outline of those further nonlinear processes is given.

Mixing of frequencies:

While SHG describes the distinguished formation of overtones of a fundamental frequency or more precise of two excitation fields $\vec{E}_1$ and $\vec{E}_2$ whereas the general case of such a frequency mixing is referred to as sum-frequency generation (SFG). Thus, SHG represents a special case of SFG using the same incoming frequency ω, but two different frequencies ω_1 and ω_2 can be utilized to create the sum of them, c.f. Figure 2.4 a) and b). Analogously the same holds for a generated wave resulting in the difference of both excitation fields as referred to as difference-frequency generation (DFG). According to equation (2.13) it yields for those two processes:

$$\vec{P} = \epsilon_0 \tilde{\chi}^{(2)} \left(\vec{E}_1^2 \cos^2(\omega_1 t) + \vec{E}_2^2 \cos^2(\omega_2 t) + 2\vec{E}_1^2 \vec{E}_2^2 \cos(\omega_1 t) \cos(\omega_2 t) \right) \qquad (2.46)$$

Both processes can be delineated as a creation and annihilation of the involved photons, whereas for SFG the two incoming low energetic photons are annihilated and a higher energetic photon is created.

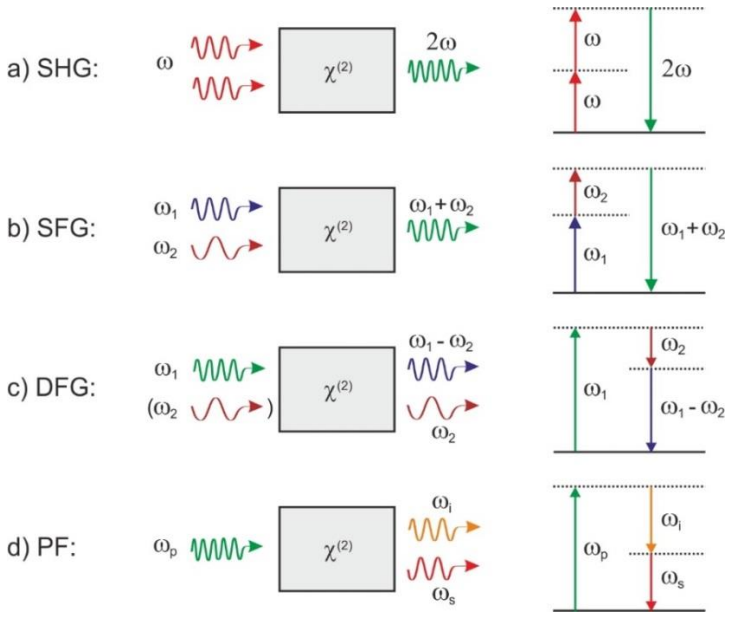

Figure 2.4: *Scheme to exemplify the various types of frequency mixing processes a) second-harmonic generation, b) sum-frequency generation, c) difference-frequency generation and d) parametric fluorescence taken from* [40].

The opposite holds for DFG. Here, two photons $\omega_1 > \omega_2$ enter a nonlinear medium and ω_1 is annihilated in favor for ω_2 and a new photon ω_3, so that it holds $\omega_3 = \omega_1 - \omega_2$. The lower energetic photon is amplified since it triggers a stimulated decay of the excited state from ω_1.

Optical rectification:

Based on equation (2.13) and utilizing certain addition theorems the polarization may also comprise the components $\vec{P} = \vec{P}_1 + \vec{P}_0 + \vec{P}_2$. Besides the obvious linear term $\vec{P}_1$ and the SHG term $\vec{P}_2$ a further constant and frequency-independent component $\vec{P}_0 = \frac{\epsilon_0}{2}\chi^{(2)}\vec{E}_0^2$ arises and is called optical rectification. That implies that this term does not contribute to any generation of a newly induced wave, but creates a sort of DC-field in the particular nonlinear crystal due to the fact that the sign change of $\vec{P}$ is not collinear respectively parallel to the respective change of the applied field. Hence, a sinusoidal oscillation of the excited ions is observable. This effect has been discovered in 1962 by Ward et al. in KDP crystals [54].

Spontaneous parametric down-conversion:

In the course of this work, various periodically poled structures are investigated from which some shall serve as a platform for single photon emission sources especially for heralded respectively entangled photons. This can be achieved via spontaneous parametric down conversion (SPDC). In contrast to second-harmonic generation SPDC is a fluorescence process seeded by vacuum-fluctuations. A photon-pair is created yielding the frequencies $\omega_{pump} = \omega_{signal} + \omega_{idler}$ according to energy conservation. Nevertheless, the process also demands an intense radiation field like for SHG. Alike to SHG a successful phase-matching is crucial here – in contrast to amplified spontaneous emission (ASE) - and furthermore momentum conservation forces that the two resulting photons propagate under a smaller angle.

The type of the SPDC process is distinguished between the particular polarization of either the pump photon and the polarization state of the signal and idler photon. If all three polarizations are parallel to each other type-0 SPDC is at hand, whereas the output photons are equally polarized but orthogonal to the pump photon it is called type-1 SPDC and type-II describes the perpendicular case of the output photons. Therefore, the polarization state of the output photons is correlated. For quantum optic experiments this enables the prediction of one polarization state by knowing the other one, which is given by the two correlated so called heralded photons. For this the technique of group velocity matching can be utilized [55]. The standard consideration of the propagation behavior of those two photons is the collinear case as they travel in the same direction along the optical axis of the crystal. This standard SPDC experiments can be found in numerous publications especially for waveguide patterns in bulk crystals exhibiting a strong mode confinement with high efficiencies [56]. Phase-matching as a measure to enable SPDC or enhance its efficiency is often created via birefringent phase-matching including all of its drawbacks like the determined collinear propagation for instance. Quasi phase-matching also offers more flexible options to treat a SPDC process. The periodic grating compensation $k_G = 2\pi/\Lambda$ is necessary to fulfill the momentum conservation. This leads to the phase mismatch $\Delta k = k_p - k_s - k_i - 2\pi/\Lambda$. QPM can also enable a non-collinear propagation case, referred to below as SPDC with counter-propagation, which offers many advantages over the standard case [57], [58].

The sign of the idler wave vector becomes positive for this arrangement $\Delta k = k_p - k_s + k_i - \frac{2\pi}{\Lambda}$ offering various other characteristics for the heralded output photons (Figure 2.5).

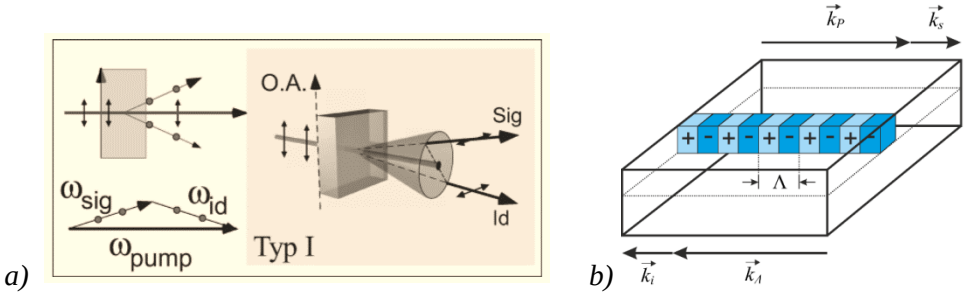

Figure 2.5: *Principle sketches for SPDC a) in type-I phase-matching regime showing energetically the course of the particular photons* [59] *and b) in counter-propagating arrangement including the QPM momentum circumstances and the grating period Λ.*

A counter-propagation arrangement forces the output photons the exit the crystal in the contrarious directions in order to not violate momentum conservation because the periodic grating contributes with the fitting momentum to compensate for the pump photon's one. The obviously most striking advantage of counter-propagating photons is their spatial separation by the retention of the heralded character. Additionally one can utilize the distributed feedback and distinct narrower frequency spectra which are helpful for a broad amount of fiber optics due to the smaller Δk. The group velocity mentioned above has not be taken into account here so severely because the spatially separated output photons may feature different wavelengths and a dichroic element can help to skim the pump photon. Nevertheless a counter-propagation arrangement makes some demands to the technological feasibility. The utilized wavelength is dependent on the order *m* and on the chosen SPDC type. Higher order *m* processes have been demonstrated so far but ideally *m* = 5, 3 or 1 is desired. For this, the crucial point is the fabrication of ultra-short domains (submicron range). In LN domain periods of several microns have been achieved, whereas for KTP a 3rd-order conversion process challenges the current investigations requiring periods between 1,0 µm to 1,2 µm and a 1st-order conversion process requires Λ = 0,35 µm - 0,40 µm [60]. This work gives insight into the recent investigation of both material platforms reaching the submicron poling limit and serve as a basis for SPDC heralded photon-pair sources.

Third-order nonlinear optical effects:

Despite the utilization of second-harmonic generation as a 2nd-order nonlinear optical effect in this work a brief overview of 3rd-order nonlinear optical effects shall be given. As motivated in subsection 2.1.1 SHG requires a non-inversion symmetry of the crystal. In crystals with an inversion-symmetric composition even terms within the Fourier series are canceled out here leaving the nonlinear cubic term and the further odd terms non-vanishing instead. This cubic term for instance enables for a dependence of the refractive index on the incident intensity $n = n_0 + \gamma|E|^2$. On the microscopic scale dipoles of the particular medium are rearranged – in the case of intense incident radiation induced by this radiation - which has a direct influence on the light-matter interaction like the refractive index manipulation.

THG: Besides an external d.c. field as the trigger for 3rd-order nonlinear optical effects can also be induced via three involved waves. For the case of three equal wavelengths ω analogous to SHG with two incident waves the process is called *third-harmonic generation* (THG) and the relevant tensor is here also given as $\chi^{(3)}$ [30]. The case for three different incident wavelengths is portrayed as FWM below. In comparison to typical SHG materials like $LiNbO_3$ or $KTiOPO_4$ prominent materials for THG are LiB_3O_5 or BaB_2O_4 [61].

Kerr effect: An occurrence of 3rd-order nonlinear effects is due to an intense external field, which can be a pure optical excitation, or also a d.c. field. The simplest effect represents the *d.c. Kerr effect* – also called quadratic electro-optic effect - at which the refractive index is proportionally altered to the squared d.c. field as outlined above. It is often to be found in electro-optic shutters [33]. As also mentioned above the refractive index can also be intensity dependent.

EFISH: In the framework of 3rd-order effects a second-harmonic can be generated connected to an external d.c. field. This phenomenon is called electric-field-induced second-harmonic (*EFISH*). Materials with a vanishing 2nd-order nonlinear tensor but a $\chi^{(3)}$ like Si, SiO_2 or Si_3N_4 can be utilized to create SHG via the control of an external d.c. field according to: $I_{EFISH} \propto \left|P^{(2)}\right|^2 = \left|\chi^{(2)}(E^{\omega})^2 + \chi^{(3)}(E^{\omega})^2 E^{DC}\right|^2$. This EFISH application has been demonstrated in p-i-n junctions for instance [62]. EFISH is also demonstrated for the nonlinear microscopy setup in this work as outlined exemplarily in section 3.3.

FWM: Hitherto frequency conversion processes with three involved waves have been discussed. 3rd-order effects also enable *general four-wave-mixing* (FWM). Here, in contrast to SHG two waves propagate coherently in opposite directions. A third wave can be bent off by those two waves and hence, a fourth wave is generated. This process is also very sensitive to the phase-matching conditions of the involved waves. Besides classical applications FWM can also be utilized for entangled [63] and single photon sources [64].

Self-focusing: The intensity-dependence of the refractive index in the 3rd-order effects framework can lead to an anisotropic change of the refractive index in terms of the beam profile. Due to the spatial distribution of such a profile, the refractive index is altered very drastically in the vicinity of the beam waist respectively the pulse center. In the range of the pulse edges, i.e. smaller intensities, the refractive index hardly changes. There is a phase curvature, since the optical path length is increased in the center. Thus the medium acts like a lens. which may also increase the effect in the beam center as a kind of feedback loop. Thus, the effect is called *self-focusing* [65].

2.2 Ferroelectric domains

The main focus of this work lies on the analyzation of periodically poled ferroelectric materials by means of spectroscopy and microscopy methods. In order to understand those results and further explanations for the contrast mechanism for instance one has to take a closer look at the fundamental nature of such ferroelectrics and the formation mechanism of domain walls as explicated in the following subsections.

2.2.1 From Curie temperature to spontaneous polarization

As introduced in section 2.1 ferroelectric materials draw their characteristic property from the spontaneous polarization. The occurrence of such a spontaneous polarization is directly connected to crystals with a distinguished polar axis. Those crystals are found within a cluster of 11 classes from the overall 21 non-centrosymmetric crystal classes. They lack an inversion center and thus have a polar axis enabling nonlinear processes like SHG. If a temperature dependence of the spontaneous polarization is present, these crystals are called pyroelectric. The temperature dependence of the crystals follows the *Curie-Weiss*-law which sets up a correlation between the optical susceptibility χ, the temperature and the so called Curie-constant C:

$$\chi = \frac{C}{T - T_C} \tag{2.47}$$

Two temperature regimes result from this law: Below the Curie-temperature T_C any domain formation is long-term stable and the phase is called ferroelectric, whereas at higher temperatures the spontaneous polarization disappears within the paraelectric phase. For the materials $KTiOPO_4$ and $LiNbO_3$ as investigated in this work T_C marks a point of a phase-change [66]. If the temperature is equal to T_C the phase transition is of 2nd order [67]. KTP features this second-order transition at a temperature of about 945 °C [68] and LN at 1140 °C [69].

This phase change is described within the Landau-theory. In such a 2nd order transition, a continuous displacement of atoms occurs, changing the symmetry in the considered region. A distinction is made between ferroelectrics, in which the polarization results from the arrangement of the atoms, and non-genuine ferroelectrics. Ferroelectricity in an electrically crystal arises from a displacment Δd of different charges Q in the unit cell of the crystal. According to [70] the resulting polarization is the sum of all dipole moments p_i within the unit cell:

$$P = \frac{1}{V}\sum_i p_i = \sum_i \Delta d \cdot Q_i \tag{2.48}$$

The spontaneous polarization can be perceived as an analogon of a thermodynamic balanced state. The equation above indicates that there is no time dependency. Landau-theory distinguishes between ferromagnetic materials only featuring 2nd order transitions whereas the electric counterpart does feature both orders. This discrimination is done via the order parameter M which may act steadily or like a Heaviside function. From Landau-theory the Gibbs-energy for such an entire transition is given in terms of the order parameter and local quantities:

$$G(p,T,M) = G_0(p,T) + \frac{A(p,T)}{2}M^2 + \frac{B(p,T)}{4}M^4 \tag{2.49}$$

The system is characterized via the parameters A and B. The order parameter is always zero for $T > T_C$ and for $T < T_C$ it converges slightly above zero. The transition to the paraelectric phase is performed as the order parameter and hence the polarization becomes redundant for $T > T_C$. Furthermore one can consider a transition from ordered to orderless states. Here, the order of the p_i vanish but the dipoles remain due to the temperature rise. Another case is a twist of two different subordinated crystal lattices against each other leading to a generation of dipole moments due to shifting ions as in perovskites for example. LN features both transition types whereas KTP is dependent on alternating Ti-O bonds.

The occurrence of the spontaneous polarization on the atomic scale at this transition point is derived in the following for both materials. For $LiNbO_3$ in the ferroelectric phase the Li^+ and Nb^{5+} ions are shifted in relation to the planes of the oxygen octahedrons along the optical c-axis, c.f. Figure 2.6. Hence a typical Nb-Li vacancy is apparent which reiterates periodically due to the crystallographic lattice. The direction of the displacement of the polarization equals the dipole moments. The oxygen atoms are grouped orthogonal towards the c-axis. For congruent $LiNbO_3$ with an excess of Nb some Li-vacancies and general vacancies are filled with Nb-atoms [71], [72].

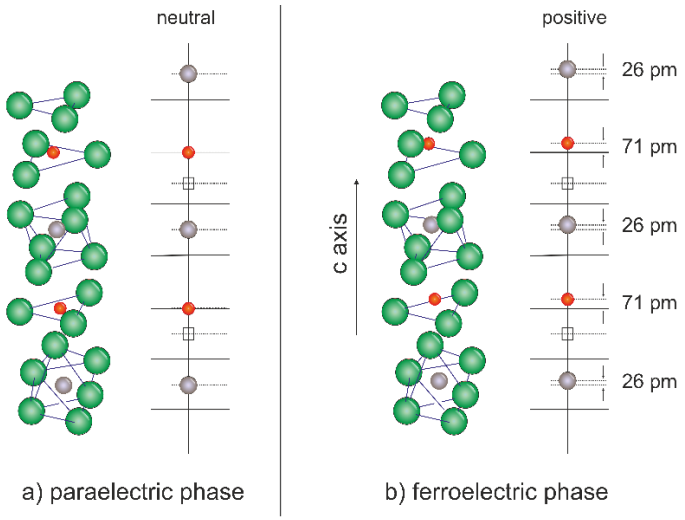

Figure 2.6: *Comparison of paraelectric and ferroelectric phase of $LiNbO_3$ via a ball-and-stick sketch.*

The paraelectric phase is characterized by the configuration that the Li- and Nb-atoms are not displaced but either centrally besides the oxygen atoms or centrally in between them. The calculated values for the displacement within Figure 2.6 taken from [73] hint that the cations are moving likewise on both stable positions.

The occurrence of the spontaneous polarization in $KTiOPO_4$ is based on another configuration of the involved atoms. For the case $T > T_C$ (paraelectric) the material features a higher symmetry within in its crystal group [35] whereas for $T < T_C$ the crystal composition is slightly changed and the lattice symmetry is reduced or lower. For KTP the potassium ions are capable to occupy two different positions within the lattice due to the Ti-O bonds. These bonds alternately vary in length, c.f. Figure 2.7 and hence also the Ti-ions of the octahedral can be on two positions. The potassium ions have a monovalent behavior and exhibit the possibility to be 8- or 9-fold coordinated in relation to the oxygen atoms as indicated by the two potassium atoms K(1) and K(2) in Figure 2.7. Together with the Ti-ions they lead to the spontaneous polarization in the material.

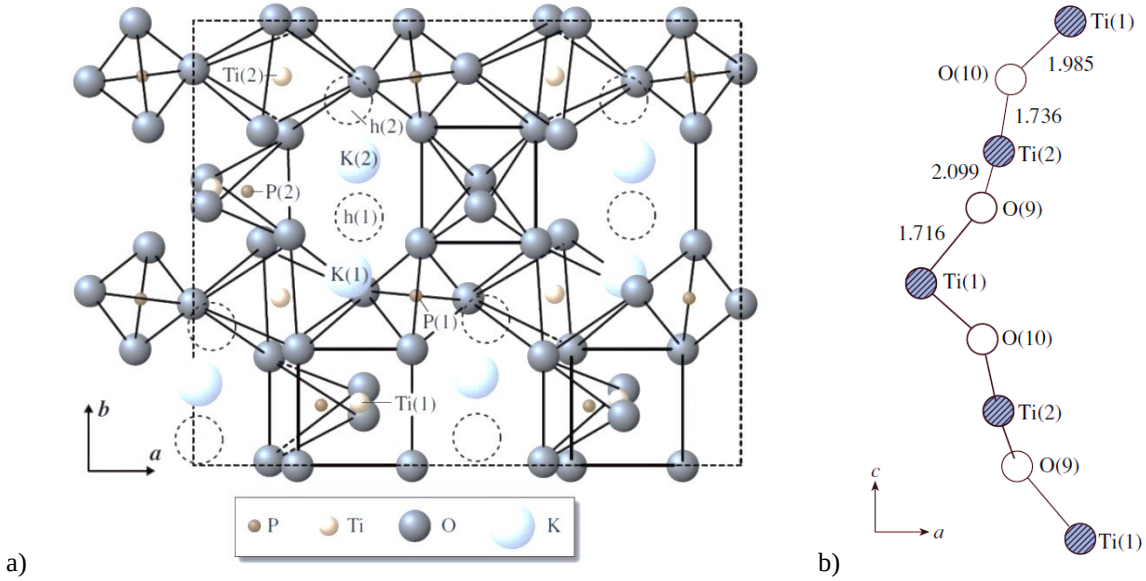

Figure 2.7: *a) Illustration of the changed crystallographic structure of KTP when a spontaneous polarization is at hand within the ferroelectric phase adapted from* [74]. *Potassium ions occupy the spotted locations. Axis a = x, axis b = y. Inset b) sketches the displaced Ti octahedrons as the origin of the spontaneous polarization in KTP from* [75]. *Axis a = x, axis c = z.*

A comprehensive understanding of the exact reason for the nonlinear properties i.e. the occurrence of the spontaneous polarization is still not at hand but two aspects have already been investigated. According to [76] the alternating Ti-O bonds give rise to an enduring dipole moment along the c-axis. They act as one-dimensional channels with the two possibilities for the titanium as ions or octahedrons to occupy a site. Furthermore the tetrahedrons of the PO_4 bonds as well as the potassium-oxygen bonds can also be a reason for the occurrence of the spontaneous polarization [77]. The replacement of the potassium with other elements prominently rubidium as it is used for the waveguide fabrication is apparently very crucial for the nonlinear properties of KTP especially for the domain inversion characteristics. Since the general features of the occurrence of the spontaneous polarization on an atomistic level and for both materials have been explained, the polarization reversal and the properties of ferroelectric domain walls will now be examined in the next subsection.

2.2.2 Aspects of domain inversion

With the knowledge that ferroelectric crystals are capable of providing a long-term stable phase for domains below the Curie-temperature one can discuss their formation and applications. According to [78] and [79] the spontaneous polarization, which is inherent in the previously discussed materials, can be reversed by exceeding coercive field strength. For LN this can be achieved by applying an external electric field in the range of kV per mm. A spatially confined area of a distinctly oriented spontaneous polarization is called a ferroelectric domain and adjoined domains with different polarizations are separated by ferroelectric domain walls.

A full polarization reversal shows a nonlinear behavior and is depicted as a hysteresis curve in Figure 2.8. The hysteresis behavior is related to ferromagnetic materials but shows a steeper shape in general. Furthermore, ferroelectric domains are connected to distinguished axis of the particular crystal. Hence, the possible ways to orientate the polarization are given via the ratio between the symmetric elements between the para- and ferroelectric phase and this leads to the differentiation of uniaxial and biaxial (or multiaxial) ferroelectric materials. The hysteresis curve shown in Figure 2.8 starts in the origin of the diagram when a pristine ferroelectric crystal is subjected to an external electric field E exceeding the coercive field strength $+E_c$ and reaches its maximum at a saturated point (2) where all dipoles are orientated parallel to the external field. In addition to this the rare case of dielectric charging in a ferroelectric crystal is indicated as point (3) in the figure. In order to reverse the polarization the same external electric field has to be applied but with the opposed polarity passing the point of the contrary coercive field $-E_c$ and eventually reaches the point of saturation (6 lower left). Coming from point 2/3 the point 4 indicates the value of the residual polarization $+P_r$ which stays in the material when the external field is turned off.

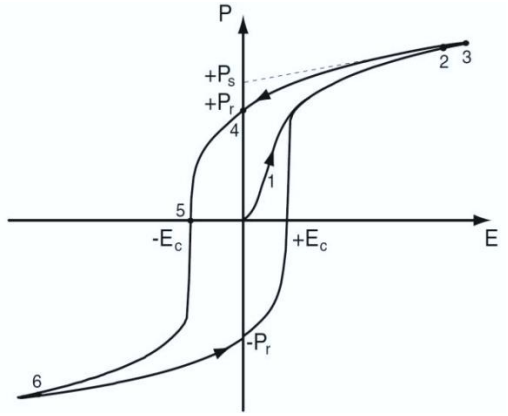

Figure 2.8: *Sketch of the hysteresis loop of a full polarization reversal within a ferroelectric material in dependence of an applied external electric field adapted from* [80]. *It starts in the origin of coordinates and follows the delineated arrows.*

The compensation of the material surface charges is done via the so called displacement current, which can be estimated by the equation $Q = 2 \cdot P_s \cdot A$, where a charge Q is determined via the spontaneous polarization P_s and the considered area A. Besides the description of a domain reversal in terms of the hysteresis loop the spatial evolution of an emerging domain is also very crucial for the understanding of domain dynamics. Typically electric field assisted poling is the method of choice for domain inversion in ferroelectrics.

Here, an external electric field is applied via electrodes in an antiparallel way towards the existing internal polarization (Figure 2.9). The poling process starts with the growth of inverted domains from nucleation spots via nano-domains that grow in forward and lateral direction with different growth velocities to finally form a homogeneous domain. For KTP domains grow along the c-axis with 50 up to 200 µm/s whereas the y- and x-directions only with 10-30 µm/s and 0.2-1.2 µm/s respectively [81]. In case of LN domain growth velocities along the a-axis are in the order of 30 µm/s [82].

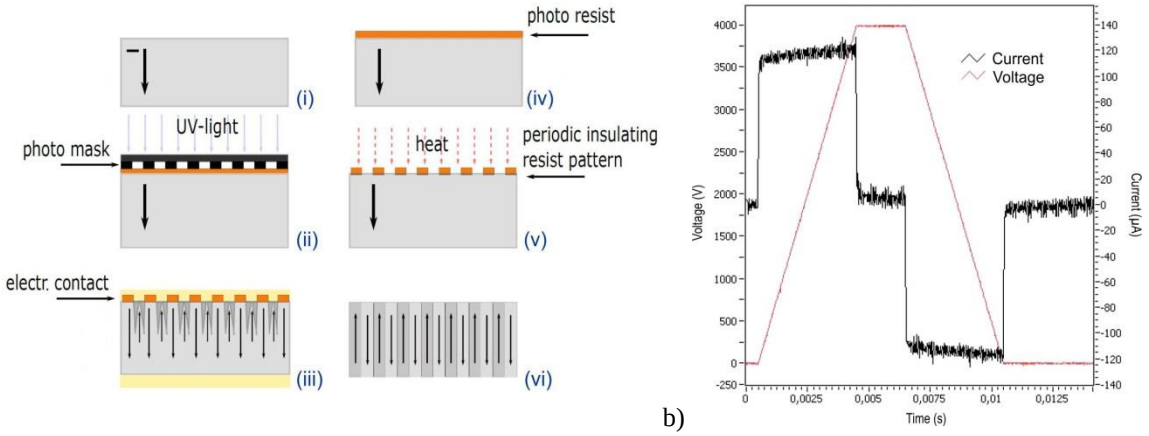

Figure 2.9: *a) Schematic for electric field assisted poling with details of the domain inversion process* [83]. *b) Graph of example pulse for domain reversal in ferroelectrics with course of voltage (red) and current (black) for a constant slewing-rate* [84].

Different samples of one material may feature various coercive fields strengths due to factors ranging from defects over vacancies to intended modifications like doping. For the characterized material systems within this work the coercive field strengths are about 2,1 kV/mm for flux-grown KTP [81] and approximately 21 kV/mm for congruent LN [85] (whereby these values are in the range of the particular spontaneous polarization P_s).

The design of the electrical pulse shape is one of the crucial aspects for a successful poling process. Depending on the particular sample and material different poling pulse designs have to be utilized. The samples analyzed in this work are commonly poled via the high-voltage generator Trek 20/20c. The corresponding equation for the electrical context here yields $I = (C_{load} + C_x) \cdot dU/dt$, where C_{load} describes the capacitive part of the generator's output impedance and C_x the one of the external circuit. The derivative is responsible for the steepness of the rising or falling slope [84]. The pulse shape shown in Figure Figure *2.9* b) is typical for a ferroelectric domain inversion. One advantage over a square wave pulse is the slower rising slope. This reduces the current peak that occurs when charging the capacitors is reduced. From a constant slewing rate follows a constant current according to formula above. Thus, during charging and discharging of the capacitance, a rectangle is generated in the current. The decreasing slope is necessary to avoid a back-switching of the domains while growing through the material by stabilizing them, see [84], [86] for further details. This can be improved via an additional DC-offset. Besides the shape of one single pulse the application of multiple pulses has drawn much attention in recent investigations on poling experiments considering the number and duration of the pulses [87]. The impact of these different pulse characteristics is also subject of the samples investigated in this work.

The fabrication of high aspect ratio domain gratings throughout the whole depth of bulk-substrates using the conventional electric field is influenced by inherent non-uniformities and intrinsic defects.

Furthermore extrinsic doping has an additional impact on the poling properties. To circumvent this problem surface-near domain inversion has been applied, where the field modulation contrast is highest. Such surface periodic poling approaches (SPP) are well suited for nonlinear optical waveguide devices where light is confined to a thin surface guiding layer or stripe. The most important SPP techniques are e-beam writing [88], direct writing using focused UV-laser radiation [89], phase mask assisted all-optical poling with UV-light [90], EFM based techniques [91], controlled overpoling [92], full cover electrode method [93] and stemper technique [94]. Direct e-beam writing promises the highest field modulation contrast, but the local deposition of electronic charge on a grounded substrate by e-beam bombardment can easily create local electric fields that surpass the coercive field strength significantly [95]. The direct writing techniques using UV-light suffer from the diffraction limited soft intensity modulation, which together with defects in the substrate leads to strong variations of the domain duty cycle and wall imperfections. Contolled Overpoling and the stemper method seems to be promising strict periodicity without any stitching errors [9].

Switch of polarization:

For applications with periodically poled domain structures the transition of 180° domains with contrarily polarity are taken into account. For the evolution of the material polarization throughout a domain boundary different types of domain walls can be defined (Figure 2.10). Ferromagnetic domain walls are mostly formed in the so-called Bloch- or Néel-type. The Ising-type of domain walls is much more of note for this work since it describes the behavior of ferroelectric domains.

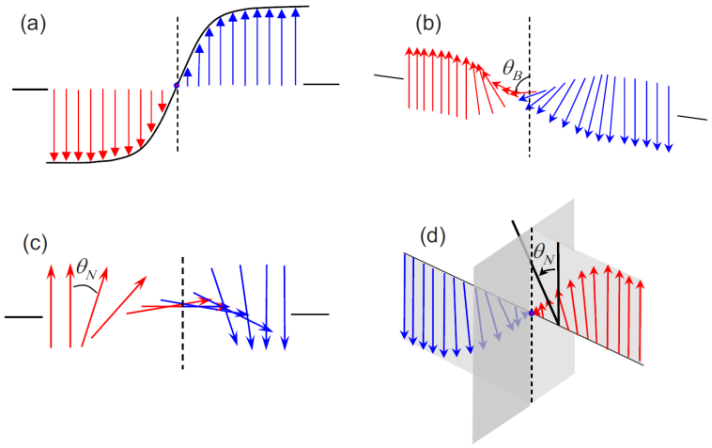

Figure 2.10: *Collocation of different types of domain walls: (a) Ising-, (b) Bloch-, (c) Néel- and (d) Ising-Néel type* [96].

Here, the transition from one domain to another is governed by an interplay between the material strain and the ruling polarization. Such a domain transition commonly takes place in the extent of a couple of unit cells (several hundreds of nm). Within the scope of optical resolution and measurement methods the quantification of the domain wall width is also subject of various investigations and a big challenge within the ferroelectrics community. In real systems such a behavior is disturbed by point-like defects and defect structures which can completely pin a domain wall in terms of an energy exchange.

Structure sensitive methods:

In order to visualize the transferred ferroelectric domain structure a pool of methods is at hand. An invasive method utilizes chemical etching for a surface near characterization. Here, one exploits the anisotropic circumstance that the contrary poled areas feature different etching rates; hence the periodic structure is transformed to the surface topology. The detrimental side of this method is its irreversible character and its dependency on the crystallographic structure and orientation (applicable on z-cut LN, but hardly in x- or y-cut LN).

Another surface-sensitive method is the piezoresponse force microscopy (PFM). As a non-invasive method it uses a back-electrode-contacted sample and sensitively scans its surface with a cantilever by means of the arising fields. A ferroelectric domain structure becomes visible via the material strain which occurs at domain walls. However, this method is also limited to the surface-near region. For a depth-dependent characterization of the domain structure here the samples have to be layer-ablated and therefore it becomes an invasive method.

Two established non-invasive methods for the 3-dimensional analysis are the SH-microscopy and the µ-Raman spectroscopy which both allow for imaging the ferroelectric domain structure in the confocal regime. These latter two methods are applied within this work.

2.3 Ferroelectric material systems

Due to their versatile properties LN and KTP represent well established platforms within the field of integrated optics especially for $\chi^{(2)}$–based nonlinear processes. They exhibit large electro-optic, elasto-optic, piezoelectric and nonlinear coefficients. Within these materials domain grids enable efficient quasi phase-matching in bulk and waveguide structures. Amongst others, such periodically poled domain structures are essential for many applications in the field of quantum optics, where single photon propagation as well as pure quantum states are crucial. The general characteristics of the two material systems used here are described below.

2.3.1 $LiNbO_3$ platform

Lithium niobate is a prominent ferroelectric material originating from the ABO_3 ferroelectric cluster accompanied by $LiTaO_3$ and $BaTiO_3$ for instance within the perovskites and yields the space symmetry group *R3C* and the *3m* point group when considering the ferroelectric phase [97], [98]. This group obviously features an oxygen octahedron. The ferroelectric character of the material has been confirmed by the hysteresis behavior of the material polarization dependent on the applied electric field. Besides the optical nonlinearity further important properties are its piezo- and pyroelectricity, electro-and acousto-optical traits as well as photo-refractivity [99]–[103].

LN is pulled via the Czochralski process [47], [104] from the melt consisting of the two ingredients Nb_2O_5 and Li_2O. One can either fabricate stoichiometric LN ($[Li_2O]/[Li_2O+Nb_2O_5]$ = 50 mol%, c.f. Figure 2.11), which is to be found within the lithium depleted area or congruent LN which features a ratio of [Li]/[Nb] = 0.969, hence a distinct part of lithium is deficient within the crystal as well as in the melt.

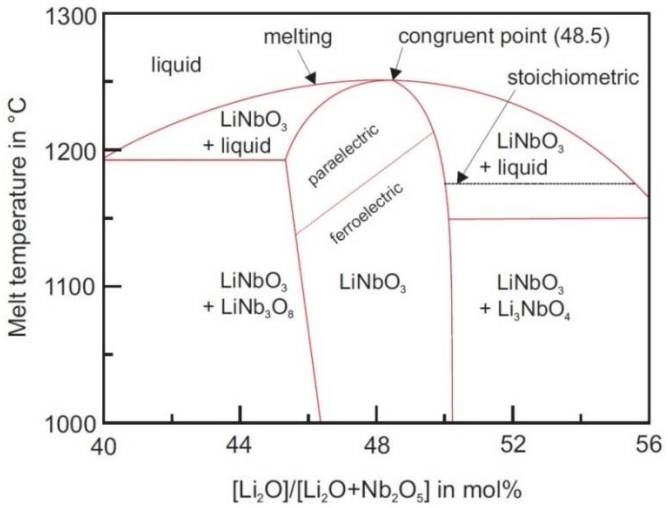

Figure 2.11: *Plot of phase diagram of LN according to its Li_2O-Nb_2O_5 melt system* [105], [106].

Congruent LN features a homogeneous ratio of lithium and niobium over the entire crystal along the crystallographic c-axis in the melt, whereas stoichiometric LN depicts variations of this ratio here.

According to [105] a spread of about 10^{-3} of this ratio can lead to crucial influences regarding the aforementioned optical properties of LN and in terms of the quality commonly congruent LN is widely used instead of stoichiometric. The congruent point is reached at a temperature of 1253°C featuring an equilibrium of fluid and solid phase. Due to the lithium deficiency, the crystal exhibits a larger amount of antisite defects which leads to so called $LiNbO_3$ islands within a phase separated temperature region.
As to be seen in Figure 2.12 the crystallographic c-axis (or z-axis) is determined by the lithium and niobium cations as well as a vacancy with respect to the oxygen sub lattice. Hence, the crystal features a permanent dielectric polarization along this axis and these occurring stacking sequences.

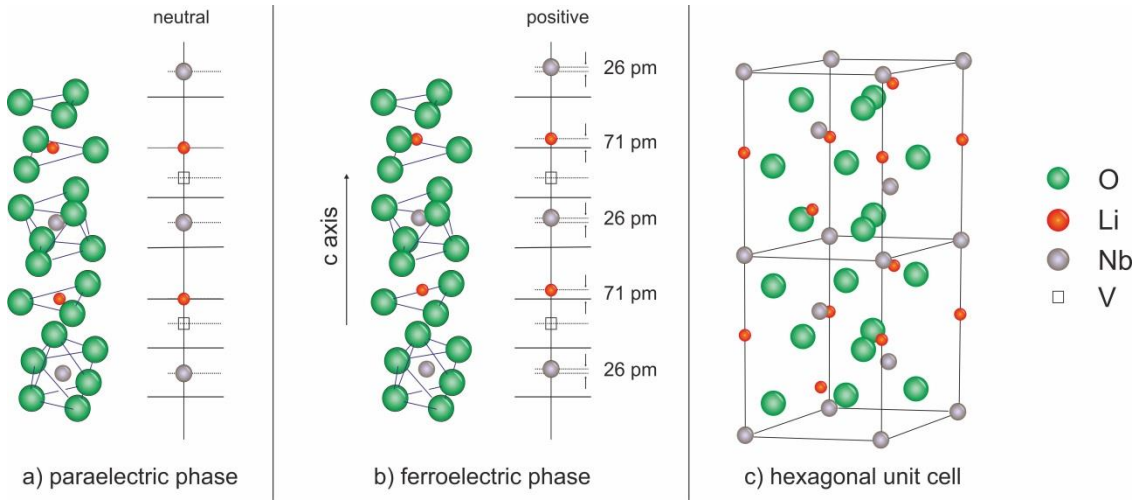

Figure 2.12: *Sketches of the crystallographic structure of $LiNbO_3$ adapted from* [40]*: a) paraelectric phase, b) ferroelectric phase, c) unit cell.*

The oxygen atoms are placed orthogonal to the c-axis. Below 1145°C LN is ferroelectric and the inversion symmetric paraelectric phase is settled above. Here, the lithium atoms are shifted to be central within the oxygen planes and the niobium ones are between them in contrast to the ferroelectric phase. The direction of this shift from the para- to ferroelectric phase is directly correlated to the spontaneous polarization, so that the positive direction of this axis is determined via cooling induced positive charge surplus, whereas the y-axis' positive direction via a negative charge surplus at the crystal surface. Furthermore, the aforementioned properties like pyroelectricity are deduced from the resulting anisotropy of this shift. Since the position of the crystallographic axes for the trigonal crystal symmetry is not unambiguous, there are also several possibilities for lithium niobate to define the crystallographic axes, these are then arranged rhombohedral, hexagonal and orthohexagonal. For the optical observation the orthohexagonal system is generally used to which all tensors of the lithium niobate refer.

Congruent LN shows a dependency of the Curie temperature from its stoichiometric ratio in accordance with the relation $T_c = 9095.2 - 369.05 \cdot C + 4.228 \cdot C^2$ [107]. The coercive field strength is given amongst other crucial material properties in Table 2 whereas the internal electric field is approximately 21 kV/mm for congruent LN. Furthermore congruent LN shows a distinct asymmetric behavior when multiple polarization reversals are performed; also the coercive field strength rises. Here, the internal electric field is equal to half of the difference of forth and back poling field strength [85]. This behavior does not apply for stoichiometric LN whose internal field is dependent on the niobium concentration.

Material trait	*Stoichiometric LN*	*Congruent LN*
Dielectric constants ϵ_{11}^T, ϵ_{33}^T for low ν	54, 42	84, 30
Dielectric constants ϵ_{11}^S, ϵ_{33}^S for high ν	42, 41	44, 29
Refractive index n_o, n_e (for λ = 633 nm)	2.288, 2.190	2.286, 2.203
NL coefficients (for λ = 633 nm): d_{33}^S, d_{31}^S, d_{22}^S (pm/V)	42, 5, 2.5	34, 6, 3
Coercive field strength (kV/mm)	0.2 - 4	21
Curie temperature (°C)	1206	1140
Pyroelectric coefficient ($\mu C/m^2K$)	-	95
Sellmeier coefficients A_1, A_2, A_3 and A_4 for n_0	4.9048, 0.11775, 0.21802, 0.027153	
Sellmeier coefficients A_1, A_2, A_3 and A_4 for n_e	4.5820, 0.09921, 0.21090, 0.021940	

Table 2: *Overview of crucial properties of stoichiometric and congruent $LiNbO_3$ with values taken from* [69], [72], [85], [108]–[113].

Further properties of $LiNbO_3$ are its optical transparency range which is between 350 nm where absorption begins up to the point of phonon-absorption at about 5000 nm [40]. Due to the uniaxial optical built-up of the crystal the material is birefringent and features an ordinary and an extraordinary refractive index n_0 and n_e, whereas the latter one is lower than the first and both can be calculated via the Sellmeier equation which yields [111]:

$$n^2 = A_1 + \frac{A_2}{L^2 - A_3^2} - A_4 L^2 \tag{2.50}$$

These calculated refractive indices are used in combination with the definition of a wave vector k_i for the determination of a desired domain period Λ for quasi phase-matching.

The utilization of very intense light fields may cause optical damage to the material which manifests as a light induced refractive index change. According to [114], [115] a doping with MgO for instance can drastically reduce the photo refractivity and hence increase the damage threshold.

2.3.2 $KTiOPO_4$ platform

Since the first synthetization of KTP at the end of the 19th century by Ouvrard [116] and the nonlinear optical characterization in the 1970s by Zumsteg et al. [76] the material has become a major material platform for the modern fields of integrated and quantum optics [15], [81]. Besides the aforementioned material properties it features a very high optical damage threshold and a wide transparency range. A special property of the material is its ionic conductivity [23], [75], [117].

KTP is classified to a crystal family with the general notation $MTiOXO_4$ which then includes all its isomorphs. The place marker M can include elements like potassium, thallium, rubidium or ammonium for instance, whereas the place marker X holds for phosphorus or arsenic. In case of rubidium exchanged waveguides in KTP the most likely notation here is $K_xRb_{1-x}TiOPO_4$. For all combinations an orthorhombic structure is present and they belong to the point group *mm2* (room temperature); respectively space group $Pna2_1$ [35]. Figure 2.13 shows a brief overview of the crystallographic structure of KTP and indicates within its dotted frame that the unit cell is built up of 64 atoms.

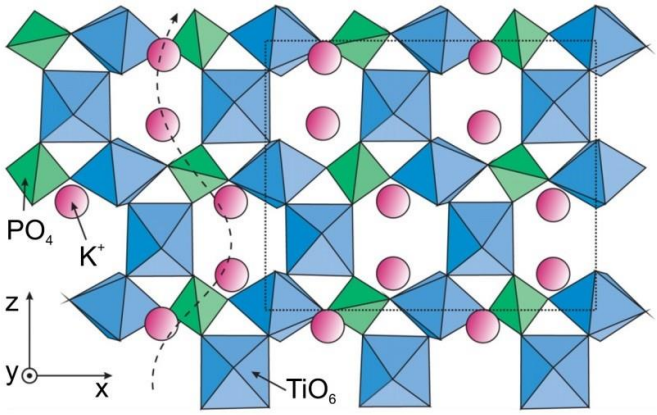

Figure 2.13: *Texture of KTP crystallographic structure as seen for the xz-plane. Potassium ion channels are indicated with dotted line, responsible for the ionic conductivity* [118].

The crystallographic structure consists of phosphorus oxide that forms tetrahedrons and the titanium oxide which builds octahedrons. Additionally the figure also indicates with the dotted sine-like line that the hedral texture leads to the situation that the remaining highly coordinated potassium ions are set up like a rope that has the effect of a channel. Regarding its bonding those ions either connected to the tetra- or octahedral oxygen atoms. These positions are called *K1*- or *K2*-site. Such a rope-like sequence of the potassium ions results in a polar behavior which might be connected to the ionic conductivity originating from a translation of the potassium vacancies. According to [81] this conductivity is much stronger along the crystallographic c-axis (z-axis) as compared to the other two axes. Beyond this KTP's ionic conductivity is governed by its certain stoichiometry. For this, one has to distinguish between flux-grown or hydrothermally grown KTP.
Due to the non-stoichiometric structure of flux-grown KTP more potassium ions are at hand and therefore the ionic conductivity increases. This can be circumvented with an immersion in a KNO_3 bath [119] or a lowered temperature during the growth process [120] which may lead to an almost disappearing ionic conductivity at the expense of an increasing coercitivity [121].

The flux-growth process is defined within a temperature region between 700°C and 1000°C (use of admixture). A very accurate growth temperature control is required here to prevent the emerging of defects and to precisely aim for the Curie temperature point in order to obtain a single domain crystal [122]. For the hydrothermally process a substantially lower temperature region between 350°C and 600°C is used [123]. Whereas flux-grown KTP can be fabricated at normal air pressure the hydrothermal process requires several orders of magnitude higher pressure. The advantage of this process is the fabrication of high quality KTP in terms of its stoichiometry and especially the absence of defects and vacancies and hence a lowered ionic conductivity but this requires longer growth durations.

At a Curie temperature of 945°C [68] KTP undergoes a second-order phase transition to the ferroelectric phase. Here the ferroelectricity of the material is induced via the long and short Ti-O bonds leading to an almost negligible altered crystal symmetry compared to the paraelectric phase Figure 2.14. This sequential arrangement of those Ti-O bonds affords the potassium ions to either take place in the residual vacant sites. Those sites are indicated with dotted rings in the figure.

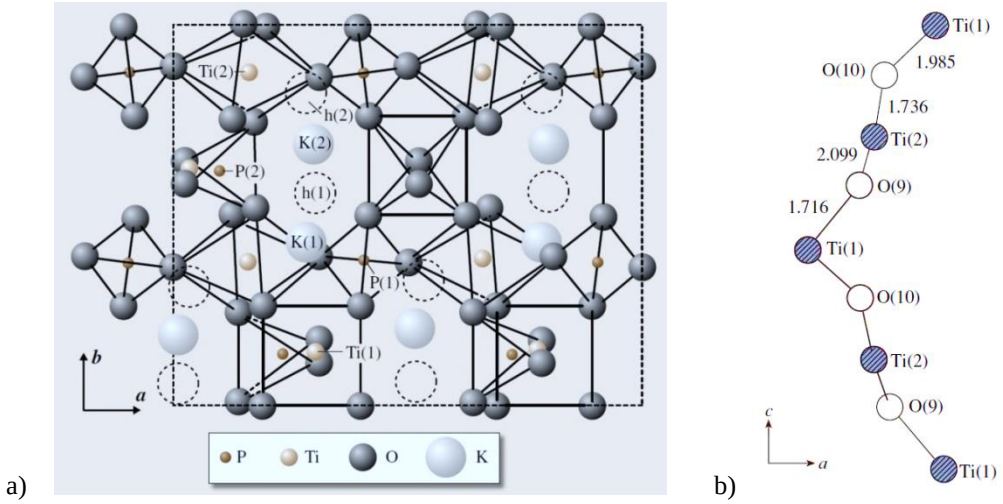

a) b)

Figure 2.14: *a) Depiction of the changed crystallographic structure of KTP when a spontaneous polarization is at hand within the ferroelectric phase adapted from* [74]. *Potassium ions occupy the spotted locations. Axis a = x, axis b= y. Inset b) sketches the displaced Ti octahedrons as the origin of the spontaneous polarization in KTP from* [75]. *Axis a = x, axis c = z.*

The potassium positions K(1,2) and the possible other sites h(1,2) remain usually fixed in the paraelectric phase which also leads to an increased symmetry in that phase. This is not the case for the ferroelectric phase. A similar behavior accounts for the alternating Ti-O bonds. The titanium octahedron can occupy either the position Ti(1) or Ti(2) leading to the optical nonlinearity due to the dipole moment created by this periodic alternation of this Ti-O string length parallel to the crystal's c-axis.

Within KTP the process of gray tracking [124] can be found which is induced by the application of very intense radiation like tightly focused laser fields, externally applied electric fields, c.f. periodic poling, or X-rays retrieving electron color centers in a photo-chemically development of Ti^{4+} ions. Gray tracks lead to an internal damage of the material or the overall destruction of the material respectively [125]. Darkened tracks feature a very increased optical absorption and this may alter the anisotropy of the linear material characteristics [126].

Regarding the poling characteristics of KTP its inherent pyroelectricity has to be taken into account since it may also influence the poling when temperature variations occur [127]. A correct determination of the dispersion of KTP is crucial for the fabrication of efficient nonlinear optical devices since the desired QPM period has to be calculated with it [83]. For this one can approximate the dispersion via the Sellmeier-equation [49]:

$$n_i(\lambda) = A + \frac{B}{\lambda^2 - C} + \frac{D}{\lambda^2 - E} \tag{2.51}$$

Since KTP is an optical biaxial material the relevant refractive indices are listed Table 3.

Material trait	*Value for $KTiOPO_4$*
Dielectric constants ϵ_{11}^S, ϵ_{22}^S, ϵ_{33}^S, for high ν	11.9 ± 0.2, 11.3 ± 0.2, $17.5 > 0.4$
Dielectric constants ϵ_{11}^T, ϵ_{22}^T, ϵ_{33}^T, for low ν	11.6 ± 0.2, 11.0 ± 0.2, 15.4 ± 0.3
Refractive index n_x, n_y, n_z (for λ = 1064 nm)	1.740, 1.748, 1.830
n_x, n_y, n_z (for λ = 800 nm)	1.750, 1.758, 1.844
n_x, n_y, n_z (for λ = 532 nm)	1.779, 1.790, 1.887
n_x, n_y, n_z (for λ = 400 nm)	1.827, 1.844, 1.965
NL coefficients (for λ = 880 nm): d_{33}^S, d_{32}^S, d_{31}^S, d_{24}^S, d_{15}^S (pm/V)	18.5, 4.74, 2.76, 3.92, 2.04
NL coefficients (for λ = 1064 nm): d_{33}^S, d_{32}^S, d_{31}^S, d_{24}^S, d_{15}^S (pm/V)	16.9, 4.35, 2.54, 3.64, 1.91
Coercive field strength (kV/mm)	2.1
Curie temperature (°C)	945
Pyroelectric coefficient ($\mu C/m^2K$)	7
Damage threshold (MW/cm^2)	500 - 1000
Band gap (eV)	3.2

Table 3: *Overview of crucial properties of $KTiOPO_4$ with values taken from* [37], [68], [81], [128]–[130].

Besides the deliberate treatment of KTP with an ion exchange for the waveguide fabrication other forms of defects within the material can alter its characteristics. It is reported that annealing can transfer Ti^{4+} ions to Ti^{3+} [74], which has a crucial influence on the SHG efficiency.

2.3.3 Waveguide fabrication

In general the guiding of electromagnetic waves within a medium is governed by the concept of total internal reflection. This is achieved via a refractive index difference between a core and the surrounding cladding. The refractive index n_1 of the guiding layer or core is higher than the cladding's n_0, c.f. Figure 2.15. Commonly light is coupled into a waveguide via one of the end facets and is then confined in the higher index region. This is described via the condition $n_1 \sin(\pi/2 - \phi) \geq n_0$ including the opposite angle ϕ of the incident angle θ. Hence, it follows for the incident angle $\sin\theta = n_1 \sin\phi \leq \sqrt{n_1^2 - n_0^2}$ and the angular limit for the coupling is given under the assumption $\Delta n \approx 0{,}01$:

$$\theta \leq \arcsin\sqrt{n_1^2 - n_0^2} = \theta_{max} \approx \sqrt{n_1^2 - n_0^2} \tag{2.52}$$

Analog to objective lenses, the front facet of a waveguide features a numerical aperture. This is equivalent to the maximum light acceptance angle $\theta_{max} = NA \cong n_1\sqrt{2\Delta n}$. According to [131] typical values are about $NA = 0.21$ with $\theta_{max} = 12°$ and $\Delta n = 0.01$.

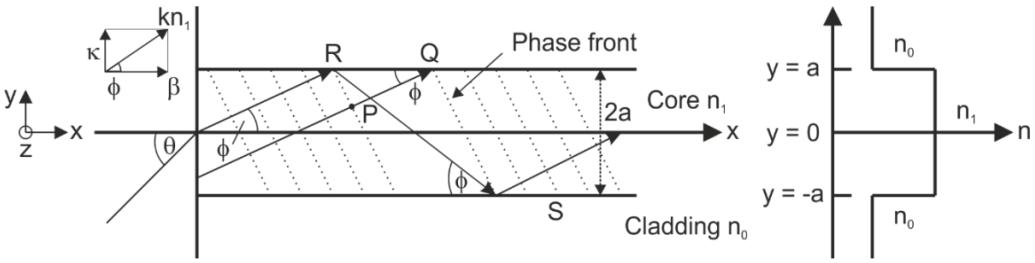

Figure 2.15: *Principal sketch of refractive-index profile and phase fronts within a waveguide adapted from* [131]. *Note that the coordinate system is settled for the typical wave propagation along the x-axis of a ferroelectric crystal and a periodic poling would be along the y-axis here.*

Regarding the optical guided modes within a waveguide with their phase fronts normal to the propagation direction the wavenumber is given as kn_1 with $k = 2\pi/\lambda$ and $\lambda = \lambda_c/n_1$. One obtains the two propagation constants for the lateral direction $\beta = kn_1 \cos\phi$ and $\kappa = kn_1 \sin\phi$. Furthermore a (complex) reflection coefficient can be derived to obtain the phase shift $\Phi = -2\tan^{-1}\sqrt{2\Delta n/\sin^2\phi - 1}$.
From geometrical considerations one can define the distance $\overline{PQ} = l_1 = (2a/\tan\phi - 2a\tan\phi)\cos\phi = 2a(1/\sin\phi - 2\sin\phi)$ as well as the distance of $\overline{RS} = l_2 = 2a/\sin\phi$. Since waveguides are often utilized for SHG applications successful phase-matching is given for both light rays here via:

$$(kn_1 l_2 + 2\Phi) - kn_1 l_1 = 2m\pi \tag{2.53}$$

Additionally also a condition for the propagation angle ϕ can be derived. Each light ray fulfilling those conditions is then denominated a mode.

Optical waveguides are distinguished by the way they are implemented in the particular substrate material. Figure 2.16 shows two major types of waveguides employed in ferroelectric crystals.

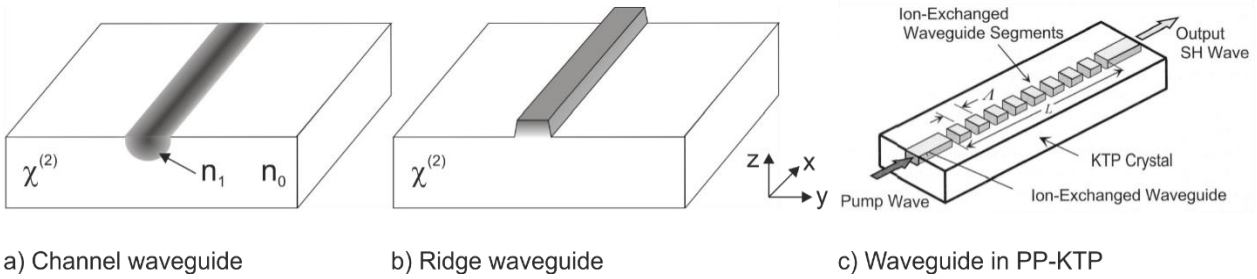

Figure 2.16: *Overview of waveguides types adapted from* [132] *and* [133]*: a) In-diffused channel waveguide in a ferroelectric, b) Ridge waveguide on $\chi^{(2)}$-material and c) principal sketch of periodically poled ion-exchanged waveguide in KTP.*

Channel waveguides – as also analyzed in this work – attain the refractive index difference via the surface-near in-diffusion of another element into the substrate material like Ti in $LiNbO_3$ [134] or Rb in $KTiOPO_4$ [135]. The replacement of such alkali ions in the latter leads to an alteration of the coercive field whereas the ionic conductivity and its dielectric characteristics are also changed. Further techniques for waveguide fabrication in KTP is laser writing changing the refractive index via the material strain [136] and implanted He^+-ions in the KTP substrate [137] amongst others.
Ridge waveguides can also be fabricated in LN, LNOI and KTP. Such waveguides come up with an increased mode number since the mode confinement is quite high. This method provides highest efficiencies in LN [138] and enable for an improved optical wave guiding, higher efficiencies for nonlinear devices as well as lowered thresholds for integrated-optical lasers. In this material fabrication by inductively coupled plasma (ICP) etching [139] or annealed proton exchange (APE) [140] can be utilized. KTP ridge waveguides have been developed first via a combination the implantation of Si-ions and a dicing method [141]. Such a dicing is performed via a diamond blade and can also be combined with a carbon ion irradiation [142].

Waveguide fabrication in LN:

For the fabrication of (periodically poled) waveguides in LN a well-established method is to use congruent z-cut LN and in-diffuse Ti to create the refractive index difference which is described in the following according to [143]. Additionally rare-earth elements like Erbium can be used to enhance the wave-guiding properties especially for the telecom range [144].

The principal process is sketched in Figure 2.17. First the crystals are cut along the crystallographic x-axis owing to the hexagonal crystallographic structure. The additional doping with Erbium is done via the deposition of an approximately 30 nm thick Erbium layer on to the –z surface (inset a). This is done in the temperature region of the Curie temperature since the dopant features a very slow in-diffusion. During this step the Erbium oxidates and one obtains a certain diffusion profile whereby the diffusion depth is sufficient to provide the desired mode profiles in the waveguide.

The actual waveguide is fabricated via the deposition of Ti on to the Er-doped surface with a depth of around 100 nm. In order to define the waveguides in their width the deposited Ti layer is defined by a lithography step. For that photo resist is deposited on the layer and photo-lithographically strips with the desired waveguide width are defined and created via a subsequent wet etching step (inset b).

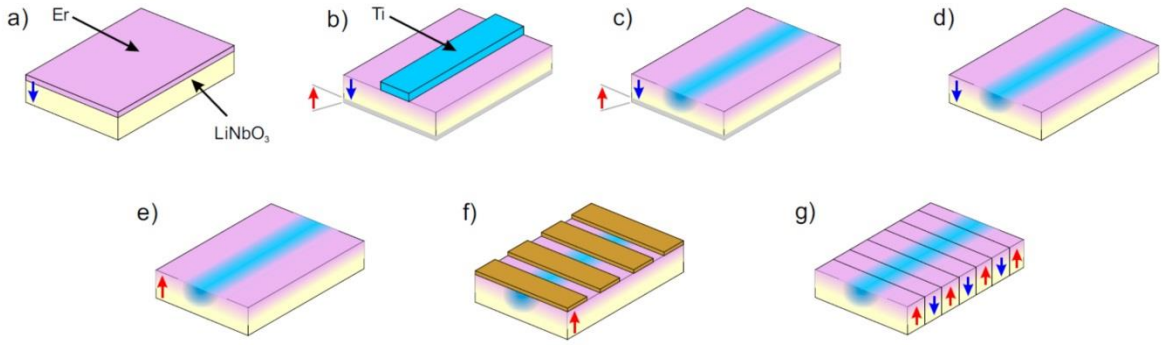

Figure 2.17: *Schematically steps for the fabrication of a periodically poled channel waveguide in $LiNbO_3$ via the in-diffusion of Ti adapted from* [143].

This width is chosen to fulfill the particular demands for the targeted modes. In the following the Ti is in-diffused at a temperature of 1060 °C for 7.5 hours (inset c). The substrate is then re-oxidized in a pure oxygen atmosphere for one hour at the same temperature. As before with the in-diffusion of erbium, the process must take place sealed in order to prevent, as far as possible, an out-diffusion of Li_2O. As indicated with a red arrow in the figure a tiny domain inverted layer is formed in this process and has to be grinded down (inset d). After the fabrication of the waveguide the sample has to be periodically poled. This is done in two steps. The entire crystal represents a single domain at that point and thus the spontaneous polarization is completely reversed in a first step in order to ensure that the waveguides are on the +z surface (inset e). Analog to the waveguide fabrication a metallic periodic pattern is placed oriented orthogonal to the waveguides on top of those via a photo-lithographical process (or alternatively via liquid electrolyte) to apply the electric field poling throughout the sample.

According to [145] waveguides in x-cut LNOI are commonly fabricated as rib loaded waveguides. They are dry etched with an Ar^+ plasma instead of reactive ions due to a selective etching behavior of the latter one. Further techniques for waveguide fabrication in LNOI are ridge waveguides via diamond blade dicing [146], chemical mechanical polishing [147], wet etching [148] or proton exchange [149]. Within the chosen technique a SiO_2 layer is deposited as a mask on top of the LN thin film, whereas the height of the layer is connected to the etching depth. Via reactive ion etching the mask is transferred on to the thin film. The width of the SiO_2 mask is determined by the etching depth. This etching also affects the thin film and leads to inclined sides with a certain angle (see Figure 5.27). Hence, the mask width directly determines the bottom width of the waveguide. With the further parameters namely the sidewall angle and the etching depth one can determine the waveguide top width. Improvements of the fabrication parameters give rise to reach much smaller sidewall angles and hence provide flexible new tailored integrated optical devices [145].

Waveguide fabrication in KTP:

In KTP waveguides with marginal losses can usually be fabricated via laser writing [150], He^+-ion implanting [137] or ion exchange besides further more experimental methods. The waveguides investigated in this work have been fabricated via a surface-near Rb-exchange. Here potassium is exchanged by rubidium ions which are provided via a melt leading to a defined region with higher refractive index. The waveguide itself is designed and determined via predefined grooves within the fabrication mask so that the exchange takes place only at those unsealed areas.

Figure 2.18 shows the fabrication steps towards such channel waveguides. A 80 nm thick titanium layer is used as mask material to avoid any oxidation impact in contrast to aluminum for instance. The waveguide areas are determined via a structured photoresist pattern on top of the Ti-layer. Using EDTA as an etchant the remaining resist and the laid bare titanium is removed after a finished development. The fabricated strips scales (here 1.5 µm to 4.5 µm) are adapted to the utilized wavelength.

The exchange of potassium with rubidium alters the unit cell extensions, which leads to a warping of the sample. To circumvent this the opposite side of the sample is fully covered with a Ti-layer [83].

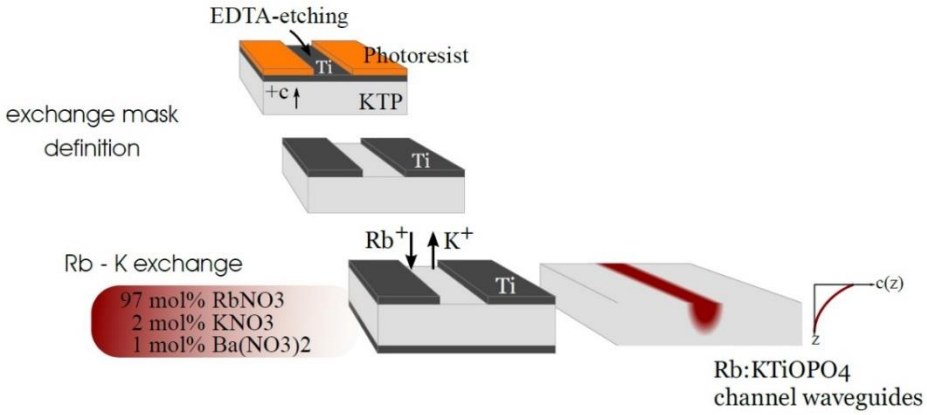

Figure 2.18: *Schematically steps for the channel waveguide fabrication in KTP via a selective exchange of rubidium taken from* [83].

After the photolithographic patterning Rubidium exchange is performed via a melt consisting of a composition of $RbNO_3$, $Ba(NO_3)_2$ and KNO_3 (prior to the melt process the potassium is soaked in a KNO_3 bath to decrease the influence of the ionic conductivity [119] which enables for more homogeneous initial wafers). Depending on the targeted application of the waveguides the particular stoichiometry of this composition has to be adapted.

For integrated waveguide structures a periodically domain inversion is applied. For this either the crystal is entirely periodically poled before the waveguide is fabricated or an existing waveguide is poled. The former procedure yields a more homogeneous domain pattern throughout the crystal in terms of duty cycle but a chemical backswitching of domains has been observed here. The latter procedure delivers waveguides which are rather homogeneous and the poling area is constricted to the waveguide extents. This is an advantage for sequential lithography methods like e-beam or laser lithography. Nevertheless, the periodic poling is conducted in a non-homogeneous substrate which features a varying coercive field strength.

The chosen poling technique here is electric field poling. Here the poling structure is also defined photolithographically. The sample face is contacted with an electrolyte gel (mixture of salt, deionized water and isopropyl alcohol) or any metal contact and on the opposing face a back-electrode is created via a mixture of gold and palladium. The waveguide front facets, i.e. the x-face of the sample, are commonly polished. This is necessary for determining the SHG efficiency with a monitoring technique and a successful in-coupling in general. As scheduled from the fabrication process the waveguides shall feature depth extensions (z-direction) between 5 and 10 µm. This corresponds to the penetration depth of the Rb exchange with distinct profiles. The analysis of such Rb-concentration profiles can be found in [151].

3 Characterization techniques

3.1 Pre-characterization via confocal microscopy

In the course of this thesis different material platforms are mainly investigated in terms of Raman spectroscopy and SHG microscopy for a profound insight into their ferroelectric domain characteristics, but before those main investigations a pre-characterization of the samples has been performed. Therefore, optical (confocal) microscopy implemented on the particular setup itself as well as via a commercial confocal laser-scanning microscope is utilized.

The fundamental concept of confocal microscopy has been developed by Minsky in the 1950s resulting in a patent [152]. Further improvements lead to the nowadays commonly known pointwise acquisition of intensities via a confocal application [153]. Confocal microscopy also comes with an increased resolution compared to common microscopy. This has been shown in the 1970s [154] and is discussed below. Widespread applications of this technique have become possible since the advent of the laser.

Confocal principle:

Conventional microscopy is characterized by a simultaneous respectively parallel acquisition of all points of signal intensity with the Rayleigh criterion as its general resolution limit. The idea of the confocal principle on the contrary consists of the pointwise excitation/illumination and detection. Inevitably a sample has then also to be scanned pointwise. The confocal regime offers an effective resolution in all three Cartesian coordinates and enables therefore the three-dimensional scanning of samples.

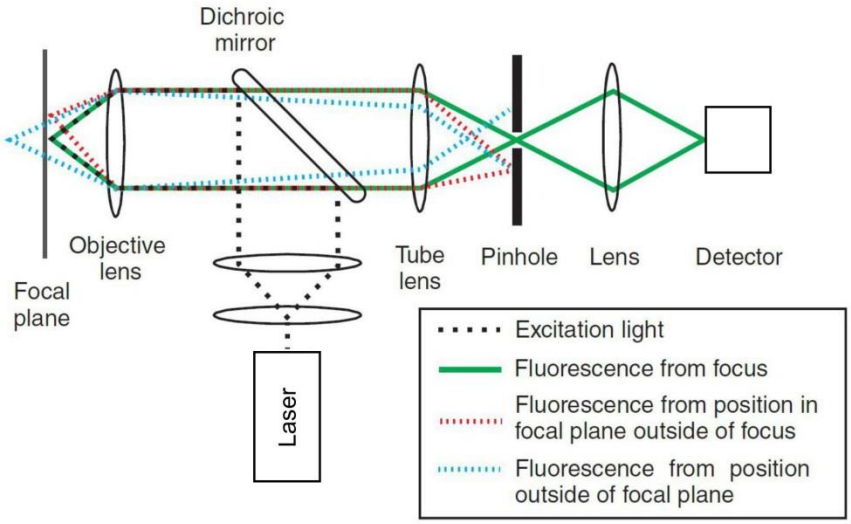

Figure 3.1: *Schematic illustration for the explanation of the confocal principle* [155].

As to be seen in Figure 3.1 the crucial part of the confocal principle is a pinhole in front of the detector set in the optical path confocal to the excitation path so that both planes are conjugated to each other.

This leads to a spatial filtering because information below or above the focal plane are cut out. In addition to this, the lateral and axial resolution is increased as well as a particular filter effect with an attenuation of diffuse light [156]. Hence, the resulting images are richer in contrast. Depending on the size of the utilized pinhole the axial resolution respectively the degree of confocality can be determined. The large depth of field enables on the one hand for a high lateral resolution and on the other hand for the acquisition of axially confocal slices. This makes tomography of transparent specimen possible.
Confocal microscopes can operate in two different scanning modes. Either the sample is moved under a fixed illumination or the latter is varied for the scanning procedure. This technique is also called flying spot microscope. Technically, it is performed via a scan mirror that allows for the scanning of the plane parallel to the objective lens. The automated scanning via the mirror yields the advantage of a high scanning speed under the premise of a sufficient strong signal. This scanning mode is utilized within the *Olympus LEXT OLS 4000* exemplified in a paragraph below. The reversed mode uses a fixed illumination path while the sample is point wisely translated. Here, the accuracy of the entire measurement system is only dependent on the sample actuators hence all optical paths are fixed. This mode is used in the nonlinear microscopy as well as in the Raman spectroscopy setup.

Diffraction limited resolution power:

In order to quantify the enhanced resolution of the confocal regime compared to common microscopy one has to derive the resolution power in general and adapt it to the confocal regime. For this, the Huygens-Fresnel-principle has to be taken into account for the diffraction at a circular aperture. The Huygens-principle describes in the wave-optical picture that each point on a wave front serves as an origin for a newly created wavelet. From Fresnel comes the consideration of interference phenomena. Those two aspects can be connected within the Kirchhoff theory of diffraction. As a special case of the Fresnel description the Fresnel-Kirchhoff diffraction integral based on a homogeneous wave equation can be stated [157]:

$$U(P) = -\frac{iA}{2\lambda}\int\int_{\mathbb{A}} \frac{e^{ik(s+r)}}{s \cdot r}(\cos(n,r) - \cos(n,s))dS \tag{3.1}$$

Here, λ denotes the wavelength, A is the amplitude and r and s distances from the point source to the circular aperture. One can adopt the simplifications that the focal length f of the lens is larger than the aperture itself. That corresponds to a converging of the spherical wave fronts of the form $E(r,t) = \frac{A \cdot e^{ikr}}{r} \cdot e^{-i\omega t}$ and especially the paraxial approximation, i.e. the diffracted waves only feature small incident angles. With those presumptions one can derive the Debye integral which depicts a field consisting of the superposition of plane waves in the solid angle element $\frac{dS}{f^2} = d\Omega$:

$$U(P) = -\frac{i}{\lambda}A\int\int_{\Omega} e^{-ik\cdot\vec{q}\cdot\vec{R}}d\Omega \tag{3.2}$$

Following a more elaborate notation of the vectors $\vec{q}$ and $\vec{R}$ via dimensionless coordinates and the solid angle element to $\Omega = dS/f^2 = a^2\rho\, d\rho\, d\theta/\mathrm{f}^2$ the integration along θ is the same like the diffraction integral within the Fraunhofer diffraction theory.

The remaining integration is along ρ and the resulting integral yields:

$$U(P) = -\frac{2\pi i}{\lambda}\frac{a^2 \cdot A}{f^2} e^{i\left(\frac{f}{a}\right)^2 \cdot u} \cdot \int_0^1 J_0(v\rho)\, e^{-i\frac{1}{2}u\cdot\rho^2} \rho\, d\rho \tag{3.3}$$

Here, $J_0(v\rho)$ denotes the Bessel-function of zeroth order. This integral containing the *Bessel*-function can be solved – either numerically or via general *Lommel*-functions $U_i(u,v)$ and $V_i(u,v)$ - to obtain the so called point spread function (PSF). The overall amplitude $U(P)$ at one certain spatial point can be calculated with those Lommel-functions leading to an entire intensity $I(u,v)$ in the detection path:

$$\mathrm{I}(u,v) = |U(u,v)|^2 = \left(\frac{\pi \cdot |A| \cdot a^2}{\lambda f^2}\right)^2 \left(\frac{2}{u}\right)^2 [U_1^2(u,v) + U_2^2(u,v)] \tag{3.4}$$

This expression for the overall intensity can be used as the basis to give a quantitative determination of the resolution power of either a common microscopy system as well as of one within the confocal regime. For this, the PSF is considered. It has to be noted that deviant to the theoretical ideal case the effective PSF consists of all superposed PSF fractions emerging in the entire optical paths, hence the resolution and imaging capability of respective setup is determined by those. In the following an ideal objective lens is assumed and the PSF is calculated with the two normalized coordinates u and v introduced above.

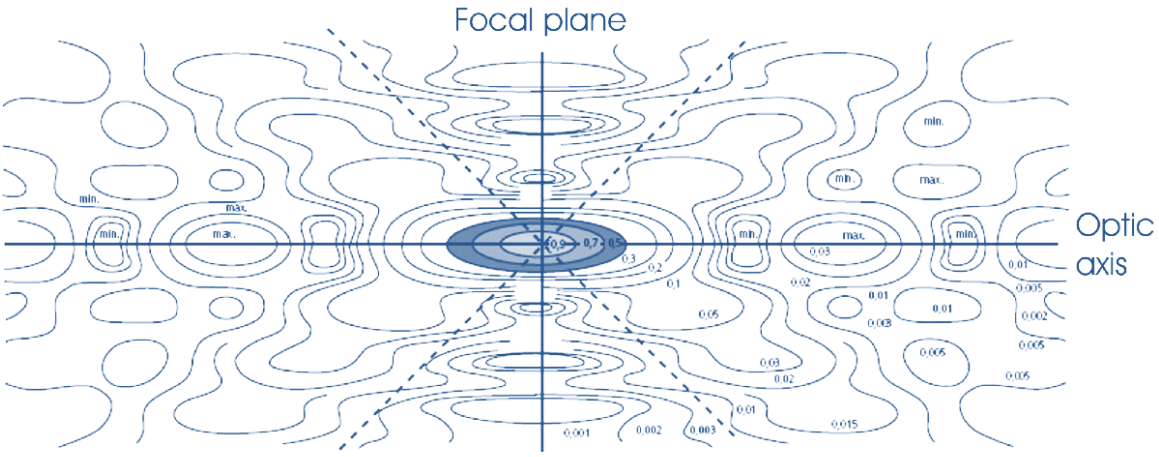

Figure 3.2: *Normalized intensity distribution in the focal-near region with stipulated areas of equal luminosity taken and adapted from* [158] *with the normalized coordinate u along the optical axis and v orthogonal to it.*

The resolution can be determined either along the optical axis which is connected to the normalized coordinate u and also in the lateral directions referring to v, i.e. within the focal plane. For the latter case one has to consider equation (3.4) and assume $u \to 0$. This yields the *Airy* function which is analogous to the case of Fraunhofer diffraction on the circular aperture [156]:

$$I(0,v) = I_0 \left(\frac{2 \cdot J_1(v)}{v}\right)^2 \tag{3.5}$$

According to [159] the lateral resolution is obtained via the full width at half maximum of the Airy function $I(0, v_{FWHM}) = 0.5I_0 = I_0\left(\frac{2\cdot J_1(v_{FWHM})}{v_{FWHM}}\right)^2$ with $v_{FWHM} \approx \pm 1.616$, c.f. Figure 3.2. The reference further states the normalized coordinates as $u = \frac{2\pi}{\lambda}\left(\frac{a}{f}\right)^2 z$ and $v = \frac{2\pi}{\lambda}\left(\frac{a}{f}\right) r$ and it follows with the dispersion relation $k = n\frac{2\pi}{\lambda}$ for the lateral resolution with a given numerical aperture *NA*:

$$r_{FWHM} \approx 0.541 \underbrace{\left(\frac{f}{a}\right)}_{\approx 1/\sin(\alpha)} \frac{\lambda}{n} \approx 0.541 \frac{\lambda}{NA} \tag{3.6}$$

Referring to [158] the overall intensity distribution along the optical axis is described via a sinc-function $I(u, 0) = I_0\left(\frac{2}{u}\right)^2 \left[2\sin\left(\frac{u}{4}\right)\right]^2 = I_0 \cdot \left[\text{sinc}\left(\frac{u}{4}\right)\right]^2$ and hence according to the FWHM criterion it yields for $u \approx \pm 5.566$. Analogously the axial resolution for a common microscopy regime is then given as:

$$z_{FWHM} \approx 1.772 \frac{\lambda n}{(NA)^2} \tag{3.7}$$

It should be noted that such a non-confocal microscope is only capable of an improvement of its resolution power by the ratio of the utilized excitation wavelength to the detection wavelength (in the case of SHG microscopy for instance as used in this work). The two characterizing functions namely the Airy-function and the sinc-function are normalized depicted in Figure 3.3. The Airy-function for both lateral directions forms the general shape of the PSF, c.f. section 4.1 for the detailed treatment of the PSF and the sinc-function describes the intensity behavior along the optical axis.

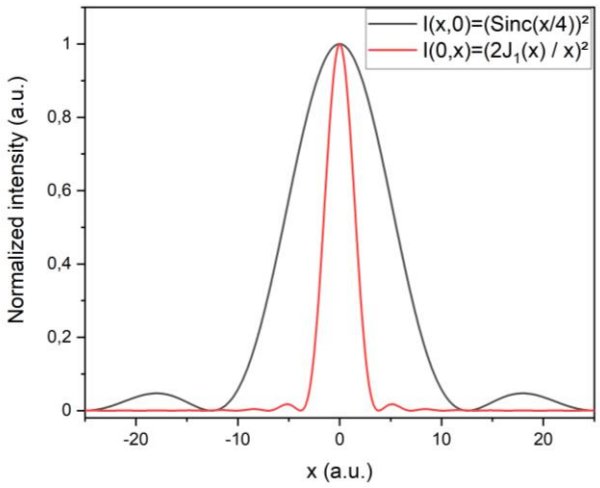

Figure 3.3: *Airy functions as calculated normalized intensity distribution along the optical axis (black curve) and in the focal plane (red curve).*

The Airy-unit is equivalent to the diameter of an airy-disc and is calculated via the Rayleigh-criterion $AE = 1.22 \cdot \frac{\lambda}{NA}$. In the confocal regime lateral quantities are often specified in AE and axial extents in Rayleigh-units via $RE = \frac{n \cdot \lambda}{NA^2}$ for an independent depiction. The application of a very small pinhole, i.e. below a quarter Airy-unit the optical system's two point spread functions (illumination and detection PSF) are in the same size and can be treated as superimposed. Hence, the PSF respectively the intensity of equation 3.5 is squared a second time:

$$I(u,v) = I_{Det}(u,v) = \left|U_{Obj}(u,v)\right|^4 = I_0 \left(\frac{2 \cdot J_1(v)}{v}\right)^4 \tag{3.8}$$

Its shape is shown in Figure 3.3 (sharp maximum, weak side lobes). The resulting PSF of the amplitude of the utilized objective lens can then be taken for the determination of the resolution power in a confocal regime analogously as done above via those presumptions, i.e. here $\frac{\sqrt{2}}{2} = \left(\frac{2 \cdot J_1(v_{FWHM})}{v_{FWHM}}\right)^2$ with $v_{FWHM} \approx \pm 1.616$ and the FWHM criterion:

$$\mathrm{r_{FWHM}} \approx \frac{0.541}{\sqrt{2}} \left(\frac{1}{NA}\right) \lambda \approx 0.363 \frac{\lambda}{NA} \tag{3.9}$$

The same procedure has to be calculated for the axial resolution:

$$\frac{2 \cdot 5.566}{\sqrt{2}} \approx \frac{2\pi}{\lambda \mathrm{n}} (NA)^2 z_{FWHM} \quad \text{with} \quad z_{FWHM} \approx 1.253 \frac{\lambda n}{(NA)^2} \tag{3.10}$$

Hence, a confocal regime offers an increased resolution power by a factor of $1/\sqrt{2}$ compared to common microscopy due to the superimposed illumination and detection PSF. It has to be noted that the resolution power in the confocal regime is dependent on the diameter of the chosen pinhole giving a certain prefactor which has to be adapted to the equations above if the pinhole size exceeds roughly one Airy-unit.

Olympus LEXT OLS4000:

For the pre-characterization a commercial confocal laser scanning microscope (CLSM) *LEXT OLS4000* from the vendor *Olympus* has been utilized. It features an operating wavelength of 405 nm from a semiconductor laser to obtain a high resolution according to the various equations derived above ("the lower the wavelength the higher the resolution"). According to its official data sheet for planar measurements the repeatability is given with $3\sigma_{n-1} = 0.02\ \mu m$ for an objective lens with a magnification of 100x and the accuracy is given with $\pm 2\%$ of the measurement value. For height measurements a scale resolution of 0.8 nm respectively 1.0 nm for display resolution is quoted. The CLSM comes up with a revolving set of five objective lenses (NA = 0.15, 0.30, 0.60, 2x 0.95 and respective working distances). For standard measurements either a micrograph image or a more elaborated laser-scanning image can be obtained, whereby the CLSM works in a reflected-light mode. On the basis of an image acquired via the laser-scanning a vast scope of evaluation techniques can be performed to analyze the samples in a more detailed fashion, e.g. step or area/volume measurements considering geometric tools, investigations

referring to surface roughness or particles and via performing an xz-scan of transparent samples film thicknesses can be retrieved. Moreover the CLSM offers the opportunity to apply difference interference contrast (DIC) to highlight transparent phase-affected objects and thus enhance the imaging quality. Figure 3.4 shows the schematic diagram of the CLSM's optical pathways and a comparison of two acquisition modes.

a) 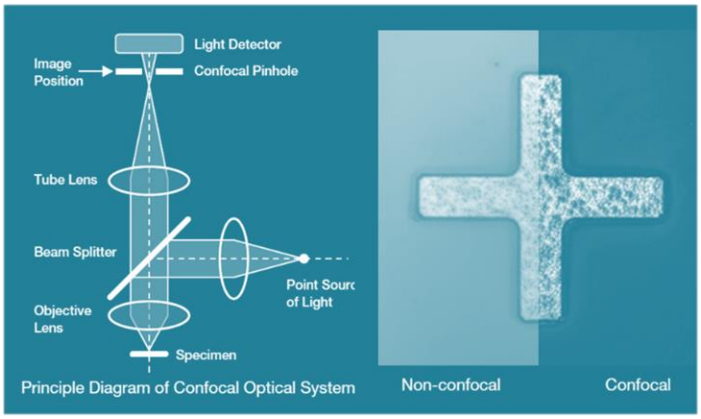

b) 

Figure 3.4: *a) Optical pathway of Olympus LEXT OLS4000, and comparison between non-confocal and confocal application of the LEXT OLS4000 taken from* [160]*, b) image of the OLS4000 as used in the cleanroom facilities of the University Paderborn.*

To exemplify the scope of operation of the CLSM the result of a depth-scan mentioned above is shown in Figure 3.5. LNOI wedge samples in x-cut as well as in z-cut have been measured in terms of the inclination of the sawed wedge structures by means of xz-scans mentioned above. From the measured raw xz-data fits can be generated and furthermore evaluated afterwards to extract information about the inclination and layer thickness. Hence, this has been used to quantify the coherent interaction length of second-harmonic microscopy for thin-film lithium niobate in contrast to bulk lithium niobate [161]. In this measurement mode the native CLSM software also provides angle measurements, refractive index correction and direct thin film layer thickness information.

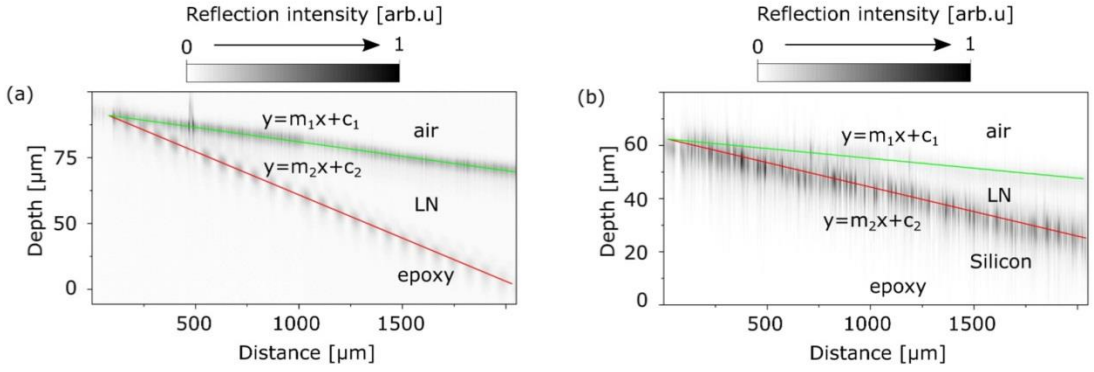

Figure 3.5: *Different types of measurement performed with OLS4000 CLSM: Laser scanning cross section of an (a) x-cut LNOI sample and (b) z-cut LNOI sample after wedge fabrication, c.f. supplemental of* [161].

3.2 Raman spectroscopy

One of the two major methodology parts utilized in this work to analyze the various samples is Raman spectroscopy. This subchapter briefly outlines the underlying Raman effect and gives an overview of the experimental instrumentation and various extensions to it. It finally closes with example applications which have also been conducted in the framework of this thesis but thematically overreach the central measurements of this work.

Raman effect:

The Raman effect has been discovered in 1928 by C.V. Raman [162], [163], whereas a theoretical prediction of the effect dates from 1923 by A. Smekal [164]. Both showed that light can be scattered and not only be absorbed when resonance processes are taken into account. Basically the Raman effect describes the emerging of an inelastic scattered light in addition to the elastic scattered Rayleigh light from a specimen. An external alternating field, i.e. laser for instance, is responsible for the oscillation of the valence electrons of the excited molecules. A dipole moment featuring the same frequency as the incident light is induced and leads to elastic scattered Rayleigh light. Raman discovered inelastic scattered light parts which have either a decreased (Stokes-scattering) or increased (Anti-Stokes-scattering) frequency compared to the Rayleigh light. He reasoned that the frequency-shift corresponds to distinct oscillation- or rotation-frequencies of the particular molecule. It has to be noted that the Raman scattered light is not coherent in contrast to the elastic scattered one because the frequency-shift only stems from the molecule properties and is independent from the incident light's frequency.

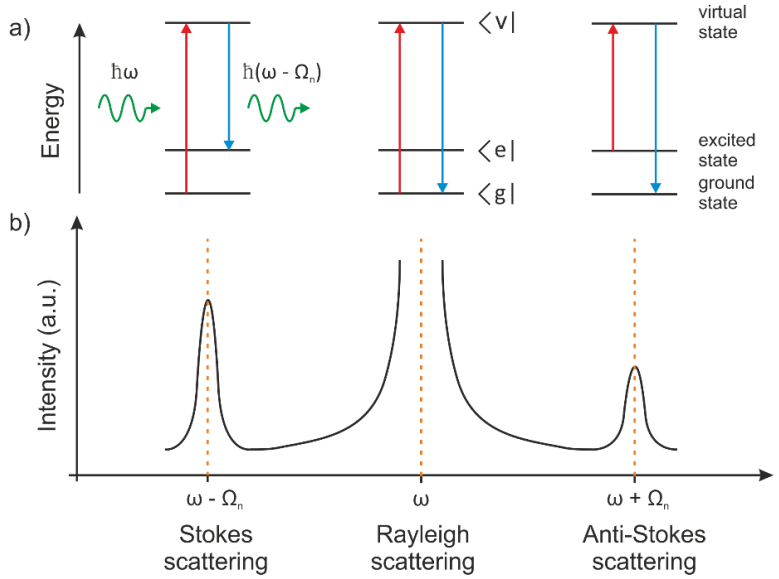

Figure 3.6: *Schematic illustration for the explanation of Raman scattered light, which is distinguished between Stokes lines (less energetic than incident light) and Anti-Stokes lines (more energetic that incident light) for a) the energetic/quantum mechanical description and b) corresponding Raman spectrum with the three types of scattered light in this process.*

The quantitative mathematical description of the Raman effect can be made with a classical approach. The induced dipole moment introduced above can be stated as:

$$\mu(t) = E_0 \alpha_{ij} \, cos(2\pi t v_0) \tag{3.11}$$

The external field is characterized by the frequency v_0 and amplitude E_0 and α_{ij} is the polarizability of the particular molecule which is a second order tensor and directly connected to the molecule's symmetry. A molecule can offer an own permanent dipole moment p which also contributes to the entire dipole moment $\mu(t) = p + \alpha_{ij} E(t)$ leading to an amplitude modulated dipole oscillation implicating that an additional electromagnetic wave is generated apart from sum- or difference-frequencies. Both parts of this equation are dependent on the molecule's coordinates (electron shell and nucleus). For reasons of simplification no resonance at a certain frequency ω is assumed, thus the electronic contribution vanishes and dipole moment and polarizability can be expressed in coordinates normalized with respect to the *n-th* nucleus equilibrium position q_0 via a Taylor-series when p or α_{ij} are dependent on the distance q_n:

$$p = p_0 + \sum_n^Q \left(\frac{\partial p}{\partial q_n}\right)_{q=q_0} q + \cdots \quad \text{and} \quad \alpha_{ij} = \alpha_{ij,0} + \sum_n^Q \left(\frac{\partial \alpha_{ij}}{\partial q_n}\right)_{q=q_0} q + \cdots \tag{3.12}$$

With these two equations for both terms a comprehensive equation for the dipole moment $\mu(t)$ can be given under the presumption of a harmonic oscillation of the frequency Ω_0 of the particular nuclei resulting in slight amplitudes in the vicinity of their respective equilibrium positions. The particular vibration has the form $q = q_0 \cos(\Omega_n t)$. The comprehensive equation for $\mu(t)$ is then obtained by utilizing an addition theorem for multiplied cosine functions and inserting equation (3.12) in the vibration equation above:

$$\mu(t) = p_0 + \sum_n^Q \left(\frac{\partial p}{\partial q_n}\right)_{q=q_0} q_0 \cos(\Omega_n t) + \alpha_{ij,0} E_0 \cos(\omega t) + \frac{q_0 E_0}{2} \sum_n^Q \left(\frac{\partial \alpha_{ij}}{\partial q_n}\right)_{q=q_n} [\cos((\omega - \Omega_n)t) + \cos((\omega + \Omega_n)t)] \tag{3.13}$$

The different parts of equation (3.13) describe various effects occurring when an electromagnetic radiation is scattered at a molecule [165]. Permanent dipoles do emit their obvious radiation indicated with the first term p_0. The second part apparently comprises the dependence of p from the coordinates q_n, hence a change of the dipole moment. This is connected to an absorption of the frequency Ω_n and refers to an infrared activity of the respective vibrational mode. Reflected radiation - same frequency as incident light - respectively elastic scattered light is described via the third term and encompasses the Rayleigh scattering. Finally, the Raman effect is treated within the last term due to the change in the polarizability. Here one can account for two kinds of radiation, which can be expressed as sidebands of the entire scattered light: the increased frequency $\omega + \Omega_n$ as Anti-Stokes scattering and $\omega - \Omega_n$ as Stokes scattering, c.f. Figure 3.6. Each vibrational mode is Raman-active when its polarizability changes. All this refers to the Raman effect of 1st order. Higher order ranks in the equations above lead to anharmonic behaviors. One distinguishes between longitudinal optical (LO) and transversal optical modes (TO). These branches occur in crystals without a symmetry center and LO modes may induce an additional e-field in piezoelectric crystals changing the bond energies and thus the frequencies. According to [166] these two mode branches are connected via the *Lydanne-Sachs-Teller* relation $v_{LO}/v_{TO} = (\epsilon_0/\epsilon_\infty)^{0.5}$.

For an exemplification of the different activities of vibrational modes, Figure 3.7 gives an overview. The easiest case a) comprises a symmetric two-atomic molecule where the given vibration only changes the polarizability but not any displacement of the charge concentration. Case b) offers both changes, whereas for the molecule in c) the particular vibration is crucial for the so called selection rules. In many cases the rule of mutual exclusion cancels out one of the two activities because many molecules lack a symmetry center. Thus, both spectroscopy methods should be used complementary.

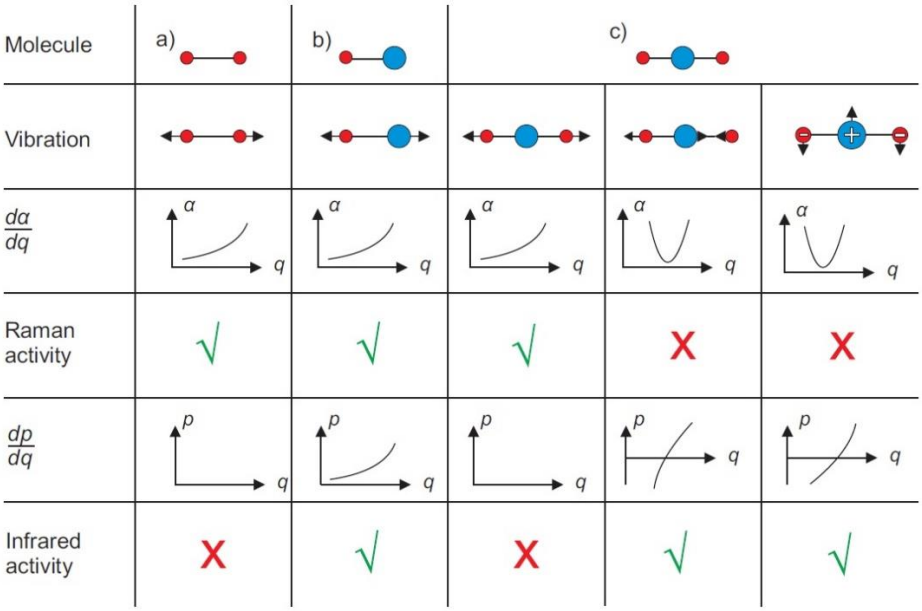

Figure 3.7: *Tabulation of the selection rules for the Raman- and IR-activity of a molecule with two and three atoms (adapted from* [167]*).*

A comparison between the intensity of Stokes and Anti-Stokes can be given by a quantum mechanical treatment on the Raman effect. According to the energy relationship derived above Raman lines originating from Stokes scattering are settled from a lowered vibrational quantum number ν and increase in it. The opposite holds for Anti-Stokes scattering. Stokes lines feature a higher intensity than Anti-Stokes lines when considering the occupation probability within the quantum mechanical treatment, which is different for the two processes due to the Boltzmann statistics. As to be seen in Figure 3.6 the Anti-Stokes process starts from an excited state implying a decreasing occupational probability at lowered temperatures. Thereby the intensity ratio can be stated as:

$$\frac{n_i}{n_0} = \frac{I_{Anti-Stokes}}{I_{Stokes}} = e^{-\frac{h\nu_{vib}}{k_B T}} \tag{3.14}$$

By means of a quantum mechanical description the Stokes/Anti-Stokes intensity ratio, the treatment of rotational vibrations for the Raman effect omitted above and any resonance phenomena like coherent respectively stimulated anti-Stokes Raman scattering can be explained. This is done by taking into account Fermi's golden rule to describe any absorption or emission processes in a resonant manner via transition rates and a certain perturbation theory approach.

Experimental setup:

The Raman measurements within this work have been performed via a µ-Raman spectroscopy setup which enables for a noninvasive investigation of the samples. As outlined in Figure 3.8 the instrumentation is set up in a backscattering geometry and consists of four principal parts.

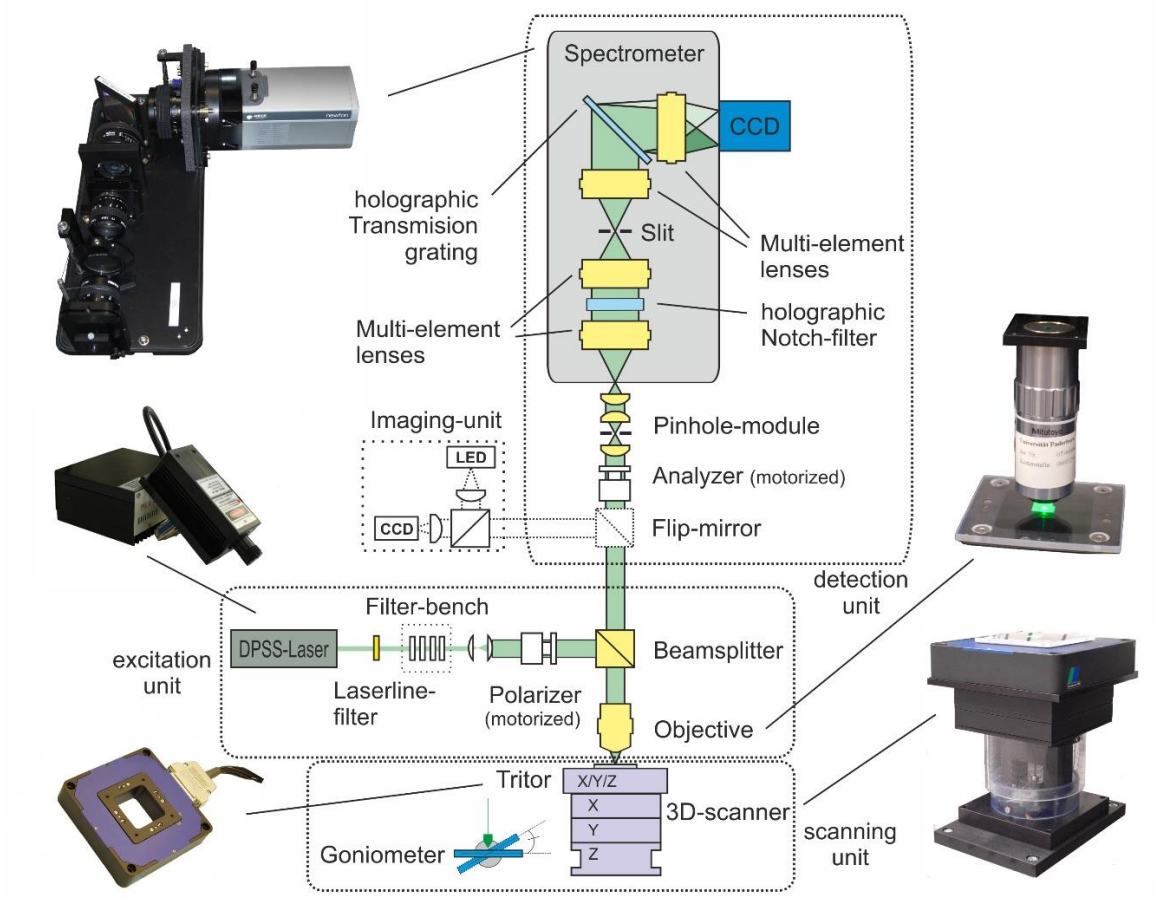

Figure 3.8: *Sketch of the confocal µ-Raman setup utilized for Raman imaging. The setup can be sectioned into an excitation path, a scanning unit, a conventional microscope as a display unit and the spectrometer as the detection part (including the pinhole module for confocal application).*

The excitation path features a continuous wave diode-pumped solid state (DPSS) laser (frequency doubled Nd:YAG with $\lambda = 532$ nm, $P = 50$ mW). To obtain a narrow linewidth a laserline filter is used. Furthermore the beam is expanded to secure a homogeneously illuminated objective lens (Infinity corrected M Plan Apo 100x / 0.70, f = 200) whereas the beam passes a dichroic beamsplitter before. Between the neutral density filter bench and the beam splitter a motorized polarizer with a half-wave plate is set in as well as a motorized analyzer at the beginning of the detection path to obtain polarization resolved measurements.

The collimated beam reaches the sample on top of the scanning unit consisting of the *Piezosystem Jena Tritor 200/20 SG*, which is responsible for the fine scanning procedure ($\Delta x, y = 80$ µm, $\Delta z = 20$ µm for closed-loop mode, accuracy of 1 nm) in all three dimensions, and the 3D-scanner with two *CN110* piezo-actuators for approximate lateral movement (each lateral range: 35 mm, accuracy: 50 nm) and a stepper-driven actuator for height adjustment (axial range: 25 mm, accuracy: 1 µm).

In this backscattering geometry the Raman signal and Rayleigh scattered light passes the beam splitter again and is coupled into the detection path beginning with a motorized polarization analyzer following an (optional) pinhole module with a diameter of 10 µm. This is used to enhance the axial resolution as outlined in subsection 3.1. In the spectrometer the Rayleigh scattered light is attenuated via the notch filter by six orders of magnitude in order to avoid any blooming from the laser light. The spectra are commonly plotted from 100 cm^{-1} onwards. The entire *Holospec f/1.8* spectrometer is from the manufacturer *Kaiser Optical Systems* and features a holographic transmission grating that splits the incident beam (formed by a slit) into two spectral lines from 0 cm^{-1} to 2000 cm^{-1} and from 2000 cm^{-1} to 4000 cm^{-1} on the *Andor Newton BI* CCD camera.
Splitting into two separate lines on the detector through the grating inevitably leads to higher resolution. According to equations 3.9 and 3.10 the best optical resolution with the pinhole module can be estimated to $\Delta x, y < 350\,\mathrm{nm}$ and $\Delta z = 2000\,\mathrm{nm}$ which is crucial for imaging Raman. For single point measurements, the spectral resolution is the striking parameter. This is obtained via the linear dispersion of the grating given with $\Delta g = 2 - 3\,\mathrm{cm}^{-1}$ and the equation $\Delta r_{spectral} = \Delta g \cdot b_{slit}/g_{pixel} = 2.3\,\mathrm{cm}^{-1}$ with a pixel size $g_{pixel} = 26\,\mu\mathrm{m}$ and the slit size of $b_{slit} = 25\,\mu\mathrm{m}$. Decisive parameters for those estimations for this setup are the numerical aperture, the slit size and the fact that for imaging Raman smaller steps than the optical resolution are used to provide a small overlap of the measured points to resolve the typical structures.

In the course of this work the aforementioned Raman setup has been augmented in terms of the technical setup by implementing a goniometer to tilt the samples along one distinct axis. This opens a more widespread analysis because the directional dependence of the Raman effect due to the tensor leads to different emerging modes as well as to changes in the intensity or its ratio according to [168]. The plain spatial tilting is performed by intermediate steps with the goniometer. The different scattering geometries are described via the Porto's notation which takes into account the scattered light $k_{i,s}$ and the two polarization units $e_{i,s}$. The notation then reads $k_i(e_i e_s)k_s$. Hence, for backscattering geometry a four-fold set of polarization states can be used for the standard polarization dependent measurements and on purpose any intermediate steps in between. The Raman tensor is then connected with this notation via the relation $I \propto |e_s \cdot R \cdot e_i|^2$.

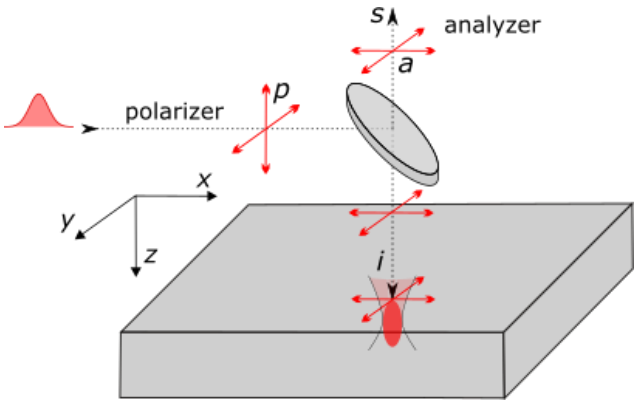

Figure 3.9: *Illustration of the Porto's notation according to a crystal's symmetry geometry. The incident direction (i), the scattering direction (s) and the directions of the polarizer (p) and analyzer (a) are specified to the crystallographic axes. Adapted from* [169].

Furthermore the investigations with this Raman setup have been refined by improving the data processing afterwards. To extract the relevant information from the acquired spectra a numerical approach is utilized which fits each distinct Raman peak with a Lorentzian function $I(\omega) = \frac{A}{2\pi}\frac{\Gamma}{(\omega-\omega_c)^2+\Gamma/4} + y_0$.

For this ω depicts the Raman shift of the particular peak's intensity and ω_s denotes the center peak frequency of it. The two other parameters are required to describe the integrated intensity area at the FWHM while y_0 is the linear offset. This post-processing is based on the *non-linear least square fits* algorithm.

Usage example: 2D materials:

Besides the established ferroelectric materials which are analyzed in this work and also within the work group of *Prof. Dr. Zrenner*, the continuative work group part of *Prof. Dr. Jöns* also investigated 2D materials namely heterostructures based on different chalcogenides with the long-term goal to fabricate and work with moiré patterns out of those overlaid monolayers. To determine and verify the structural composition and the layer thickness respectively the layer number Raman spectroscopy and also SHG microscopy have been used. In the following a heterostructure of one layer tungsten selenide and one layer molybdenum selenide on a silicon dioxide / silicon substrate (1L-WSe_2/1L-$MoSe_2$ on SiO_2 (90 nm)/Si) has been investigated in order to identify the two different (overlaid) flakes via their Raman spectrum and give a mode assignment. In a first step a 1L-$MoSe_2$ flake is transferred onto the SiO_2 (90 nm)/Si substrate via exfoliation. The same has been performed with a tungsten selenide monolayer onto the other flake. A specified region of those overlaid flakes has been measured on the particular perceived $MoSe_2$ flake, the WSe_2 flake and the overlapping region, c.f. Figure 3.10.

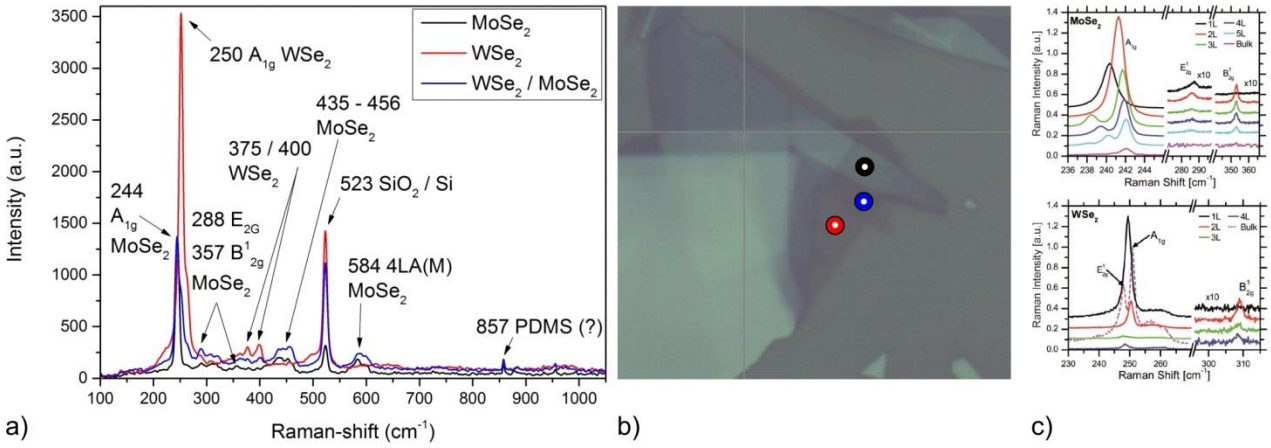

Figure 3.10: *Collocation for measurements on 2D material flakes: a) overlaid measured Raman spectra of the three different flakes, b) corresponding color-coded measurement locations of the flakes and c) Raman spectra for comparison from Tonndorf et al.* [170] *for the two single flakes.*

As a reference Tonndorf et al. [170] can be used for a mode comparison to clearly identify the vibrational modes of $MoSe_2$ as well as of WSe_2. A reasonable polarization dependent analysis is not appropriate for this sample because the arbitrary orientation of the particular flakes during the exfoliation process cannot be reproduced or determined.

As to be seen in Figure 3.10 the flake structure has been measured on three different spots to obtain a spectrum for the $MoSe_2$-, the WSe_2-flake and the heterostructure (see color-coded dots and color-coded spectra). Additionally the results on those two single flakes in terms of the layer number is also set in Figure 3.10 c) by Tonndorf et al. [170]. Especially for the WSe_2-flake it becomes obvious that the samples feature a monolayer because a two layer or bulk spectrum diverges in terms of the Raman shift as well as the additional peak shoulder. From the comparison of the spectra in Figure 3.10 a) one can clearly identify the heterostructure area due to the featuring $MoSe_2$ peak as well as the WSe_2 in the shoulder in the spectral range between 240 cm^{-1} and 270 cm^{-1}. Furthermore the spectrum gives a hint for the used polydimethylsiloxane (PDMS) used in the fabrication process at 857 cm^{-1}. The modes of the separate monolayers are to be found at the modes given by various literature. This specific mode assignment performed for the heterostructure analyzed here is given in the following table.

ν (cm^{-1})	Mode	Assignment	Reference
244	A_{1g}	$MoSe_2$	Tonndorf et al., Optics Express, Vol. **21**, No. 4, 4908 (2013)
255	A_{1g}	WSe_2	Tonndorf et al., Optics Express, Vol. **21**, No. 4, 4908 (2013)
288	E_{2g}	$MoSe_2$	Ghosh et al., J. Mater. Res., Vol. **31**, No. 7 (2016)
357	B^1_{2g}	$MoSe_2$	Liu et al., RSC Adv. **8**, 25514 (2018)
357 / 400	E^1_{2g}	WSe_2	Zhao et al., Nanoscale, **5**, 9677 (2013) Wang et al., Scientific Reports **7**, 46694 (2017)
435 - 456	3LA(M)	$MoSe_2$	Nam et al., Scientific Reports **5**, 17113 (2015)
523	-	SiO_2 / Si	Borowicz et al., Sci. World J., 208081 (2013) Borowicz et al., Adv. Nat. Sci. **3** (2012) 045003
584	4LA(M)	$MoSe_2$	Zhang et al., Nano Lett. 2019, **19**, 9, 6284–6291
847-857	-	PDMS (?)	Cruz-Felix et al., Heliyon **6** (2020) e03064

Table 4: *Assignment for the measured phonon modes of 1L-WSe_2/1L-$MoSe_2$ on a SiO_2(90nm)/Si heterostructures.*

3.3 Nonlinear microscopy

Alongside the pre-characterization and Raman investigations this work consists of the nonlinear analysis performed via a confocal second harmonic microscopy setup which is presented in this section by introducing the primary function of the setup and its basic parameters, enhancements like the scanning pinhole module or the pulse compressor and application examples.

Experimental setup:

The SHG microscopy setup consists of three significant modular-based parts and features a backscattering geometry as depicted in Figure 3.11. That implies in general that pulsed laser light is focused according to the confocal principle introduced in subsection 3.1 via an objective lens. This corresponds to a pointwise excitation. All of the information respectively second harmonic generated light is here collected via the same objective. A detector – here realized as a single photon detector (avalanche photo diode) – receives this spatially filtered, i.e. pointwise detection - information. Besides the spatial filtering a spectral filtering is applied for the distinction between linear and nonlinear generated light. The pointwise detection is enhanced via a positioning unit for all three dimensions. A further metrological parameter is the employment of polarization optics for various polarimetric analyses.

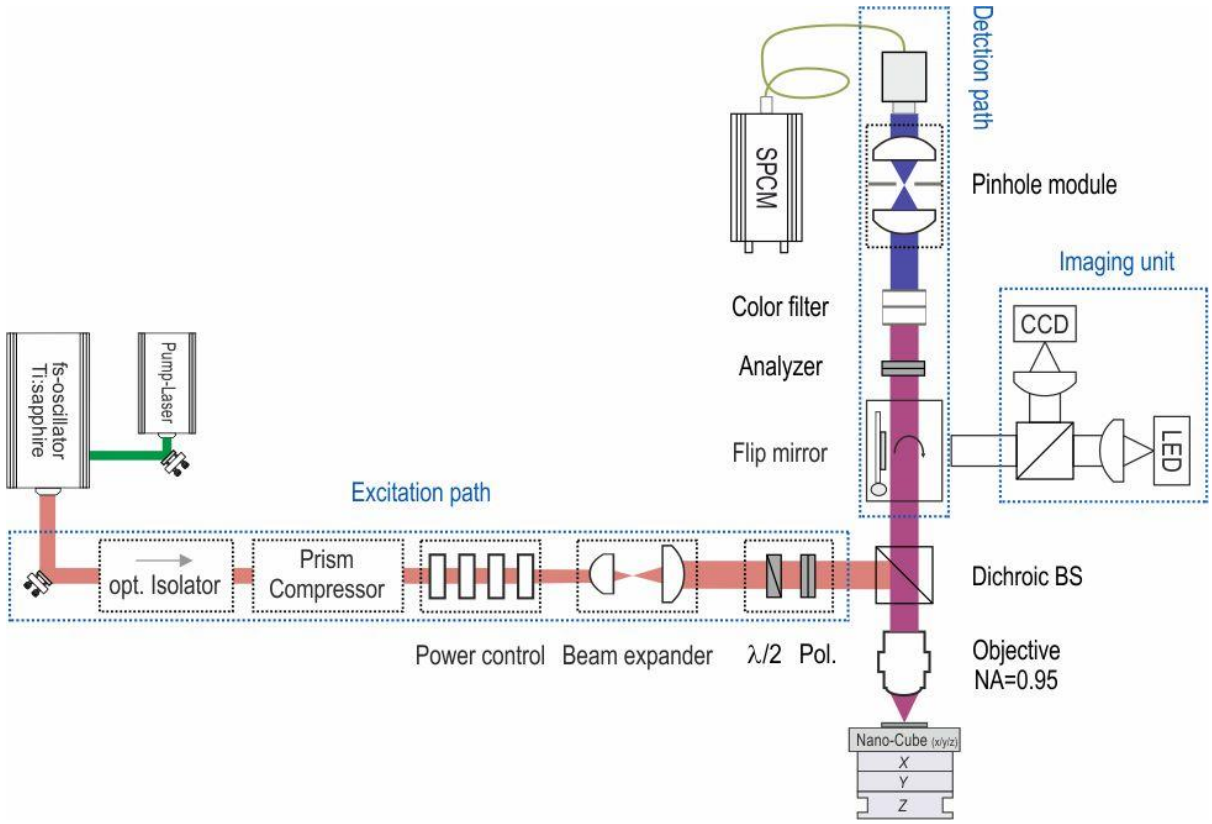

Figure 3.11: *Schematic depiction of the second-harmonic microscopy setup used in this work.*

Starting with the excitation path the first part exhibits the generation of the intense laser light via a titanium-sapphire oscillator (*Femtosource compact fs20*, $P_P = 500$ mW, mode-locked at $\lambda_{exc} = 800$ nm) pumped via a diode-pumped solid state laser (*Coherent Verdi V6*, $\lambda = 532$ nm, 5 W cw).

The pulse duration is factory-provided with 20 fs and a repetition rate of 80 MHz. By means of a neutral density filter bench the output power of the pulse laser can be reduced in order to avoid irreversible damaging of the samples depending on their particular damage threshold value. A typical chosen initial power is about to be 40 mW. Next to the oscillator a broadband optical isolator (Newport ISO-05-800-BB) is placed to avoid back coupling from the optical system into the oscillator followed by a two-prism pulse compressor (*APE femtoControl KIT*) for maintaining the desired pulse duration. Detailed information regarding the compressor and pulse duration are given below this paragraph. The filter bench and a keplerian beam expander are set behind the prism compressor. Before reaching the dichroic beam splitter the excitation polarization is determined via an angle-controlled $\lambda/2$-plate with subsequent linear polarizer. The dichroic beam splitter is designed to feature a reflection of 95 % for wavelengths above 700 nm whereas the transmission is about 80 % for the wavelength range of 400 nm – 680 nm. Both hold for an angle of 45° and p- as well as s-polarized light. Focusing is performed via an infinity corrected objective lens[1]. In order to enhance the pointwise excitation and to perform multidimensional scans the particular sample is fixed on a two-fold nano-positioning unit. A raw adjustment of the laser focus on the sample is performed via two coupled piezo-actuated linear stages (*mechonics ag CN110*, $\Delta x, y = 50$ nm, range: 35 mm) and a spindle stroke adjuster ($\Delta z < 1$ µm, range: 20 mm). The actual scanning is precisely done via a *Piezosystem Jena Nanocube* ($\Delta x, y, z = 2$ nm, range: 80 µm). Due to the backscattering geometry the linear and nonlinear signal emerging from the focal interaction volume is collected again from the objective and passes the beam splitter towards the scanning pinhole module. After that a bandpass filter cuts out the linear fraction. Optional the signal can be coupled into a common display unit via a motorized mirror. A wire-grid polarization analyzer is used to determine the excitation polarization. Finally the signal is fiber-coupled into the single-photon detector (*SPCM, id100-MMF50, ID Quantique*) based on a Si-avalanche photodiode.

Many of the aforementioned optics especially the optical isolator, the objective lens and the polarization optics unfortunately add positive dispersion to the pristine ultrafast laser pulse. Hence, the setup has been extended with the pulse compressor made in a two-grating sequence in order to compensate this positive dispersion via an equivalent amount of negative dispersion for the original pulse duration. In principle, one makes use of the dispersion created by the two prisms P1 and P2 depending on the distance of the two prisms to each other and the type of glass, c.f. Figure 3.12. The consequence of the arrangement is that the spectrally split up laser pulse via P1 then shows its spectral divergence. Thus, the weak refracted red part has to travel a longer distance through P2 than the blue part leading to a time delay, which equals a negative group velocity dispersion (GVD) [171]. The desired dispersion can be adjusted by changing the distance between the prisms. Without the compressor the pulse duration on the sample has been determined via an optical auto correlator (*APE Carpe*) to be about 1 ps instead of the pristine 20 fs factory-given respectively measured 76 fs directly after the oscillator out coupling. In order to estimate the required amount of negative dispersion the group dispersion delay of the system GDD_{system} and of the compressor have to be zero together and one can determine the prism distance by:

$$GDD_{system} = GVD_{Prism} * d_{Prisms} + 2 \cdot d_{Path,P1} \cdot GVD_{Bulk} + 2 \cdot d_{Path,P2} \cdot GVD_{Bulk} + GDD_{right\ angle} \tag{3.15}$$

[1] If not stated otherwise an *OLYMPUS MPLAPON100X M Plan Apochromat* with NA = 0.95 has been utilized.

According to the dispersion values given from the compressor vendor for 800 nm the prism distance has been set to be $d_{Prism} = 40$ cm with an estimated $GDD_{system} \approx 2500$ fs^2. With the pulse compressor set up in this arrangement the pulse duration is $\tau_{FWHM} \approx 60$ fs respectively $\tau_{Gauss} \approx 42$ fs (measured on resolution edge of auto correlator) on the sample. Hence, the extension of the setup with the pulse compressor restores the pristine pulse duration. The advantage of using short pulse lengths is amongst others that the nonlinear signal increases due to higher electric field amplitudes enabling the excitation of the desired intense $|E|^2$-fields and that the SNR and sample lifetime is enhanced. Broadened pulses or not to mention continuous wave radiation with low amplitudes in the same power regime like a pulsed excitation instead require higher output powers and this may harm the sample [172].

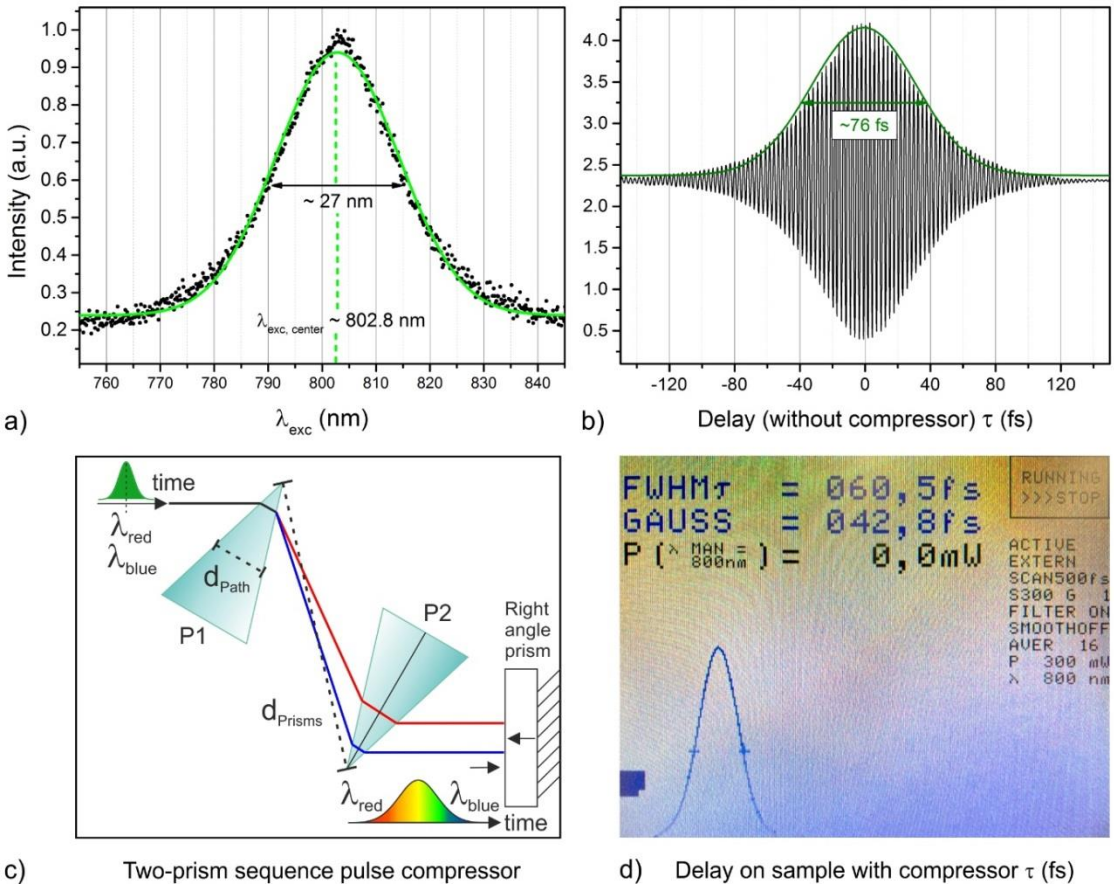

Figure 3.12: *Collage of the pulse characterization: a) Linewidth and center wavelength of the Ti:Sa-laser emission, b) pristine pulse shape and duration of emission from a) as optical auto correlated delay without utilization of pulse compressor, c) schematic sketch of pulse compressor and d) re-compensated pulse duration with use of compressor on sample.*

One central feature of this setup is the scanning pinhole module, which enables at first glance for providing a confocal regime via the utilization of a 0.5 µm aperture. This improves the possible resolution of the system according to the aforementioned theory in subchapter 3.1. In addition to this, the module is able to scan the intensity distribution within the focal plane via a three-dimensional sectioning. For this distinguished measurement technique the pinhole lenses are adjustable in all three directions so that this corresponds to a movement of the pinhole as also sketched in Figure 3.13. The pinhole aperture consists of a Ni-substrate (thickness: 2.5 µm) and a lens adjusting mechanism based on ceramic piezo-actuators.

The maximum adjustment range is 6 µm x 6 µm with an accuracy of 5 nm. Since the setup delivers a point-wise excitation the utilization of the scanning pinhole module gives the opportunity to create a false-color image of the focus of the objective lens represented within the back focal plane between the pinhole lenses. This image represents the coherent 2D intensity distribution in the focal plane. Its scale is contingent on the objective lens focal length and the one of the first pinhole lens. This additional imaging technique can be utilized for unraveling domain wall contrasts for instance when the overall integrated intensity changes due to interference effects at domain walls as described in-depth in subchapter 4.2.

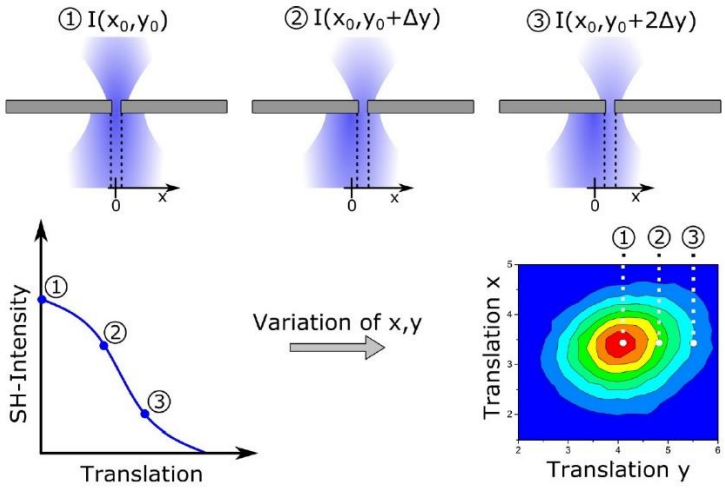

Figure 3.13: *Schematical presentation of the two-dimensional mode of operation of the scanning pinhole module. Step 1 indicates the central position within the scanning coordinate system at x = 0 and y = 0 of the pinhole; the maximum intensity is transmitted through the pinhole. The further two positions show a translation of the pinhole in y-direction for instance which is accompanied with a decreasing intensity since the intensity distribution within the back focal plane is centrosymmetric in this example.*

The system resolution is determined for its best values in the confocal regime according to equations (3.9) and (3.10) with the system parameters of the highest numerical aperture of NA = 0.95 and the excitation wavelength of λ = 800 nm. Hence, for the lateral resolution power it yields:

$$\Delta r_{FWHM} \approx 0.363 \frac{\lambda}{NA} \approx 300 \text{ nm} \tag{3.16}$$

The axial resolution power within the confocal regime and a dry objective lens (n = 1) unfolds to:

$$\Delta z_{FWHM} \approx 1.253 \frac{\lambda n}{(NA)^2} \approx 1100 \text{ nm} \tag{3.17}$$

These theoretical values can be surveyed via predefined test structures for the lateral resolution power, which are experimentally with approximately $\Delta r_{FWHM} \approx$ 310 nm in the range of the theoretical value. Regarding the axial resolution a depth scan along the system defined z-axis on a mirror delivers the required FWHM which is an immediate indication of the depth resolution. This can be performed in the linear and nonlinear excitation regime. With a fit for the occurring sinc-function the theoretical value can be confirmed.

Use case EFISH:

As a demonstration of the usability of the nonlinear microscopy setup and the second harmonic generation process electric-field-induced second harmonic generation (EFISH) in silicon dioxide is briefly presented. For more detailed information see [173].
Besides the investigation of ferroelectric materials, the SHG as part of the third order nonlinear process of electric-field-induced second harmonic generation is investigated due to its promising qualities for background-free nonlinear electro-optical sampling for instance and the fact that the nonlinearity can be adjusted via the external electric field. SiO_2 is a material with a disappearing second order nonlinearity and a non-zero $\chi^{(3)}$. From theory it is known that in this EFISH process an applied electric DC field between two electrodes leads to a strong SHG signal in relation to the commonly obtained background signal in those samples without an applied field. The measurements are performed in the same setup used in this work but without the utilization of the scanning pinhole module. Hence, this EFISH experiment serves as a use case of the setup. SiO_2 as the material of choice is used here due to its widespread use in the telecommunication field and because of its larger bandgap compared to silicon and the acceptable values in terms of optical bandwidth, low absorption and dispersion and also its phase-matching conditions.

As a sample a 1 mm thick uncoated $\lambda/10$ fused silica substrate is used on which 100 nm thick gold patterns as the electrodes on a 10 nm thin chromium film as an adhesive layer are fabricated via electron beam lithography. The fabricated sample is shown in Figure 3.14 in four different ways. The electrodes are wire-bonded to the voltage supply. As to be seen in the inset d) of the figure the SHG signal is obtained via single point measurement in between two electrodes in dependence of an applied DC field. Hence, the following results do not depict line- or area-scans which delineate one or two spatial dimensions as scanning directions with the SHG signal as the intensity but connect the SHG intensity at the distinct point with the applied voltage showing the characteristic quadratic-like course of the SHG signal.

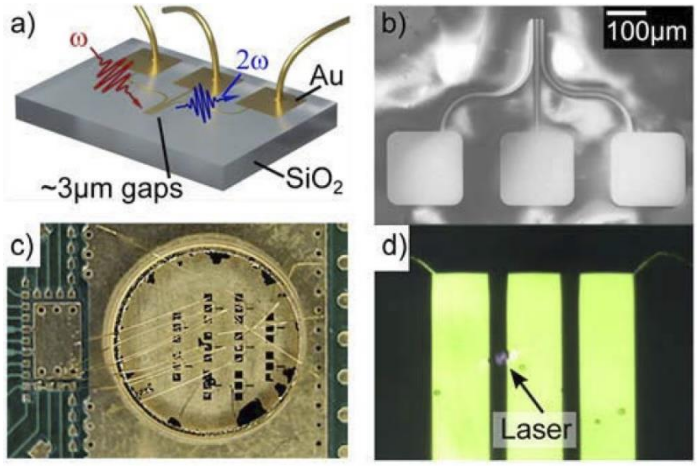

Figure 3.14: *Overview of the SiO_2 sample layout for EFISH investigation with a) sketched device layout indicating the process, b) SEM recording of one threefold electrode structure before wire bonding, c) photographic image of the entire connected sample and d) micrograph of measurement are between two selected electrodes in-situ with the 800 nm laser of the SHG microscopy setup.*

From the theoretical point of view, the externally applied DC field is responsible for a breakup of the inversion symmetry of the third-order nonlinear material, which leads to the generation of the second-harmonic light which can then be measured. The detailed theoretical treatment for the simulation results presented in the following figures are also to be found in [173]. Regarding the experimental side any phase mismatch influencing the SHG signal is negligible in contrast to the intense excitation light and also due to the fact that the z-resolution of the setup is way below the coherence length $l = \lambda/\left[2(n_{2\omega} - n_{\omega})\right] \approx 24$ µm. The simulated static field distribution between two electrodes is depicted in Figure 3.15 a) for a voltage of 250 V whereas inset b) shows the course of the squared effective nonlinear polarization with respect to the applied voltage. The deviation especially in the lower voltage region here is due to the dark count rate of the photon detector (≈ 50 cps) and also occurring surface contributions to the SHG signal. The measurement parameter from b) to the axis of ordinates is also chosen for inset c) that shows the depth dependence of the nonlinear signal for simulation and experiment. A good accordance can be stated here, but one has to note that the disparities of the latter two insets arise from different integration volumes and the intense confined SHG region in the surface vicinity. Especially from the insets b) and c) one can grasp the functionality of the SHG microscopy setup from basic one- or two-dimensional scans which distinctly characterize the nonlinear behavior of the investigated material. It should be noted here that the setup as outlined Figure 3.11 is used for these experiments with a single-mode fiber with a core diameter of 2 µm instead of the scanning pinhole module which leads to a z-resolution of $\Delta z_{FWHM} = 1.6$ µm instead of the calculated value in equation (3.17).

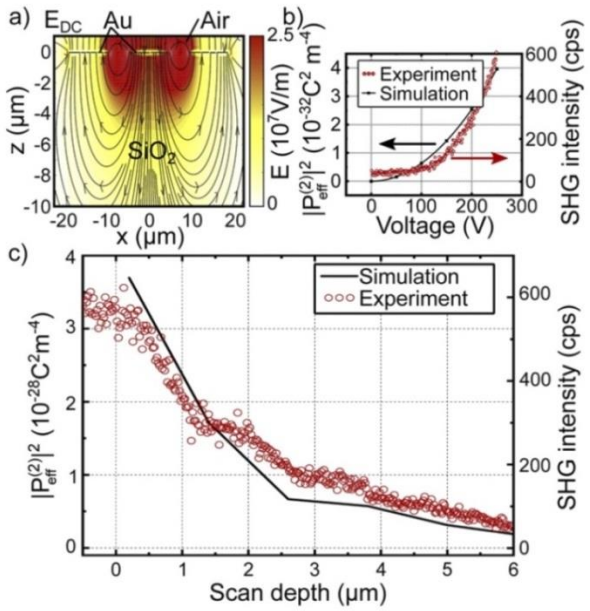

Figure 3.15: *Collage of simulation and experimental results on SiO_2 by means of SHG microscopy three-dimensional finite integration technique (FIT): a) Simulation of the external static DC electric field at an electrode voltage of V = 250 V, b) Delineation of squared internal polarization against respectively SHG intensity against the applied voltages for experiment and simulation and c) Measured and simulated depth profile of the both values from inset b).*

Additional measurements are performed with the setup on the sample as outlined in Figure 3.16. The insets a) and b) distinctly confirm that the SHG signal intensity can be adjusted via the external DC-field since a nonlinear behavior is characterized by the typical parabolic curve which is seen for higher voltages in the course of a rising excitation power. Furthermore, a power-law dependence is observed so that for higher voltages the expected exponent of 2 can be reached. The occurrence of this power-law is still subject of investigation at this point but can possibly be related to a further polarization within the SiO_2 at higher voltages since one has to take into account that the morphological structure of the material is not comprehensively investigated. Nonetheless, this deviation does not affect the detectability of the nonlinear signal here and also the purpose of the material for future applications.

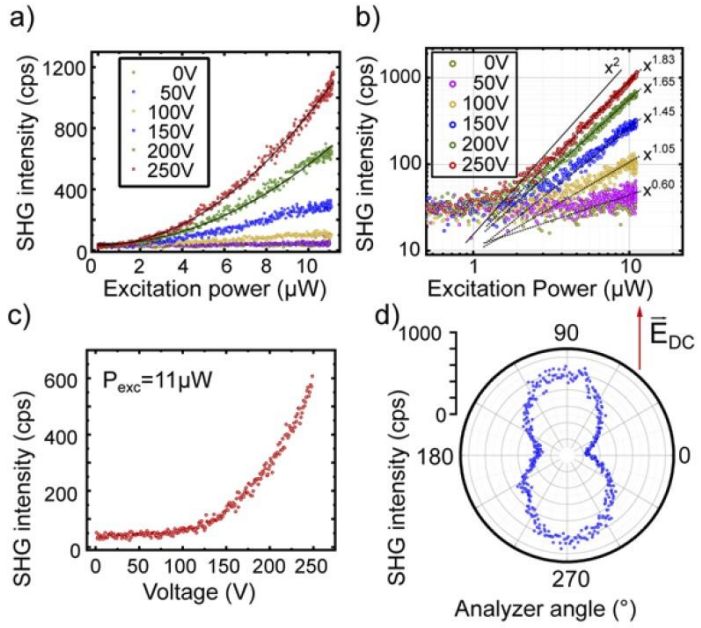

Figure 3.16: *Collage of SHG intensity functions: a) linear delineation of excitation power dependence, b) double-logarithmic delineation of excitation power dependence, c) voltage dependence at $P_{exc} = 11\ \mu W$ and d) polarization dependence with respect to the E-field orientation.*

Furthermore, the expected polarization dependence of the SHG signal in terms of the external DC field is confirmed with the setup via its utilization of the polarizer and analyzer. Figure 3.16 d) shows that the SHG signal is very strong for a linearly polarized state parallel to the orientation of the DC field. This also substantiates the fact that successful EFISH could be demonstrated.

4 Fundamental studies

4.1 Nonlinear light matter interaction

In the framework of confocal SHG microscopy the nonlinear light matter interaction within the aforesaid ferroelectrics has to be clarified for the tight focusing regime, cf. [174]. The theoretical concept is based on a vectorial model instead of a scalar wave approximation, which is not suitable anymore for the high focusing regime. Due to the strong focusing the various electric field constituents are able to couple with additional elements of the nonlinear tensor. Therefore the focal field distribution of the excitation light, the nonlinear light matter interaction (SHG) as well as the PSF of the nonlinear answer with their respective parameters has to be considered. On the experimental side mapping the nonlinear field distribution in the back focal plane is realized by an adapted scanning pinhole module.

4.1.1 Model development:

For the vectorial modeling the entire beam path has to be considered in four sectioned steps beginning with the primary E-field distribution of the excitation laser beam when it enters the material also called the illumination PSF. Secondary the model takes a look at how the material affects this distribution and finally the PSF within the detection path is determined via a calculation of its dyadic Green's function.

Part 1: Illumination PSF:

The entire consideration begins with the fundamental light E_{Inc} which has a distinguished linear polarization state and is assumed as a plane wave. Via a dichroic beam splitter the signal is coupled into a (dry) objective lens which is characterized by its numerical aperture $NA = \sin(\theta_{1,max} = \alpha)$. The plane wave character makes its amplitude independent from the displacement from the optical axis. In order to ensure this, the beam waist is enlarged via the Keplerian beam expander.

For the mathematical treatment the E-field distribution $\vec{E}_{focus}$ as well as the material's refraction $\vec{E}_{med}$ at the interface air/sample are delineated via a vectorial diffraction integral, here as the vectorial Debye integral with a dependence on the polar coordinates ρ_f, z_f and ϕ_f and Fresnel transmission coefficients t_v and t_p for both polarization states. It follows as:

$$\vec{E}_{focus} = const \cdot \int_0^{\alpha} \int_0^{2\pi} \vec{E}_{med} \cdot e^{ik_2 z_f \cos(\theta_2)} e^{ik_1 \rho_f \sin(\theta_1) \cos(\Phi - \phi_f) + ik_0 \Psi_{ill}} \times \sin(\theta_1)\, d\theta_1 d\Phi \tag{4.1}$$

$$\vec{E}_{med} = \left[\vec{E}_{obj} \cdot \vec{n}_{\phi}\right] t_v \vec{n}_{\phi} + \left[\vec{E}_{obj} \cdot \vec{n}_{\theta_1}\right] t_p \vec{n}_{\theta_2} \tag{4.2}$$

Before entering the material at the aforementioned interface the objective lens alters the incident light field by its refraction, including the angle θ_1. Using the beam expander, it is valid to assume the incident field $\vec{E}_{Inc}$ as a constant vector. Hence, the polarization orientation is also determined via it.

This leads to $\vec{E}_{obj} = [\vec{E}_{inc} \cdot \vec{n}_{\phi}]\vec{n}_{\phi}\sqrt{\cos(\theta_1)} + [\vec{E}_{inc} \cdot \vec{n}_{\rho}]\vec{n}_{\theta_1}\sqrt{\cos(\theta_1)}$ and equation 4.1 can be rearranged by the help of short forms of the integrals and solved for Φ:

$$\vec{E}_{focus}(\rho_f, \phi_f, z_f) = \begin{pmatrix} E_x(\rho_f, \phi_f, z_f) \\ E_y(\rho_f, \phi_f, z_f) \\ E_z(\rho_f, \phi_f, z_f) \end{pmatrix} \propto \begin{pmatrix} I_{00} + I_{02}\cos(2\phi_f) \\ I_{02}\sin(2\phi_f) \\ -2iI_{01}\cos(\phi_f) \end{pmatrix} \tag{4.3}$$

The overall intensity of the excitation is then the sum of all three entries. By means of common numerics the 1D-integrals $I = \int_a^b f(x)dx = \lim_{\Delta x \to 0} \sum_i^{i_{max}} f(x_i = a + i \cdot \Delta x)\Delta x \approx \sum_i^{i_{max}} f(x_i)\Delta x$ are solved with the number of points i_{max}. Via a self-coded *MATLAB* algorithm the E-field distribution within this focal plane can be determined, c.f. Figure 4.3 a).

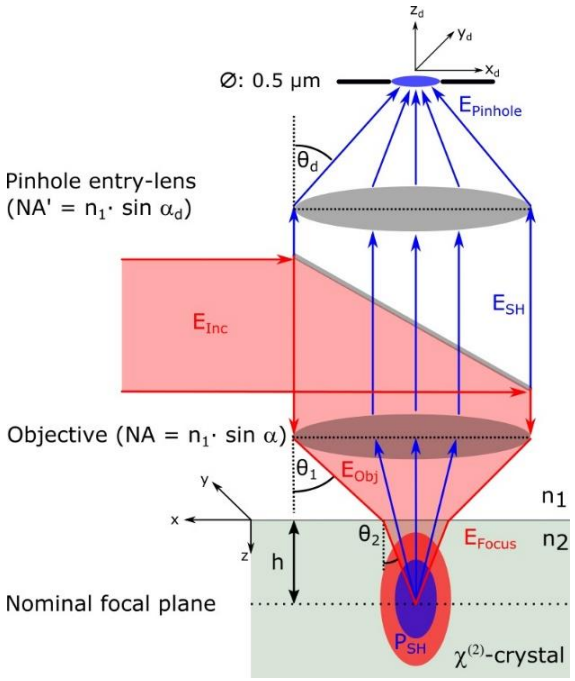

Figure 4.1: *Visualization of the used simulation parameters according to an idealized experimental setup. The incoming light (λ = 800 nm) is coupled into the objective via a dichroic beam splitter and within the material frequency doubled light (blue) is emitted in backscattering geometry. Transmitted through the beam splitter it is focused on the pinhole.*

It gets obvious that for a tightly focused system new elements within the E-field distribution occur. The exemplary case for an x-polarized excitation and its newly induced elements in the two other directions is shown simulated in Figure 4.2. For the case of NA = 0.95 as it is commonly used in this work especially the z-element shares are responsible for the enlargement in x-direction of the overall intensity [175].

Thus, one has to keep the resulting relations of amplitudes in mind:

$$\frac{\max[I_x]}{\max[I_x]} = 1.0\,, \quad \frac{\max[I_y]}{\max[I_x]} = 0.0071 \quad \text{and} \quad \frac{\max[I_z]}{\max[I_x]} = 0.185 \tag{4.4}$$

Furthermore, it should be noted that from the aforementioned consideration the shape of the intensity's profile line is different for x- and y-direction due to the refraction of the lens, which affects radial components differently than the angular ones. This eventually leads to an elliptical shape of the distribution.

The three single integrals within equation 4.3 finally yield

$$I_{00} = \int_0^{\alpha} \sqrt{\cos(\theta_1)}\,\sin(\theta_1) \times \big(t_v + t_p \cos(\theta_2)\big) J_0\big(k_1 \rho_f \sin(\theta_1)\big) e^{ik_2 z_f \cos(\theta_2) + ik_0 \Psi_{ill}}\, d\theta_1,$$
$$I_{01} = \int_0^{\alpha} \sqrt{\cos(\theta_1)}\, t_p \sin(\theta_1) \sin(\theta_2) J_1\big(k_1 \rho_f \sin(\theta_1)\big) e^{ik_2 z_f \cos(\theta_2) + ik_0 \Psi_{ill}}\, d\theta_1$$
$$\text{and } I_{02} = \int_0^{\alpha} \sqrt{\cos(\theta_1)}\,\sin(\theta_1) \times \big(t_v - t_p \cos(\theta_2)\big) J_2\big(k_1 \rho_f \sin(\theta_1)\big) e^{ik_2 z_f \cos(\theta_2) + ik_0 \Psi_{ill}}\, d\theta_1.$$

Within these three particular exponents the certain function Ψ_{ill} is new and accommodates for a real system with phase-mismatch leading to further phase stakes. Such an aberration is described by $\Psi_{ill} = h(n_2 \cos(\theta_2) - n_1 \cos(\theta_1))$. Here, h serves as a kind of offset between the sample position and the focus out of it. The two angles arise from Snell's law.

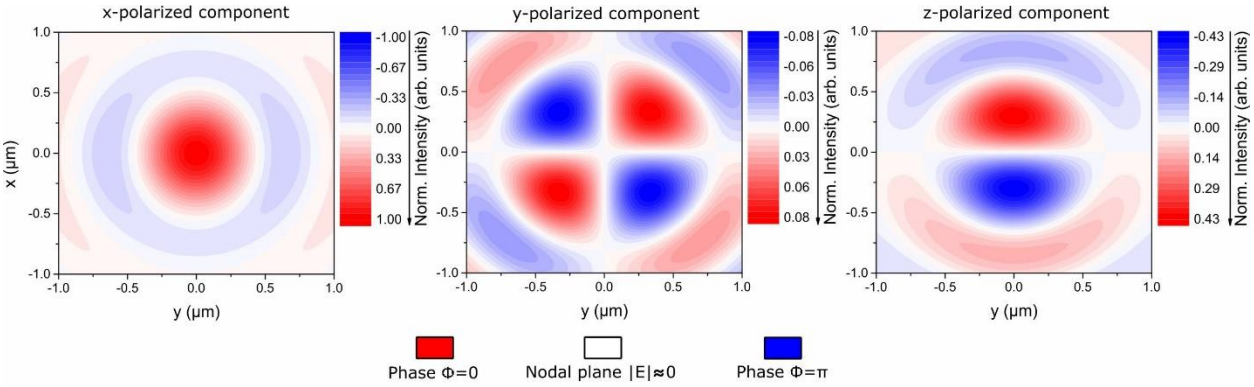

Figure 4.2: *Simulated two-colored contour plots for the excitation laser light separated for its three polarization components within a tightly focused system (NA = 0.95), whereas for the z-component its real part is shown. The wavelength is set to be $\lambda = 800$ nm. Different signs are analogous to a phase change of π.*

Part 2: Light matter interaction:

Since the focus has entered the optical nonlinear material – in our case – SHG takes place as outlined in subchapter 2.1.1. The material's nonlinear tensor is for this model multiplied with the previously calculated tensor product of equation 4.3. It yields a 3 x 6 matrix form. In its general form the product has the form of equation (4.5) but one has to note that the tensor for the investigated materials in this work do feature a different tensor than depicted in this equation, c.f. equations (2.35) a) & b):

$$\vec{P}_{SH} = \begin{pmatrix} P_x \\ P_y \\ P_z \end{pmatrix} = \begin{bmatrix} d_{11} & d_{12} & d_{13} & d_{14} & d_{15} & d_{16} \\ d_{21} & d_{22} & d_{23} & d_{24} & d_{25} & d_{26} \\ d_{31} & d_{32} & d_{33} & d_{34} & d_{35} & d_{36} \end{bmatrix} \cdot \begin{pmatrix} E_x^2 \\ E_y^2 \\ E_z^2 \\ 2E_zE_y \\ 2E_zE_x \\ 2E_xE_y \end{pmatrix} \tag{4.5}$$

This step adds the particular material properties to the model and the E-field distribution with this received polarization from the focal volume finds its way to the detector.

Part 3: Detection PSF:

The obtained E-field distribution is now translated towards the pinhole respectively the detector. According to [176] this can be modeled via a Green's function. If one assumes the focal point within the material as the infinitesimal origin of the radiation that inherits the spatial dipole radiation properties and also the fact that in the tightly focused regime a determined objective lens prompts a $\vec{k}$-filtering, this distribution is called the detection PSF. Hence, the field is given by [176], [177]:

$$\vec{E}_{Pinhole}(\vec{r}_d) = const \cdot \int \overleftrightarrow{G}(\vec{r}_d, \vec{r}) \vec{P}(\vec{r}) d^3r \tag{4.6}$$

The Green's function is here delineated as the dyadic PSF $\overleftrightarrow{G}(\vec{r}_d, \vec{r})$ of this beam path. It has to be noted that for $\overleftrightarrow{G}(\vec{r}_d, \vec{r})$ its parts for z are omitted due to the difference in NA between objective and pinhole lens [176] and the dyadic PSF constitutes as:

$$\overleftrightarrow{G} \propto \begin{bmatrix} B_{00} + B_{02}\cos(2\phi) & B_{02}\sin(2\phi) & -2iB_{01}\cos(\phi) \\ B_{02}\sin(2\phi) & B_{00} - B_{02}\cos(2\phi) & -2iB_{01}\sin(\phi) \\ 0 & 0 & 0 \end{bmatrix} \tag{4.7}$$

From [178] one gets the particular integrals:

$B_{00} = \int_0^{\alpha_d} \frac{1}{\sqrt{\cos(\theta_1)}} \sin(2\theta_d) \times \left(t_v + t_p \cos(\theta_2)\right) J_0(k_d \rho_d \sin(\theta_d)) e^{-ik_d z_d \cos(\theta_d) - ik_0 \Psi_{det}} \, d\theta_d,$

$B_{01} = \int_0^{\alpha_d} \frac{1}{\sqrt{\cos(\theta_1)}} \times t_p \sin(\theta_2) \sin(2\theta) J_1(k_d \rho_d \sin(\theta_d)) e^{-ikz_d \cos(\theta_d) - ik_0 \Psi_{det}} \, d\theta_d$

and $B_{02} = \int_0^{\alpha_d} \frac{1}{\sqrt{\cos(\theta_1)}} \sin(2\theta_d) \times \left(t_v - t_p \cos(\theta_2)\right) J_2(k_d \rho_d \sin(\theta_d)) e^{-ik_d z_d \cos(\theta_d) - ik_0 \Psi_{det}} \, d\theta_d.$

Again t_v and t_p delineate transmission coefficients, whereas Ψ_{det} is the negative aberration function. J_i are 1st kind Bessel-functions with the particular order i.

The dyadic PSF is only contingent on the distance of both points $r_d - r$. Finally the overall square of the values of all detection PSF points gives the E-field distribution of the nonlinear signal in the back focal plane.

4.1.2 Model results:

The corresponding modeled results for the linear excitation PSF (Figure 4.3 a), the nonlinear material polarization within the focus (Figure 4.3 b) and the SH answer in the back focal plane (Figure 4.3 c) are presented exemplarily for x-polarized excitation light. The intensity ratio from equation (4.4) within the excitation field is also obvious here.

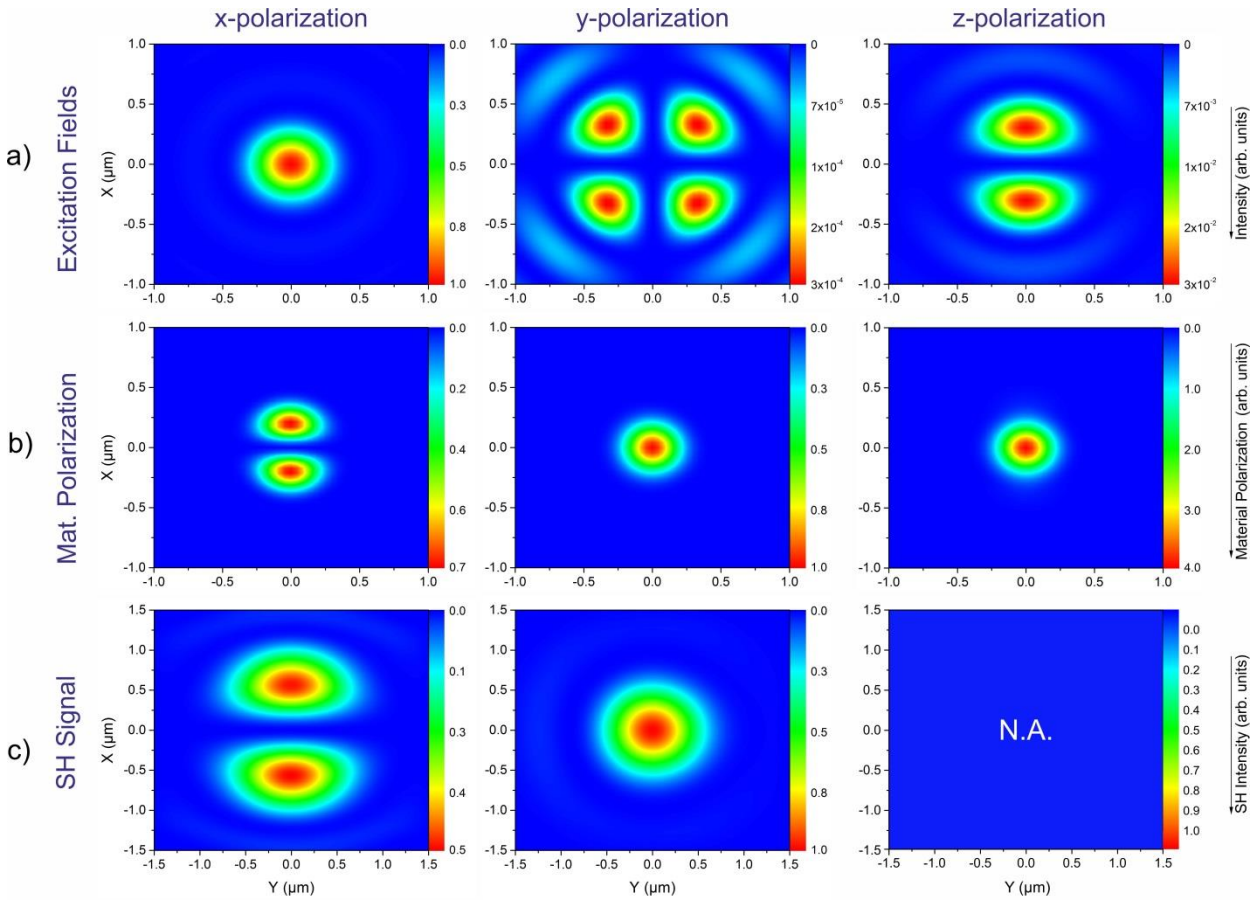

Figure 4.3: *Calculated set of respectively normalized E-field distributions of a) the linear incident light in the focus region without any material, b) contribution of the nonlinear material polarization (LN) within the focus and c) convoluted nonlinear signal (LN) within the pinhole (back focal plane).*

The split pattern of the x-polarization part within the SH signal originates from the lack of possible entries within the nonlinear tensor which can couple to the squared x-components. Thus, the pattern is created via the combination of x- and z-components connecting to the off-diagonal d_{31} element. From this one can directly determine the symmetry of the particular material polarization. No z-components for the SH signal are shown since only polarization parts within the plane are contributing.

Figure 4.4 shows the according SH signal in the back focal plane for KTP.

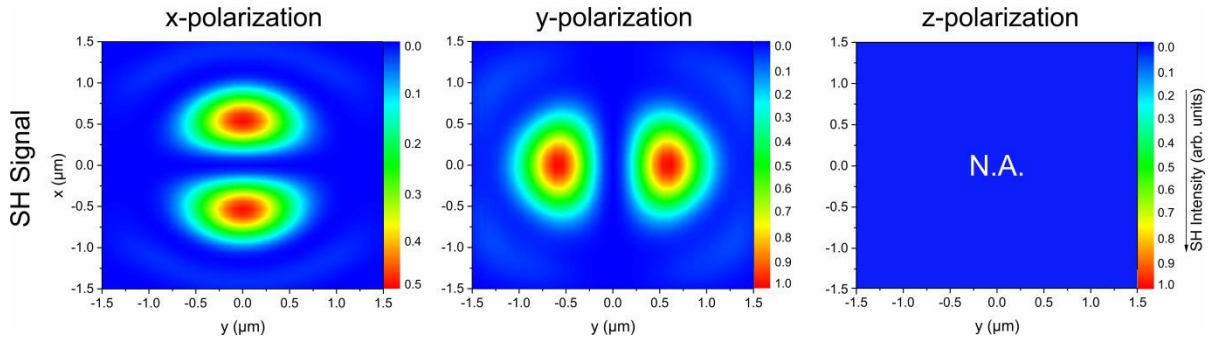

Figure 4.4: *Calculated set of respectively normalized E-field distributions of a) the linear incident light in the focus region without any material, b) contribution of the nonlinear material polarization (KTP) within the focus and c) convoluted nonlinear signal (KTP) within the pinhole (back focal plane).*

4.1.3 Experimental validation of vectorial model:

For $LiNbO_3$ and $KTiOPO_4$ bulk crystals the theoretical model is experimentally validated by obtaining the nonlinear answer in the back focal plane via the focal imaging technique. As outlined before the combined approach makes use of the backscattering geometry and the chosen measurement geometry of the crystals is z-cut. According to equations 2.35 one can obtain the effective $\chi^{(2)}$-tensors $\vec{\vec{d}}_{LN}$ and $\vec{\vec{d}}_{KTP}$ for both materials and fill in the particular elements with values given by literature [30], [37], [38], [69]. Besides these material inherent parameters further values are taken into account: NA = 0.95, $P_{inc} = 100$ mW, $\tau_{int} = 100$ ms and linear polarized light. The integrals from equation (4.3) have to be squared to fulfill the form of equation (4.5):

$$\begin{pmatrix} E_x^2 \\ E_y^2 \\ E_z^2 \\ 2E_zE_y \\ 2E_zE_x \\ 2E_xE_y \end{pmatrix} = \begin{pmatrix} I_{00}^2 + 2I_{00}I_{02}\cdot\cos(2\phi_f) + I_{02}^2\cdot cos(2\phi_f)^2 \\ I_{02}^2\cdot\sin(2\phi_f)^2 \\ -4I_{01}^2\cos(\phi_f)^2 \\ -4iI_{02}I_{01}\sin(2\phi_f)\cos(\phi_f) \\ -4iI_{00}I_{01}\cos(\phi_f) - 4iI_{02}I_{01}\cos(2\phi_f)\cos(\phi_f) \\ 2I_{00}I_{02}\sin(2\phi_f) + 2I_{02}^2\sin(2\phi_f)\cos(2\phi_f) \end{pmatrix} \approx \begin{pmatrix} I_{00}^2 + 2I_{00}I_{02}\cdot\cos(2\phi_f) \\ 0 \\ 0 \\ 0 \\ -4iI_{00}I_{01}\cos(\phi_f) \\ 2I_{00}I_{02}\sin(2\phi_f) \end{pmatrix} \quad (4.8)$$

In this equation an approximation is to be found which only accounts for integrals with a superior order, i.e. $I_{00} \gg I_{01} \gg I_{02}$ here for the exemplary x-component excitation. Together with the particular material polarization tensor – here $LiNbO_3$ - the approximated final polarization field yields:

$$\begin{pmatrix} P_x \\ P_y \\ P_z \end{pmatrix} = \begin{bmatrix} 0 & 0 & 0 & 0 & d_{31} & -d_{22} \\ -d_{22} & d_{22} & 0 & d_{31} & 0 & 0 \\ d_{31} & d_{31} & d_{33} & 0 & 0 & 0 \end{bmatrix} \begin{pmatrix} E_x^2 \\ E_y^2 \\ E_z^2 \\ 2E_zE_y \\ 2E_zE_x \\ 2E_xE_y \end{pmatrix} \approx \begin{pmatrix} -4id_{31}I_{00}I_{01}\cos(\phi_f) \\ -d_{22}I_{00}^2 \\ d_{31}I_{00}^2 \end{pmatrix} \quad (4.9)$$

Figure 4.5 recaps all the previous steps for $LiNbO_3$ in the scattering geometry z(xx)-z for instance. According to the Porto's notation in this example the excitation light is x-polarized. Thus, only the combined x- and rather weak z-components from $2E_zE_x$ are induced via the d_{15} element. The tensor given in Figure 4.5 is more precise than the one in equations (2.35b) or (4.9). Those equations are simplified by using symmetry arguments according to [36] and all equal elements are labeled the same, i.e. $d_{15} \mathrel{\widehat{=}} d_{31}$.

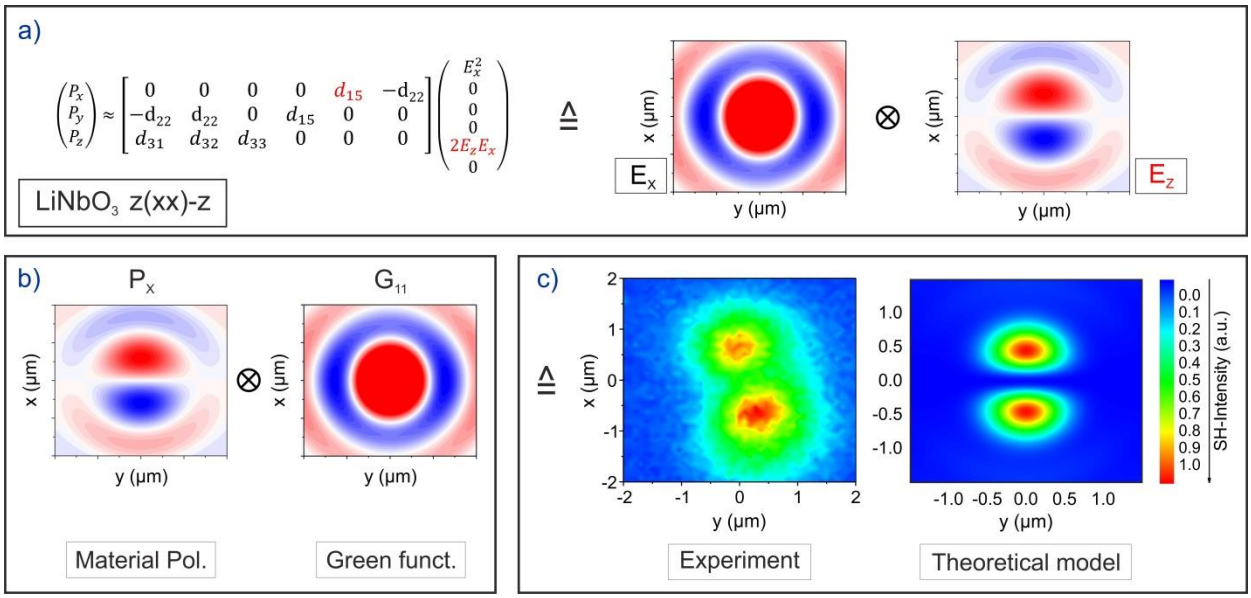

Figure 4.5: *Sketch for the explanation of the emergence of the E-field distribution within the back focal plane in bulk $LiNbO_3$ for z(xx)-z. a) Formation of the excitation field as a split pattern due to the E_x and E_z components. b) Material polarization creates a split pattern P_x oscillating in x-direction. From the dyadic Green's function x-dipoles are gathered via the element G_{11}. c) In the back focal plane the eventual split pattern is observable.*

As depicted in Figure 4.5 a) the z-component is already split up from the excitation side in terms of phase and amplitude and hence the product with the rotational symmetric x-component gives qualitatively the split pattern from P_x in Figure 4.5 b). The translation of this pattern is conducted via the Green's function G_{11} generally introduced before. Finally the emission split pattern for this scattering geometry is to be seen in the back focal plane, c.f. Figure 4.5 c).

With the optical components on the one hand and the pulse characteristics as well as the assumption of a monochromatic wave within the simulation on the other hand one obtains a temporal and spectral incoherence. This is the reason for scaling differences seen between simulation and experiment.

For y-polarized excitation light the material polarization oscillates in z-direction stemming from the coupling of d_{32} to E_y^2 which is quite stronger than the other elements in this context (Figure 4.6).

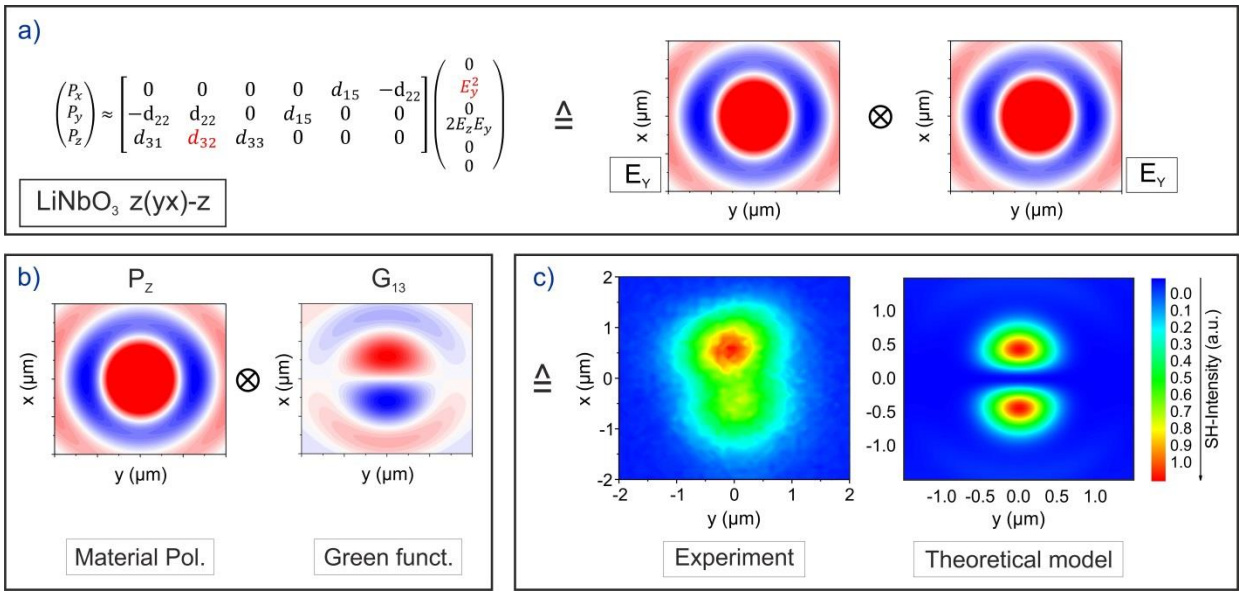

Figure 4.6: *Sketch for the explanation of the emergence of the E-field distribution within the back focal plane in bulk $LiNbO_3$ for z(yx)-z. a) Formation of the excitation field as a rotational symmetric pattern due to the squared E_y component. b) Material polarization creates a rotational symmetric pattern P_z oscillating in z-direction. From the dyadic Green's function z-dipoles are gathered via the element G_{13}. c) In the back focal plane the eventual split pattern due to G_{13} is observable.*

The y-polarized components are rotational symmetric due to the permutation. The dyadic Green's function provides a split pattern when a high NA is used and z-components are observed within the x-parts via its G_{13} element and its typical dipole emission. It should be noted that such a high NA enables addressing of oscillating components along the optical axis and therefore in LN the strongest nonlinear coefficient is taken into account whereas the remaining other coefficients are neglected to zero for the qualitative explanation. The simulations include all coefficients and those obviously influence the pattern quantitatively.

Material system LN:

The experimentally captured intensity distribution patterns for the different scattering geometries are depicted and compared with the modeled data in Figure 4.7. The nonlinear tensor for $LiNbO_3$ yields:

$$\begin{pmatrix} P_x \\ P_y \\ P_z \end{pmatrix} = \begin{bmatrix} 0 & 0 & 0 & 0 & d_{31} & -d_{22} \\ -d_{22} & d_{22} & 0 & d_{31} & 0 & 0 \\ d_{31} & d_{31} & d_{33} & 0 & 0 & 0 \end{bmatrix} \begin{pmatrix} E_x^2 \\ E_y^2 \\ E_z^2 \\ 2E_zE_y \\ 2E_zE_x \\ 2E_xE_y \end{pmatrix} \approx \begin{pmatrix} -4id_{31}I_{00}I_{01}\cos(\phi_f) \\ -d_{22}I_{oo}^2 \\ d_{31}I_{00}^2 \end{pmatrix} \quad (4.10)$$

As explained above splitting patterns are observable for x-polarized detection. In contrast to low NA experiments the high NA focusing leads due to the cosine term, c.f. integration in equation (4.3), to a split pattern (for low NA no x-polarized light would occur here because the I_{00}-integral to be the only contributing one and no split pattern would be at hand).

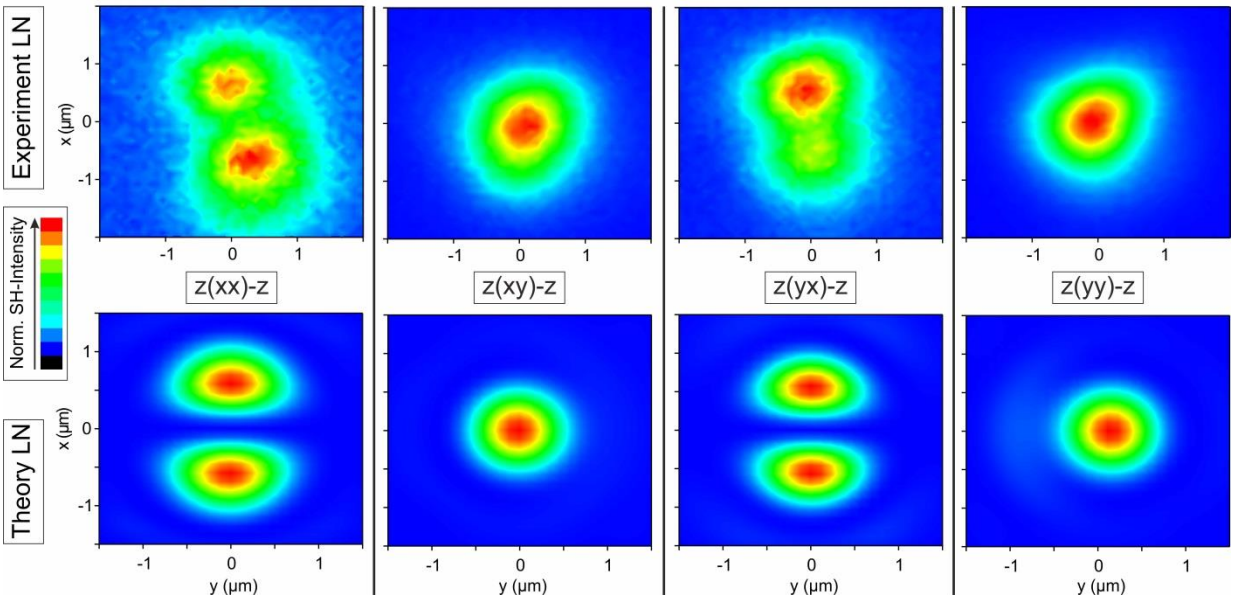

Figure 4.7: *Comparison of calculated and measured intensity distributions of the SH answer of z-cut bulk $LiNbO_3$ within the back focal plane. An excitation close to the surface is assumed. The maximum of the graphs is normalized to the highest intensity of the detection polarization.*

The results demonstrate good agreement between model and experiment, whereas besides aforementioned simplifications other nonlinear effects like self-focusing e.g. can also vary the outcome of the results.

Material system KTP:

The resulting nonlinear field distributions in the back focal plane are also calculated and experimentally obtained for $KTiOPO_4$. Corresponding results are shown in Figure 4.8. KTP only exhibits split patterns different to LN. This is due to the less nonlinear tensor elements coupling to z-incident light. For x-polarized excitation light the according polarization field is given by:

$$\begin{pmatrix} P_x \\ P_y \\ P_z \end{pmatrix} = \begin{bmatrix} 0 & 0 & 0 & 0 & d_{15} & 0 \\ 0 & 0 & 0 & d_{24} & 0 & 0 \\ d_{31} & d_{32} & d_{33} & 0 & 0 & 0 \end{bmatrix} \begin{pmatrix} E_x^2 \\ E_y^2 \\ E_z^2 \\ 2E_zE_y \\ 2E_zE_x \\ 2E_xE_y \end{pmatrix} \approx \begin{pmatrix} -4id_{15}I_{00}I_{01}\cos(\phi_f) \\ 0 \\ d_{31}I_{00}^2 + 2I_{00}I_{02} \cdot \cos(2\phi_f) \end{pmatrix} \quad (4.11)$$

It gets obvious that the material polarization features a two-fold split pattern for the x-component with this excitation, which is also apparent within the comparison of experiment and simulation in Figure 4.8.

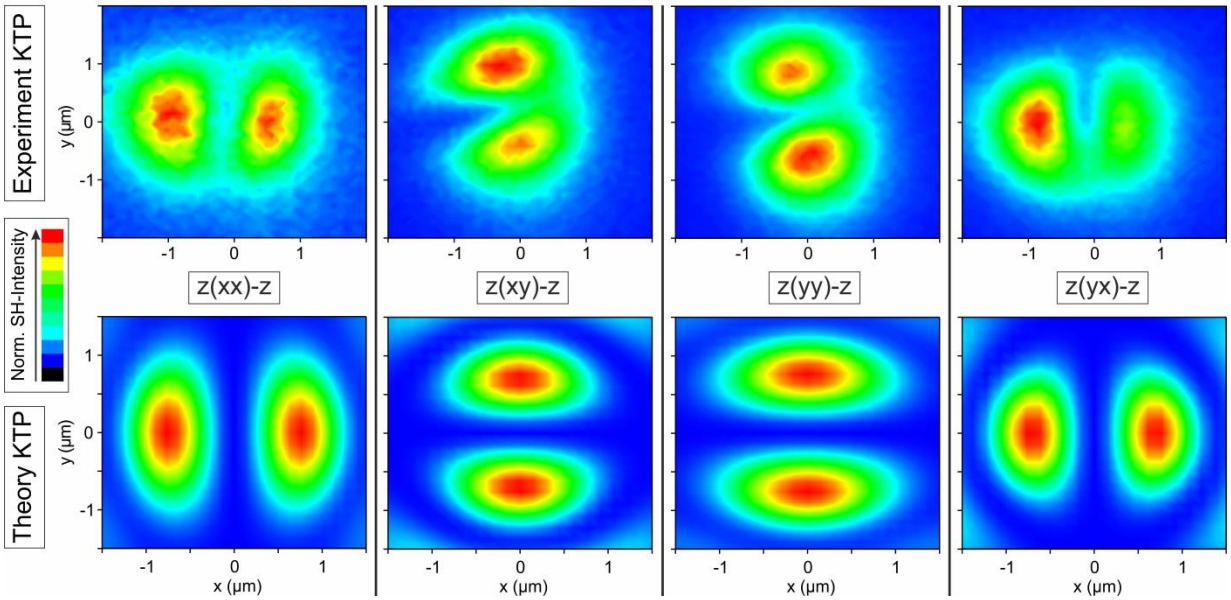

Figure 4.8: *Comparison of calculated and measured intensity distributions of the SH answer of z-cut bulk $KTiOPO_4$ within the back focal plane. An excitation close to the surface is assumed. The maximum of the graphs is normalized to the highest intensity of the detection polarization.*

Regarding the split pattern of the z(xy)-z geometry the explanation becomes more sophisticated. An intense z-polarized component is the reason for the latter one, hence it couples via the G_{23} element of the dyadic PSF ($\sim B_{01}\sin\phi$) to the y-polarization and a split pattern occurs. The pinhole's low NA is responsible here that this term is not really striking but it can still be noticed under the circumstance when no 1st order y-component polarization is found within the focal area. With respect to the nonlinear tensor actually no d_{3x}-elements are addressed in this scattering geometry, but since they are so high, a contribution cannot be fully neglected. When a low NA (< 0.55) for the excitation is assumed experiments also verified that the split terms in KTP disappear due to noise.

Interim summary:

To clarify the nonlinear contrast mechanism in domain mapping of ferroelectric materials a theoretical concept especially for the tightly focused regime based on a vectorial model has been developed. For experimental validation the spatial distribution of the nonlinear response was directly mapped in the back focal plane. Based on the numerical model the observed data can be explained and interpreted, whereby the experimental data are in good accordance to the theoretical predictions. It is shown that the split-pattern of electrical field components couple to off-diagonal elements of the nonlinear susceptibility resulting in a detectable nonlinear split-pattern in the back focal plane. Therefore, this technique is sensitive to the nonlinear susceptibility tensor and spatial variation of it and thus allows for an assignment of specific tensor elements to certain features of the nonlinear answer. Furthermore distinct coefficients can be separately addressed which couple in collinear beam direction to polarization components. With the combined theoretical and experimental approach the symmetry of the nonlinear optical susceptibility could be identified and the ratios of its coefficients could be estimated qualitatively. Overall, a powerful tool for the structural elucidation of ferroelectric domain structures based on the locally varying symmetry of the nonlinear susceptibility at the domain transition is available.

4.2 Nonlinear contrast mechanism

SHG microscopy represents a common technique for the visualization of ferroelectric domain structures. Thereby these noninvasive methods exploit the confocal regime. Especially for tightly focused regimes the surface near nonlinear contrast mechanism has not been understood so far. It stands to reason that the presence of domain walls is associated with a local change in susceptibility, such that their symmetry or strength is altered or the emerging of new tensor elements is indicated. In recent studies the local symmetry has been investigated by polarimetric measurements on domain walls like non-Ising types [179]. Such a local modification of the nonlinear susceptibility can explain the appearance of dark and light lines as the DW contrast in principle. Often SHG contrast is commonly explained by interference effects [180]–[182]. Considering interference effects one can assume a domain wall with nanometer-wide extensions which is illuminated by a linear polarized laser beam with a typical beam waist in the range of 200 nm up to 300 nm. Due to the inverted spontaneous polarization on the one side of the DW half of the laser beam induced SH intensity features a different phase to the other SH light which ends up in a destructive interference of both parts and eventually in a dark DW contrast considering the far field. According to the vectorial model introduced in subchapter 4.1 axial components of the excitation polarization do also feature a certain phase distribution and give rise to crucially contribute to the E-field distribution within the back focal plane when illuminating domain walls. A positive or bright SH contrast can be anticipated when taking into account phase leaps or triggering tensor elements laying on off-axis positions, e.g. when several components of the polarization are mixed. In order to consider all of those possible effects to clarify the origin of the SH contrast on domain walls the upcoming presented results obviously feature the already introduced high numerical aperture of 0.95 in order to trigger those newly induced components, cf. [183].

In a first step the ferroelectric domain structure and the corresponding nonlinear contrast behavior is obtained via confocal SHG microscopy in backward scattering geometry. Regarding the methodology and especially the pinhole mode of operation one has to distinguish between two general procedures here. Within the confocal regime typical line-, area and depth-scans are performed by varying the sample position with respect to both a fixed laser focus and pinhole position (Figure 4.9 a).

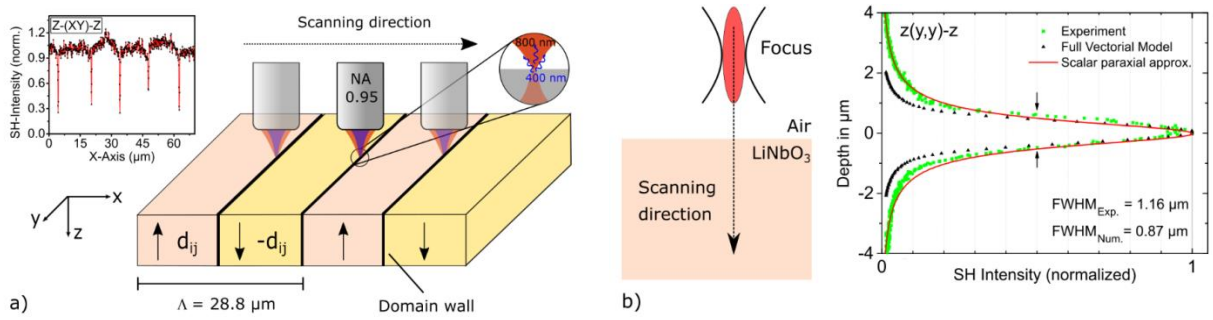

Figure 4.9: *Schematics for a lateral line-scan with respect to a static pinhole (a) and for an axial line-scan (in depth) allowing to determine the definition of the surface region (b). Additionally a scalar paraxial approach is included in the depth profiles to compare data from vectorial model and experiment.*

The subsequent presented results are obtained at the surface-near region. Obviously, the phase-mismatch increases in this constellation with $\Delta k \approx 73.74\ \mu m^{-1} \gg 0$ for $\Delta k = 2k_1 - k_2$ with $k_2 < 0$ due to the backscattering. Hence, the strong obtained SH-signal just arises from the interface area.

Furthermore, all this implies that in contrast to a transmission geometry ([30], [180]) birefringence or wavelength dependency can be neglected since all wave vectors point in the equal direction. The two latter references quote the following integral to describe the signal traveling back from the interface:

$$I_2(z_0; \Delta k, b) \propto \left| \int_L^{z_0} \frac{e^{i\Delta k z'}}{(1+2iz'/b)}\, dz' \right|^2$$

The integral limits and the phase-mismatch have to be adapted for the backscattering case. Here z_0 corresponds to the depth-axis whereas $b = k\omega_0$ is the confocal parameter of the assumed Gaussian beam and L serves as the opposite interface on the sample rear side. This means for a backscattering geometry that L is equal to infinity as the crystal is too bulky and hence the only dependence lies on the Gaussian focus position z_0 with respect to the medium. This treatment is a paraxial approximation of the model featuring a larger full width at half maximum due to the deficient consideration of the influence of the high NA in contrast to the full vectorial approach used in this work (inset of Figure 4.9 b). Also the experimental data show a larger FWHM because of deviations from a perfect illumination. As the vectorial approach assumes a plane wave for the excitation beam it represents a more idealized case.

Domain structures in $LiNbO_3$:

In order to study the nonlinear contrast mechanism within domain structures in $LiNbO_3$ typical confocal images of periodically poled z-cut LN have been acquired. The investigated specimen features a specified period length of $\Lambda = 28.8$ µm, whereby domain inversion alternates in x-direction. Nonlinear images of the z-face for the standard scattering geometries are shown in Figure 4.10.

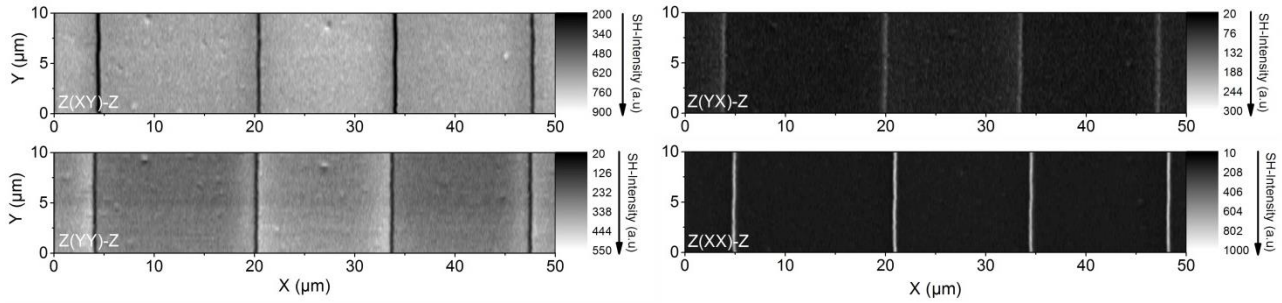

Figure 4.10: *Set of surface-near SH-area scans of the periodically poled $LiNbO_3$ sample for different scattering geometries revealing various contrast behaviors concerning the domain wall signal.*

One can clearly perceive the distinct contrast of the domain walls to the domains whereas z(xx)-z and z(yx)-z show a positive (enhanced) signal at the domain walls and the remaining two scattering geometries feature a lowered signal.

The outcome of such standard images of PPLN is also commonly known in literature [184]–[186], which partly confirms this behavior. Some different previous studies report only a positive DW contrast [179], in which measurements have not been performed in the surface-near region (focus depth: 100-300 µm). To clarify this issue depth scans for different focus depths (at surface and in 35 µm depth) have been performed. The result for the z(yy)-z scattering geometry is depicted in Figure 4.11.

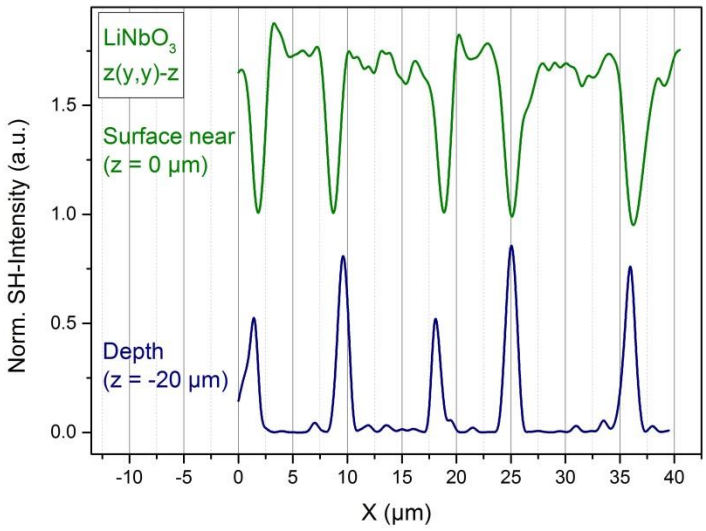

Figure 4.11: *Comparison of two line-scans performed on the surface and more than 20 µm within the sample for z(yy)-z scattering geometry indicating a contrast flip due to different prevalent contrast mechanisms.*

It can be confirmed that in the depth the contrast switches from dips to peaks which is also affirmed by Flörsheimer et al. [186]. It is also reported that this may relate to either the backscattered *Čerenkov*-like SHG [187]–[189] or newly induced tensor elements [179]. Due to the phase-related contrast contribution in a deeper crystal position a domain wall can serve as an origin for reversed momentum contributions that may successfully fulfill the phase-matching condition which would refer to the transmission geometry set *Čerenkov*-like SHG. Furthermore it can act as a depth-expanded area of enlarged nonlinear susceptibility values. For tightly focused surface-near measurements this is hardly visible due to the interference contrast as the most contributing parameter here.

The central part of the nonlinear contrast mechanism clarification utilizes the theoretical-experimental approach performed via the vectorial model and the focal mapping. Regarding the material polarization, the aforementioned tensor from equation (4.9) in its contracted notation is employed for the simulations. On the basis of [38] and [69] one can estimate the magnitude ratio of the relevant tensor elements $d_{33} \approx 36$ pm/V, $d_{31} \approx 6$ pm/V and $d_{22} \approx 3$ pm/V to $d_{33}:d_{31}:d_{22} \approx 12:2:1$ which is crucial for the simulations. The calculated results are presented in arbitrary units and normalized.

In order to represent the domain walls correctly within the simulations the spatial behavior respectively allocation of the $\chi^{(2)}$-tensor has to be taken into account. As a tradeoff of neglecting any further sophisticated compositions of the domain wall like in [179], the tensor is modeled with a Heaviside-function characteristic, i.e. that at a domain wall the tensor flips its sign. Mathematically this yields:

$$\overleftrightarrow{d}(\vec{r}) = \begin{cases} \overleftrightarrow{d}, & x < x_{DW}, z \geq 0 \\ -\overleftrightarrow{d}, & x \geq x_{DW}, z \geq 0 \\ 0, & z < 0 \end{cases} \tag{4.12}$$

For all scattering geometries the SH intensity distributions in the back focal plane have been acquired experimentally via the scanning pinhole module in the transition region between two contrarily poled domains and compared with the simulation results (Figure 4.12, Figure 4.13).

In the presence of a domain wall, the signal pattern looks different to the bulk case, which is present in all four scattering geometries. Figure 4.12 exhibits the two scattering geometries with y-polarized detection (rotational symmetric intensity distribution for a single domain).

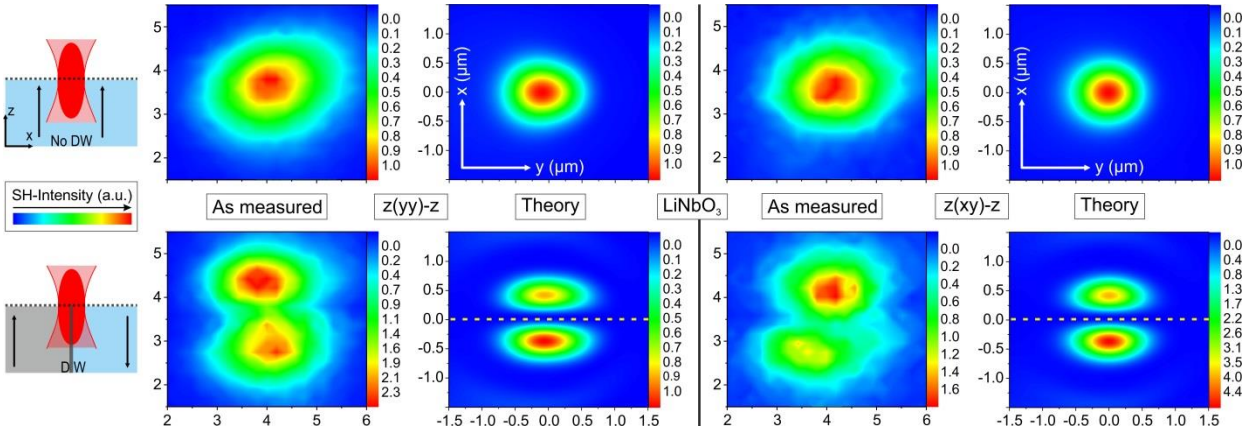

Figure 4.12: *Experimentally acquired and simulated SH intensity distributions in the back focal plane for LN at the transition region of contrarily poled domains for y-polarized detection. In the particular topmost row of both figures the bulk back focal plane signal without the presence of any domain wall is shown.*

According to the vectorial model one can explain this due to the coupling of E_y^2 to the d_{22}-element respectively E_x^2 to the d_{21}-element. Ideally focused on the domain wall the center of the back focal plane shows no intensity in between the split pattern. Due to destructive interference at this position the domain wall leads to a phase flip of π because the nonlinear tensor is assumed to be rotated, c.f. equation (4.12). Therefore these two scattering geometries are supposed to exhibit a dip, respectively lowered signal at a domain wall within standard scanning nonlinear microscopy.

The corresponding nonlinear patterns for x-polarization defined detection are depicted in Figure 4.13. In case of x-polarized excitation their x- and z-components are connected with the d_{15}-element leading to the two-fold pattern in phase as well as in amplitude for a single domain. The scattering geometry z(yx)-z also shows a two-fold intensity pattern in the back focal plane for no domain wall since the z-component of the incoming polarization is a non-split one convoluted with the two-fold dyadic Green's function's G_{13}-element, c.f. Figure 4.6. This element arises from the combination of the d_{32}-element with y-components.

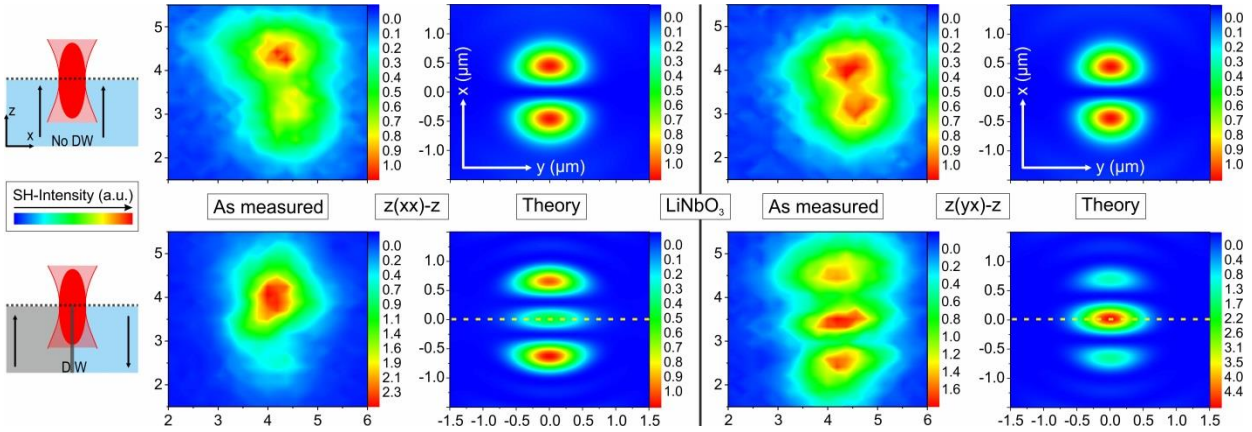

Figure 4.13: *SH intensity distribution within the back focal plane of $LiNbO_3$ acquired experimentally and simulated on and besides a domain wall and on bulk for x-polarized detection scattering geometries.*

For the z(xx)-z scattering geometry the presence of a domain wall leads to a three-fold splitting of previous two-fold pattern due to constructive interference. Differences between experiment and simulation in this case may probably rely on experimental imperfections and the weak integrated signal which may then be very sensitive to those small local variations within the nonlinear tensor.
The case z(yx)-z shows also a transformation of the two-fold pattern into a three-fold one because some amount of phase is added and the phase adjustment enables for an increased signal at the back focal plane center. In contrast to z(xx)-z the highest signal is to be found on the central maximum of the pattern (at the domain wall) for this geometry.

For a comparison of these results with those of recent publications working with larger (> 10 µm) pinholes, line-scans have been performed for all scattering geometries without the scanning pinhole module (diameter: 0.5 µm). In this case the fiber-core serves as a large pinhole instead. The experimental data are validated via the previously utilized vectorial model (see Figure 4.14).

For all scattering geometries the full vectorial model matches very well the experimental behavior. A comparison of these line-scans in terms of the expected type of domain wall contrast with the nonlinear patterns of the back focal plane, shown in Figure 4.12 and Figure 4.13, confirms the intensity dip for y-polarized detection as well as intensity peaks for x-polarized detection at the domain boundaries. One has to note, that the intensity of the line-scans is normalized to the particular maximum intensity of the bulk case without any domain wall apparent.

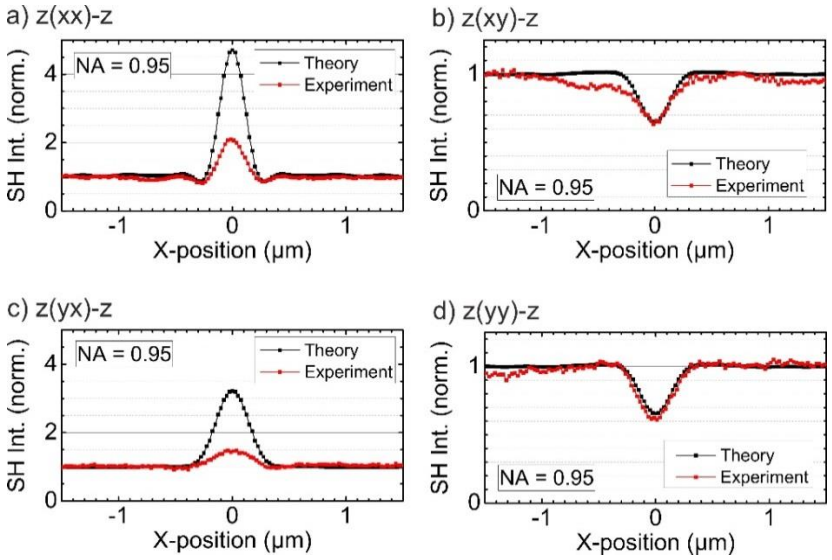

Figure 4.14: *Set of line-scans for each scattering geometry acquired on the sample surface experimentally (red) as well as calculated (black) with a large pinhole (> 10 µm). A qualitative match of simulation and experiment regarding contrast sign and its characteristics is apparent.*

The nonlinear contrast for the case of y-polarized signal exhibits a congruent manner which can obviously be explained by the direct coupling of the incident laser polarization to the respective tensor elements. The experimental captured domain wall signals for the case of x-polarization show a barely lower signal than the corresponding simulations, which can be ascribed to the stronger influence of the axial polarization components, explained above. Furthermore, it has to be noted that the two latter geometries (z(xx)-z, z(yx)-z) only feature more than a twentieth amount of entire integrated intensity than the other two geometries. Thus, these lower intensity results are more likely prone to discrepancies to the idealized model including especially a perfect illumination and the spatial characteristics of the particular tensor elements. Previous work has also reported about such aberrations for these geometries [179]. Apart from those deviations the combined experimental and theory approach delivers qualitatively and mostly quantitatively good accordance.

The line-scans also provide information about the resolution of the applied SHG microscopy. According to [176] and [158] the resolution can therefore be read as $\Delta s \approx 0.514\,\lambda/\sqrt{2}NA$ with the pump wavelength λ and a given numerical aperture NA. As the setup is working at $\lambda = 800$ nm and high focusing NA = 0.95 is employed the resolution yields $\Delta s \approx 306$ nm here. In Table 5 for the FWHM of domain wall signals experimental and theoretical data are compared for the four scattering geometries.

Scattering geometry	Experiment	Theory
z(xx)-z	214 ± 3 nm	225 ± 3 nm
z(xy)-z	325 ± 7 nm	300 ± 3 nm
z(yx)-z	325 ± 13 nm	325 ± 2 nm
z(yy)-z	344 ± 16 nm	287 ± 3 nm

Table 5: *Compilation of the FWHM values of the four scattering geometries from the experimental as well as calculated domain wall signatures presented in Figure 4.14.*

Apart from z(xx)-z the geometries yield an experimental FWHM nearby the resolution limit of the setup. For these cases the incoming polarization field is linearized and the contribution of any axial respectively right-angled components is quite low. For the z(xx)-z case linear x- and orthogonal z-components are mixed. Due to the high NA z-components are underneath the calculated resolution limit as also reported in the literature [190] for linear microscopy. Subsequently a domain wall is represented with a lowered FWHM. This finding can give an opportunity to perform measurements on the edge of the common resolution limit and beyond if the experimental prerequisites allow for a well-defined addressing of the scattering geometry (e.g. via focus shaping).

Domain structures in KTP:

The analysis of domain structures in KTP are performed on a periodically poled z-cut sample with a period length of $\Lambda = 7.6$ µm. Hence, the domain walls are oriented along the crystallographic y-axis. Likely to the analysis on $LiNbO_3$ the domain walls and the surrounding area are investigated via SHG microscopy. In order to obtain information about general SHG contrast behavior of KTP, line- and area-scans are performed for the different scattering geometries (see Figure 4.15). Here solely for all scattering geometries a positive SH contrast was found.

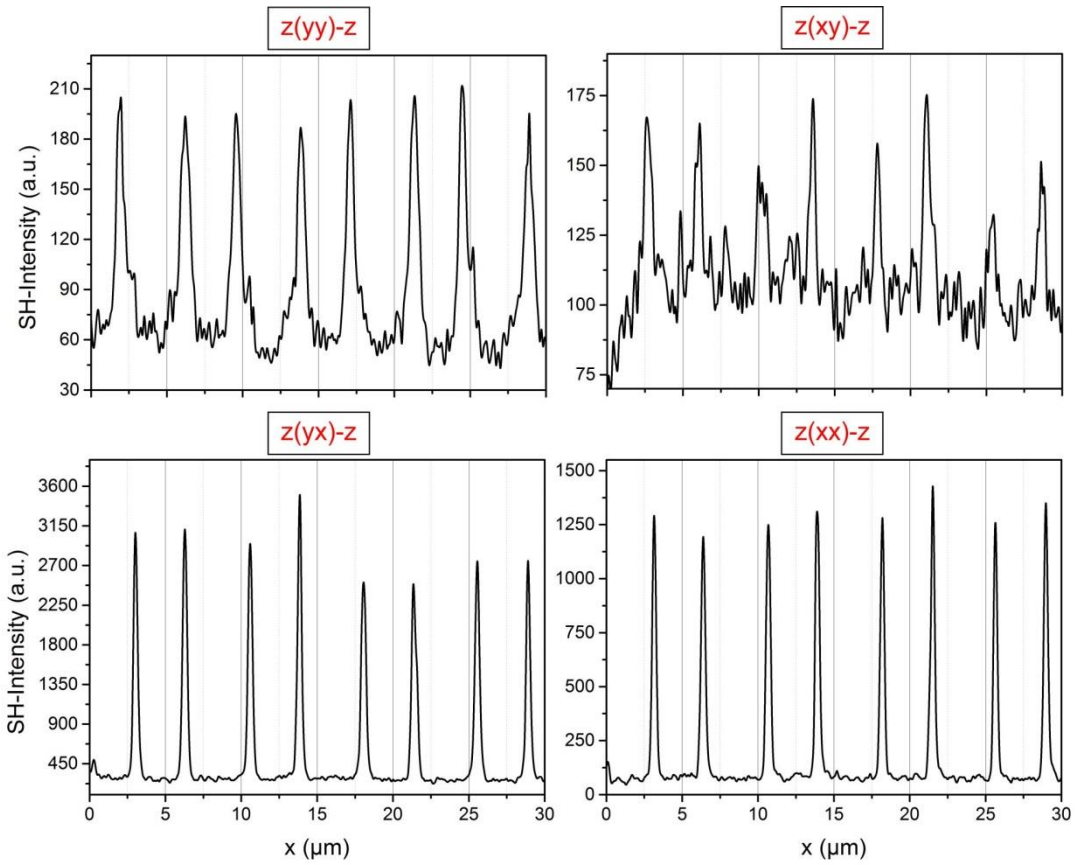

Figure 4.15: *Set of four line-scans on periodically poled $KTiOPO_4$ acquired with showing the thoroughly positive domain wall contrast in this material.*

This typical behavior is also reported and confirmed in literature [191]. For this positive contrast the magnitude of signal enhancement depends on the particular scattering geometry. However, as to be seen later (analysis of the back focal plane) this seems like a discrepancy to the theoretical prediction, since a negative contrast for the scattering geometries z(xy)-z and z(yy)-z is expected.

For nonlinear analysis within the back focal plane the nonlinear tensor in its contracted notation (equation 2.35) is used. The strengths of the tensor elements yield: $d_{33} \approx 18.5$ pm/V, $d_{31} \approx 2.76$ pm/V and $d_{15} \approx 2.04$ pm/V [37]. Likely to LN the contrast mechanism can be explained via a phase contrast combined with a rotated tensor. Furthermore structural changes at the transition region induce locally new tensor elements which have a strong influence on the material polarization and therefore on the nonlinear field distribution in the back focal plane. The corresponding patterns at the transition region of domains with opposite polarity are gathered for the relevant scattering geometries and compared to the particular theoretical data (see Figure 4.16 - Figure 4.19).

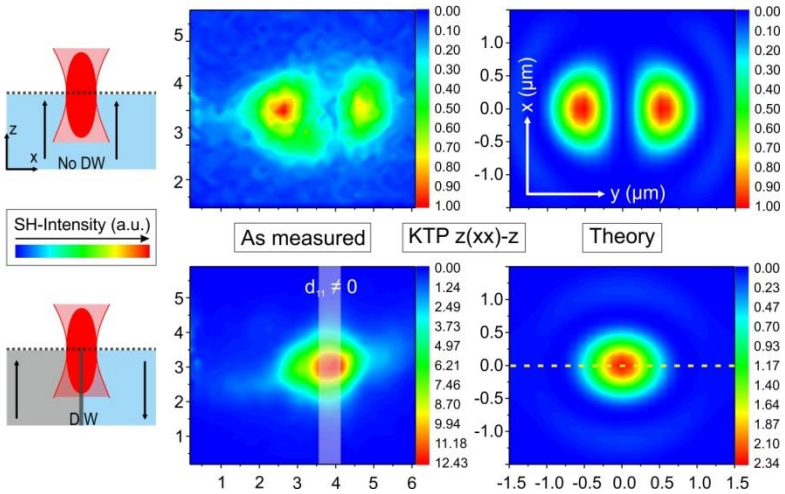

Figure 4.16: *SH intensity distribution within the back focal plane of $KTiOPO_4$ acquired experimentally and simulated on and besides a domain wall and on bulk for z(xx)-z scattering geometries.*

For the z(xx)-z geometry the nonlinear field distribution undergoes a change from a two-fold split pattern (single domain) to a rotational symmetric pattern at the domain boundary (Figure 4.16). Hence, one can expect a positive contrast due to the accumulated phase gain ending up in a positive interference. The central spot exhibits an intensity several times stronger compared to the single domain signal. The discrepancy concerning different intensity ratios between experiment and simulation could be explained by direct coupling with an emerging element $d_{11} \neq 0$ at the domain wall (discussed later).

A slightly different case can be observed for z(yx)-z scattering geometry (Figure 4.17). Here the contrast also turns out to be positive at the domain wall originated by a central peak flanked by two side-peaks with a lowered intensity forming also a three-fold pattern.

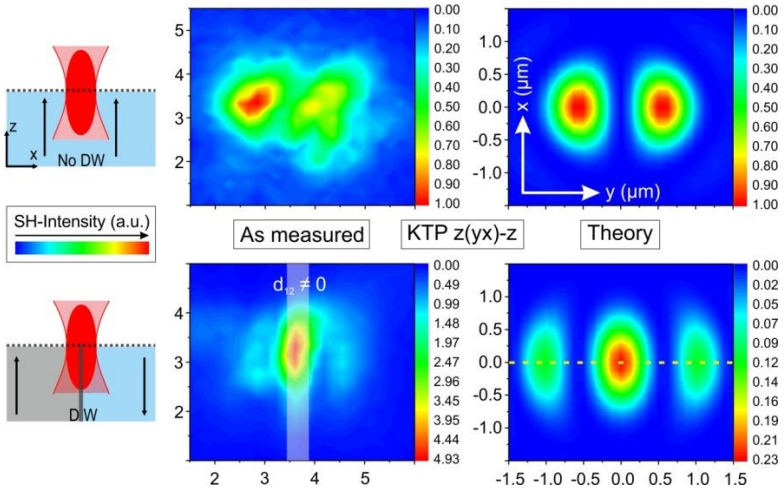

Figure 4.17: *Experimental acquired and simulated SH pattern for the z(yx)-z scattering geometry within the back focal plane of $KTiOPO_4$ at the transition region of contrarily poled domains.*

For the z(yx)-z geometry the nonlinear field distribution evolves from a two-fold split pattern (single domain) to three-fold split pattern at the domain wall. For the theoretical prediction the nonlinear signal of a single domain is about 5 times smaller compared to the central peak intensity within the field distribution which arises from the domain boundary. Here the positive contrast is only present for the high confocal application (small pinhole diameter, central position) otherwise the integrated signal should lead to a negative contrast. On the contrary the experimental data feature a flipped intensity ratio, here the center peak intensity is about 5 times higher compared to the single domain signal resulting in a steady positive contrast. This can give rise to the assumptions that new elements may have been locally added to the nonlinear tensor of the material which couples with the commonly zero elements d_{11} and d_{12}. For this case new tensor elements for the simulations have to be taken into account.

Based on the theory side the scattering geometries z(xy)-z and z(yy)-z feature a four-fold splitting at a domain wall which can be attributed to a newly added phase. The experimental validation for the z(xy)-z geometry is shown in Figure 4.18.

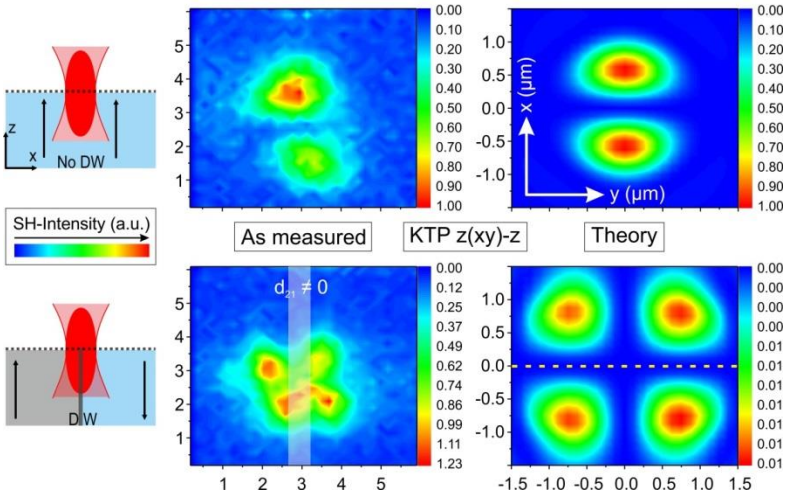

Figure 4.18: *SH intensity distribution within the back focal plane of $KTiOPO_4$ acquired experimentally and simulated at and besides a domain wall and for a single domain for z(xy)-z scattering geometry.*

In accordance with the theory the experimental data show a changeover from a two-fold pattern (single domain) to a four-fold one when approaching a domain wall with differences in the intensity ratios. Here, the intensity evolution also shows a contrary behavior. For the experimental data the signal increases when approaching the domain wall, whereas the simulation data predict a steady decrease. From the model side a negative contrast would be expected whereby the involved intensities are extremely small and would vanish within the signal noise. The small positive contrast arising from the experimental data again stands for the reason of the presence of new induced elements ($d_{21} \neq 0$) within the susceptibility tensor. An analogous behavior can be found for the z(yy)-z scattering geometry (Figure 4.19).

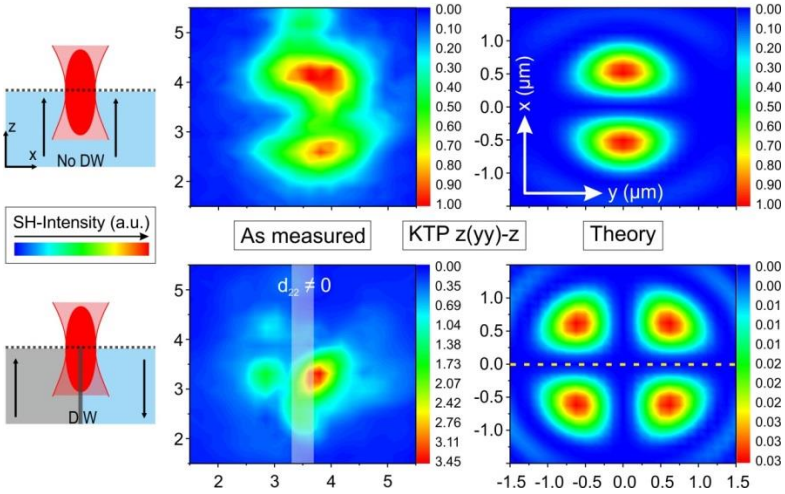

Figure 4.19: *SH intensity distribution within the back focal plane of $KTiOPO_4$ acquired experimentally and simulated on and besides a domain wall and on bulk for z(yy)-z scattering geometries.*

Again the four-fold pattern for the nonlinear intensity distribution at the domain wall becomes visible. Attributed to the mixture of the pattern itself originating from the aforementioned phase contrast and the new element(s) ($d_{22} \neq 0$) occurring on the domain wall the experimentally acquired four-fold pattern appears to be disfigured.

The principle functionality of the vectorial model especially the phase contrast aspect could be validated via the experimentally acquired nonlinear intensity distributions within the back focal plane in the vicinity of a domain wall. Deviations of both the field distributions and the intensity ratios give rise to new emerging tensor elements within the domain wall region. Hence, one can explain the solely positive nonlinear contrast within KTP and if applicable determine the strength of the particular tensor elements. If a low-symmetry tensor is assumed, which for KTP means a transition from a *mm2*- symmetry to a mixed symmetry for example of 2- and *m*-symmetry, new directly coupling elements in the nonlinear tensor arise (equation 4.13). In this tensor the previously identified elements are included. The altered tensor has six new elements being unequal zero, which are not as high as the pristine elements but are still responsible for the obtained distinct contrast due to the non-apparent direct coupling for z-cut KTP.

$$d_{KTP,new} = \begin{bmatrix} d_{11} \neq 0 & d_{12} \neq 0 & 0 & d_{15} \neq 0 & d_{15} & 0 \\ d_{21} \neq 0 & d_{22} \neq 0 & 0 & d_{24} & d_{15} \neq 0 & 0 \\ d_{31} & d_{32} & d_{33} & 0 & 0 & 0 \end{bmatrix} \qquad (4.13)$$

Exemplarily such a tensor modification is presented for the z(xx)-z scattering geometry. For that the direct coupling d_{11}-element ($d_{11} \approx -d_{24}$) is implemented within the tensor. The results from the adapted simulation are subsequently shown opposed to the experimental data (see Figure 4.20).

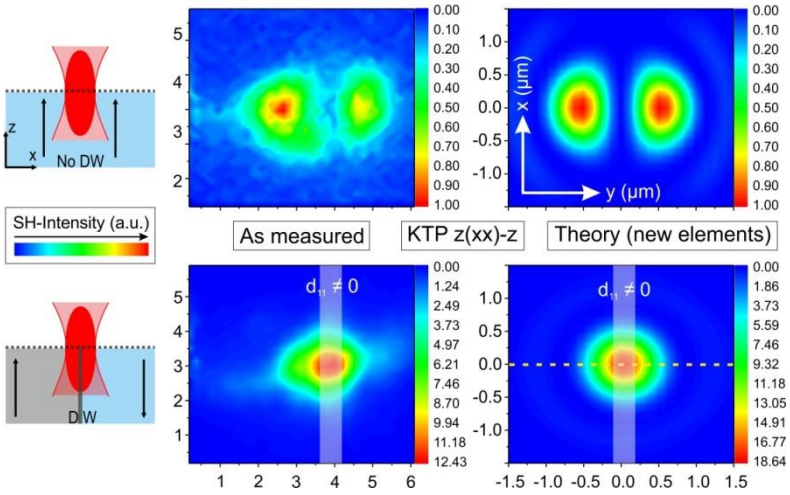

Figure 4.20: *SH intensity distribution within the back focal plane of $KTiOPO_4$ for z(xx)-z scattering geometry with altered simulation parameters regarding the newly induced tensor element $d_{11} \neq 0$.*

As a result of the implementation of the new tensor element the nonlinear contrast is in the same magnitude for experiment and simulation and the patterns are more congruent now.

Interim summary:

The nonlinear light–matter interaction in the vicinity of domain walls has been analyzed and modeled for the surface-near region of both, periodically poled LN and KTP. For both material systems the experimentally acquired nonlinear response in the back-focal plane is in very good accordance to the simulation data gathered from a numerical calculation (vectorial approach, considering point-spread functions and SHG). Here, a detailed analysis shows that the main nonlinear contrast mechanism is based on the sign change of the nonlinear susceptibility at the domain transition. Thus, the characteristic contrast patterns are a result of constructive or destructive interference in the near-surface region. Another important contrast mechanism is represented by polarization components induced by the strong focusing and a coupling of differently polarized light components to off-axis elements. Furthermore, the local appearance of new tensor elements could be identified as a third effect on the nonlinear contrast, which dominates when smaller numerical apertures are considered.

4.3 Vibrational properties

In order to conduct detailed Raman investigations on periodic structures or devices like waveguides a basic knowledge of the vibrational modes is necessary. In the following two subchapters the fundamental Raman fingerprints of LN and KTP are presented for different scattering geometries. Furthermore certain structure sensitive modes for Raman imaging are shown and discussed.

4.3.1 Raman analysis of $LiNbO_3$

Lithium niobate is also investigated in terms of its fundamental Raman active vibrational modes for the use of further measurements. Due to the rhombohedral unit cell LN features two formula units with each 5 atoms which lead to 5 A_1 and 5 A_2 mode clusters and 10 E modes. It has to be noted that one A_1 mode and the two of the two-fold degenerated E modes are acoustic phonons. This results in $\Gamma_{LN\,vib} = 4A_1 + 5A_2 + 9E$ = 27 optical phonons. These modes have to be distinguished whether they are infrared or Raman active. A_1 vibrations account for both. The same characteristic holds for the E modes, whereas the A_2 modes are not perceptible in both cases. Furthermore, a certain degeneracy between the longitudinal and transversal optical vibrations is present for LN. Hence, the aforementioned sum leads to 27 optical phonons when LO and TO phonons are considered for each cluster. Since the material belongs to the symmetry group C_{3v} the dependence of the particular utilized polarization or scattering geometry can foreshadow the behavior of the vibrations when the Raman tensor R_{LN} is considered [165], [167]:

$$A_1(z) = \begin{pmatrix} a & 0 & 0 \\ 0 & a & 0 \\ 0 & 0 & b \end{pmatrix}, E(y) = \begin{pmatrix} c & 0 & 0 \\ 0 & -c & d \\ 0 & d & 0 \end{pmatrix}, E(-x) = \begin{pmatrix} 0 & -c & -d \\ -c & 0 & 0 \\ -d & 0 & 0 \end{pmatrix} \tag{4.14}$$

From the diagonal filled axis one can see for instance that the A_1 modes are moving along the crystallographic z-axis. Further information like the occurrence of either A or E vibrations in the particular scattering geometries can be extracted from the Raman tensor. The relation $I \propto |e_s \cdot R \cdot e_i|^2$ provides the basis for the prediction of the occurring modes in terms of the Porto's notation, c.f. [118] by linking the relevant Raman tensor elements to the geometry species.

In order to provide an overview of the fundamental modes all three crystallographic faces are considered. The spectra of all scattering geometries of z-incident light are given in Figure 4.21. For the sake of completeness the spectra of the two crossed polarizations are presented although both are expected to look alike since the Raman tensor is symmetric. This behavior is validated within the spectra. Beginning with the set of z-face Raman spectra one can identify A_1-LO modes as well as E-TO modes. The former ones are distinct features of these scattering geometries since those longitudinal vibrations spread along the crystallographic z-axis. From the spectra one can read the A_1-LO modes at 274 cm^{-1}, 330 cm^{-1}, 432 cm^{-1} and 871 cm^{-1}. The latter vibration is striking especially for the parallel scattering geometries due to its overall highest intensity. This is also apparent in a weaker peak for the crossed polarizations. These findings conform with previous findings in the material [192], [193].

In contrast to the parallel polarizations the E-TO modes, which originate here from the selection rules of the material, are more detailed to be seen within the crossed polarizations for z(p_i , p_s)-z. The E-modes are to be identified at 151 cm^{-1}, 237 cm^{-1}, 263 cm^{-1}, 321 cm^{-1}, 367 cm^{-1}, 581 cm^{-1} and 664 cm^{-1} whereas the last mentioned vibration is very barely visible and often discussed in the literature whether it accounts for an E-TO mode. This is often accompanied with the identification of the weak mode below 750 cm^{-1} [194]. This scattering geometry set of z-incident light connects the c^2 element with the TO vibrations and a^2 to the A_1-LO modes.

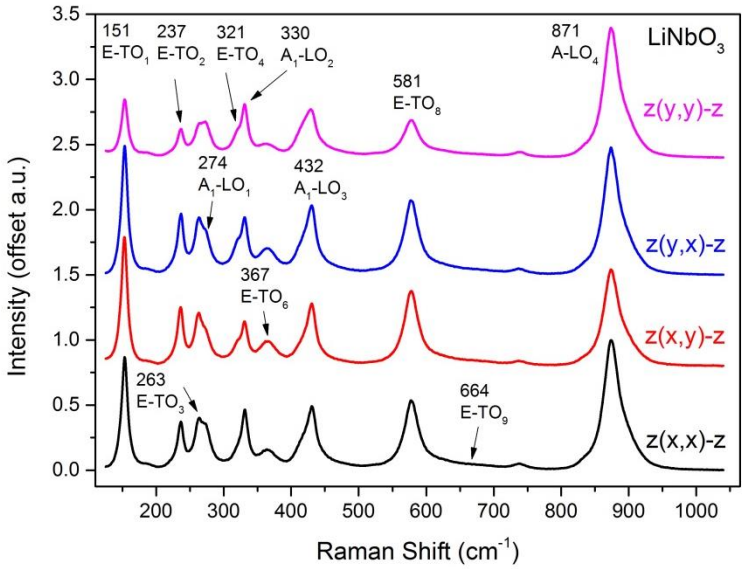

Figure 4.21: *Fundamental (normalized) Raman spectra of $LiNbO_3$ for comparison in all fours scattering geometries of z-incident light.*

The y(p_i , p_s)-y side features longitudinal E-vibrations and A_1-TO modes since the particular LO and TO modes never occur together in one symmetry specie for A_1 or E. The responsible Li and Nb ions for the TOs of the A_1 specie are phase-aligned in their movement. Figure 4.22 shows the four fundamental spectra of y-face LN with the A_1-TO modes at 254 cm^{-1}, 276 cm^{-1}, 333 cm^{-1} and 633 cm^{-1}. Exemplarily the first TO vibration at 254 cm^{-1} is very distinctly visible for the parallel polarizations. Here, the Nb atoms are propagating contrarily to the oxygen atoms [195]. The A_1-TO_2 accounts for oscillating Li-ions whereas the two further TO modes are aligned in their movement along the crystallographic x- and y-axis and conduct a flexural respectively a stretching vibration of the oxygen niobium bond [195]. This turns out in so called breathing modes.

The other vibrations in here are the E-LO modes which only occur in the y(p_i , p_s)-y scattering geometry. It can be stated that these modes are likely inconsiderable since they feature a lowered intensity than their E-TO counterparts. From the literature it is known that the y(p_i , p_s)-y scattering geometry is therefore often linked to the occurrence of leakage modes [196].

The y(x,x)-y scattering geometry is connected with the Raman tensor element a^2 for the TO modes and c^2 for the LO modes. For the crossed polarizations it is the d^2 element and y(z,z)-y links the b^2 element to the A_1-TO vibrations.

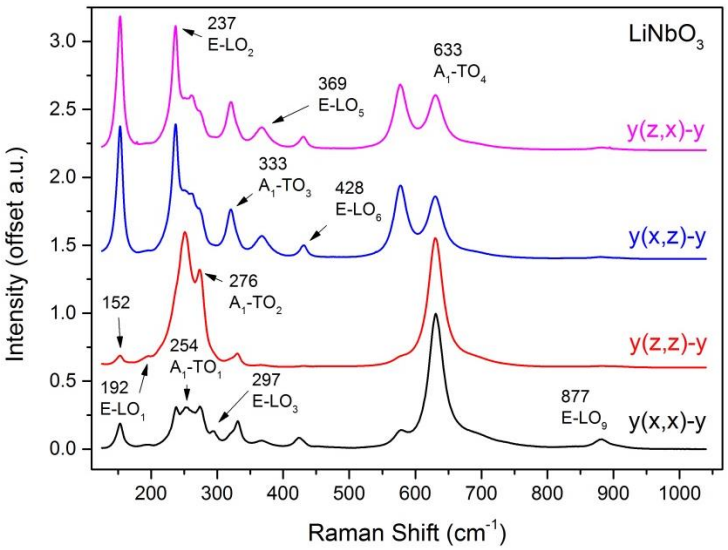

Figure 4.22: *Fundamental (normalized) Raman spectra of $LiNbO_3$ for comparison in all fours scattering geometries of y-incident light.*

The set of x(p_i , p_s)-x scattering geometries features E-TO vibrations as well as A_1-TO modes. The E-TO modes are mostly present for crossed polarizations as seen in Figure 4.23 which underlines the aforementioned behavior of these modes for z-incident light and crossed polarizations. Regarding the Raman tensor x(y,y)-x is connected with the elements $a^2 + c^2$, x(z,z)-x with b^2 and the crossed polarizations with d^2.

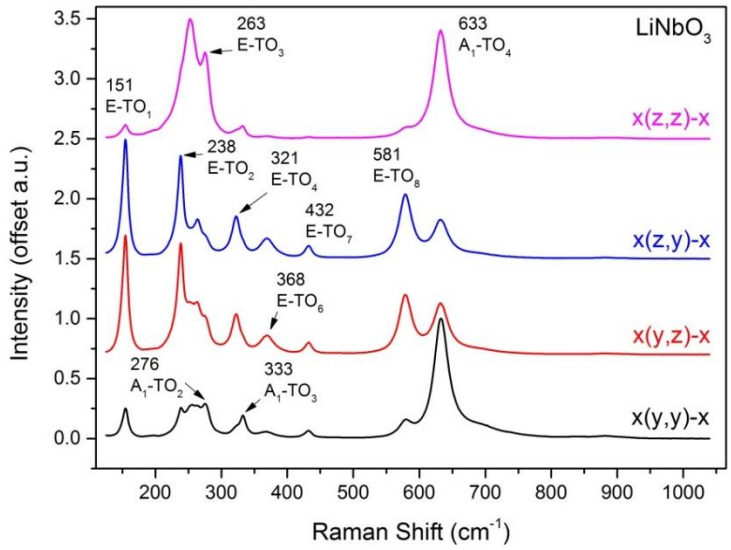

Figure 4.23: *Fundamental (normalized) Raman spectra of $LiNbO_3$ for comparison in all fours scattering geometries of x-incident light.*

An overview of the observable occurring vibrational modes in LN is given in Table 6 connecting the experimentally obtained modes with the particular scattering symmetry and specie. Furthermore, comparable literature values are given in the table. Besides all these unambiguously identifiable phonon modes in LN several modes are missing in this listing which are accounted by several authors [196]–[199].

Raman Shift (cm^{-1}) experimental	*Raman shift (cm^{-1}) literature*	*Symmetry specie*
252-255 / 274	239	A_1-TO_1 / A_1-LO_1
273-274 / 330	289	A_1-TO_2 / A_1-LO_2
331-333 / 432	353	A_1-TO_3 / A_1-LO_3
632-633 / 871	610	A_1-TO_4 / A_1-LO_4
150-151 / 192	148	E-TO_1 / E-LO_1
237 / 237	216	E-TO_2 / E-LO_2
262-263 / 297	262	E-TO_3 / E-LO_3
320-321 / -	320	E-TO_4 / -
367-369 / 366, 426	380/391	E-$TO_{5/6}$ / E-$LO_{5/6}$
432 / 456	423	E-TO_7 / E-LO_7
580-581 / -	579	E-TO_8 / -
664 / 879	667	E-TO_9 / E-LO_9

Table 6: *Comprehensive overview of occurring TO and LO Raman modes in LN comprising all relevant symmetry species for the three backscattering polarization geometries and comparable literature values* [200].

4.3.2 Raman analysis of $KTiOPO_4$

In contrast to LN with its 27 optical phonons the description of the fundamental Raman fingerprint is more elaborate for $KTiOPO_4$. Analog to LN the theoretical prediction leads to $\Gamma_{KTP_{vib}} = 47A_1 + 48A_2 + 47B_1 + 47B_2$ = 189 optical phonons [201] which is due to the crystal built up of KTP introduced before featuring eight units. Not analog to LN any of these phonons can be omitted since it does not come to any degeneracy here. This leads to a Raman tensor from the symmetry group C_{2v} (orthorhombic):

$$A_1 = \begin{pmatrix} a & 0 & 0 \\ 0 & b & 0 \\ 0 & 0 & c \end{pmatrix}, A_2 = \begin{pmatrix} 0 & d & 0 \\ d & 0 & 0 \\ 0 & 0 & 0 \end{pmatrix}, B_1 = \begin{pmatrix} 0 & 0 & e \\ 0 & 0 & 0 \\ e & 0 & 0 \end{pmatrix}, B_2 = \begin{pmatrix} 0 & 0 & 0 \\ 0 & 0 & f \\ 0 & f & 0 \end{pmatrix} \tag{4.15}$$

The Raman tensor gives several hints what is to be expected for the fundamental spectra and it connected symmetry types by again using the equation $I \propto |e_s \cdot R \cdot e_i|^2$, which connects the intensity with the Raman tensor and thus all scattering geometries, cf. [118].

In order to give a basis for the further presented detailed Raman spectroscopy results of KTP a comprehensive set of the Raman spectra for the different scattering geometries is given in Figure 4.24. For the sake of completeness it has to be noted that the crossed polarizations are only given once per scattering geometry group since both crossed polarizations show the same spectra, cf. Raman tensor. The spectra are normalized and corrected for a background.

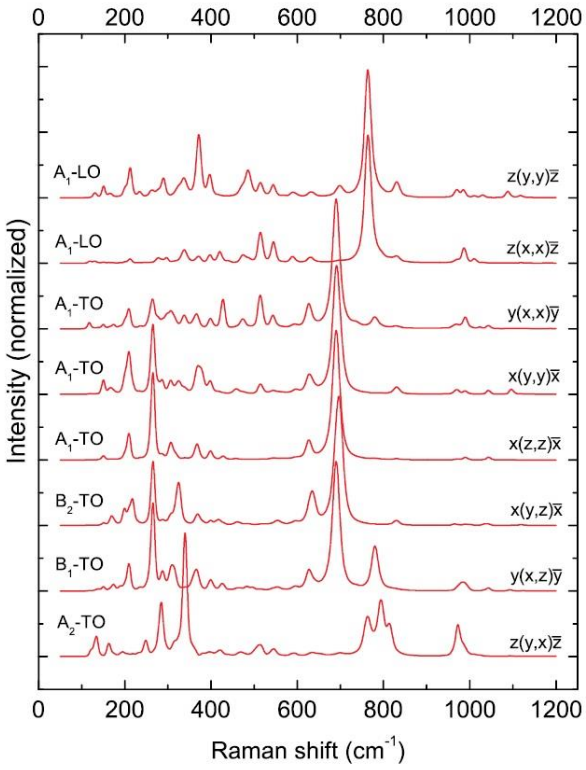

Figure 4.24: *Delineation of the fundamental (normalized) Raman spectra of $KTiOPO_4$ for comparison in each symmetry specie (left lable) respectively the scattering geometry (right lable) from* [118].

For KTP it is also differentiated between TO and LO phonons. In terms of the symmetry types one can only observe LO phonons within the A_1 group and TO phonons in each group. Since group theory predicts 189 optical phonon modes for KTP it is obvious that each scattering geometry features many phonon modes. For that one can account for typical features of the symmetry groups as the A_1-TO group shows intense peak areas around 209 cm^{-1}, 267 cm^{-1} and 691 cm^{-1} whereas this holds for the LO one only for 760 cm^{-1} for instance. All spectra are comparable in terms of the appearance of several spectral areas. Below 200 cm^{-1} no intense features are at hand, whereas up to 350 cm^{-1} some strong peaks characterize this region followed by a mean intensity area to 690 cm^{-1}. The outstanding KTP peaks visible in each symmetry group are localized in between 690 cm^{-1} and 800 cm^{-1}. Several further peaks are found in the remaining area up to 1200 cm^{-1}. It should be noted that a similarity of some of the A_1-LO peaks (625 cm^{-1} and 693 cm^{-1}) and the A_1-TO and B_2-TO spectra are due to the certain k-vector allocation of the excitation optics, cf. [118].

Since the two striking bonds within the KTP crystallographic structure are the TiO_6 octahedron and the PO_4 tetrahedron the vibrational modes are likely to be ordered for these bonds.
The octahedron is assigned to perform six different vibrations. According to [202] in general half of them are Raman active and the others IR active but for KTP the crystallographic structure is different for the transition from the para- to ferroelectric phase which leads to six Ti-O bonds with different lengths resulting in altered selection rules. As a consequence all vibrations can be measured in terms of Raman spectroscopy. These six vibrations are sketched in Figure 4.25.

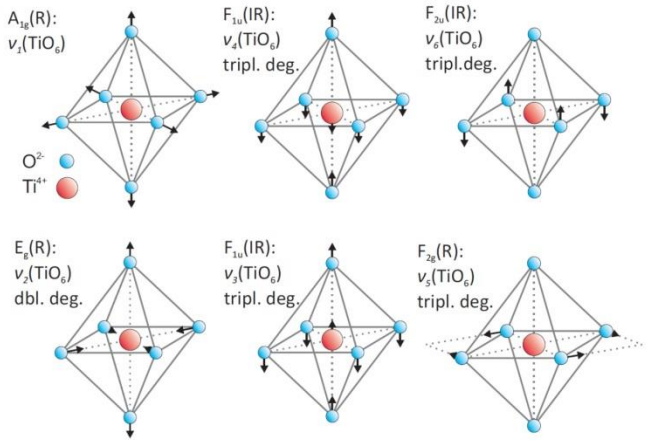

Figure 4.25: *Ball-and-stick model of the six TiO_6 octahedron vibrations of KTP with black arrows indicating the movement direction of the respective atom according to* [199], [202].

According to [202] the first mode provides two peaks since the octahedron offers two sites. The next vibration is likewise also linked to the double sites of the octahedron. From its movement the first mode is a very suitable example of a breathing mode because the octahedron is stretched uniformly and symmetric in all directions. This results in the intense and prominent peak at around 693 cm^{-1} depending on the scattering geometry. The first three vibrations are responsible for peaks in the range above 400 cm^{-1} whereas the other vibrations are found in the range between 200 and 400 cm^{-1}.

A list of the particular modes for the vibrations $\nu_1(TiO_6)$ to ν_6 (TiO_6) is given in Table 7 with literature values for comparison and the respective symmetry species.

TiO_6 vibration	Raman Shift (cm^{-1}) experimental	Raman shift (cm^{-1}) literature	Symmetry species
υ_1 (TiO_6)	691 697	692.8 698.8	A_1(xx); A_1(yy) B_2(yx)
υ_2 (TiO_6)	627	629.4	A_1(zz)
υ_3 (TiO_6)	814 830	818.6 832	A_2(yx) A_1(zz); B_2(yx)
υ_4 (TiO_6)	306 339	309.2 341.3	A_1(zz) A_2(yx)
υ_5 (TiO_6)	264 288	267.8 289.2	B_2(yx) B_1(zx)
υ_6 (TiO_6)	209	212.1	A_1(zz)

Table 7: *Overview of occurring Raman modes in $KTiOPO_4$ related to the TiO_6 octahedron with literature values* [201], [202] *and its symmetry species.*

The PO_4 tetrahedron does not lead to different P-O bonds in terms of their lengths in contrast to the octahedron due to its symmetric shape [203]. Likewise to the octahedron the occurring four vibrations of a tetrahedron are sketched for KTP in Figure 4.26.

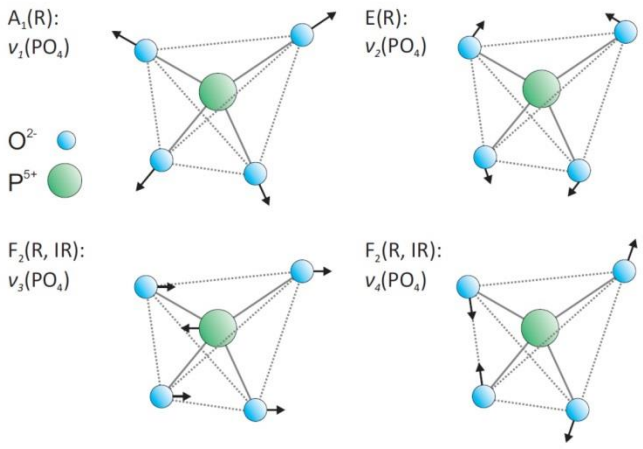

Figure 4.26: *Ball-and-stick model of the four PO_4 tetrahedron vibrations of KTP with black arrows indicating the movement direction of the respective atom according to* [199], [202].

All four modes $\nu_1(PO_4)$ to ν_4 (PO_4) are observable in a Raman spectrum. As to be seen in the figure the first vibration is again the prominent breathing mode. Analog to the octahedron the tetrahedron also demands two sites within the crystallographic structure of KTP. Hence, the first two vibrations are responsible for respectively two peaks in the spectra.

As indicated in the figure the other two vibrations are of F symmetry. The particular modes for the vibrations $\nu_1(PO_4)$ to ν_4 (PO_4) are given in Table 8 with literature values for comparison and the respective symmetry species.

PO_4 vibration	Raman Shift (cm^{-1}) experimental	Raman shift (cm^{-1}) literature	Symmetry species
υ_1	972 983	975.2 980.5	$A_2(yx)$ $B_1(zx)$
υ_2	369 399	369.1 400.1	$A_1(zz)$ $A_1(zz)$
υ_3	1000 1044	1003.8 1045.9	$B_2(yx)$ $A_1(zz)$
υ_4	514 545	516.1 544.8	$A_2(yx)$ $A_2(yx)$

Table 8: *Overview of occurring Raman modes in $KTiOPO_4$ related to the PO_4 octahedron with literature values* [201], [202] *and its symmetry species.*

Besides these two components of the KTP crystal structure the potassium ions cannot be omitted here. In a low frequency region below 350 cm^{-1} they are responsible for some peaks [202], [204].

Raman imaging of KTP:

Likewise to LN typical structure sensitive modes for Raman imaging in KTP are to be found in the range of 680 – 730 cm^{-1} (see Figure 4.27), at 760 cm^{-1} or 783 cm^{-1}.

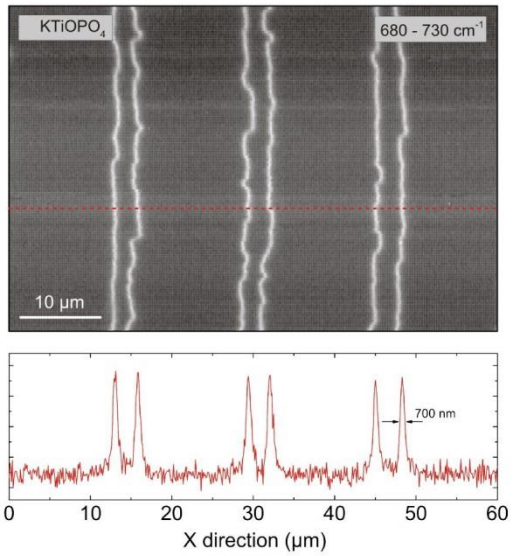

Figure 4.27: *Example of Raman imaging (area scan) of KTP generated by the integrated intensity of the vibration at 680 – 730 cm^{-1} (upper inset). Domain walls feature an increased Raman intensity for this mode which also becomes evident in the corresponding line scan (lower inset). The FWHM of a DW signal is also indicated with 600 nm* [205].

Interim summary:

The vibrational properties were recorded in the form of Raman fundamental spectra for bulk LN and KTP, which form the basis for further analyses such as those using Raman imaging. A polarization-dependent analysis was performed and the various scattering geometries were presented in a coherent manner. Furthermore, a tabular overview of the occurring vibrational modes is given for both materials, which shows the literature values as well as the relevant symmetry species in addition to the experimentally measured wavenumbers. The occurrence of the modes is explained in connection with the respective crystal structure, which, for example, is explained in more detail for KTP with the TiO_6 octahedrons as well as the PO_4 tetrahedrons.

4.4 Fingerprints of domain structures

Based on the fundamental spectra and the knowledge of structure sensitive vibrational modes periodically poled ferroelectric structures are investigated in this subchapter. Such an analysis gives a fundamental understanding of the particular response of the Raman signal for domain inversions and at domain walls which helps for the understanding and interpretation of further studies on functional structures like periodically poled waveguides for instance. Furthermore a mode assignment for these fingerprints of domain structures is provided here.

4.4.1 Structure sensitive modes in $LiNbO_3$

In lithium niobate distinct modes are very sensitive to crystallographic changes especially the change during a domain inversion process. This sensitivity is the basis for Raman imaging of ferroelectric domain structures. Such sensitivity can turn out in a varying Raman intensity, a different Raman shift or different half widths for the area of the domain compared to the domain walls. Table 9 lists the fundamental Raman modes and emphasizes the ones which distinctly feature any change at a domain wall.

Raman Shift (cm^{-1}) experimental	*Raman shift (cm^{-1}) literature*	*Symmetry specie*
252-255 / 274	239	A_1-TO_1 / A_1-LO_1
273-274 / 330	289	A_1-TO_2 / A_1-LO_2
331-333 / 432	353	A_1-TO_3 / A_1-LO_3
632-633 / 871	610	A_1-TO_4 / A_1-LO_4
150-151 / 192	148	E-TO_1 / E-LO_1
237 / 237	216	E-TO_2 / E-LO_2
262-263 / 297	262	E-TO_3 / E-LO_3
320-321 / -	320	E-TO_4 / -
367-369 / 366, 426	380/391	E-$TO_{5/6}$ / E-$LO_{5/6}$
432 / 456	423	E-TO_7 / E-LO_7
580-581 / -	579	E-TO_8 / -
664 / **879**	667	E-TO_9 / E-LO_9

Table 9: *Comprehensive overview of occurring Raman modes in LN with all relevant symmetry species for the three backscattering polarization geometries and comparable literature values* [200].

Analogous to the scanning principle used in SHG microscopy, a line or area is scanned point by point to obtain a complete spectrum for each point. The gray scale image is then generated by plotting the integrated intensity for the previously chosen sensitive mode for instance or one of the other parameters. As aforementioned the results for these parameters can be improved by using a fitting routine by means of a Lorentzian function. Since the material is thoroughly studied in terms of Raman spectroscopy and recent publications dealt with the assignment which modes are structure sensitive for LN this subchapter should give a comprehensive overview of it.

Since a domain inversion respectively the emerging of domain walls proceeds along the crystallographic z-axis Raman images are taken by standard for the $z(p_i , p_s)$-z scattering geometries. From the fundamental spectra it is known that E-TO modes and A_1-LO vibrations occur here. The sensitivity for DWs of the y-face of LN is for example investigated in [205]. In principle, most of the modes show a certain sensitivity but several modes are more prominent to be used for imaging.

LN phonon modes which provide a very good contrast can for example be found in the range of 560 cm^{-1} to 630 cm^{-1} [206]–[208]. This includes prominently the E-TO_8 mode. Furthermore the E-TO_6 and E-TO_9 vibrations are often used for the visualization of periodic domain structures in this material. Figure 4.28 shows an example of an area scan taken for the E-TO_8 vibration and a corresponding line scan.

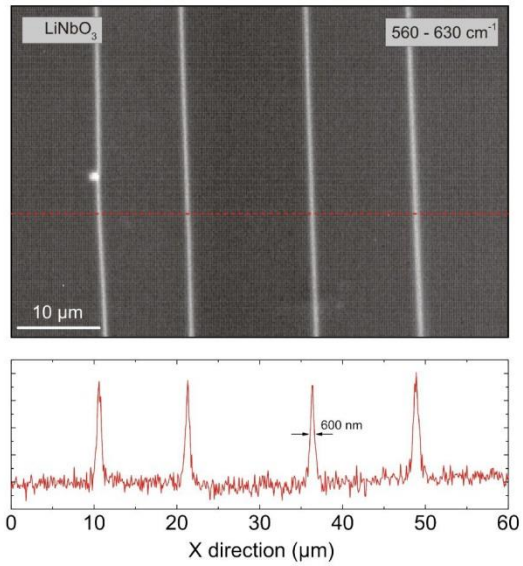

Figure 4.28: *Example of Raman imaging (area scan) of LN generated by the integrated intensity of the E-TO_8 vibration at each scanned point which is to be found between 560 – 630 cm^{-1} (upper inset). Domain walls feature an increased Raman intensity for this mode which also becomes evident in the corresponding line scan (lower inset). A FWHM of the DW signal is also indicated with 600 nm* [205].

The domain walls appear in this delineation as white lines indicating an increased integrated Raman intensity. This is also clearly seen in the line scan. Furthermore the FWHM of the DW signal is given with 600 nm here. The known domain period length of $\Lambda \approx 28$ µm and the duty cycle of 60:40 can be clearly resolved with Raman imaging here.

4.4.2 Structure sensitive modes in $KTiOPO_4$

A fundamental study of the vibrational fingerprints of periodically poled domain structures in KTP – accompanied analogously with SHG measurements - is indispensable for the comprehension of the poling sequence in order to control it for the development of tailored nonlinear optical devices based on periodically poled structures. Since the domain inversion runs along the crystallographic z-axis and the investigated sample is fabricated with walls parallel to the y-axis it seems likely to analyze these two crystal faces, cf. [209].

For the analysis of z- as well as the non-polar y-surface a 10x6x1 mm (x by y by z) piece of a flux-grown single-crystalline wafer is used as the sample with a prior check of the homogeneous stoichiometry of the wafer to avoid any local deviations. The sample is provided with a periodic poling made via a standard optical lithography process. The aimed poling period here is $\Lambda = 7.6$ µm on the –z surface as sketched in Figure 4.29.

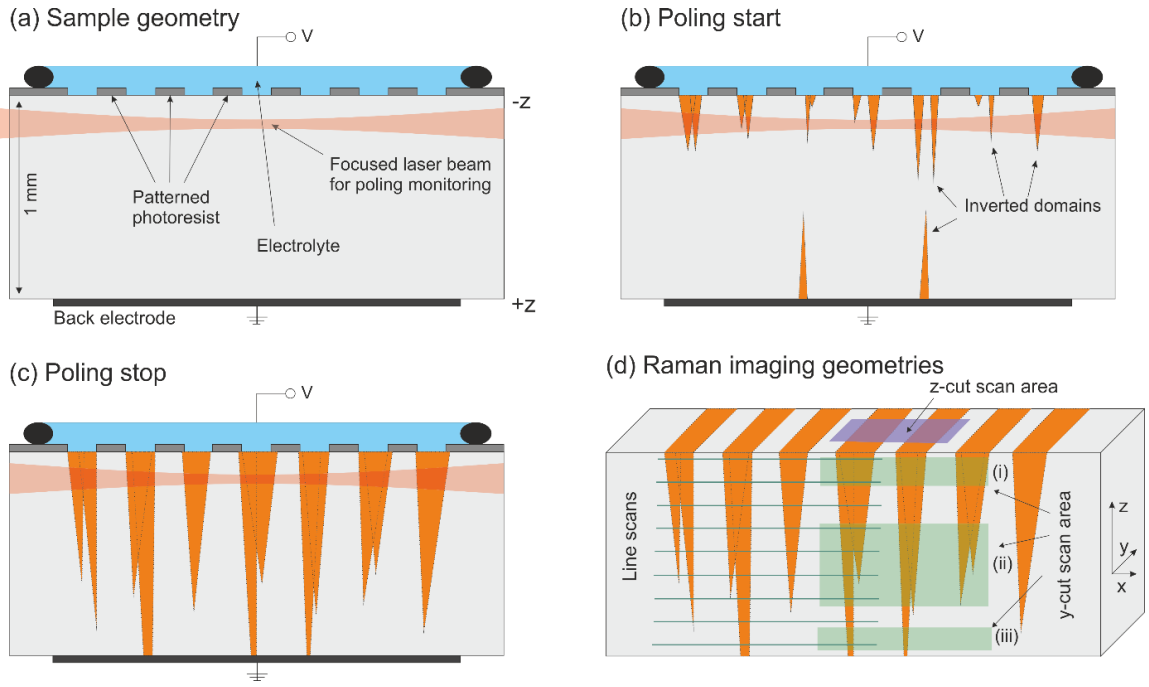

Figure 4.29: *Collage of principle sketches: a) Explanation of poling and its monitoring setting, b) start of the periodic poling procedure in which the inverted domains emerge from nucleation sites below the contacted poling grid with the first pulse, c) when several pulses are applied those domains have grown deeper or entirely through the crystal to the +z surface and an adjusted duty cycle is achieved in the monitoring area, d) illustration of the various measurement areas and its geometries.*

According to the coordinate system as inset within the figure it becomes obvious that the domains are aligned parallel to the y-axis. Hence, the electrical contacting is on the z-surfaces on which several high voltage pulses have been applied. This corresponds to the fabrication process for periodically poled waveguide structures in KTP. Subsequently to the fabrication process an optical monitoring is performed to verify a successful poling. Usually this is done in the surface-near regime since waveguides feature typical depth of 10 µm and the periodic poling should at least be adequate for this depth.

Via an electro-optic effect based monitoring technique [210], [211] the poling parameters are determined because the birefringent KTP forces the incoming laser light polarized 45° to the crystal's z-axis to exit in an elliptical polarization state. The light is then linearized again and furthermore the part parallel to the z-axis undergoes a voltage-dependent phase shift because of the Pockel's effect. The resulting voltage-dependent oscillation of the signal can then be utilized for the determination of an ideal 50/50 duty cycle because at this point of the poling process this oscillation disappears due to a missing net phase shift induced by half of the domains inverted. Pulses have to be applied until this point.

Besides the technical sample layout for the poling process, Figure 4.29 also shows the succession of a poling process in terms of the domain inversion evolution according to [212], [213]. With the first voltage pulse the domains below the electrically contacted areas begin to grow along the z-axis from nucleation spots. This can happen on both polar faces of the sample. Subsequently the domains grow in a forward movement which is often accompanied by a sideway growth along the x- and y-directions. It can also happen that domains close to each other can merge. According to [81] one has to differentiate between the speed of the domain switching in terms of the particular direction. Whereas the growth speed along the z-axis is between 50 and 200 µm/s, the y-direction only features 10 to 30 µm/s and the slowest speed is to be observed for the x-direction with 0.2 to 1.2 µm/s. This anisotropic behavior for the growth speeds is a huge advantage of the material KTP for the realization of ultrashort domain periods [214], [215].

Regarding the waveguide fabrication with periodically poled domain structures a surface-near successful poling validated via the aforementioned monitoring is usually sufficient but does not offer a comprehensive insight into the poling characteristics throughout the entire crystal depth. As indicated in Figure 4.29 c) the domain inversion will feature discontinuities and incomplete areas. For the analysis of these features Raman measurements are performed on the z-face as well as on the y-face of the sample since both sides do depict a domain wall contrast [205]. On both sides the resolution can be maximized in the surface-near region. For the y-face the confocal regime of the setup allows for a deeper insight into the crystal while acquiring cross-sections which is presented together with respective nonlinear microscopy results in subchapter 5.1.

Raman analysis of z-cut PP-KTP:

From the literature [205] it is established that domain walls distinctly alter the Raman spectrum. The signatures of domain walls in ferroelectrics, here in KTP, are most likely to be investigated in terms of the Raman shift respectively the central peak position ω_c, the full-width-at-half-maximum (FWHM) or differences of the intensity of the particular peaks. This has to be evaluated for the specific phonon modes. For instance intensity changes of the various modes are indicated via a difference spectrum. Figure 4.30 shows the Raman spectrum of a single domain in KTP, the Raman spectrum on a domain wall and the corresponding difference spectrum in the scattering geometry z(y,y)-z. Moreover the figure shows exemplarily an area under one Lorentz-like peak which is used to fit such a peak to obtain a spatial mapping for the visualization of domain structures. From the difference spectrum one can see that both spectra only vary by intensity differences of a few percent and respectively several peaks shift in the range of a few cm^{-1}.

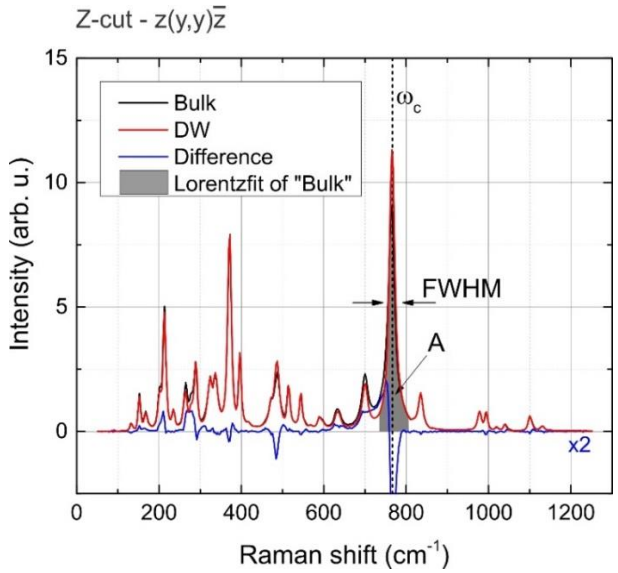

Figure 4.30: *Comparison of the Raman spectra of one domain wall to the corresponding bulk material for the scattering geometry z(y,y)-z. The difference spectrum shall highlight the changes.*

Such small changes can be related to the diffraction-limited resolution utilized here and also to the spatial extent of the domain wall reaching at most a unit cell [216]. Generally those changes in Raman spectra induced by domain walls are commonly explained via strain in the presence of DWs [216], [217] which enables elasto- and electro-optic coupling [207] via the strain-affected piezo-electric effect [218]–[220]. Furthermore such spectral changes can be related to selection rules [221]. For this one has to perceive a domain wall as a planar defect which always comes up with a corresponding momentum. This implies that any phonons propagating oblique to the particular incidental direction become apparent in the spectrum by such spectral changes [199], [221]. This is confirmed by angular dependent measurements in KTP [199]. Figure 4.30 exemplifies this with its prominent peak, which is an A_1-LO phonon. This mode shows a wavenumber decrease at increasing angles of incidence with intensity increases in the range 690-700 cm^{-1}. Hence, the as-measured spectrum on a DW is in some extent always a superposition with the underlying bulk material spectrum due to the limited optical resolution all those information can account for the intensity decrease of this peak and that it slightly spectrally shifts with the corresponding broadening.

For the scattering geometry utilized in Figure 4.30 a tabular mode assignment is given in Table 10 which accounts for the three evaluation parameters at a single domain and at a domain wall with the particular differences between both positions.

Mode z(y,y)-z (cm^{-1})	Intensity Bulk (a.u.)	Intensity DW (a.u.)	Δ_{Int} (%)	FWHM Bulk (cm^{-1})	FWHM DW (cm-1)	Δ_{FWHM} (cm^{-1})	Shift Bulk (cm^{-1})	Shift DW (cm^{-1})	Δ_{Shift} (cm^{-1})
151	2427	2675	10	7.6	7.7	0.1	150.8	150.8	0
212	8538	8904	4	5.4	5.6	0.2	211.9	211.8	-0.1
263	4002	5104	28	10.1	11.1	1	263.5	263.8	0.3
287	7152	7829	9	8.6	11.8	3.2	288.4	287.9	-0.6
323	9527	7625	-20	15.7	14	-1.7	323.2	323.2	0
336	9097	6748	-26	18.7	15.7	-3	335.5	335.1	-0.4
370	21203	19978	-6	11	11.3	0.3	370.8	370.9	0.1
396	5722	5602	-2	8.3	8.2	-0.1	395.9	395.9	-0.1
486	10440	7457	-29	16	20.2	4.2	485.8	486.5	0.7
514	3356	3115	-7	9.1	8.5	-0.6	514.4	514.4	0
544	2421	2250	-7	7.5	7.6	0.1	544.5	544.4	-0.1
634	4553	6933	52	19.3	24	4.7	633.7	633.5	-0.2
700	9202	9756	6	16.2	16.4	0.2	700.2	700.2	0
766	42889	39612	-8	16.1	17.2	1.1	766.1	765	-1.1
836	5343	4505	-16	15.1	13.7	-1.4	835	835.2	0.2
979	1407	1500	7	8.8	9.1	0.3	978.3	978.2	-0.1
995	2444	1269	-48	10.4	7.6	-2.7	994	994.3	0.2
1100	1825	1505	-18	10.8	9.5	-1.3	1100.6	1100.8	0.2

Table 10: *Summary of central peak shift, intensity changes and FWHM values for the measured phonon modes in z(y,y)-z scattering geometry at a single domain and at a DW in KTP.*

Pursuant to the aforementioned measurement and evaluation mode for a spatial mapping by displaying the integrated intensity of one distinct mode it is possible to generate false-color images of a domain wall periodically poled areas. Such images can therefore also be depicted for intensity changes, FWHM and changes of the central peak position.

The outstanding peak at 760 cm^{-1} is taken for instance to visualize the periodic domain pattern with respect to the three evaluation parameters, cf. Figure 4.31. One can see in Figure 4.31 (a) an intensity drop within this scattering geometry z(y,y)-z, a broadened linewidth (b) and also that the central peak wavenumber shifts to lower values more than 1 cm^{-1}. Nonetheless the periodic domain pattern is distinctly obvious regardless of the evaluation parameter. The aforementioned domain period of 7.6 µm as well as the duty cycle is matching. Furthermore this collocation of the three evaluation parameters suggests that the shift of the central peak wavenumber is most suitable for the visualization of periodically poled patterns. This stands to reason because such shifts are not prone to be affected by any disturbances on the sample surface and the corresponding intensity differences.

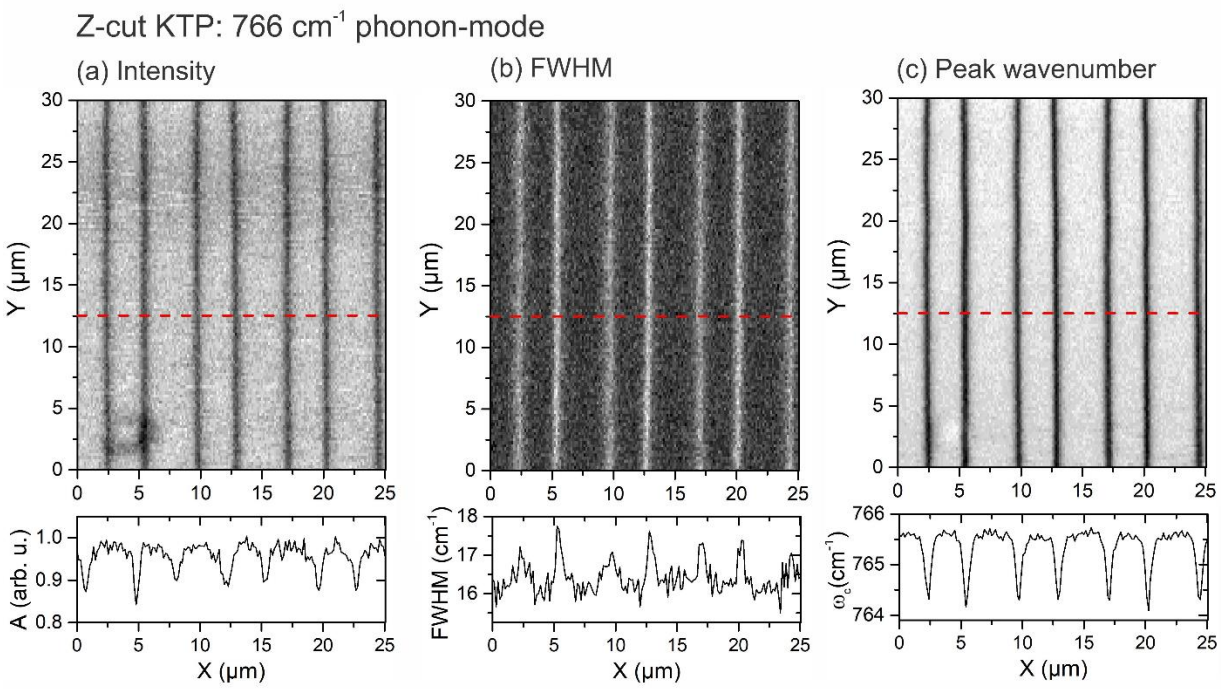

Figure 4.31: *Monochromatic images obtained via the integrated intensity of the 766 cm^{-1} phonon mode in z(x,x)-z scattering geometry of periodically poled KTP dependent on the evaluation parameters (a) intensity variation, (b) FWHM and (c) shift of peak wavenumber.*

Analog to the z(y,y)-z scattering geometry the mode assignment for the z(x,x)-z scattering geometry is given in Table 11.

Mode z(x,x)-z (cm^{-1})	Intensity Bulk (a.u.)	Intensity DW (a.u.)	Δ_{Int} (%)	FWHM Bulk (cm^{-1})	FWHM DW (cm-1)	Δ_{FWHM} (cm^{-1})	Shift Bulk (cm^{-1})	Shift DW (cm^{-1})	Δ_{Shift} (cm^{-1})
120	5861	5911	1	5.3	5.7	0.3	120.4	120.3	0.1
212	4656	4998	7	8.2	8.7	0.5	212.6	212.4	-0.2
279	9550	8642	-10	17.9	16.8	-1.1	278.6	278.3	-0.3
296	5559	3627	-35	9.5	6.8	-2.7	295.7	296	0.3
336	12842	12530	-2	12.2	12.3	0.1	336.8	336.7	-0.1
370	6128	11030	80	12.3	18.6	6.3	369.8	368.9	-0.9
396	5259	5212	-1	7.6	7.4	-0.2	396.3	396.4	0
419	9115	9297	2	9.2	9.9	0.7	419.5	419.8	0.3
473	7239	7434	3	11.3	12.1	0.8	472.9	472.8	-0.1
514	19605	19058	-3	8.2	8.4	0.1	514	513.9	0
544	11239	10306	-8	7.2	6.9	-0.2	544.2	544.3	0
589	3133	3318	6	8.5	9.6	1.1	589.2	589.4	0.1
631	3886	4421	14	13.4	14.9	1.5	631.3	631.2	-0.2
766	85522	77002	-10	16	17.3	1.2	765.8	764.6	-1.2
995	10247	10171	-1	10.4	11.2	0.9	995.2	995.3	0.1
1020	2018	1733	-14	8.3	10.1	1.8	1019.6	1019.8	0.2

Table 11: *Summary of central peak shift, intensity changes and FWHM values for the measured phonon modes in z(x,x)-z scattering geometry at a single domain and at a DW in KTP.*

Raman analysis of y-face PP-KTP:

The scattering geometries z(p_i , p_s)-z are likely to confirm the successful poling at the surface and fundamental spectral characteristics. More additional information is obtained when investigating the non-polar y-face of KTP. In a first attempt, the domain wall specific phonon modes have to be evaluated via the spectral comparison of bulk and DW as performed for the z-face before. According to [205] the y-face scattering geometries are only useful when looking at crossed polarization states like y(x,z)-y or y(z,x)-y since the domain wall contrast is sufficiently high here. This is related to the directional respectively angular habit of those geometries.

Figure 4.32 shows the bulk and DW spectrum with the helpful difference spectrum for the first mentioned y-face scattering geometry. This figure is accompanied with Table 12 that lists all relevant phonon modes for this scattering geometry in order to give a phonon mode assignment. One can therefore for instance assign the 287 cm^{-1} mode to the ν_5-TiO_6-vibration. Also linked to the TiO_6-octahedron is the 313 cm^{-1} mode but as the ν_4-vibration. The phosphorous PO_4 tetrahedron features the 991 cm^{-1} ν_1-mode.
These TiO_6-octahedron related modes are very susceptible to intensity changes when considering domain wall spectra but this behavior does not hold for the FWHM. On the contrary, spectra taken from z-faces feature a reversed behavior. LO-phonons for instance which often inherit an angular dependency or other phonons with this property are likely to be a hint that polar contingents can be found in them.

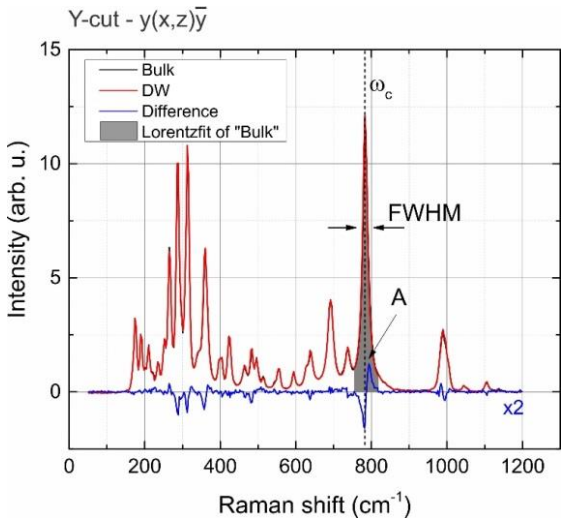

Figure 4.32: *Comparison of the Raman spectra of one domain wall to the corresponding bulk material for the scattering geometry y(x,z)-y. The difference spectrum shall highlight the changes.*

A sensitivity for both aforementioned features is found for the 991 cm^{-1} mode in the context of domain walls. Its corresponding ν_1-mode undergoes a constriction of its width for a DW spectrum. Hence, defects which are related to broadening half widths can be neglected at the measured point. For other modes like for the ν_2-PO_4-mode at 360 cm^{-1} and the ν_3-TiO_6-mode at 783 cm^{-1} such a FWHM widening is observed. Their directional behavior is particularly different for all three sample geometry faces and the FWHM features further differences. As aforementioned, the shift of the center peak frequency is most promising to be the best indicator for the most sensitive domain wall related modes. Besides this frequency shift, modes like at 313 cm^{-1} also exhibit an intensity change and other modes like at 360 cm^{-1} and 737 cm^{-1} FWHM changes, too. For the ν_1-TiO_6-vibration at 783 cm^{-1} a center peak shift is observable.

Mode y(x,z)-y (cm^{-1})	Intensity Bulk (a.u.)	Intensity DW (a.u.)	Δ_{Int} (%)	FWHM Bulk (cm^{-1})	FWHM DW (cm^{-1})	Δ_{FWHM} (cm^{-1})	Shift Bulk (cm^{-1})	Shift DW (cm^{-1})	Δ_{Shift} (cm^{-1})
175	5026	5198	3	8.2	8.3	0.1	174.6	174.7	0.1
190	1712	1680	-2	4.7	4.7	-0.1	190.3	190.3	0.0
210	1246	1660	33	5.1	6.3	1.3	209.7	209.8	0.1
265	8015	8172	2	8.4	8.3	-0.1	265.4	265.4	0.0
287	8325	7656	-8	7.4	7.9	0.5	287.2	287.2	0.1
313	11860	10815	-9	10.1	9.8	-0.3	313.0	313.2	0.2
360	10980	11004	0	14.7	15.6	0.9	359.8	360.2	0.4
400	4235	3636	-14	19.8	18.7	-1.1	400.0	400.1	0.1
423	2571	2521	-2	10.1	10.6	0.6	423.1	423.3	0.1
514	3356	3115	-7	9.1	8.5	-0.6	514.4	514.4	0.0
544	2150	1579	-27	15.0	13.4	-1.7	554.1	554.4	0.3
691	8095	8214	1	17.7	18.1	0.4	691.5	691.6	0.1
737	1117	2488	123	11.6	18.9	7.2	737.7	737.3	-0.4
783	19738	20040	2	15.3	16.7	1.3	783.2	784.0	0.9
991	9999	8495	-15	28.8	27.0	-1.7	991.1	990.4	-0.6

Table 12: *Summary of central peak shift, intensity changes and FWHM values for the measured phonon modes in y(x,z)-y scattering geometry at a single domain and at a DW in KTP.*

Furthermore, there are two more modes at hand for the tetrahedrons and the octahedrons. It can be stated that de- and increasing shifts are related to those further vibrations. This in turn can appropriately be linked to domain wall induced strain.

Since the phonon mode at 783 cm^{-1} features by far the largest center frequency shift with 0.9 cm^{-1} this mode is very likely to be utilized for a two-dimensional mapping of the transferred domain structure in this scattering geometry as a result of the phonon mode assignment. For all three evaluation parameters the B_1-TO phonon mode at this frequency is plotted in Figure 4.33. It is very obvious that the mapping ability is given for the peak shift whereas the FWHM is barely useful for it and any intensity change is in vain here.

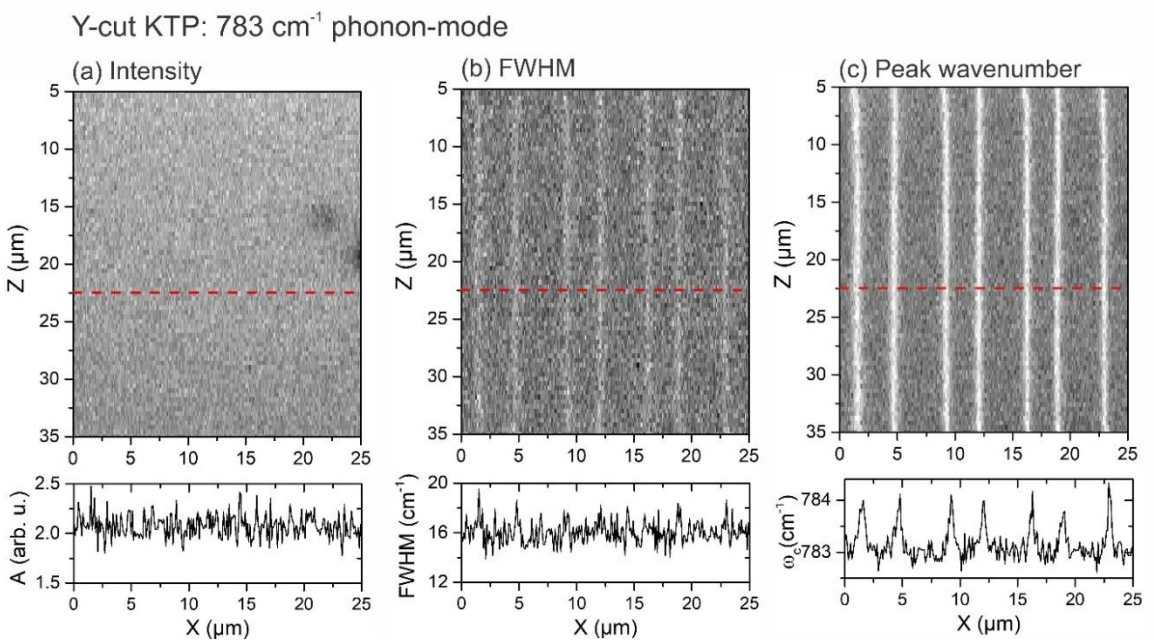

Figure 4.33: *Monochromatic images obtained via the integrated intensity of the 783 cm^{-1} phonon mode of the y-surface of periodically poled KTP dependent on the evaluation parameters (a) intensity variation, (b) FWHM and (c) shift of peak wavenumber.*

As a result this mode can promisingly be used for a proceeding analysis of the non-polar y-face of KTP within the scattering geometry y(x,z)-y in terms of the domain wall emerging into the depth of the crystal, i.e. along the z-direction. According to the findings gathered in Table 12 one can find positive shifts up to nearly one reciprocal centimeter from the bulk peak when examining domain walls.

Interim summary:

The fingerprints of periodically poled domain structures have been analyzed especially for KTP by means of its structure sensitive Raman modes for z-cut as well as the non-polar y-cut. In this context a comprehensive assignment of the structure sensitive modes has been given for those both faces of KTP. This assignment comprises the analysis parameters intensity, FWHM and Raman shift on both domain and domain wall. Raman imaging of the periodically poled has been conducted in terms of those evaluation parameters for both faces revealing various features of poling pattern.

5 Tailored waveguide structures

Within the framework of this work functional tailored structures stemming from a periodically poled ferroelectric structure are analyzed. These are in particular periodically poled waveguide structures in LN and KTP which are commonly characterized with the optical method regarding its mode shapes, losses and conversion efficiency. Besides this information which is important for the fabrication side a thorough analysis in terms of both central measurement methods (SH and Raman) is performed as a feedback loop with the fabrication side in order to obtain insights for an immediate improvement. This chapter comprises investigations on nonlinear tailored structures in bulk LN and KTP as well as for x-cut thin film LN by means of the two analysis techniques.

5.1 Periodically poled $KTiOPO_4$ structures

Tailored periodically poled $KTiOPO_4$ devices are analyzed via µ-Raman spectroscopy and nonlinear characterization in terms of their ferroelectric domain structure for both bulk material and Rb-exchanged waveguides, c.f. [209]. In case of their vibrational properties it is shown that any variations of the FWHM, the center frequency or the intensity of the Raman mode itself can be utilized to highlight differences between the pristine and inverted domains as well as the domain wall sensitive modes. Local material properties are also investigated for the pristine KTP area as well as for the rubidium exchanged area namely the waveguide. Here, specific modes with various vibrational signatures in the surrounding of domain walls and the waveguide area are found. The imaging Raman spectroscopy gives detailed information as it is sensitive for different content of the characteristic material features whereas the SHG microscopy can be furthermore used to visualize larger areas of waveguide structures in terms of the homogeneity of the periodical poling along the waveguide in z-face geometry or the poling evolution along the y-surface of the crystal due to the eminent faster measurement time here.
A periodically poled waveguide in KTP is hence analyzed in terms of imaging Raman spectroscopy. From the three aforementioned fitting parameters the shift of the respective mode is utilized here exemplarily to emphasize the different influence of the various vibrational modes onto the imaging result. The z(x,x)-z scattering geometry is favorable for the analysis since it yields several usable modes. Figure 5.1 shows three gray scale Raman imaging results for the vibrational modes at 120 cm^{-1}, 766 cm^{-1} and 995 cm^{-1} for this scattering geometry and with the absolute frequency shift as the analysis criterion. The three images are taken on the same area on a rubidium in-diffused waveguide in KTP. As to be seen the mode at 120 cm^{-1} is very likely to be used to visualize the spatial extents of the waveguide and is commonly connected to the K^+-ions. Furthermore, the periodic poling is visible in the waveguide as well as slightly in the pristine KTP. It has to be noted that a certain overpoling is responsible for the deviation from a 50/50 duty cycle. Beyond this one can see that the Raman shift of this mode is not homogeneous over the entire mapping area as the waveguide features a periodic variation of the grey scale; the original non-inverted parts are the darker parts of it. The boundary of the waveguide to the bulk material comprises a shift to lower wavenumbers and that can give rise that this boundary region is very affected of material strain.

When the same mapping area is considered for the 766 cm^{-1} mode in terms of the Raman shift, this mode on the contrary is not connected to any material deviation like the aberration of the unit cell since it stems from the frozen-phonon calculation and thus vacancies or defect structures can be connected with it. It becomes obvious that this mode is mostly sensitive to the domain walls as the boundaries of the inverted and pristine areas. The waveguide can be recognized as a slightly lighter area in the middle of the mapping. Such a different behavior of the indication of the sensitivity can be roughly explained by the commingling of several scattering geometries here especially at the domain walls, as if the specimen is inclined in a certain amount relative to the measurement plane. The full model of this treatment is found in [205]. Part (c) of the figure depicts absolute frequency shift of the 995 cm^{-1} mode as a third instance for the spatial mapping capabilities of imaging µ-Raman spectroscopy on periodically poled waveguides in KTP since it features a better contrast than variations of the intensity or the FWHM. Comparable to the 120 cm^{-1} mode the extents of the waveguide as well as the periodic poling become visible very distinctly. This comprises the domain walls and distinguishable poled areas within the waveguide which is demarcated from the bulk material via diminished wavenumbers at this transition. This can in turn suggest a higher tension of the material.

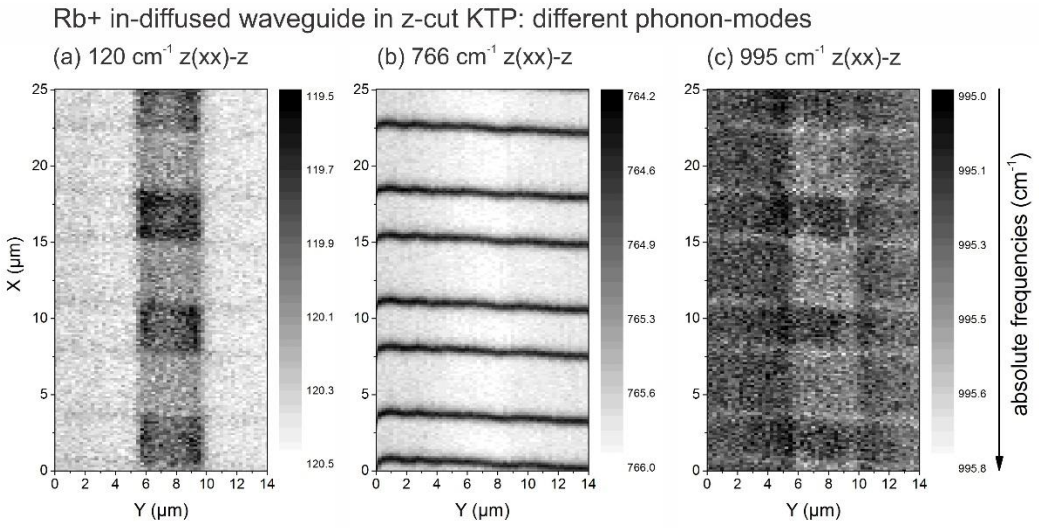

Figure 5.1: *Threefold mapping of a periodically poled waveguide in Rb^+ in-diffused $KTiOPO_4$ for z(x,x)-z scattering geometry by means of imaging µ-Raman spectroscopy and the absolute Raman frequency shift as the analysis criterion to emphasize the different fingerprints for the selected modes.*

Besides the Raman imaging analysis of such a homogenously poled KTP sample with a subsequently fabricated waveguide the investigation of a different sample shall be presented here which shows the influence of the waveguide fabrication on an existing periodic domain grating. In recent studies [83], [86] it has been shown that the stability of the inverted domains can be highly influenced by the temperature treatment within the rubidium exchange process. A validation for this behavior has been performed by means of nonlinear microscopy and the result is presented in Figure 5.2. For the visualization the z(x,x)-z scattering geometry has been used to obtain strong DW contrast. The sample has been designed for a planned poling period of 7.6 µm. One can clearly see a discrepancy between the duty cycle of the differently poled domains within the Rb-exchanged area (indicated with a dotted rectangle) and besides the waveguide.

The unwanted duty cycle unequal to 50:50 is here commonly related to a backswitching of the poled domains in favor of broadened as-grown domains again. During the waveguide fabrication an annealing step leads to a thermal activation and the instability of the poled domains promotes the backswitching process.

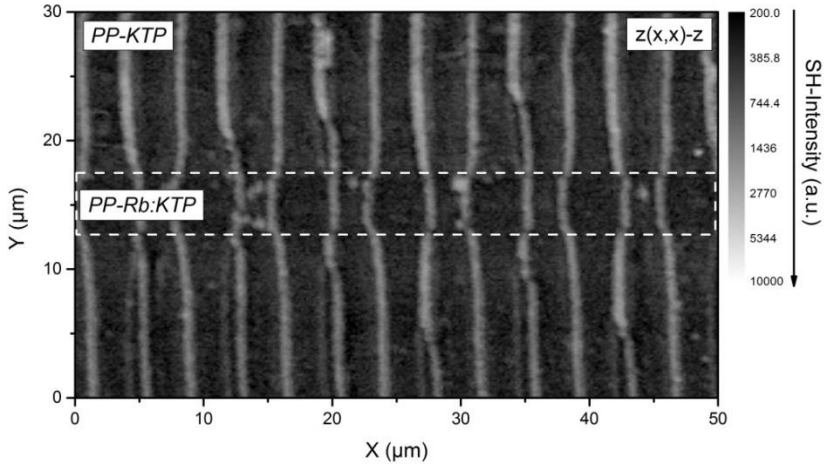

Figure 5.2: *Nonlinear area-scan of a 3.5 µm broad waveguide fabricated in a previously throughout periodically poled KTP crystal for the scattering geometry z(x,x)-z (Δx,y = 100 nm). A different duty-cycle is to be seen for the waveguide area and besides it as well as embedded domains within the waveguide.*

Furthermore one can see inclusions or embedded domains in the as-grown domains within the Rb-exchanged area. So called chemical poling is accounted for this which is only feasible on the –c side of KTP. This also confirms which domains are as-grown and inverted ones.

The spatial mapping of periodically poled waveguides by means of confocal Raman spectroscopy is not only limited to scattering geometries for the z-face of KTP but also applicable for the investigation of the waveguide end-facets (x-face) or to investigate the domain wall evolution along the z-axis (y-face). Whereas waveguide end-facets in terms of diffusion depth profiles and shape are investigated in [199] and [151] a closer look on to the y-face of periodically poled waveguides in Rb^+ indiffused KTP is given in the following subsection. Similar to the investigation of periodically poled KTP and its domain wall evolution as presented in section 4.4.2 confocal Raman spectroscopy is utilized here but accompanied with SHG microscopy results in order to underline the comparability of both methods here considering the fingerprints of a waveguide in a previously periodically poled material. From preliminary studies [222] the scattering geometry for the Raman analysis is chosen as y(x,z)-y and as the mode the vibration at 783 cm^{-1} serves in order to acquire a reasonable signal-to-noise ratio her. For the SHG measurement y(z,z)-y provided the most satisfying contrast. Regarding the sample the periodic poling (Λ = 7.6 µm) is performed over the entire crystal in a first step and the waveguide is fabricated afterwards whereas there is also the possibility to create a sample with a periodically poled waveguide in KTP the other way round. The method used for this sample gives the opportunity to investigate the waveguide as well as the domain wall evolution in depth. Figure 5.3 shows the comparison of both analysis methods on the same y-face of the sample. The image section is chosen to feature the air/sample-surface interface, the waveguide extension and the further evolution of the domain walls in depth.

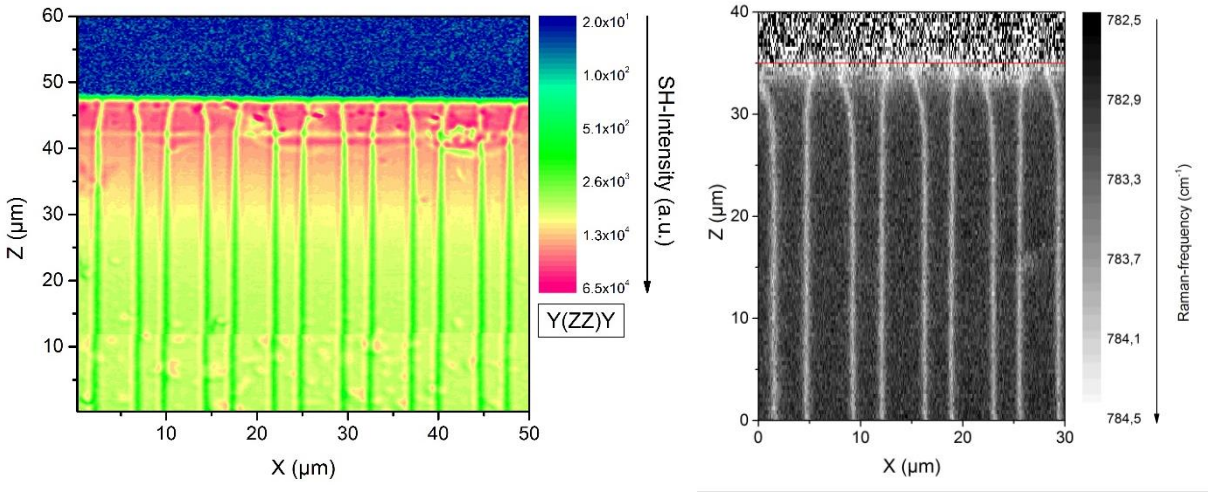

Figure 5.3: *Comparison of confocal SHG microscopy (left) and Raman spectroscopy (right) mapping of a periodically poled waveguide in Rb^+ in-diffused $KTiOPO_4$ for y(z,z)-y for SHG and y(x,z)-y scattering geometry for Raman. The analysis criterion for the Raman analysis is the Raman shift.*

The Raman mapping spectrally shows differences within the wavenumbers of more than one reciprocal centimeter considering the domain wall / domain contrast. Above the red line the noisy area indicates the air above the sample surface. This is also indicated within the SHG mapping as the blue area with the lowest intensity. Both results show very distinctly a trumpet-shape of the domain walls very close to the sample surface. As previous investigations give rise to a back-switching of poled domains into their primary state whereas other poled domains can perform a movement to become narrower when any overpoling is at hand. This behavior occurs in samples fabricated this way and not for waveguides which are periodically poled after the exchange process. Furthermore this very obvious feature of the sample is not to be seen on the bottom side of the sample where no waveguide is at hand. Annealing attempts do also not contribute to a decrease of this behavior – which holds for waveguide samples and only poled samples. Hence, the influence of titanium can also be neglected for the explanation of the effect. In contrast to the surface-near region featuring this effect the domain wall evolution in depth shows a homogeneous duty cycle and shape of the domain walls. An attempt to explain the effect can lay within the combination of the chosen varnish thickness and the applied poling voltage. *Comsol* simulations for various varnish thicknesses and the varying voltages yield that the electric field exaggeration between the varnish or poling pads rises quicker than the electrical field strength below those pads [223].

In turn, this means that for the fabrication process the best fitting combination of varnish thickness and poling voltage has to be found in order to minimize the trumpet-shape like effect of the domains. Besides the trumpet-like shape of the domains near the sample top-surface the SHG mapping also provides information on the waveguide extents. One can see that the surface-near region from z = 47 µm down to at least z = 37 µm in Figure 5.3 features an increased SHG intensity of more than one order of magnitude compared with the intensity from a deeper region of the crystal. This distance of about 10 microns corresponds with the estimated rubidium exchange depth from the fabrication side whereas one has to note, that the diffusion depth corresponds with the waveguide width [151]. The Raman analysis here only gives information regarding the domain walls since the chosen vibrational mode is very sensitive to them and not to the material strain.

In order to extend the insight into the domain wall evolution in depth the sample is analyzed by means of SHG microscopy and Raman spectroscopy mapping on the y-face but in a deeper crystal region considering its z-axis as adumbrated in subsection 4.4.2. For three depth areas of the crystal used in subsection 4.4.2 Raman imaging gray scale mappings are performed and shown in Figure 5.4. The first three insets show the surface-near area in a depth of 5 – 35 µm. A middle region in a depth of approximately 300 µm is shown. One can observe that not all domain walls are continuous in this depth. The last of the three insets is near the bottom of the sample (970 – 1000 µm).

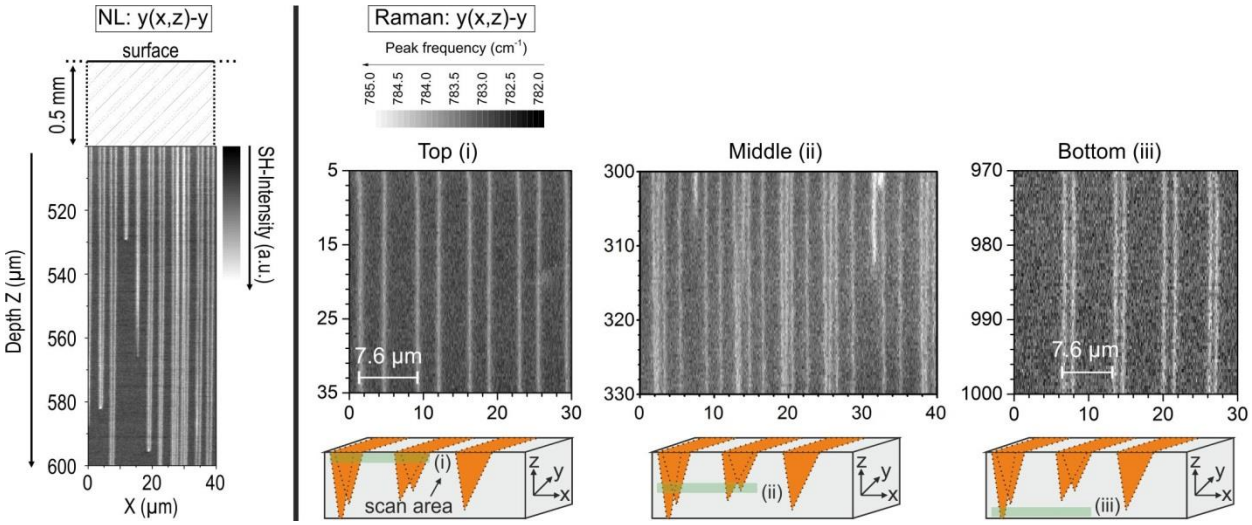

Figure 5.4: *Collage of images showing the domain wall evolution along the z-axis of KTP. Left inset: False color image of the SHG fingerprint of the periodic domain pattern for y(zx)-y scattering geometry in the middle of the crystal to visualize the domain wall evolution in depth. Right insets: Raman images of 783 cm^{-1} mode for y(x,z)-y scattering geometry grouped in (i) the surface-near region, (ii) a middle region where several irregular domain wall patterns are at hand and (iii) near the sample bottom.*

A schematic sample overview and the corresponding scale for the false color depiction are given in the remaining insets. In all depths domain walls can be observed but when looking at deeper regions several domain walls also feature an evolution perpendicular and not parallel to the crystallographic z-axis which manifests in the extent of several microns. The surface-near region shows the expected homogeneous domain patterns since the periodic poling has to be successful here due to the all-optical monitoring. This is underlined by the correct duty cycle and domain period. In the middle region again the domain pattern looks quite different compared to the surface. The domains often merge in a spike-like behavior.

A view on the particular angles of the domain evolution regarding to the z-axis, which are between 0.5° to 1°, the aforementioned ratio of growth speeds in z- and x-direction can roughly be validated, since the literature [224] reports of ratios of 200 to 250. The deviance can be related to unequal stoichiometry because the portion of potassium in a KTP crystal is likely to alter its traits [74] even for samples of the same wafer. The spatial extent is not restricted to the measured depth of 300 – 330 µm but for a broader middle region. In contrast to the top region the bottom region close to the crystal backside the periodic domain pattern looks also homogeneous but the duty cycle is very different. Nonetheless, the domain period is still prevalent. This can give rise to the assumption that all domains intended to be flipped begin to emerge from particular one nucleation spot. As indicated in the inset (d) not all inversed domains reach the bottom of the sample and inset (c) is deliberately chosen to visualize this behavior at the bottom of the sample. The aforementioned spike-like merging leads to areas with no domains down there.

Analog to the Raman analysis of the domain wall evolution in depth the corresponding nonlinear area scan presented in the left inset of Figure 5.4 is also chosen to be in the middle (z = 500 µm) of the 1 mm thick crystal. According to the schematic of Figure 5.4 the domain walls of this sample only emerged to the middle of the crystal in parts of this area. Since this sample is designed and treated from the fabrication side to serve as a periodically poled waveguide with a common exchange depth of 6 µm to 12 µm along the z-axis it is crucial here that the surface area which comprises the waveguides features a homogeneous and reliable periodic poling pattern and it is not necessary that the domain walls reach the bottom of the sample. The results matches with the verification of the SH intensity via the monitoring technique from the fabrication side [83]. Imaging on the y-face of a periodically poled KTP crystal via SHG microscopy is probably more favorable in terms of poling quality control since it offers a faster mapping and a more convenient result evaluation afterwards.

Nonlinear contrast mechanism and waveguides:

Besides the domain wall evolution in depth the y-face of KTP also gives information about the nonlinear contrast as investigated in subchapter 4.2 for the z-face of the material. Whereas the z-face yields a throughout positive domain wall contrast to all appearances the y-face of KTP as a material with a lowered bulk signal compared to LN for instance gives an indication that not only the interference is the crucial factor for the nonlinear contrast mechanism. Altering or evanescent tensor elements can be accounted for the mechanism since the bulk response originates from an indirect coupling of the excitation light with the tensor elements and any change in those can have a big influence on the sign of the contrast.

Polarization dependent nonlinear area scans for all four scattering geometries have been performed which is shown in Figure 5.5. One can see for three polarizations a negative nonlinear contrast indicated via dark lines as the domain walls. The scattering geometry y(z,z)-y features the highest signal from all of the polarizations which stems from a direct coupling to the largest nonlinear tensor element d_{33} which is more than six times higher than the second largest element d_{31}. The negative contrast in turn can be explained by the fact that at a domain wall also a reversal of the accumulated phase takes place. Considering the collinear light coming from the nonlinear light matter interaction finally a destructive interference is the result and the signal drops at that region. According to the scheme introduced in Figure 4.5 and Figure 4.6 one can derive the shape of the field distribution within the back focal plane for a single domain. In a further step one can make an outlook of how the particular shape of the field distribution there looks like taken on a domain wall. Since the respective sign of the contrast is already given via the nonlinear area scans either the contrast is explained by interference contrast or altered tensor elements.

Analog to area scans of periodically poled structures in LN or KTP in a z-cut scattering geometry a particular positive or negative domain wall contrast is obvious for y-cut scattering geometries. A negative contrast is mostly apparent for a two- or four-fold split pattern of the field distribution in the focal in which the signal drops.

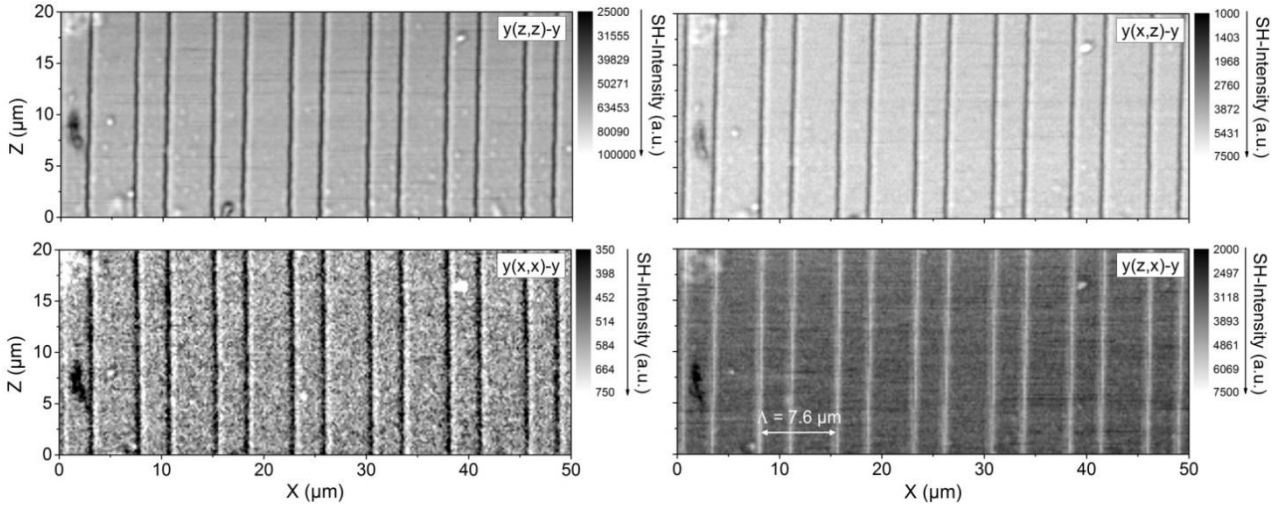

Figure 5.5: *Set of nonlinear area scans on the y-face of KTP showing domain walls along the crystallographic z-axis for the four scattering geometries. One can note that the domain wall contrast especially its sign has changed for this face.*

Since the d_{33} element directly couples with E_z^2 for y(z,z)-y a rotational symmetric pattern will result for a single domain for instance. The negative contrast here is due to a two-fold split pattern at a domain wall. The y(z,x)-y scattering geometry features a mixed coupling of the d_{15} element with E_x and E_z. Due to incident light polarized in z-direction and the permutation of the incident light's polarization for the three parts a convolution of a rotational symmetric and a four-fold pattern are at hand for the material polarization. This inevitably leads to a split-pattern for a single domain. A change towards a rotational symmetric pattern is then likely for the case at a domain wall regarding the positive contrast. The contrast of the nonlinear signal on a domain wall compared to a single domain is summarized in Table 13 for all scattering geometries based on the values from the results presented in Figure 5.5. It should be noted that the maximum values within the intensity scales of Figure 5.5 can originate from outliers and the effective average intensities for a single domain or DW are used for the contrasts in the table.

Scattering geometry	SH signal contrast (DW:Domain)
y(z,z)-y	≈ 1.0 : 2.0 (-)
y(x,z)-y	≈ 1.0 : 1.7 (-)
y(z,x)-y	≈ 2.3 : 1.0 (+)
y(x,x)-y	≈ 1.0 : 1.5 (-)

Table 13: *Listing of the domain wall contrast within the SH signal for y-cut $KTiOPO_4$ for the four scattering geometries according to the SH values of Figure 5.5.*

For a better indication of the contrast ratios the previous results are visualized in terms of the particular line scans as to be seen in Figure 5.6. One can clearly see lowest contrast ratio for the scattering geometry y(x,x)-y which is due to the high SNR here. The two scattering geometries with detection polarization in z-direction also feature a small peak on the right flank of each dip from which the signal decreases to the single domain level again. This can obviously be related to the certain shape of the point spread function for these scattering geometries. A slight deviation from a central adjustment of the pinhole for instance can lead to this and emphasizes the precision of this confocal mapping technique.

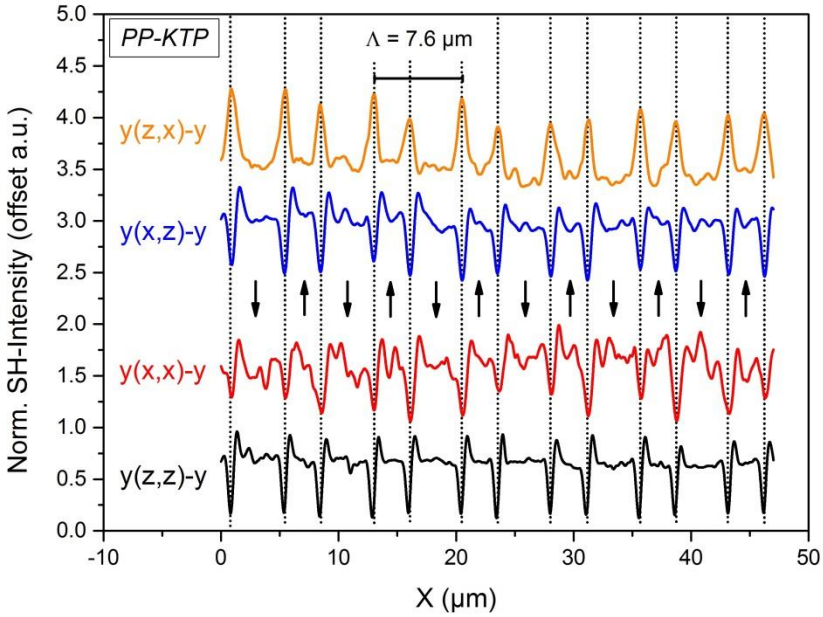

Figure 5.6: *Stacked line scans for all four scattering geometries of y-face KTP to visualize the different domain wall contrast ratios of the SH answer derived from the area scans of Figure 5.5.*

For the positive contrast shown by the y(z,x)-y scattering geometry such an inclination within the mapping is rather missing which may give rise to the assumption that the altered field distribution within the back focal plane on a domain wall has a big influence on the contrast behavior here and a misalignment of the pinhole module is rather unlikely.

With the fundamental knowledge of the nonlinear contrast behavior on the y-face of KTP and shape of the particular field distributions in the back focal plane this analysis is extended in the context of investigations for functional structures as devices for Rb-exchanged waveguides in KTP. The waveguide area can be considered as Rb:$KTiOPO_4$. Considering the nonlinear tensor $RbTiOPO_4$ or any stoichiometric alloys yield the same tensor elements due to the same space group like KTP but feature different tensor element values due to the Rb-influence [225]. For a qualitative first estimation this should turn out in a same shape for the E-field distribution in the back focal plane acquired on a single domain on a waveguide and besides it in bulk KTP as well as at a domain wall at those two positions. Thus, on these four positions a focal scan has been made for the y(z,z)-y scattering geometry for instance. Regarding the measurement this implies that the measurements for a waveguide are performed near the sample surface and for bulk KTP in a reasonable depth below the waveguide. This polarization combination yields the highest intensity and also a good contrast ratio. All four results are presented together in Figure 5.7. It has to be noted, that the acquired maximum intensities feature a difference by a factor of 10 compared to the values

of the results presented in Figure 5.5 due to a tenfold higher integration time. For the case of a single domain one can clearly see a rotational symmetric pattern for both the waveguide area as well as bulk KTP. As introduced above this is expectable since the highest tensor element d_{33} element is linked to the squared z-component of the incident light in a direct manner which is already rotational symmetric.

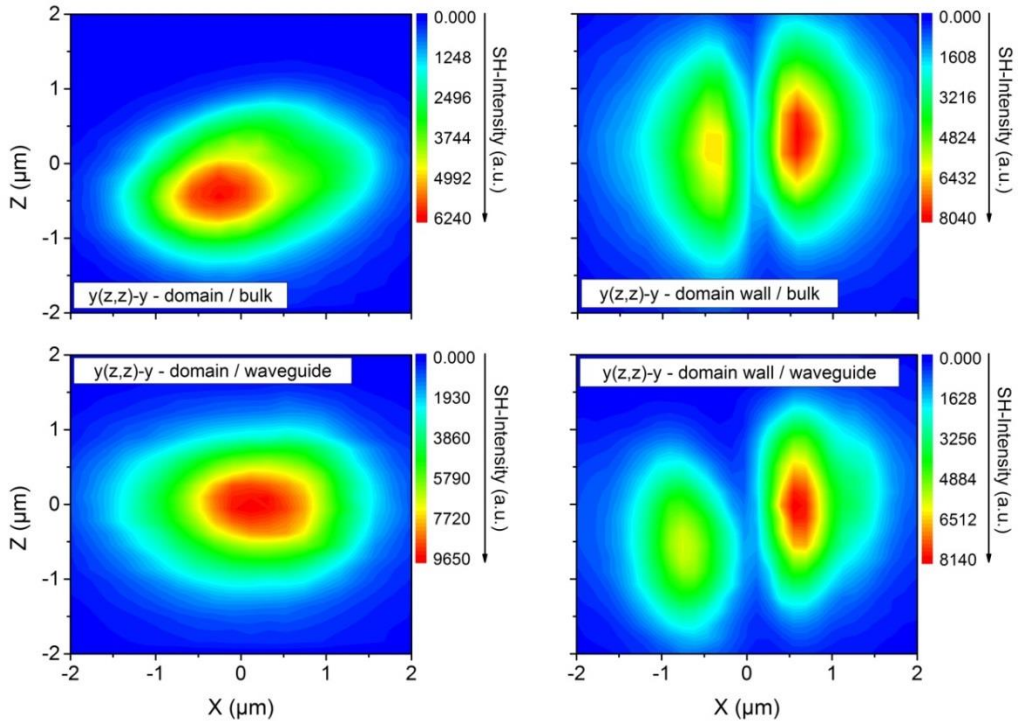

Figure 5.7: *Nonlinear focal mappings of the E-field distribution within the back focal plane of KTP for the scattering geometry y(z,z)-y on a single domain in an untreated bulk material area, on a Rb-exchanged waveguide and the same measurements at a domain wall on those two areas.*

At a domain wall the E-field distribution looks quite different. The measurements show a two-fold split pattern along the x-axis for both positions. This corresponds to the negative contrast as seen in the area scan for this scattering geometry in Figure 5.7, which is related to the destructive interference respectively the dip of the pattern. Furthermore, one can see that on the waveguide a higher intensity is found for the intensity maxima compared to bulk KTP due to the different tensor elements of the Rb:KTP alloy.

In summary one can state that the results of the focal analysis of y-face KTP and Rb:KTP yield the same qualitative behavior for both materials and only in terms of slightly higher intensities in favor for the exchanged areas the comparison underlines the variance of nonlinear tensor elements there as predicted by literature. Furthermore, the nonlinear contrast behavior for y-face KTP is quite different to the z-face due to the triggering of different tensor elements and the occurring of new elements on domain walls for the distinct scattering geometries. Waveguides with a periodic structure for a single-mode converter (design wavelength 800 nm) have been fabricated within the research project in which this thesis is embedded. Besides those Rb-exchanged channel waveguides, also ridge waveguides have been fabricated within the exchanged area via diamond-blade dicing. For those waveguides a type-II SHG at a fundamental wavelength of 792 nm has been achieved with an efficiency of 6.6 %/Wcm^2 [226]. Within the channel waveguides a type-II SHG at 801.3 nm has been achieved with an efficiency of 2.3 %/Wcm^2 [22].

Interim summary:

First, a wide variety of periodically poled KTP waveguide structures based on specific phonon modes were imaged using µ-Raman spectroscopy. Different features like domain boundaries or the waveguide itself could be detected by the local variation of sensitive vibrational modes. In the sense of a comprehensive analysis, all relevant structure faces were mapped, so that the depth profile of the domains has also been observed. The characterization was flanked by SH-microscopy. With both techniques it was shown that up to a relevant depth (waveguide region) the domains run homogeneously in depth. From a depth of approx. 500 µm, the course is disturbed, due to domain merging for instance. In addition to the nonlinear analysis of the domain transition region for z-cut KTP, the polarization-dependent nonlinear contrast behavior for periodically poled y-cut KTP was clarified and the nonlinear point spread functions within the back focal plane resulting from the waveguide were successfully recorded.

5.2 $LiNbO_3$ structures

In LN periodic domain gratings can be fabricated in all possible cuts but especially for applications considering electro-optic modulating x- and y-cut LNOI is more favorable since TM as well as TE polarization and thus the highest electro-optic coefficient r_{33} can be triggered here in contrast to z-cut LNOI which only allows for TM polarization [227], [228].

Besides this advantage of the other cuts z-cut LNOI features the drawback that it requires a back-electrode for the poling step which also influences the absorption properties of the material [17] and a removal of the lithographically created metallic electrode pattern to investigate the outcome of the poling process.

5.2.1 Domain structures in $LiNbO_3$

Periodically poled domain structures are commonly fabricated on z-face LN for various applications. This has been investigated for several decades. In the context of the analysis of functional devices the focus is put here onto periodically poled structures in the sub-µm regime. This shall pave a way towards backward-coupled PDC devices for single photon emission.

Counter-propagating PDC devices:

Ultra-short domain patterns with period lengths in the sub-micron regime are crucial for counter-propagating quantum optical processes like PDC. This is a major challenge for the fabrication of such structures. Therefore, optimized processing in terms of lithography, waveguide fabrication as well as domain inversion is essential.

For waveguide fabrication, high-purity titanium was deposited on a z-cut lithium niobate wafer by electron beam evaporation and 7 µm wide titanium strips (98 nm thin film) were defined after a lithographic process followed by wet chemical etching. The titanium was in-diffused in at a temperature of 1060 °C for 7.5 hours in a pure oxygen environment. Furthermore, it must be ensured that no Li_2O can leave the sample and also a domain inverting layer on the +z face of the sample is formed during this process, which must be subsequently erased. For more information, see reference [143].

The definition of the poling structure was done by a photolithographic process. Here, a layer of photoresist is spin-coated onto the LN surface and then developed with UV light through a chromium mask placed on top. Domain inversion is realized by electric field assisted poling via liquid electrodes on both z-surfaces. For more information, see [84]. In the case of ultrashort domain periods, lateral domain growth is reduced by applying shorter electric field pulses and higher voltages. For the desired PDC devices, a pulse length of 2 ms is electrically applied at voltages of 10-11 kV.

The fabricated PDC devices featuring period lengths ranging from Λ = 1.8 µm down to Λ = 1.0 µm. Exemplarily a micrograph of an selectively etched periodic Ti:$LiNbO_3$ structure and the corresponding confocal nonlinear image of an non-etched PDC device are shown in Figure 5.8. In both cases the extents of the waveguide as well as the periodical poling pattern with a period length of Λ = 1.73 µm becomes visible. The micrograph reveals these features since the sample surface is selectively etched due to different etch rates of the +z and –z faces for pristine and doped $LiNbO_3$ respectively. Therefore the domain structure is transferred to the surface, thus pristine and inverted domains can be identified. The noninvasive application of the SH-microscopy reveals for the specific z(xx)-z scattering geometry an enhancement of the nonlinear domain wall signal (bright lines) with high contrast. One can deduce the extent of one domain with about 860 nm. This corresponds with the projected domain period Λ = 1.73 µm. Due to the resolution of the confocal setup period lengths in the sub-micron regime are successfully separately resolvable with this technique.

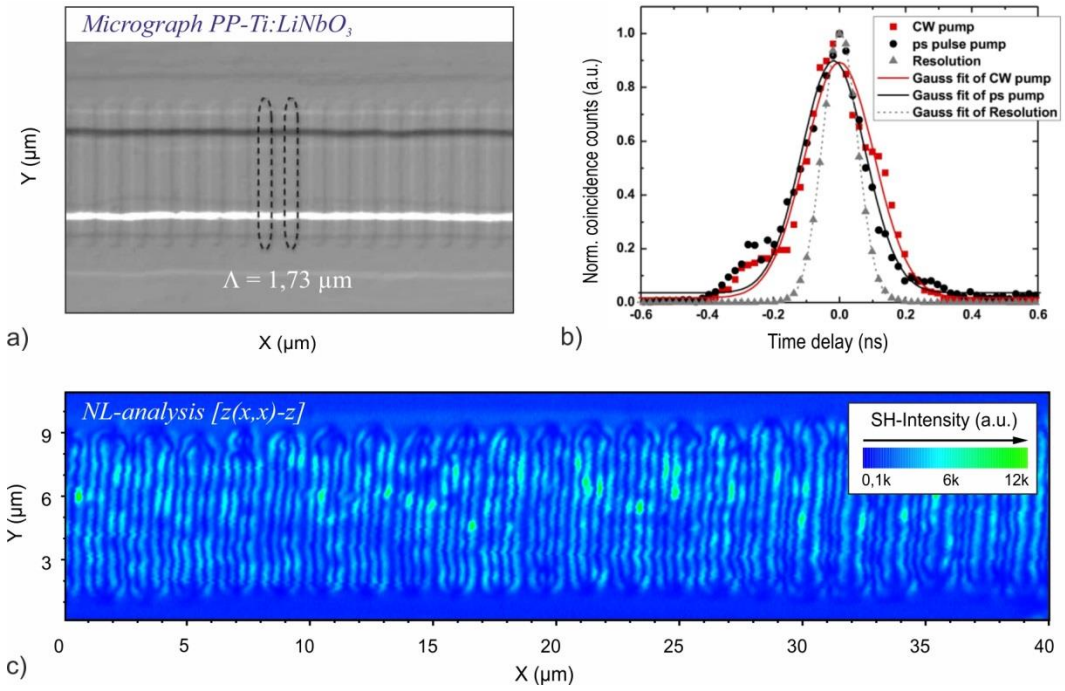

Figure 5.8: *a) Micrograph of selectively etched titanium in-diffused LN waveguide with period of Λ = 1.73 µm. b) Diagram of coincidence measurements in the time domain for a pulsed and cw excitation pump and the according fit functions. Coincidence envelopes between signal and idler from ps pulse pumping (black) and continuous-wave pumping (red). The time resolution of the detection system (grey) was obtained by using a typical co-propagating QPM PDC source with short correlation time* [229]. *c) SH-image image of the ultrashort period domain pattern of PP-Ti:$LiNbO_3$ (scan increments Δx = 50 nm u. Δx = 50 nm, integration time: 100 ms).*

Concerning photon pair generation the realized device allows for 5th order quasi phase-matching since the most contributing tensor element d_{33} can be triggered. The PDC is detectable throughout the entire 37 mm long waveguide as partly sketched in the figure above. Besides the confirmation of the homogeneity and correct duty cycle over the entire device length (37 mm) the efficiency of the counter-propagating PDC within the device has to be determined via coincidence measurements. The rate of the generated photon pairs throughout the waveguide is stated with 5 pairs/s·mW as obtained from the respective pump power dependent measurement [229].

It turns out that this sample features a pump power which is quite below the typical threshold of a mirrorless OPO because the counts obtained from the coincidence measurement exhibit a linear dependence on the pump power and therefore other cascaded processes can be neglected due to the non-quadratic manner. Here the counter-propagating PDC process is verified by characterizing the twin quality of the generated photon pairs. Thus, correlation measurements in the time and spectral domain are performed (see Figure 5.8 b). The coincidence measurements are performed with a 2 ps long pulse at a wavelength of 765 nm in a fiber based time-of-flight spectrometer. The fabricated CP-PDC device features a FWHM of approximately 250 ps. That matches with the sample interaction length of 37 mm and is conform to a narrow bandwidth in the low GHz range. Pulsed and cw pumping are very likewise due to the horizontal phase-matching function, cf. [229].

Domain structures in x-cut $LiNbO_3$:

Various applications in x-cut LN like ridge waveguides for instance and the direct access to the strongest nonlinear coefficient d_{33} make it favorable for investigations concerning applications for integrated optical devices. Thus, a periodically poled domain structure in bulk x-cut $LiNbO_3$ was analyzed by nonlinear microscopy. The sample is analyzed via pointwise scanning in the confocal regime as usual. The resulting nonlinear image is shown below.

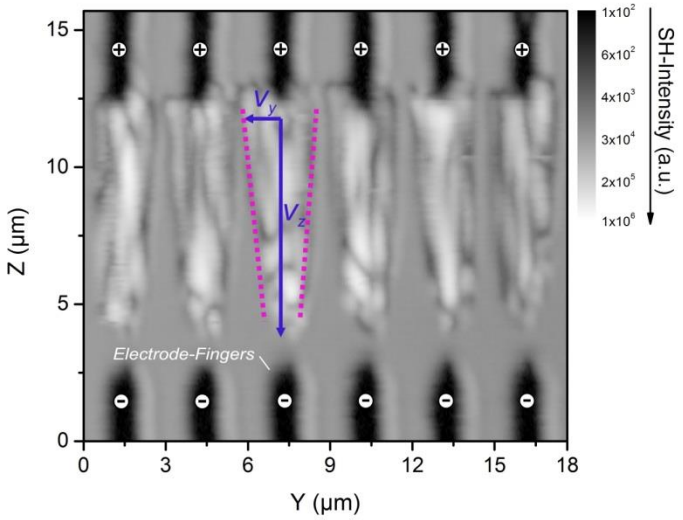

Figure 5.9: *Nonlinear image (Δz/y = 100 nm, Int.-time = 100 ms) of a periodically poled bulk crystal in x-cut LN with applied electrode structure. One can see emerging domain fragments, whereas the different domain growth velocities V_y and V_z parallel and orthogonal to the poling structure are indicated.*

The metal electrodes remaining on the sample represent areas where no nonlinear signal occurs. The opposing electrodes (distance 10 µm) are arranged so that the electric field propagates along the crystallographic c-axis (here z).

Inverted domains are then basically separated from the non-inverted domain regions by domain walls where the SH signal is depressed. It can be clearly seen here that domain fragments are present in the inversion region, which are then also correspondingly locally delimited (domain walls) and thus lead to a reduction in the nonlinear signal.

As to be seen, the domain inversion runs from the positive to the negative electrode because the lateral growth in y-direction is much more pronounced below the positive electrode ($z \approx 12$ µm) here compared above the negative electrode ($z \approx 2.5$ µm). This behavior is also indicated in the figure with green arrows for the two particular growth velocities and thus the tapered shape of the inverted domains (orange dotted lines). Such a pointed growth behavior to be seen in x- or y-face or – if applicable – in depth-scans for z-face. This exemplified result of the growth behavior in x-cut LN foreshadows and compresses the challenges which come up with domain engineering in this material configuration, i.e. evaluation of the poling voltage, possible pulse durations and repetitions, application of pre-pulses, geometry of the electrode structure like distance of opposing fingers or the shape of the electrodes amongst other determinants. These parameters are systematically investigated for periodically poled domain structures in x-cut LN as thin film material in the next subchapter.

5.2.2 Domain structures in LNOI

For the LN platform lithium niobate on insulator respectively thin film lithium niobate has drawn much attention within the community of integrated optics. This comprises amongst others waveguides, couplers, cavities or modulators for instance [18]. This novel material platform combines the specific optical advantages of bulk LN as its high nonlinear coefficient and the facilitation of QPM in it with a higher mode confinement, the precise control of the refractive index and further traits considering its thin film character as a promising functional layer sequence. Towards integrated optical devices in LNOI the results of the investigation of periodic poling in x-cut samples are presented in this section. Therefore electrode structures for field assisted periodic poling are defined lithographically on the x-face. Since the opposing electrodes are aligned along the z-axis the domain inversion takes places between the fingers when an external electric field is applied. An entire periodic domain inversion over the full electrode scale can be achieved. In terms of a feedback-loop several crucial fabrication parameters have to be iteratively optimized.

In a first step, the crystallographic quality of LNOI has been studied by means of its vibrational properties. Here the spectroscopic results are compared to the bulk crystal. Furthermore the influence of the final annealing step of LNOI within the material fabrication is discussed. In this context, the fabrication process of LNOI is taken into account (see Figure 5.10).

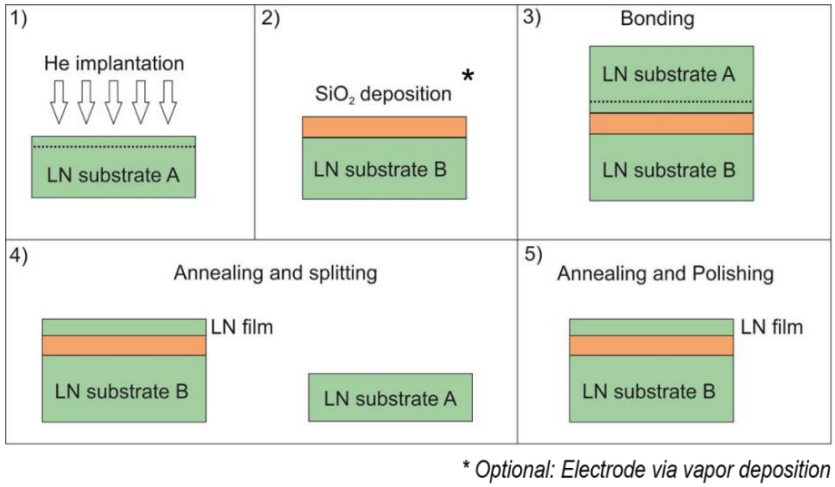

Figure 5.10: *Sequence of LNOI fabrication steps adapted from* [230]*. Depending on the particular crystal cut a back-electrode can be fabricated on top of the insulating layer by vapor deposition.*

A LN substrate is treated with an ion-implantation of Helium, which leads to a confined amorphous layer. This substrate is connected to another substrate with an insulating SiO_2 layer (via PECVD) on top, whereupon the ion-implanted face of the LN substrate is placed on the insulating layer of the second one. To get LNOI, a temperature treatment is performed, whereby the bonded system splits at the He^+-ion-induced cleavage layer into two parts. In a final step annealing is performed to recover defects stemming from the implantation process [230]. From recent experiments it is known that a precise definition of the ordinary (from 2.278 to 2.286) and extraordinary (from 2.214 to 2.202) refractive indices via such a recovering temperature treatment in LNOI becomes possible until they reach respective bulk crystal values (Figure 5.11 b)) [231].

A comparable behavior can be found for nonlinear response of ion-implanted regions where an annealing step leads to a recovery of implantation-induced defects so that the nonlinear susceptibility of the material nearly reaches the bulk level [232]. For LNOI the fabrication process utilizes He^+-implantation which also influences the crystallographic structure within the transition region. The impact of defects on the crystallographic properties is connected to vibrational fingerprints like changes in the FWHM or in the Raman shift. Hence the influence of recovering via an annealing step is studied in terms the vibrational properties as differences in the FWHM and Raman shift of specific modes are analyzed. Exemplarily the dependence of A_1-LO modes on the applied annealing temperature is presented in Figure 5.11 a).

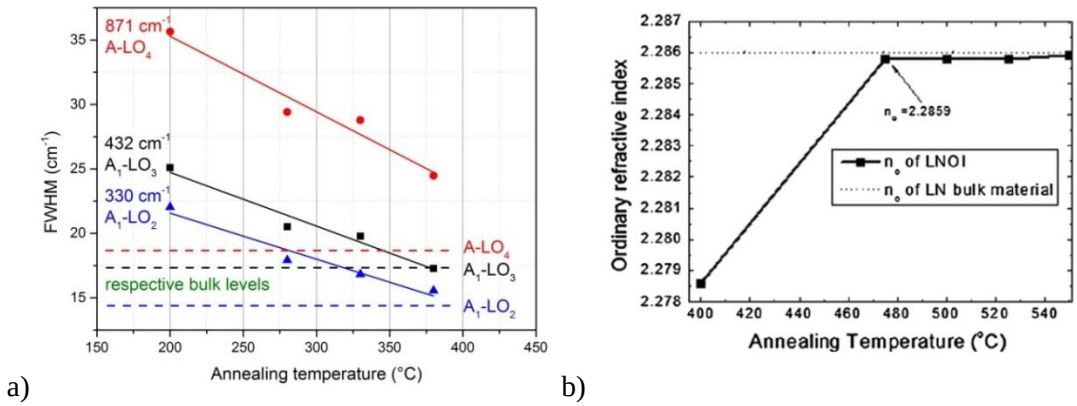

Figure 5.11: *a) Plot for the measured decline of the mode FWHM in dependence of the annealing temperature (range: 200 °C – 380 °C) for a set of LNOI samples for three selected LO modes to their respective bulk level. b) Courses of the ordinary and extraordinary refractive index of LNOI in dependence of the annealing temperature with saturation in the respective bulk level for higher temperatures* [231].

It can be found that with increasing annealing temperature the broadened FWHM of the stripped off thin lithium niobate films converge back to the half width of the bulk LN material. For the Raman shift of the E-TO_1 mode a similar behavior can be found where the Raman center frequency of the thin film LN (157,2 cm^{-1}) becomes identical to that of the bulk material (152 cm^{-1}) for a temperature of 340 °C. The aforementioned behaviors confirm that to an appropriate annealing step leads to a defect recovery within the treated crystal region. The commercially available samples (*NANOLN*) already contain the final annealing step, so that a comparison of the vibration properties can now be made by directly comparing the spectra with that of an untreated bulk sample. This is shown in Figure 5.12 for both z-cut and x-cut LNOI as exemplified for one scattering geometry respectively.

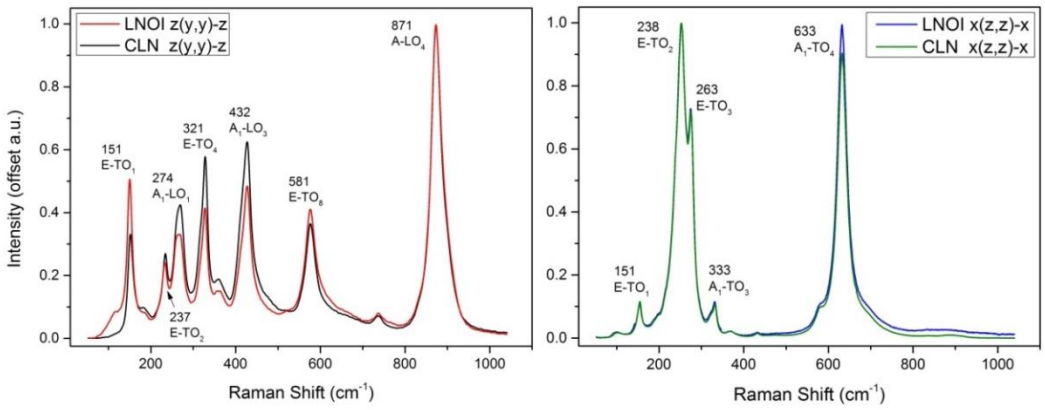

Figure 5.12: *Comparison of measured normalized Raman spectra of z- and x-cut LNOI with congruent LN.*

For all scattering geometries the x- and z-cut thin film samples show no significant changes compared to the bulk material, hence the crystallographic quality is sufficient. Concerning the periodic domain inversion within such LNOI substrates one has to realize a defined electrode structure for the application of external electric fields. Due to general advantages, such as good mode guidance (TM & TE), long-term stability of the domains and easier electrical contactability, the x-cut was preferred in this work [17]. A resist layer is spin-coated onto the positive x-face and subsequently illuminated via a laser (alternatively by e-beam) to define the electrode structure. After the resist is developed a chromium/gold layer is deposited. In a final lift-off process the remaining resist is removed and the desired metallic electrode structured is completed. Micrograph sections of realized finger electrode structures are exemplarily depicted in Figure 5.13 a). Here, the fingers are orientated parallel to the crystallographic z-axis, allowing for domain inversion in z-direction.

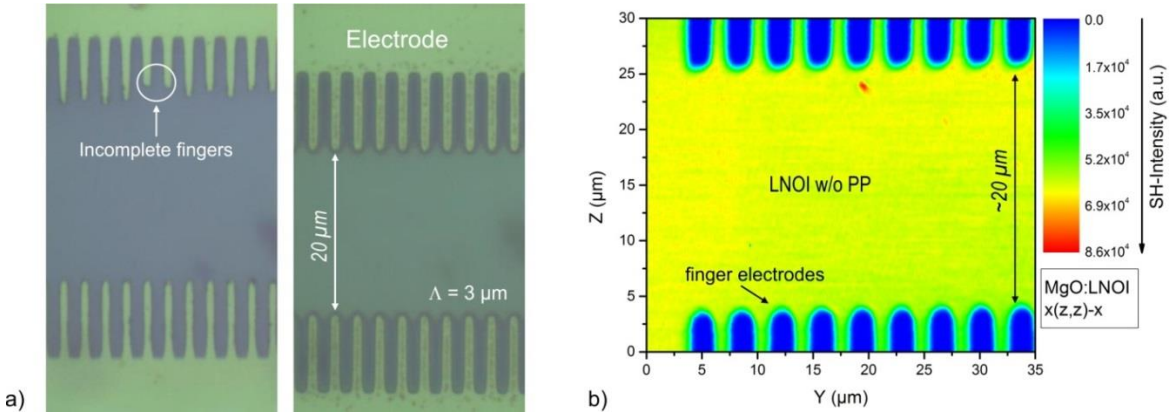

Figure 5.13: *a) Microscope images of different processed metallic finger structure on LNOI. b) SHG microscopy scan of unpoled x-cut LNOI between a finger electrode structure measured with a resolution of Δy = 100 nm and Δz = 250 nm. The integration time is 1 s and the scattering geometry yields x(z,z)-x.*

Concerning ultra-short poling periods the photo-lithographical process becomes difficult, so solitary or groups of fingers can be missing or should be not fully formed (Figure 5.13 a) left). After an appropriate optimization step electrodes can be created in sufficient quality (Figure 5.13 a) right). The produced electrodes feature an aimed poling period of Λ = 3 µm, where the finger yield a width of 1.5 µm and a length of 10 µm. The distance of the opposed electrodes is chosen to be 20 µm, which is crucial for the value of the applied electric field (> coercive field strength).

A corresponding section of such a finger electrode structure on x-cut LNOI before the poling step is mapped via SHG microscopy (Figure 5.13 b)). Here, the metal electrodes yield no nonlinear signal (screening against the nonlinear material) whereas the nonlinear signal from the free area of the thin film material is detectable and appears spatially homogeneous due to non-inverted regions (single domain). Furthermore one can see a slight signal increase at the contour of each finger which is attributed to the exact definition of the level contrast of the false color image. In case of inverted domains after field assisted poling signatures from the domain walls should become visible. Therefore the nonlinear answer of such structures is analyzed in terms of polarization.

In Figure 5.14 corresponding line scans perpendicular to a periodically poled LNOI structure are presented for all four scattering geometries. Note, that the intensity values are normalized to show the principal behavior, so that the nonlinear contrast cannot be extracted from these graphs.

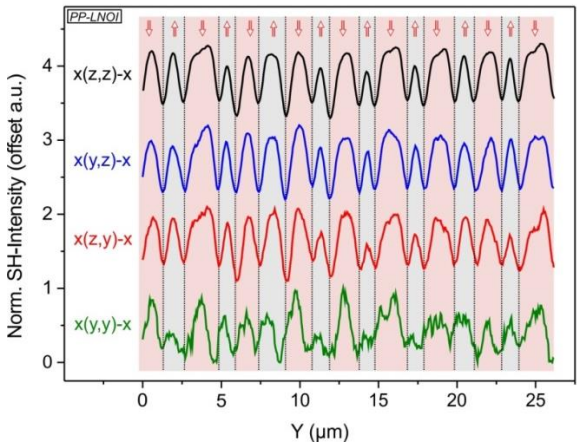

Figure 5.14: *Stacked nonlinear line scans along a structure on x-cut LNOI (sample: LNOI MgO 300 b11) for all scattering geometries which is periodically poled with a voltage of 900 V and a pulse duration of 1ms. The step width of the line scan is Δy = 50 nm at an integration time of 1 s.*

In contrast to z-cut LN here the nonlinear signal arising from the domain walls is reduced compared to the domain signal for all scattering geometries. Whereby the strongest nonlinear contrast is found for the x(z,z)-x configuration with a contrast of $I_D/I_W \sim 10$, the contrast for the other scattering regimes is given for x(y,z)-x by a factor of 5, for x(z,y)-x by a factor of 3 and for x(y,y)-x by a factor of 2 so that in the following this scattering geometry is applied for studying x-cut LNOI.

Domain inversion in congruent LNOI:

The fabrication of periodic domain structures in congruent x-cut thin film $LiNbO_3$ proves to be challenging. Therefore, as a first step, poling experiments were performed under variation of the poling voltage. The samples investigated here have an electrode spacing of 40 µm, and the voltages were varied from 1.2 kV to 2.0 kV for the electric field poling (Figure 5.15).

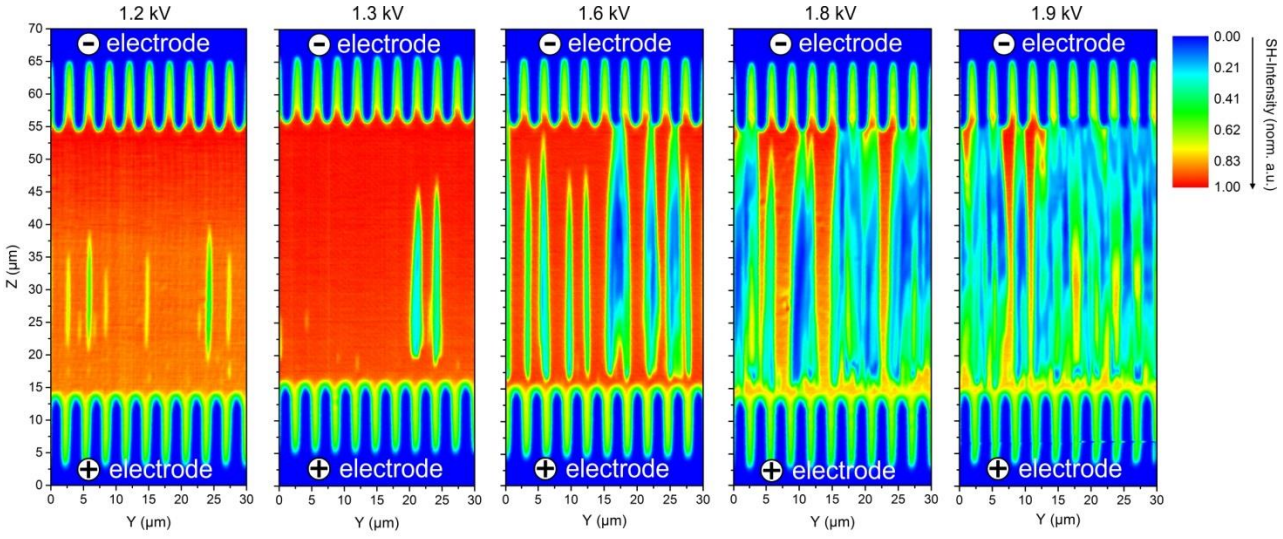

Figure 5.15: *Series of nonlinear area scans of congruent x-cut LNOI (600 A60-b35) with no prepulses applied for different poling voltages and a pulse duration of 1 ms. Here, the scan resolution yields Δy = 100 nm, Δz = 200 nm and the integration time is 1 s and the scattering geometry x(z,z)-x is chosen.*

In all nonlinear images of the poling structures, domain fragments (lowered SH-signal via domain walls) can be recognized, which are detached from the desired poling structure. These fragments are not located between the opposite electrode fingers (no SH-signal) but exclusively in the intermediate regions. The origin of these fragments seems to be connected to the e-beam lithographic process due to the periodic occurrence in the intermediate regions. The scale of these fragment regions extends for higher voltages to a width of $\Lambda/2$, so that such regions may merge for strong electric fields. Over the entire voltage range, no homogeneous domain structure has been obtained in the present material system. The reason for this is the existence of the aforementioned embedded domain fragments which overlap with domain filaments emanating for higher voltages (from 1.7 kV) from the electrodes. However, in accordance to literature, domain growth in congruent LNOI occurs from the positive to the negative side for the fragments as well as the filaments originating from the electrodes. This issue of embedded fragment formation was also investigated at the edge of the poling structure. In this respect, Figure 5.16 compares the nonlinear area scan of an edge region with one from the central region of the poling structure at a voltage of 1.5 kV.

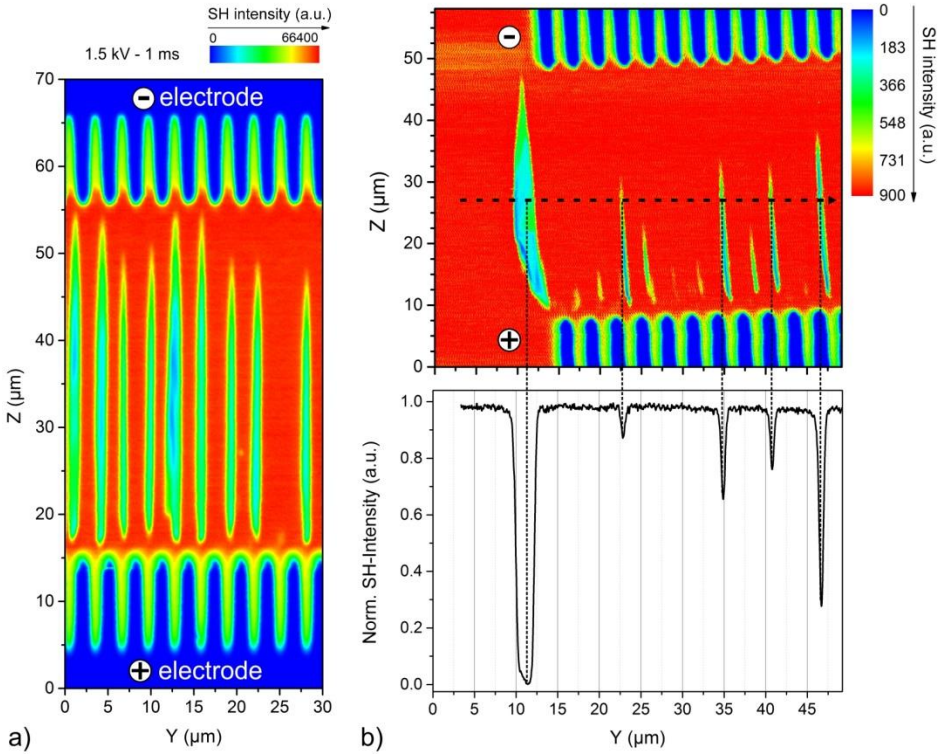

Figure 5.16: *a) Nonlinear area scan of congruent x-cut LNOI (600 A60-b35) with no prepulses for a poling voltage of 1.5 kV and a pulse duration of 1 ms in the central area of the electrode structure. b) Nonlinear area scan with corresponding line scan on the margin area of the same electrode structure. For both scans the resolution yields* $\Delta y = 100$ *nm,* $\Delta z = 200$ *nm at an integration time of 1 s and the scattering geometry x(z,z)-x.*

Embedded domain fragments are visible in both the inner and outer regions of the poling structure, with a pronounced fragmentation region becoming apparent at the edge of the poling structure, which has a maximum width of $\Delta y = 3$ µm. This is due to a field enhancement, which is large enough, to range from the positive to the negative electrode in this region.

In a further step, it was investigated how a previous complete multiple domain reversal of the congruent material affects the actual poling process. The samples to be investigated again have a distance between the electrodes of 40 µm. Periodic poling was realized by applying electrical pulses with constant duration of 3 ms and varying poling voltage. In Figure 5.17 exemplarily the nonlinear answer of a periodically poled congruent x-cut LNOI sample is depicted for a poling voltage of 1.2 kV.

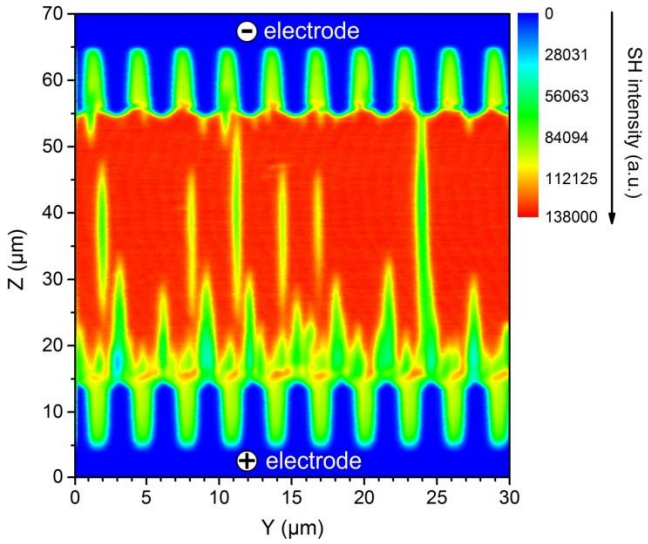

Figure 5.17: *SHG microscopy area scan of congruent x-cut LNOI (sample: LNOI 600.A60-b35) with applied prepulses for a poling voltage of 1.2 kV and a pulse duration of 3 ms. The scan is performed with a resolution of Δy = 100 nm, Δz = 200 nm. The integration time is 1 s and the scattering geometry x(z,z)-x is chosen.*

As it can be seen from the SH image also the fragment inclusions described above are found (offset from the areas between the electrodes). In addition, a poling process starts from the positive electrode fingers towards the negative electrode whereby these areas represent no homogeneous domains but rather domain fragments. This becomes obvious because these areas show a relatively uniform reduction of the nonlinear response (convulent of multiple domain walls enclosing the fragments). In contrast to the non-pretreated case, here the domain inversion at the electrode fingers begins already for lower voltages. It can be speculated that the multiple flipping of the internal polarization leads to an increased number of nucleation spots near the electrodes. The evolution of the poling behavior with increasing voltage shows that the domain growth continues from the positive side, which is also in accordance with the literature [181]. Figure 5.18 a) now proves this fact, contrasting three nonlinear images of periodically poled congruent LNOI samples (1.2 kV, 1.4 kV and 1.8 kV), appropriately pretreated by multiple poling reversals.

Since the same pulse durations were used here for the poling, it can be seen that the inversion continues to form with increasing voltage.

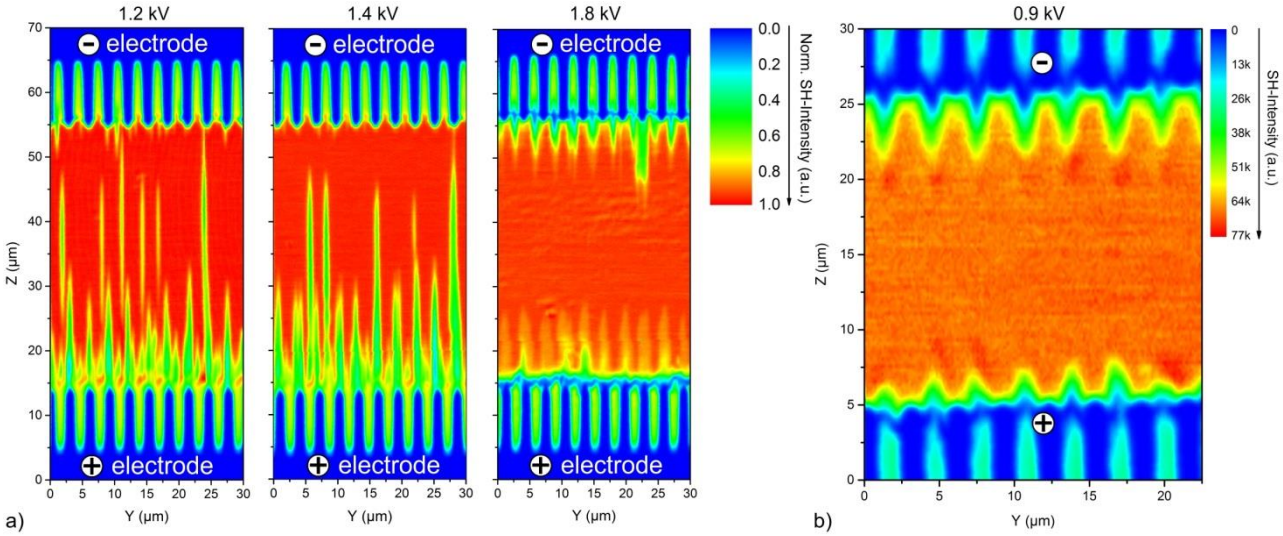

Figure 5.18: *a) Collage of nonlinear area scans of congruent x-cut LNOI (sample: LNOI 600 A60-b35) with applied pre-pulses for different poling voltages and a pulse duration of 3 ms (Scan parameters: Δy = 100 nm, Δz = 200 nm, Int. time = 1 s). b) Nonlinear area scan of congruent x-cut LNOI (sample: LNOI 600 b28) for a poling voltage of 900 V and a pulse duration of 3 ms. The scan resolution yields Δy = 150 nm, Δz = 250 nm. An integration time of 1 s and the scattering geometry x(z,z)-x is chosen.*

Furthermore, for the two samples with not too high poling voltage, one can see the fragment inclusions outside the electrode region. The nonlinear image of the sample poled with 1.8 kV indicates overpoling, since fragment inclusions are then no longer existent here. Analogous results were obtained for further congruent samples with an electrode gap of 20 µm and lower poling voltages (Figure 5.18 b)).

Further increases in voltage in the overpoled samples are then only evident in the region near the negative electrode by widening of the inverted domain regions which have not yet grown together (Figure 5.19).

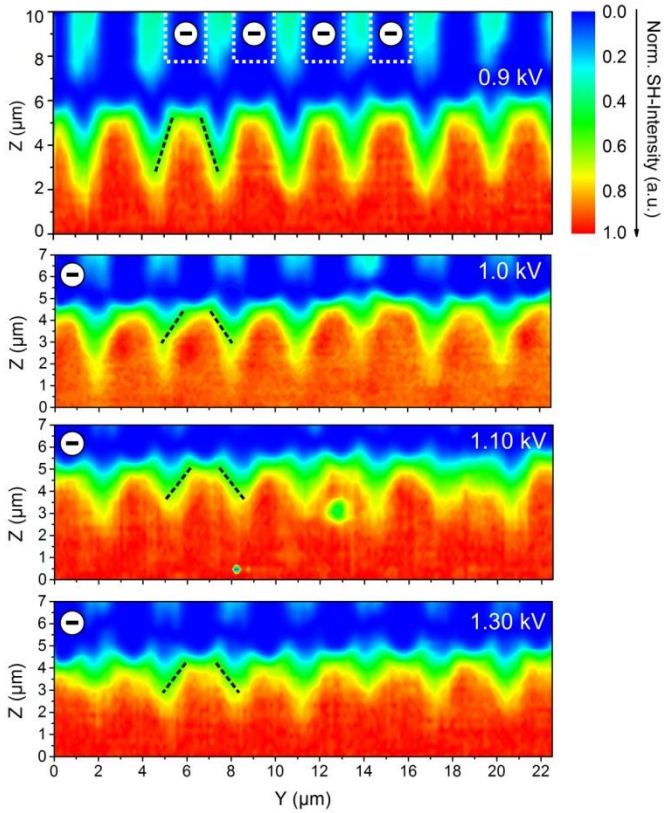

Figure 5.19: *Four nonlinear diagrams showing the broadening of the inverted domain regions near the negative electrode of congruent LNOI (sample: LNOI 600 b28) as a dependence of the applied poling voltage The scan resolution is* $\Delta y = 150$ *nm,* $\Delta z = 250$ *nm. An integration time of 1 s and the scattering geometry x(z,z)-x is chosen.*

In summary, it can be stated that "healing" of the fragment inclusions (centrally in the area next to the opposing electrodes) can only be achieved during overpoling and thus a periodic poling structure without perturbation cannot be realized here. The fragment inclusions are supposedly of fabrication nature (e.g. lithographic process). This cannot be circumvented even by repeated domain reversal of the entire sample as a treatment before the actual poling.

Domain inversion in MgO:LNOI:

MgO:LNOI represents an alternative material platform. Since the coercivity is supposedly reduced [233], the process of domain inversion is more homogeneous and it alters the dispersion properties towards increased refractive indices [234]. The in-house fabricated x-cut LNOI samples provided by the Silberhorn group analyzed in this work consist mainly of 5% MgO doped LN thin films.

To date, domain growth and the dynamics of domain inversion in MgO:LNOI do not seem to be fully understood. Thus, a wide variety of effects occur here, which make a defined domain growth complex. For example, self-assembled domain growth occurs in MgO doped LN even when the poling structure is not externally defined.

To prove this fact, a corresponding nonlinear analysis was performed at the edge of two opposing pad electrodes (without finger structure) on a MgO:LNOI sample (Figure 5.20 a)). The poling itself was performed here at a voltage of 1.4 kV and a pulse duration of 9 ms with an electrode gap of 40 µm. In the nonlinear confocal image (Δx = 100 nm, Int-time = 1 s) no nonlinear signal is obtained from the metallized electrode region as mentioned before. Furthermore, it can be seen that a self-assembled domain growth starts on the positive electrode side. Here, the nonlinear response from these areas can be understood as a collimated signal of embedded domain fragments, which then manifests itself in each case in a lowering of the nonlinear signal over a width of up to 800 nm and thus lies clearly above the actual domain wall signal of approximately 250 nm.

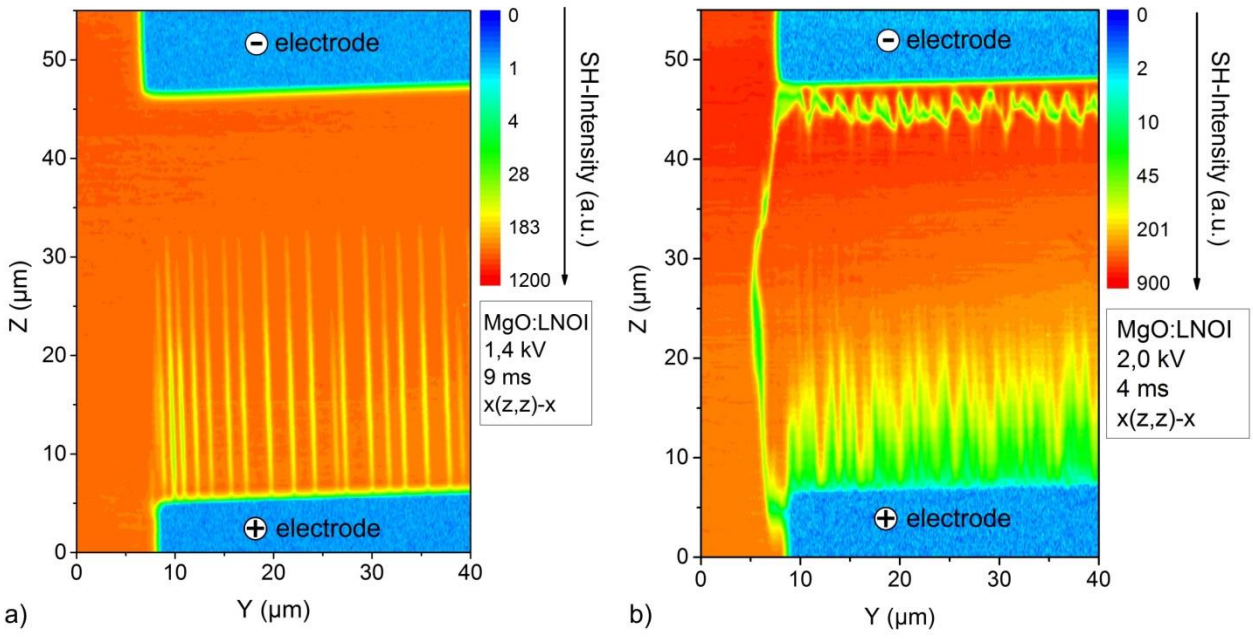

Figure 5.20: *a) Nonlinear area scan of x-cut MgO:LNOI (sample LNOI MgO 300 b9) between two plain electrode pads with an applied voltage of 1,4 kV and a pulse duration of 9 ms. b) Analog area scan for 2,0 kV and 4 ms. The scan resolution yields Δy = 100 nm, Δz = 250 nm. An integration time of 1 s and the scattering geometry x(z,z)-x is chosen.*

Figure 5.20 b) shows the result for another sample with opposing pad electrodes, where a voltage of 2.0 kV (pulse duration: 4 ms) was applied for domain inversion. Again, one can see domain growth starting on the positive side, but here the domain fragments already overlap.

Furthermore, it is noticeable that at this voltage a domain inversion also takes place on the negative electrode side and spreads towards the positive side where the extent of the inversion is not as advanced (different growth rates). The domain fragment at the edge of the electrode pads probably stems from the merging of two areas whose inversions started on the opposite electrodes and finally merged. Both the self-organized domain inversion and the domain growth on both sides with respect to polarity are interesting aspects, but prove to be extremely complex with respect to defined domain structuring and therefore their influence on the technological side is avoided as far as possible.
It stands to reason that the propagation direction of the domain inversion is related to the strength of the applied electric field. In the specific case, it can be speculated that up to a specific field strength, domain growth starts exclusively on positive electrode side (E-field is opposite to inner field). If this field is increased, the critical field in the inner part is overcome and domain growth starts also on the opposite side (negative electrode). Thus, in a specific voltage range, domain inversion takes place locally separated at both electrodes.

For the fabrication of periodic defined domain grids with a corresponding electrode structure, a precise knowledge of the poling parameters is indispensable. On the one hand, this refers to a coordinated dimensioning or geometry of the electrode structure (distance and shape) and, on the other hand, to the physical quantities (voltage strength and pulse duration) of the electric field poling. Both must ultimately be matched to each other and to the respective material system. Therefore, with respect to the electric field poling in MgO:LNOI, samples (distance of opposing electrodes: 20 µm) were first poled over a certain voltage range and analyzed accordingly by nonlinear microscopy. Here, the applied poling voltages ranged between 800 V and 1000 V. The resulting SH line scans across the poling structure are now shown comparatively in the following figure. It should be noted that the curves shown here originate from the center between the opposing electrodes. With regard to the best possible SH contrast, the x(zz)-x scattering geometry was chosen. For voltages below 800 V, there are no structures that extend over the entire area between the opposing electrodes.

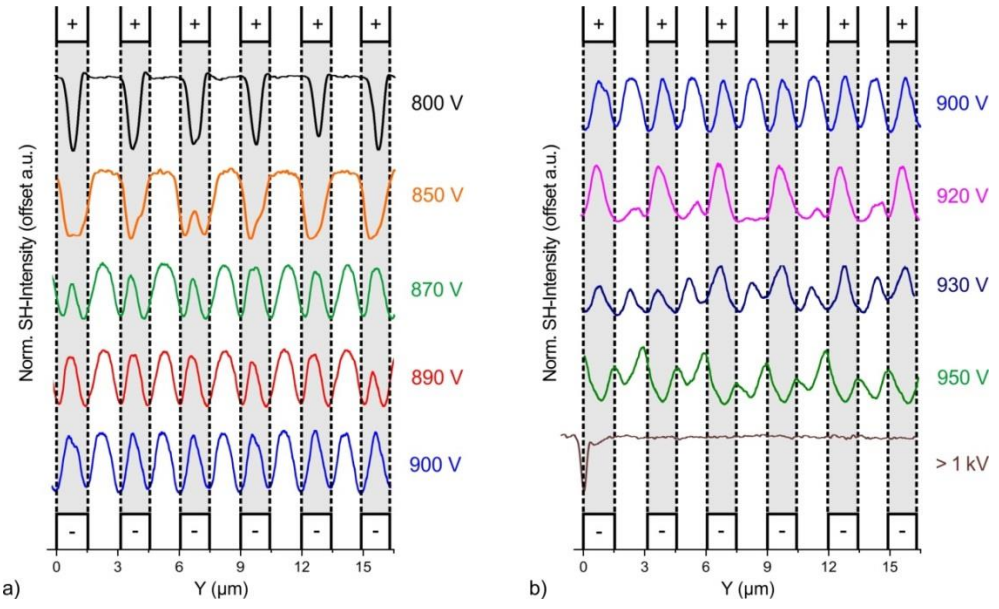

Figure 5.21: *Stacked nonlinear line scans across periodically poled structures on x-cut LNOI (MgO 300 b11/b14/b16) poled with voltages ranging from a) 800 V to 900 V and b) 900 V to >1000 V and a pulse duration of 1 ms. The scans are obtained with a resolution of Δy = 40 nm and an integration time of 1 s for the scattering geometry x(z,z)-x.*

As it can be seen from the nonlinear scans, for the samples with poling voltages of 800 V and 850 V, there is a not yet a very pronounced inverted domain. These are not yet extended domains; rather, one can assume domain fragments, which can be seen in the lowering of the nonlinear response. The original domain, on the other hand, has a width approximately of the order of the poling period of 3 µm. However, for poling voltages between 870 V and 900 V, approximately a 50/50 duty cycle appears, which is correspondingly the relevant voltage range. For voltages between 900 V and 1 kV, there is a disturbed course of the nonlinear signal, which finally ends in a merging of the inverted domains for poling voltages above 1 kV due to overpoling. Here, only the transition from the original region outside the electrodes to the completely inverted domain is recognizable, which is evidenced here by a signal dip on the one domain wall located at the edge. For illustration purposes (see Figure 5.22), three nonlinear signal curves perpendicular to the domain structure of LNOI samples poled at 700 V, 900 V and 1000 V are now supplemented by corresponding sketches of the domain structure.

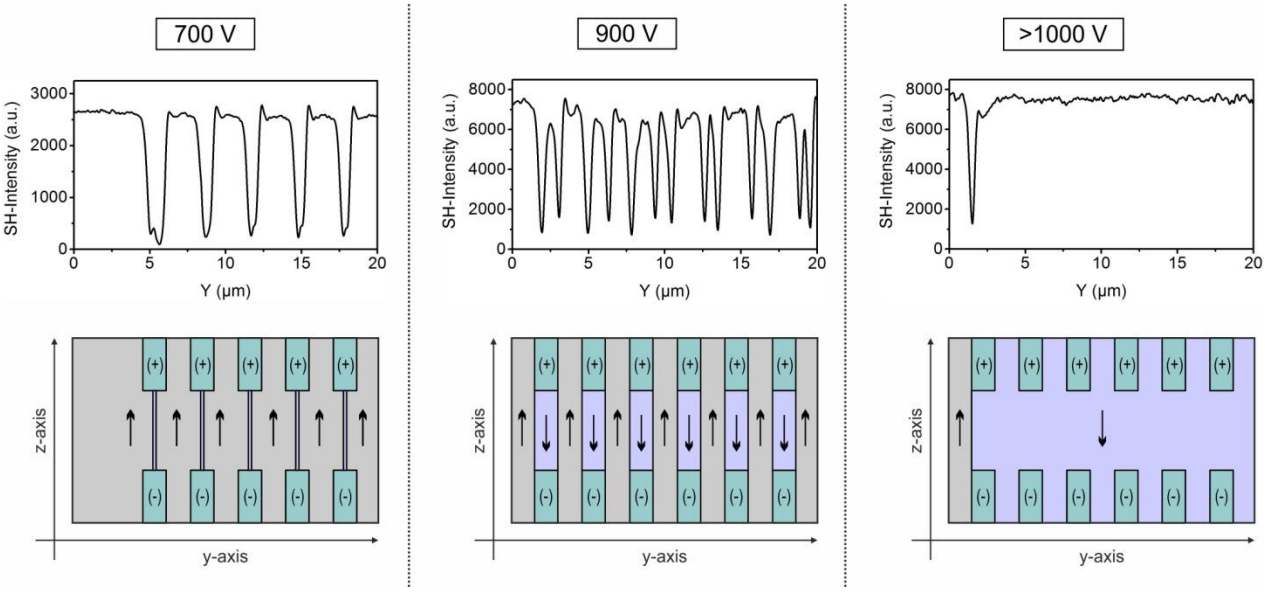

Figure 5.22: *Illustration of the nonlinear signal course perpendicular to a periodically poled structure in x-cut MgO:LNOI (300 b8/b11) for three different poling voltages measured with a resolution of Δy = 40 nm, an integration time of 1 s and the scattering geometry x(z,z)-x). Corresponding sketches show the particular extent of the inverted domains and their domain boundaries which match with the dips in the nonlinear signal.*

For domains running over the entire area, which also have a homogeneous shape or parallel alignment direction to the z-axis, the analysis of a line perpendicular to the domain structure in the area between the electrodes is sufficient to conclude on the transferred domain lattice. To account for the aforementioned problem regarding the interpretation of line scans, a case of non-homogeneous progression between the opposing electrodes is now shown in Figure 5.23. Therefore the results of an area scan and two line scans of different z-positions for a periodically poled MgO:LNOI sample are compared.

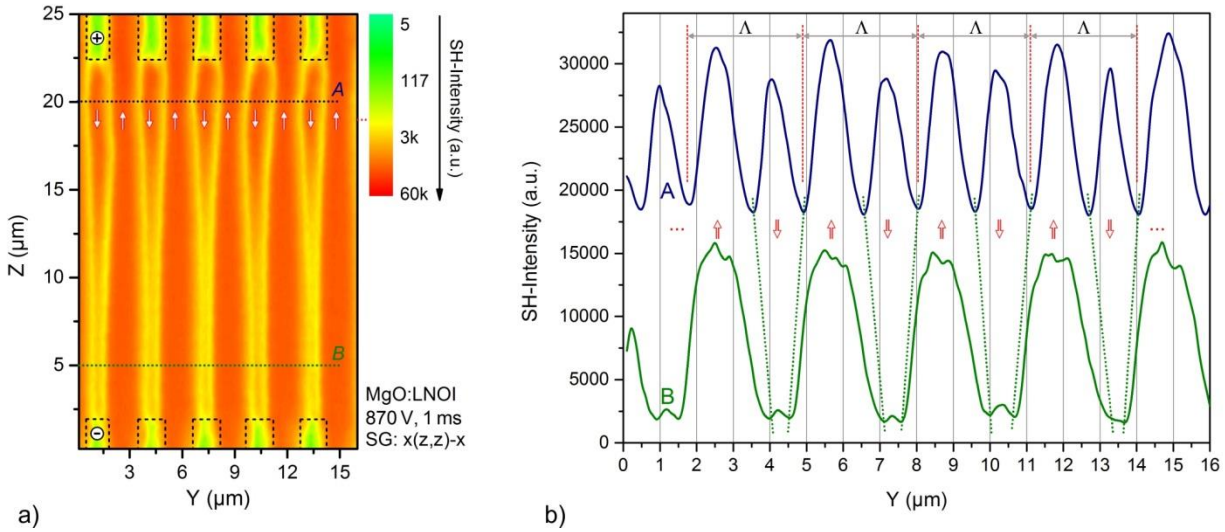

Figure 5.23: *a) Nonlinear area scan of a transferred ferroelectric domain pattern in x-cut MgO:LNOI (300 b14) inverted with a voltage of 870 V and a pulse duration of 1 ms. The scan is obtained with a resolution of Δy = 100 nm and Δz = 250 nm, an integration time of 1 s and the scattering geometry x(z,z)-x. b) Corresponding line scans performed at the indicated positions in inset a) with a step width of 80 nm.*

The area scan (Figure 5.23 a)) clearly shows inverted domain areas separated from the original area by walls. Accordingly, the nonlinear signal from the area of the domain walls is strongly reduced compared to that of the domains. The inverted domains have different widths along the z-axis, which decrease from the positive electrode to the negative electrode. If corresponding line scans are now performed at different z-positions, it becomes clear that the duty cycle varies with z. For the courses of line scans indicated in the area scan, a duty cycle of almost 50/50 (blue curve) results in the specific case only near the positive electrode, whereby the domain boundaries are not exactly parallel to the z-axis. For the scan near the negative electrode, the inverted domains are less extended in relation to the non-inverted ones (green curve).

Based on the nonlinear preliminary analysis using line scans, an extension was made by imaging the ferroelectric domain structure. The results are presented in Figure 5.24 below for the predefined voltage ranges.

Below a poling voltage of 700 V, there are no inversion regions running homogeneously between the opposite electrode fingers. It is clear that here an analysis based on line scans cannot provide the required information. For this lower voltage range, corresponding SH signatures of inversion could only be observed for line scans facing the electrodes. To illustrate this, the results from nonlinear area scans are shown as an example in the following figure, where the LNOI samples were poled with different voltages (here for pulse durations ≤ 4 ms).

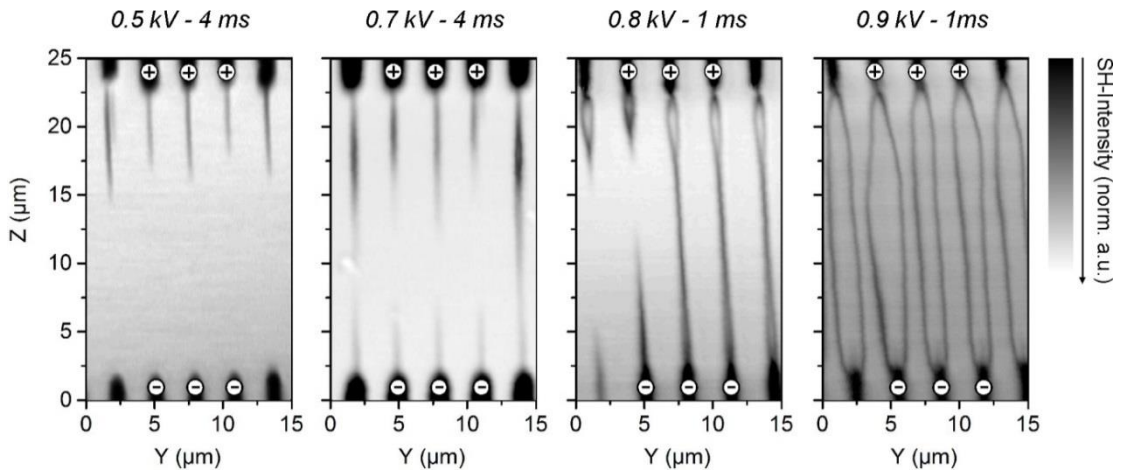

Figure 5.24: *Stack of four nonlinear area scans measured with a step width of Δy = 100 nm and Δz = 200 nm and an integration time of 1 ms on x-cut MgO:LNOI (300 b8/b11) with a periodically inverted domain structure poled at different voltages and pulse durations for the scattering geometry x(z,z)-x.*

From the series of SH imaging analysis, it can be seen that initially at lower voltages, poling originating from the positive electrode appears in the form of filaments. Depending on the pulse duration and/or poling voltage, an inversion starting from both electrodes is then visible, whereby the domain growth starting from the positive and negative electrodes converges. Here, the inversion areas pointing towards each other already partially connect. Furthermore, one can already recognize the first, somewhat extended areas of inverted domains. It is clear that the inversion process is linked to the voltage, pulse duration and electrode structure. On the material-specific side, the direction-dependent propagation velocity of the inversion is essential, among other factors. In this context, it can be concluded from the nonlinear images that the domain growth from the positive and negative electrode side shows different velocities in both forward and sideway direction. Here, the influence of MgO doping on the poling behavior needs to be clarified. Especially in MgO:LNOI, the parameter finding for the optimal domain inversion turns out to be quite complex.

Starting from a voltage of about 900 V, continuous inverted domain regions with sufficient periodicity in the y-direction are obtained. Therefore, in accordance with the line scans, the further voltage range from 890 V to 950 V was investigated in more detail. Here, a poling voltage of 1 kV represents the upper limit above which complete polarization reversal of the sample occurs. In the following Figure 5.25 the resulting SH images of periodically poled LNOI domain structures are shown comparatively, whereby the poling voltage was varied for the same pulse duration (1 ms).

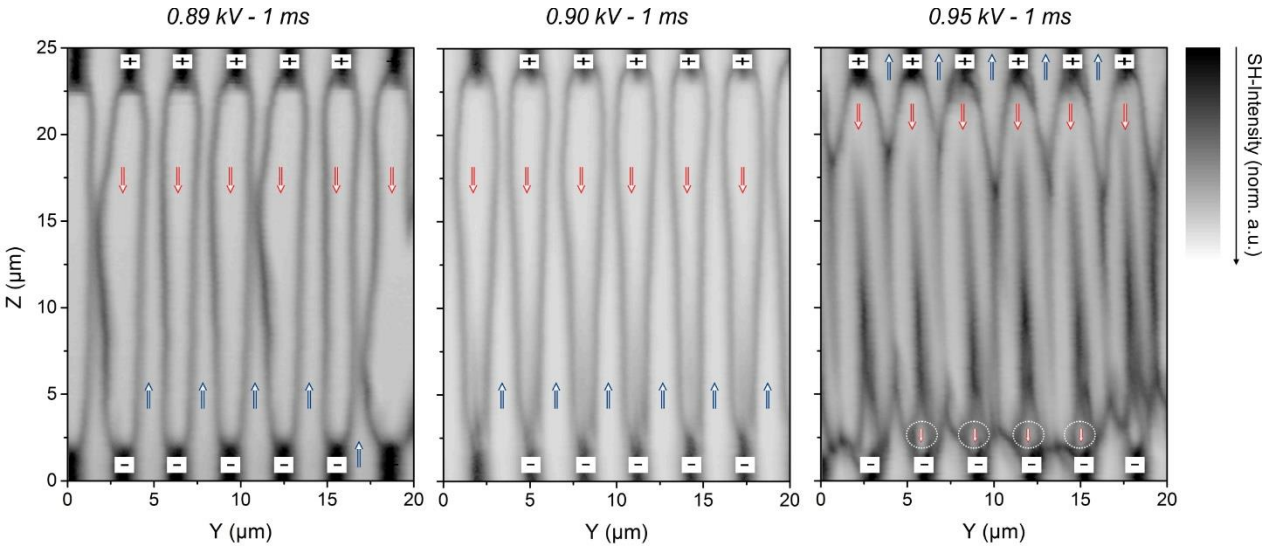

Figure 5.25: *Three SHG microcopy scans of periodically poled x-cut MgO:LNOI (300 b16). The poling is conducted for three different voltages and a pulse duration of 1 ms whereas the scans yield a resolution of Δy = 100 nm and Δz = 100 nm and an integration time of 1 ms. Red arrows indicate the inverted areas between the opposed electrodes and pristine areas are marked with blue arrows.*

The nonlinear analysis shows that, in principle, a periodic structure is present for samples poled in this voltage range. The inverted domain areas run completely from the positive to the negative electrode. At a poling voltage of 890 V, slight disturbances in the duty cycle can be seen, which may be due to disturbances in the poling structure or inherent material defects. The domain structure resulting from poling at 900 V, on the other hand, appears to be more homogeneous, but exhibits a variable duty cycle in the z-direction, which is due to the fact that on the negative electrode side the inverted regions transverse to the growth direction are not yet pronounced (domain walls taper somewhat to one point). Accordingly, a unique duty cycle of 50:50 can be defined at a specific z-position, although the domain walls do not run parallel to the c-axis. Furthermore, it should be noted here that for another sample with exactly the same poling parameters, fabrication steps and layer thickness, the domain structure shows a different picture (cf. Figure 5.24 right). Thus, it becomes clear that comparable sample quality and exact sample preparation are indispensable for a reproducible realization of defined domain structures. Compared to the two samples discussed above, the structure based on poling with 950 V shows a different picture. The inverted regions emanating from the respective electrodes are now separated only by a thin filamentation, so that there are no non-inverted regions between the opposed electrode fingers. Furthermore, it can be seen that from the negative side an additional domain inversion started, which finally lies in the form of a domain fragment centrally in the inverted region, which started from the positive electrode. This means that there is no conventional domain structure with alternating polarity here, but rather inverted domains alternate periodically with domain fragments. Original domains are only present between the respective electrodes (on the positive as well as on the negative side) and are restricted to the region close to the electrodes, which is limited by the actual inversion (blue arrows).

Another important polarity parameter is the pulse duration, so that its influence on the domain inversion is now considered. The pulse durations were varied between 1 and 10 ms for different voltages. Figure 5.26 shows an example of the nonlinearly recorded domain structures of LNOI samples, each of which was poled at a voltage of 700 V but with different pulse durations.

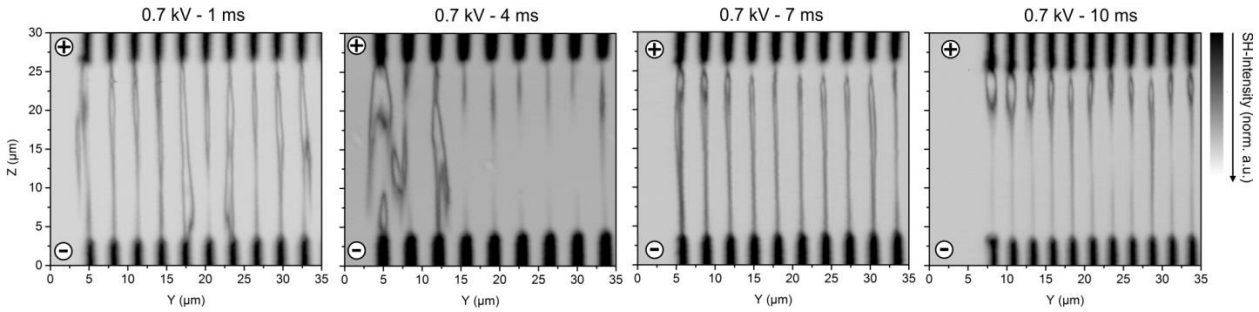

Figure 5.26: *Set of four nonlinear area scans with a resolution of Δy = 100 nm and Δz = 250 nm and an integration time of 1 ms of periodically poled x-cut MgO:LNOI (300 b8). For a constant voltage of 700 V and pulse durations between 1 ms and 10 ms the poling is conducted.*

A clear domain inversion is evident in all images acquired by SH microscopy in this series of experiments, with all inverted domains between each pair of electrodes extending over the entire range in the z-direction only for pulse durations of 1 ms, 7 ms, and 10 ms, respectively. For the sample with a pulse duration of 4 ms, the inversion does not extend over the entire range between the electrodes except for the border region. For this sample and partly also for the sample with 1 ms, material-specific or structure-specific disturbances are probably present. Furthermore, it is very clear here that the poling starts from both the positive and the negative side and that the respective inverted areas move towards each other in a directed manner. For the other cases, this bilateral domain growth can also be guessed in the domain progression, since near the positive as well as the negative electrode in each case the inverted domains show a more extended width. The width of the inverted domains (dependence on the y-propagation velocity) in these regions increases with increasing pulse duration, so that enclosed domain regions become visible. In contrast, the inversion velocity in the z-direction appears to be less affected. Measurements on samples at different poling voltages with varying pulse durations resulted in parameters for the domain inversion that were optimized specifically for the respective samples.

Thus, it becomes clear that this complex interplay of the most diverse poling parameters in conjunction with the material and structural perturbations does not provide a fixed set of parameters, but rather provides a range for a defined domain inversion. This range could be narrowed if material and structural perturbations are minimized. A successful example of this is the realization of a device based on periodically poled MgO:LNOI over a length of 5 mm. The associated nonlinear analysis is shown in Figure 5.27 below.

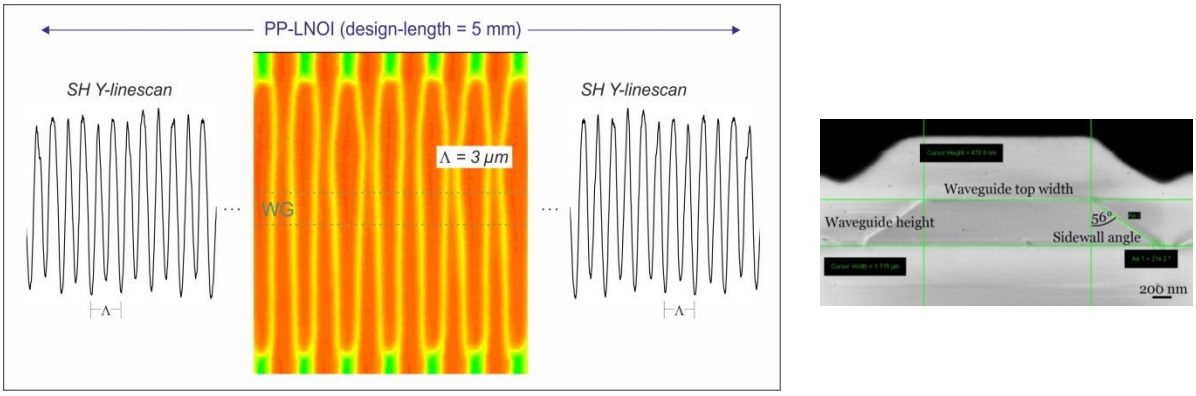

Figure 5.27: *Sketch of a final device for integrated optics on the basis of a periodically poled x-cut MgO:LNOI sample (300 b16) with a length 5 mm. The nonlinear area scan showing the domain structure is obtained with a resolution of Δy = 100 nm and Δz = 100 nm and an integration time of 1 ms. The nonlinear line scans are conducted near the end facets of the device. Furthermore, position of the waveguide within the device is implied via a dotted line. A SEM image of a front facet with the polished waveguide is shown in the right inset.*

In this context, a nonlinear area scan was first performed in the central area of the device (Figure 5.27 left image central). Here, the poling was performed at a voltage of 870 V with a pulse duration of 1 ms. The transferred domain structure with a period of Λ = 3 µm is clearly visible in the nonlinear image. Along the y-axis, inverted and original domains alternate, exhibiting nearly equal nonlinear signal strength and separation from each other by domain walls (reduced SHG signal). The extent of the inverted domains perpendicular to the domain structure is only slightly broadened in the positive electrode region compared to that at the negative electrode. This defined periodic domain structure with a duty cycle of almost 50/50 extends over the entire length of the device of 5 mm. In addition to area scans in the middle area of the sample, this was also documented by line scans at the device input and output. This result nicely documents the successful feedback-loop of the close cooperation between technology and analytics by iteratively improving the poling parameters.

Interim summary:

In LN as an established material, an optimization of the poling parameters towards small periods has been conducted via a feedback loop between technology and analytics. As a result, a device for the generation of counter-propagating PDC was realized and its characteristics were determined. Furthermore, the suitability of LNOI as an alternative platform for the fabrication of integrated optical devices was investigated. Here, the central question is related to the domain inversion process, which includes congruent as well as MgO-doped LNOI. After a general Raman spectroscopic characterization of the material system, the imaging of transferred domain structures in LNOI was performed by confocal SH microscopy. This systematically revealed the influence of specific fabrication parameters on the domain lattices to be generated, such as voltage and pulse duration on the field-assisted poling. For congruent material, it was shown that periodic poling, despite a wide variety of processing, is very problematic, which is due to domain fragmentation on the one hand and overpoling on the other. The analysis of the poling process for MgO-doped LNOI reveals the whole complexity of the fabrication of ferroelectric domain structures in this material platform.

Thus, it was shown that depending on the poling structure, self-organized domain growth can occur, which is determined by an interplay of electrode geometry and poling parameters. The domain inversion starts from the positive electrode, but above a specific threshold voltage it also starts from the negative electrode with a different growth rate. The optimum poling parameters for suitable electrode geometry have now been systematically determined in close cooperation with the technology side. In contrast to the congruent LNOI, it was shown that in the MgO-doped LNOI the fabrication of devices based on a periodic domain structure is possible. This was successfully demonstrated by the realization of a 5 mm long LNOI waveguide device with a homogeneous period length of $\Lambda = 3\ \mu m$.

6 Conclusion

Within the scope of this work, different ferroelectric material platforms were studied with respect to an optimized fabrication of quantum optical devices in the framework of a closed loop with the sample processing. The focus on the analytical side includes on the one hand the investigation of the inherent material properties respectively the generated ferroelectric domain structures and on the other hand the determination of specific process parameters for the fabrication of tailored nonlinear devices. The nonlinear bulk crystals KTP and LN were used as established base materials for integrated optics and LNOI as a promising system confining the fast lateral domain growth.

Concerning various physical issues the samples were probed by the noninvasive optical methods SHG microscopy and µ-Raman spectroscopy. Both methods are utilized in the confocal regime featuring high 3D spatial resolution and polarization dependent analysis. The visualization of domain grids was performed typically via nonlinear microscopy. Here, as an enhancement, the dispersion of the nonlinear setup was compensated by the implementation of a pulse compressor unit. Regarding the focal analysis of the generated second-harmonic signal, a scanning pinhole module was used in combination with an appropriate theoretical model allowing for the clarification of the nonlinear contrast mechanism in ferroelectric materials. In addition to domain structure imaging, Raman spectroscopy was used to analyze fundamental vibrational and stoichiometric properties of the ferroelectric domain patterns and waveguide structures. For an unambiguous interpretation of the experimental results, a deeper understanding of the occurring contrast mechanisms or the mere material properties is necessary. In this context, the studies include both fundamental physical and process-specific issues, which are not separable.

Before investigating functional structures within the different material platforms a fundamental analysis of the nonlinear contrast mechanism of ferroelectric domains has been done. For that a scanning pinhole module has been utilized to map the SH intensity distribution within the back focal plane. This gives information about the nature of the nonlinear light-matter interaction. In combination with a numerical vectorial model which describes the point-spread function one can estimate the e-field distribution within the back focal plane when the excitation field and the material properties (nonlinear tensor) are known. This method has been used on single domain LN and KTP crystals first. Here, for instance it could be shown that a split-pattern within the excitation light field does induce a split-pattern within the material response in the back focal plane. Combined with a polarization dependent analysis it is possible to distinctly address the various nonlinear tensor elements and so to conclude which element can be attributed for different features within the intensity distribution. Furthermore the possibility to estimate the nonlinear coefficient ratios is given.

This theoretical-experimental approach has then been applied to the transition region of the adjacent single domains in LN and KTP to unravel the nonlinear contrast mechanism of periodically poled structures. Most importantly it turned out that the mechanism behind the nonlinear contrast in a surface-near region is mainly due to a reversal of the nonlinear tensor elements' sign when measuring across a domain wall. The typical intensity distribution patterns within the back focal plane on a DW appear in a certain split pattern for which a constructive or destructive interference is responsible.

Besides this main reason for the contrast behavior it could be shown that one has to adapt the theoretical model by altering various tensor elements to match the experimental result so that DWs tend to be a region which probably induces new tensor elements.

The fundamental investigations within this work also cover a general Raman mode assignment for $LiNbO_3$ and $KTiOPO_4$. This should serve as a basis for further Raman spectroscopy investigations on periodically poled structures and the behavior of structure sensitive modes. Especially on PP-KTP a Raman analysis of the z- as well as y-face has been done in order to obtain a comprehensive mode assignment for the relevant structure sensitive modes on the one hand and on the other hand the ferroelectric domain structure has been imaged in a surface-near region here. This mode analysis has been performed in terms of the particular variation of the mode intensity, the center frequency and the FWHM. The surface-near investigation of both faces delivers information for the poling process regarding devices like periodically poled waveguides.

Based on these fundamental studies functional structures have been set into the focus of this work. Periodically poled waveguides in KTP have been probed not only at the surface-near region but also throughout the entire crystal depth by means of both characterization techniques. It has been shown which modes are sensitive to image only the periodically poled structure, only the waveguide or both features. Regarding the poling homogeneity it could be shown that the poling structure changes when a waveguide is fabricated into a previously entirely poled sample and that the poling process in depth revealed partly spike-like coalescences of domain fragments, variations of the designed duty cycle and not fully emerged domains. Furthermore the nonlinear contrast has also been demonstrated for y-face KTP via area-scans, where distinct deviations to the z-face can be found. The acquired e-field distribution in the back focal plane assigned to the nonlinear polarization for both single domain and domain wall are in good agreement with corresponding theoretical predictions and underlines the aspect of newly emerging tensor elements due to specific SH intensity variations. Here, the experiments comprise the analysis of bulk as well as Rb-exchanged KTP.

Considering functional LN devices, samples in z-cut and x-cut have been investigated. As a proof of principle a counter-propagation PDC device with a period length of 1.7 µm has been investigated via nonlinear microscopy. Here, the sub-µm domain wall distance could be resolved and a successful poling process verified. A brief material analysis via Raman spectroscopy has been done prior the nonlinear characterization of periodically poled structures in x-cut LNOI. Here, it has been found that a further annealing step after thin film transfer is recommended for the fabrication of LNOI samples due to defect recovering. The nonlinear analysis has been done to prove the poling behavior for different parameters for congruent LNOI and MgO-doped LNOI. For the case of c-LNOI samples with and without pre-pulses and different poling voltages have been taken into account. It turned out that for no application of pre-pulses domain fragments cannot be found in the area between two opposed electrodes but rather systematically displaced by $\Lambda/2$, which might be connected to the lithography process. The samples with applied pre-pulses also feature such inclusions but the actual poling process is more likely to be seen. Here, for higher voltages the fragments vanish. Towards the realization of functional devices in the LNOI platform the analysis gives rise to use MgO:LNOI as the material type of choice. Besides homogeneously periodically poled samples the effect of self-assembled domain growth has been detected for lower voltage ranges. To investigate this, an evaluation in terms of poling voltage and pulse duration has been done.

From a broad range the best results have been achieved in the interval between 870 V and 900 V. Regarding the pulse duration no specific value could be identified. But in connection with the respective voltage value an optimized set for the relevant test series could be obtained. Finally the SHG-scan of a PP-LNOI device could be presented which can be used for applications in integrated optics since its homogenous poling shape has been verified over an mm-scale. All in all it can be stated that, as a result of the optical techniques used here, for MgO:LNOI the range for the poling voltage and pulse duration could be narrowed down to a precise interval under the circumstance that material impairments are diminished as far as possible.

Outlook

SHG microscopy and μ-Raman spectroscopy as characterization methods for the investigation of functional structures towards nonlinear optical devices have proven to be reliable, precise and non-invasive tools. Various methodological and sample-specific extensions should underscore the points made in the relevant sections of this work.

Starting with the fundamental work of unraveling the nonlinear contrast mechanism the experimental-theoretical approach can be extended to concentrate on Cerenkov SHG as well as the utilization of a vortex retarder in order to shape the polarization in a radial or azimuthal manner compared to the standard excitation fields as introduced in this work. This would allow for the direct triggering or blanking of certain nonlinear tensor element contributions. As an effect of such a spatially inhomogeneous polarization distribution, the ratio between radial and azimuthal polarization can be defined. Finally a higher contrast of the imaging and the focal analysis would be obtained as well as a further proof of the vectorial model.

Regarding sample fabrication novel poling techniques for LNOI can be suggested, which comprises self-organized poling via alternating high voltage or bipolar poling in MgO:LNOI. Besides this, one could consider a kind of ferroelectric potential divider. This could be accompanied with a further study of the MgO-doping influence on the poling behavior and since the commercially available samples commonly feature a fixed doping concentration a series of different concentrations could be of interest, also from a theoretical side. Since some of the investigated LNOI samples have been fabricated by e-beam lithography this can be combined with an “electron-beam assisted poling”. The LNOI samples are subsequently subjected to the fabrication of waveguides in the periodically poled regions. For that the established characterization methods should be taken into account to determine the effect of this fabrication process on to the poling respectively the polarity of domains.

Bibliography

[1] Y. Cho, S. Hashimoto, N. Odagawa, K. Tanaka, and Y. Hiranaga, "Nanodomain manipulation for ultrahigh density ferroelectric data storage," *Nanotechnology*, vol. 17, no. 7, 2006, doi: 10.1088/0957-4484/17/7/S06.

[2] R. M. Roth *et al.*, "Integrable wide-free-spectral-range Fabry–Perot optical filters using free-standing LiNbO_3 thin films," *Opt. Lett.*, vol. 30, no. 9, 2005, doi: 10.1364/ol.30.000994.

[3] P. Rabiei and W. H. Steier, "Lithium niobate ridge waveguides and modulators fabricated using smart guide," *Appl. Phys. Lett.*, vol. 86, no. 16, 2005, doi: 10.1063/1.1906311.

[4] Miller Se, "Integrated Optics. Introduction," *Bell Syst. Tech J*, vol. 48, no. 7, 1969, doi: 10.1002/j.1538-7305.1969.tb01165.x.

[5] E. A. J. Marcatili, "Dielectric Rectangular Waveguide and Directional Coupler for Integrated Optics," *Bell Syst. Tech. J.*, vol. 48, no. 7, 1969, doi: 10.1002/j.1538-7305.1969.tb01166.x.

[6] A. Orieux and E. Diamanti, "Recent advances on integrated quantum communications," *Journal of Optics (United Kingdom)*, vol. 18, no. 8. 2016, doi: 10.1088/2040-8978/18/8/083002.

[7] E. Meyer-Scott *et al.*, "High-performance source of spectrally pure, polarization entangled photon pairs based on hybrid integrated-bulk optics," *Opt. Express*, vol. 26, no. 25, 2018, doi: 10.1364/oe.26.032475.

[8] S. E. Harris, M. K. Oshman, and R. L. Byer, "Observation of tunable optical parametric fluorescence," *Phys. Rev. Lett.*, vol. 18, no. 18, 1967, doi: 10.1103/PhysRevLett.18.732.

[9] D. Magde and H. Mahr, "Study in ammonium dihydrogen phosphate of spontaneous parametric interaction tunable from 4400 to 16 000 Â," *Phys. Rev. Lett.*, vol. 18, no. 21, 1967, doi: 10.1103/PhysRevLett.18.905.

[10] R. Ghosh and L. Mandel, "Observation of nonclassical effects in the interference of two photons," *Phys. Rev. Lett.*, vol. 59, no. 17, 1987, doi: 10.1103/PhysRevLett.59.1903.

[11] M. Bock, A. Lenhard, C. Chunnilall, and C. Becher, "Highly efficient heralded single-photon source for telecom wavelengths based on a PPLN waveguide," *Opt. Express*, vol. 24, no. 21, 2016, doi: 10.1364/oe.24.023992.

[12] W. Sohler *et al.*, "Integrated Optical Devices in Lithium Niobate," *Opt. Photonics News*, vol. 19, no. 1, 2008, doi: 10.1364/opn.19.1.000024.

[13] D. Zhu *et al.*, "Integrated photonics on thin-film lithium niobate," *Adv. Opt. Photonics*, vol. 13, no. 2, 2021, doi: 10.1364/aop.411024.

[14] T. Park *et al.*, "High efficiency second harmonic generation of blue light on thin film lithium niobate," 2021.

[15] G. Harder, V. Ansari, B. Brecht, T. Dirmeier, C. Marquardt, and C. Silberhorn, "An optimized photon pair source for quantum circuits," *Opt. Express*, vol. 21, no. 12, 2013, doi: 10.1364/oe.21.013975.

[16] B. Brecht *et al.*, "Demonstration of coherent time-frequency Schmidt mode selection using dispersion-engineered frequency conversion," *Phys. Rev. A - At. Mol. Opt. Phys.*, vol. 90, no. 3, 2014, doi: 10.1103/PhysRevA.90.030302.

[17] A. Boes, B. Corcoran, L. Chang, J. Bowers, and A. Mitchell, "Status and Potential of Lithium Niobate on Insulator (LNOI) for Photonic Integrated Circuits," *Laser and Photonics Reviews*, vol. 12, no. 4. 2018, doi: 10.1002/lpor.201700256.

[18] Y. Qi and L. Yang, "Integrated lithium niobate photonics," *Nanophotonics*, 2020.

[19] K. Kato, "Temperature Insensitive Shg At 0.5321 μM in Ktp," *IEEE J. Quantum Electron.*, vol. 28, no. 10, 1992, doi: 10.1109/3.159505.

[20] V. Ansari *et al.*, "Heralded generation of high-purity ultrashort single photons in programmable temporal shapes," *Opt. Express*, vol. 26, no. 3, 2018, doi: 10.1364/oe.26.002764.

[21] P. Mackwitz, M. Rüsing, G. Berth, A. Widhalm, K. Müller, and A. Zrenner, "Periodic domain inversion in x-cut single-crystal lithium niobate thin film," *Appl. Phys. Lett.*, vol. 108, no. 15, pp. 9–13, 2016, doi: 10.1063/1.4946010.

[22] C. Eigner, L. Padberg, M. Santandrea, H. Herrmann, B. Brecht, and C. Silberhorn, "Spatially single mode photon pair source at 800 nm in periodically poled Rubidium exchanged KTP waveguides," *Opt. Express*, vol. 28, no. 22, 2020, doi: 10.1364/oe.399483.

[23] J. D. Bierlein and H. Vanherzeele, "Potassium titanyl phosphate: properties and new applications," *J. Opt. Soc. Am. B*, vol. 6, no. 4, 1989, doi: 10.1364/josab.6.000622.

[24] H. Karlsson and F. Laurell, "Electric field poling of flux grown KTiOPO4," *Appl. Phys. Lett.*, vol. 71, no. 24, 1997, doi: 10.1063/1.120363.

[25] D. E. Thompson, J. D. McMullen, and D. B. Anderson, "Second-harmonic generation in GaAs 'stack of plates' using high-power CO2 laser radiation," *Appl. Phys. Lett.*, vol. 29, no. 2, 1976, doi: 10.1063/1.88989.

[26] S. J. B. Yoo, "Wavelength conversion technologies for WDM network applications," *J. Light. Technol.*, vol. 14, no. 6, 1996, doi: 10.1109/50.511595.

[27] M. M. Fejer, G. A. Magel, D. H. Jundt, and R. L. Byer, "Quasi-phase-matched second harmonic generation: tuning and tolerances," *IEEE J. Quantum Electron.*, vol. 28, pp. 2631–2654, 1992.

[28] K. F. Kneubühl and M. W. Sigrist, *Laser*, 3rd ed. Teubner, 1991.

[29] Y. V. G. S. Murti and C. Vijayan, *Essentials of Nonlinear Optics*. Chichester: John Wiley & Sons Ltd, 2014.

[30] R. W. Boyd, *Nonlinear Optics*. Academic Press, Elsevier, 2003.

[31] S. Hooker and C. Webb, *Laser Physics*. New York: Oxford University Press, 2010.

[32] H. Hora and Y. R. Shen, "The Principles of Nonlinear Optics," *Laser Part. Beams*, vol. 4, no. 318, p. 576, 1986.

[33] P. N. Butcher and D. Cotter, *The Elements of Nonlinear Optics*. Cambridge University Press, 1990.

[34] W. Voigt, *Lehrbuch der Kristallphysik*. Vieweg+Teubner Verlag, 1966.

[35] R. Masse and J. C. Grenier, “Study of the monophosphates of type M1TiOPO4 where M1=K, Rb and Ti,” *Bull. la Société Française Minéralogie Crystallogr.*, vol. 94, no. 437, 1971.

[36] J. E. Midwinter and J. Warner, “The effects of phase matching method and of uniaxial crystal symmetry on the polar distribution of second-order non-linear optical polarization,” *Brit. J. Appl. Phys.*, vol. 16, no. 1135, 1965.

[37] H. Vanherzele and J. Bierlein, “Magnitude of the nonlinear-optical coefficients of KTiOPO4,” *Opt. Lett.*, vol. 17, no. 14, pp. 982–984, 1992.

[38] I. Shoji, T. Kondo, A. Kitamoto, M. Shirane, and R. Ito, “Absolute scale second-order nonlinear-optical coefficients,” *J. Opt. Soc. Am.*, vol. B14, no. 2268, 1997.

[39] P. Günter, *Nonlinear Optical Effects and Materials*. Springer, 2000.

[40] G. Berth, “Visualisierung ferroelektrischer Domänenstrukturen in Lithiumniobat mittels konfokaler nichtlinearer Mikroskopie,” Universität Paderborn, Dissertation, 2009.

[41] L. E. Myers, R. C. Eckardt, and M. M. Fejer, “Quasi-phase-matched optical parametric oscillators in bulk periodically poled LiNbO3,” *J. Opt. Soc. Am.*, vol. B 12, no. 2102, 1995.

[42] J. Armstrong, “Interactions between Light Waves in a Nonlinear Dielectric,” *Phys. Rev.*, vol. 127, no. 1918, 1962.

[43] P. A. Franken and J. F. Ward, “Optical Harmonics and Nonlinear Phenomena,” *Rev. Mod. Phys.*, vol. 35, no. 23, 1963.

[44] S. Somekh and A. Yariv, “Phase matching by periodic modulation of the nonlinear optical properties,” *Opt. Commun.*, vol. 6, pp. 301–304, 1972.

[45] A. Yariv, *Quantum Electronics*, 2nd ed. John Wiley & Sons, 1975.

[46] A. Arie, “Green and ultraviolet quasi-phase-matched second harmonic generation in bulk periodically-poled KTiOPO4,” *Opt. Commun.*, vol. 142, pp. 265–268, 1997.

[47] A. Räuber, “Chemistry and Physics of Lithium Niobate,” *Curr. Top. Mater. Sci.*, vol. 1, p. 481, 1978.

[48] D. Jundt, “Temperature-dependent Sellmeier equation for the index of refraction, ne, in congruent lithium niobate,” *Opt. Lett.*, vol. 22, no. 20, 1997.

[49] K. Kato and E. Takaoka, “Sellmeier and thermo-optic dispersion formulas for KTP,” *Appl. Opt.*, vol. 41, no. 24, 2002.

[50] G. Wentzel, “Eine Verallgemeinerung der Quantenbedingungen für die Zwecke der Wellenmechanik,” *Zeitschrift für Phys.*, vol. 38, pp. 518–529, 1926.

[51] G. B. Hocker and W. K. Burns, “Mode dispersion in diffused channel waveguides by the effective index method,” *Appl. Opt.*, vol. 16, pp. 113–118, 1977.

[52] F. Brechet, J. Marcou, D. Pagnoux, and P. Roy, “Complete Analysis of the Characteristics of Propagation into Photonic Crystal Fibers, by the Finite Element Method,” *Opt. Fiber Technol.*, vol. 6, no. 2, pp. 181–191, 2000, doi: 10.1006/ofte.1999.0320.

[53] I. Montrosset, E. Strake, and G. P. Bava, “Guided modes of Ti:LiNbO/sub 3/ channel waveguides: a novel quasi-analytical technique in comparison with the scalar finite-element method,” *J. Light. Technol.*, vol. 6, no. 6, pp. 1126–1135, 1988.

[54] M. Bass, P. A. Franken, J. F. Ward, and G. Weinreich, “Optical Rectification,” *Phys. Rev. Lett.*, vol. 9, no. 11, 1962.

[55] P. J. Mosley *et al.*, “Heralded generation of ultrafast single photons in pure quantum states,” *Phys. Rev. Lett.*, vol. 100, no. 13, Apr. 2008, doi: 10.1103/PhysRevLett.100.133601.

[56] M. Fiorentino, S. M. Spillane, R. G. Beausoleil, T. D. Roberts, P. Battle, and M. W. Munro, “Spontaneous parametric down-conversion in periodically poled KTP waveguides and bulk crystals,” *Opt. Express*, vol. 15, no. 12, p. 7479, 2007, doi: 10.1364/oe.15.007479.

[57] M. C. Booth, M. Atatüre, G. Di Giuseppe, and M. C. Saleh, Bahaa E. A. Sergienko, Alexander V. Teich, “Counterpropagating entangled photons from a waveguide with periodic nonlinearity,” *Phys. Rev. A*, vol. 66, no. 023815, 2002.

[58] L. Lanco *et al.*, “Semiconductor waveguide source of counterpropagating twin photons,” *Phys. Rev. Lett.*, vol. 97, no. 17, 2006, doi: 10.1103/PhysRevLett.97.173901.

[59] D. Meschede, *Optik, Licht und Laser*, 3rd ed. Vieweg+Teubner Verlag, 2008.

[60] C. Eigner, “Private Communication.” 2018.

[61] V. V. Tuchin, “Second Harmonic Generation Imaging, Francesco S. Pavone and Paul J. Campagnola (Eds). CRC Press, Boca Raton, FL, 2013, 476 pages. ISBN 978-1439849149.,” *Microsc. Microanal.*, vol. 20, no. 4, 2014, doi: 10.1017/s1431927614000907.

[62] E. Timurdogan, C. V. Poulton, M. J. Byrd, and M. R. Watts, “Electric field-induced second-order nonlinear optical effects in silicon waveguides,” *Nat. Photonics*, vol. 11, no. 3, 2017, doi: 10.1038/nphoton.2017.14.

[63] B. Fan, Z. Duan, L. Zhou, C. Yuan, Z. Y. Ou, and W. Zhang, “Generation of a single-photon source via a four-wave mixing process in a cavity,” *Phys. Rev. A - At. Mol. Opt. Phys.*, vol. 80, no. 6, 2009, doi: 10.1103/PhysRevA.80.063809.

[64] H. Takesue and K. Inoue, “Generation of polarization-entangled photon pairs and violation of Bell’s inequality using spontaneous four-wave mixing in a fiber loop,” *Phys. Rev. A - At. Mol. Opt. Phys.*, vol. 70, no. 3, 2004, doi: 10.1103/PhysRevA.70.031802.

[65] E. Cumberbatch, “Self-focusing in non-linear optics,” *IMA J. Appl. Math. (Institute Math. Its Appl.*, vol. 6, no. 3, 1970, doi: 10.1093/imamat/6.3.250.

[66] A. Bussmann-Holder and N. Dalal, “Order/disorder versus or with displacive dynamics in ferroelectric systems,” *Struct. Bond.*, vol. 124, 2006, doi: 10.1007/430_2006_045.

[67] M. Trainer, “Ferroelectrics and the Curie-Weiss law,” *Eur. J. Phys.*, vol. 21, pp. 459–464, 2000.

[68] M. Satyanarayan and E. Al., “Potassium Titanyl Phosphate and Its Isomorphs: Growth, Properties, and Applications,” *Crit. Rev. Solid State Mater. Sci.*, vol. 24, pp. 103–191, 1999.

[69] D. N. Nikogosjan, *Nonlinear Optical Crystals: A Complete Survey*. New York: Springer, 2005.

[70] J. Valasek, “Piezo-electric and allied phenomena in rochelle salt,” *Phys. Rev.*, vol. 17, no. 4, pp. 475–481, 1921.

[71] S. C. Abrahams and P. Marsh, “Defect structure dependence on composition on lithium niobate,” *Acta Cryst. B*, vol. 42, no. 61, 1986.

[72] R. S. Weis and T. K. Gaylord, “Lithium niobate: Summary of physical properties and crystal structure,” *Appl. Phys. A Solids Surfaces*, vol. 37, no. 4, pp. 191–203, 1985, doi: 10.1007/BF00614817.

[73] S. Sanna and W. G. Schmidt, “Ferroelectric phase transition in LiNbO3: Insights from molecular dynamics,” *IEEE Trans.*, vol. 59, no. 9, 2012.

[74] M. Roth, *Stoichiometry and Domain Structure of KTP-Type Nonlinear Optical Crystals*. Springer Handbook of Crystal Growth, 2010.

[75] N. Voronkova and I. Sorokina, “Structure and Properties of Crystals in the Potassium Titanyl Phosphate Family: A Review,” *Crystallogr. Rep.*, vol. 52, pp. 82–95, 2007.

[76] F. C. Zumsteg, J. D. Bierlein, and T. E. Gier., “KxRb1-xTiOPO4: A new nonlinear optical material,” *J. Appl. Phys.*, vol. 47, pp. 4980–4985, 1976.

[77] D. Xue and S. Zhang, “The origin of nonlinearity in KTiOPO4,” *Appl. Phys. Lett.*, vol. 70, pp. 943–945, 1997.

[78] W. Känzig, *Solid State Physics: Advances in Research and Applications*, 4th ed. Academic Press, 1957.

[79] M. E. Lines and A. M. Glass, *Principles and Applications of Ferroelectrics and Related Materials*. OXFORD UNIV PR, 2010.

[80] J. Guyonnet, *Ferroelectric Domain Walls*. Switzerland: Springer Theses, 2014.

[81] C. Canalias, J. Hirohashi, V. Pasiskevicius, and F. Laurell, “Polarization-switching characteristics of flux-grown KTiOPO4 and RbTiOPO4 at room temperature,” *J. Appl. Phys.*, vol. 97, no. 12, 2005, doi: 10.1063/1.1940135.

[82] D. H. Jundt, G. A. Magel, M. M. Fejer, and R. L. Byer, “Periodically poled LiNbO3 for high-efficiency second-harmonic generation,” *Appl. Phys. Lett.*, vol. 59, no. 21, 1991, doi: 10.1063/1.105929.

[83] C. Eigner, “Periodically Poled Waveguides in Potassium Titanyl Phosphate for Applications in Quantum Optics,” Universität Paderborn, Dissertation, 2019.

[84] C. Eigner, “Untersuchung der Polungseigenschaften von oberflächennah Ti-diffusionsdotiertem, kongruentem Lithiumniobat,” Universität Paderborn, Bachelor thesis, 2011.

[85] V. Gopalan and M. C. Gupta, “Origin and characteristics of internal fields in LiNbO3 crystals,” *Ferroelectrics*, vol. 198, no. 1–4, 1997, doi: 10.1080/00150199708228337.

[86] P. Mackwitz, “Nonlinear analysis of periodically poled waveguides in KTP: A fundamental study,” Universität Paderborn, Master thesis, 2017.

[87] M. Younesi, R. Geiss, S. Rajaee, F. Setzpfandt, Y.-H. Chen, and T. Pertsch, “Periodic poling with a micrometer-range period in thin-film lithium niobate on insulator,” *J. Opt. Soc. Am. B*, vol. 38, no. 3, 2021, doi: 10.1364/josab.414298.

[88] A. Boulle, C. Restoin, C. Darraud-Taupiac, R. Guinebretière, and A. Dauger, "Structural characterization using X-ray diffraction of Ti indiffused periodically poled LiNbO3 fabricated by direct electron beam bombardment," *Ferroelectr. Lett. Sect.*, vol. 30, no. 5–6, 2003, doi: 10.1080/07315170390274605.

[89] A. C. Muir *et al.*, "Direct-writing of inverted domains in lithium niobate using a continuous wave ultra violet laser," *Opt. Express*, vol. 16, no. 4, 2008, doi: 10.1364/oe.16.002336.

[90] I. T. Wellington, C. E. Valdivia, T. J. Sono, C. L. Sones, S. Mailis, and R. W. Eason, "Ordered nano-scale domains in lithium niobate single crystals via phase-mask assisted all-optical poling," *Appl. Surf. Sci.*, vol. 253, no. 9, 2007, doi: 10.1016/j.apsusc.2006.09.018.

[91] G. Rosenman, P. Urenski, A. Agronin, Y. Rosenwaks, and M. Molotskii, "Submicron ferroelectric domain structures tailored by high-voltage scanning probe microscopy," *Appl. Phys. Lett.*, vol. 82, no. 1, 2003, doi: 10.1063/1.1534410.

[92] A. C. Busacca, C. L. Sones, R. W. Eason, and S. Mailis, "First-order quasi-phase-matched blue light generation in surface-poled Ti:indiffused lithium niobate waveguides," *Appl. Phys. Lett.*, vol. 84, no. 22, 2004, doi: 10.1063/1.1758776.

[93] S. Nagano, M. Konishi, T. Shiomi, and M. Minakata, "Study on Formation of Small Polarization Domain Inversion for High-Efficiency Quasi-Phase-Matched Second-Harmonic Generation Device," *Jpn. J. Appl. Phys.*, vol. 42, p. 4334, 2003.

[94] K. Kintaka, M. Fujimura, T. Suhara, and H. Nishihara, "Fabrication of ferroelectric-domain-inverted gratings in LiNbO3 by applying voltage using etched-Si stamper electrode," *Electron. Lett.*, vol. 34, no. 9, 1998, doi: 10.1049/el:19980645.

[95] A. C. G. Nutt, V. Gopalan, and M. C. Gupta, "Domain inversion in LiNbO3 using direct electron-beam writing," *Appl. Phys. Lett.*, vol. 60, no. 23, 1992, doi: 10.1063/1.106837.

[96] D. Lee *et al.*, "Mixed Bloch-Néel-Ising character of 180°ferroelectric domain walls," *Phys. Rev. B - Condens. Matter Mater. Phys.*, vol. 80, no. 6, 2009, doi: 10.1103/PhysRevB.80.060102.

[97] H. D. Megaw, "A note on the structure of lithium niobate, LiNbO3," *Acta Crystallogr. Sect. A*, vol. 24, no. 6, 1968, doi: 10.1107/S0567739468001282.

[98] N. Niizeki, T. Yamada, and H. Toyoda, "Growth ridges, etching hillocks, an crystal structure of lithium niobate," *Jpn. J. Appl. Phys.*, vol. 24, no. 318, 1967.

[99] S. C. Abrahams, H. J. Levinstein, and J. M. Reddy, "Ferroelectric lithium niobate. 5. Polycrystal X-ray diffraction study between 24° and 1200°C," *J. Phys. Chem. Solids*, vol. 27, no. 6–7, 1966, doi: 10.1016/0022-3697(66)90074-6.

[100] S. C. Abrahams, W. C. Hamilton, and J. M. Reddy, "Ferroelectric lithium niobate. 4. Single crystal neutron diffraction study at 24°C," *J. Phys. Chem. Solids*, vol. 27, no. 6–7, 1966, doi: 10.1016/0022-3697(66)90073-4.

[101] S. C. Abrahams, J. M. Reddy, and J. L. Bernstein, "Ferroelectric lithium niobate. 3. Single crystal X-ray diffraction study at 24°C," *J. Phys. Chem. Solids*, vol. 27, no. 6–7, 1966, doi: 10.1016/0022-3697(66)90072-2.

[102] K. Nassau, H. J. Levinstein, and G. M. Loiacono, "Ferroelectric lithium niobate. 2. Preparation of single domain crystals," *J. Phys. Chem. Solids*, vol. 27, no. 6–7, 1966, doi: 10.1016/0022-3697(66)90071-0.

[103] K. Nassau, H. J. Levinstein, and G. M. Loiacono, “Ferroelectric lithium niobate. 1. Growth, domain structure, dislocations and etching,” *J. Phys. Chem. Solids*, vol. 27, no. 6–7, 1966, doi: 10.1016/0022-3697(66)90070-9.

[104] B. T. Matthias and J. P. Remeika, “Ferroelectricity in the ilmenite structure,” *Physical Review*, vol. 76, no. 12. 1949, doi: 10.1103/PhysRev.76.1886.2.

[105] T. Volk and M. Wöhlecke, “Lithium niobate: Defects, photorefraction and ferroelectric switching,” in *Springer Series in Materials Science*, vol. 115, 2009.

[106] J. R. Carruthers, G. E. Peterson, M. Grasso, and P. M. Bridenbaugh, “Nonstoichiometry and crystal growth of lithium niobate,” *J. Appl. Phys.*, vol. 42, no. 5, 1971, doi: 10.1063/1.1660455.

[107] H. M. O’Bryan, P. K. Gallagher, and C. D. Brandle, “Characterization of LiNbO3 by Dilatometry and DTA,” *J. Am. Ceram. Soc.*, vol. 68, no. 3, 1985.

[108] Y. L. Chen, J. J. Xu, X. J. Chen, Y. F. Kong, and G. Y. Zhang, “Domain reversion process in near-stoichiometric LiNbO3 crystals,” *Opt. Commun.*, vol. 188, no. 5–6, 2001, doi: 10.1016/S0030-4018(00)01137-8.

[109] S. T. Popescu, A. Petris, and V. I. Vlad, “Interferometric measurement of the pyroelectric coefficient in lithium niobate,” *J. Appl. Phys.*, vol. 113, no. 4, 2013, doi: 10.1063/1.4788696.

[110] Y. Kondo *et al.*, “An increase of more than 30% in the electrooptic coefficients of Fe-doped and Ce-doped stoichiometric LiNbO3 crystals,” *Japanese J. Appl. Physics, Part 1 Regul. Pap. Short Notes Rev. Pap.*, vol. 39, no. 3 B, 2000, doi: 10.1143/jjap.39.1477.

[111] G. J. Edwards and M. Lawrence, “A temperature-dependent dispersion equation for congruently grown lithium niobate,” *Opt. Quantum Electron.*, vol. 16, no. 4, 1984, doi: 10.1007/BF00620081.

[112] A. Grisard, E. Lallier, K. Polgár, and Á. Péter, “Low electric field periodic poling of thick stoichiometric lithium niobate,” *Electron. Lett.*, vol. 36, no. 12, 2000, doi: 10.1049/el:20000741.

[113] C. Liao, H. M. Chang, and B. H. Yang, “Scenario of electropoling on the molecular scale within a stoichiometric lithium niobate,” *J. Appl. Phys.*, vol. 102, no. 8, 2007, doi: 10.1063/1.2800997.

[114] D. A. Bryan, R. Gerson, and H. E. Tomaschke, “Increased optical damage resistance in lithium niobate,” *Appl. Phys. Lett.*, vol. 44, no. 9, 1984, doi: 10.1063/1.94946.

[115] R. Sommerfeld, “Der Einfluss weiterer Verunreinigungen auf das photorefraktive Verhalten Fe-dotierter LiNbO3-Kristalle,” Universität Osnabrück, Dissertation, 1989.

[116] M. L. Ouvrard, “Recherches sur les phosphate double de titane, d’étain et de cuivre,” *Comptes Rendus*, vol. 111, pp. 177–179, 1890.

[117] G. Hansson, H. Karlsson, S. Wang, and F. Laurell, “Transmission measurements in KTP and isomorphic compounds,” *Appl. Opt.*, vol. 39, no. 27, 2000, doi: 10.1364/ao.39.005058.

[118] M. Rüsing, C. Eigner, P. Mackwitz, G. Berth, C. Silberhorn, and A. Zrenner, “Identification of ferroelectric domain structure sensitive phonon modes in potassium titanyl phosphate: A fundamental study,” *J. Appl. Phys.*, vol. 119, no. 4, 2016, doi: 10.1063/1.4940964.

[119] O. Driesner, “Vergrabene Lichtwellenleiter in Kalium Titanyl Phosphat,” Paderborn University MA thesis, 2014.

[120] G. Rosenman, A. Skliar, D. Eger, M. Oron, and M. Katz, "Low temperature periodic electrical poling of flux-grown KTiOPO4 and isomorphic crystals," *Appl. Phys. Lett.*, vol. 73, no. 25, 1998, doi: 10.1063/1.122851.

[121] Q. Jiang, M. N. Womersley, P. A. Thomas, J. P. Rourke, K. B. Hutton, and R. C. Ward, "Ferroelectric, conductive, and dielectric properties of KTiOPO4 at low temperature," *Phys. Rev. B - Condens. Matter Mater. Phys.*, vol. 66, no. 9, 2002.

[122] Q. Jiang, P. A. Thomas, K. B. Hutton, and R. C. C. Ward, "Rb-doped potassium titanyl phosphate for periodic ferroelectric domain inversion," *J. Appl. Phys.*, vol. 92, no. 5, 2002, doi: 10.1063/1.1496125.

[123] G. Gashurov and R. F. Belt, "Tunable Solid State Lasers for Remote Sensing," *Springer Berlin*, 1985.

[124] G. M. Loiacono, D. N. Loiacono, T. McGee, and M. Babb, "Laser damage formation in KTiOPO4 and KTiOAsO4 crystals: Grey tracks," *J. Appl. Phys.*, vol. 72, no. 7, 1992, doi: 10.1063/1.351520.

[125] Q. Zhang, G. Feng, J. Han, B. Li, Q. Zhu, and X. Xie, "High repetition rate laser pulse induced damage in KTP crystal: Gray-tracking and catastrophic damage," *Optik (Stuttg).*, vol. 122, no. 15, 2011, doi: 10.1016/j.ijleo.2010.06.051.

[126] B. Boulanger, I. Rousseau, J. P. Feve, and E. Al, "Optical studies of laser-induced graytracking in KTP," *IEEE J. Quantum Electron.*, vol. 35, pp. 281–286, 1999.

[127] P. Urenski and G. Rosenman, "Pyroelectric effect in KTiOPO4 and family crystals with monodomain and domain patterned structures," *J. Phys. D. Appl. Phys.*, vol. 33, no. 16, 2000, doi: 10.1088/0022-3727/33/16/320.

[128] J. Bierlein and C. Arweiler, "Electro-optic and dieelectric properties of KTiOPO4," *J. Phys. Chem. Solids*, vol. 60, pp. 1983–1988, 1999.

[129] M. E. Hagerman and K. R. Poeppelmeier, "Review of the Structure and Processing-Defect-Property Relationships of Potassium Titanyl Phosphate: A Strategy for Novel Thin-Film Photonic Devices," *Chem. Mater.*, vol. 7, no. 4, 1995, doi: 10.1021/cm00052a004.

[130] A. H. Reshak, I. V. Kityk, and S. Auluck, "Investigation of the linear and nonlinear optical susceptibilities of KTiOPO4 single crystals: Theory and experiment," *J. Phys. Chem. B*, vol. 114, no. 50, 2010, doi: 10.1021/jp1072878.

[131] K. Okamoto, *Fundamentals of Optical Waveguides*, 2nd ed. Academic Press (Elsevier, Inc.), 2006.

[132] L. Gui, "Periodically Poled Ridge Waveguides and Photonic Wires in LiNbO3 for Efficient Nonlinear Interactions," Universität Paderborn, Dissertation, 2010.

[133] T. Suhara and M. Fujimura, *Waveguide Nonlinear-Optic Devices*. Springer, 2003.

[134] R. V. Schmidt and I. P. Kaminow, "Metal-diffused optical waveguides in LiNbO3," *Appl. Phys. Lett.*, vol. 25, no. 458, 1974.

[135] W. Bierlein, J., Ferretti, A., Brixner, L., and Hsu, "Fabrication and characterization of optical waveguides in KTiOPO4," *Appl. Phys. Lett.*, vol. 18, pp. 1216–1218, 1987.

[136] G. Laurell, F., Calmano, T., Müller, S., Zeil, P., Canalias, C., Huber, "Laser-written waveguides in KTP for broadband Type II second harmonic generation," *Opt. Express*, vol. 20, no. 22308–22313, 2012.

[137] A. Zhang, L., Chandler, P., Townsend, P., Alwahabi, Z., McCaffery, "Second-harmonic generation in ion-implanted KTiOPO4 planar waveguides," *Electron. Lett.*, vol. 16, no. 1478, 1992.

[138] T. Umeki, O. Tadanaga, and M. Asobe, "Highly Efficient Wavelength Converter Using Direct-Bonded PPZnLN Ridge Waveguide," *IEEE J. Quantum Electron.*, vol. 46, no. 1206–1213, 2010.

[139] H. Hu, R. Ricken, and W. Sohler, "Etching of Lithium Niobate: From Ridge Waveguides to Photonic Crystal Structures," 2008.

[140] M. Yamada, N. Nada, M. Saitoh, and K. Watanabe, "First-order quasi-phase matched LiNbO3 waveguide periodically poled by applying an external field of efficient blue second harmonic generation," *Appl. Phys. Lett.*, vol. 62, no. 435, 1993.

[141] J.-H. Zhao, X.-F. Qin, and F.-X. Wang, "Thermal annealing property of KTiOPO4 planar and ridge waveguides formed by MeV Si ion implantation," *Opt. Mater. Express*, vol. 3, no. 426, 2013.

[142] C. Chen, C. E. Rüter, and M. F. Volk, "Second harmonic generation of diamond-blade diced KTiOPO4 ridge waveguides," *Opt. Express*, vol. 24, no. 16434, 2016.

[143] G. Schreiber, "Quasi-phasenangepaßte Frequenzkonversion mit periodisch gepolten Ti:LiNbO3 Wellenleitern," Universität Paderborn, Dissertation, 2001.

[144] R. Brinkmann, "Integriert optische Verstärker in Erbium-dotiertem LiNbO3," Universität Paderborn, Dissertation, 1994.

[145] L. Padberg, "Tailored Devices for Integrated Quantum Photonics," Universität Paderborn, Dissertation, 2022.

[146] M. F. Volk, S. Suntsov, C. E. Rüter, and D. Kip, "Low loss ridge waveguides in lithium niobate thin films by optical grade diamond blade dicing," *Opt. Express*, vol. 24, no. 2, 2016, doi: 10.1364/oe.24.001386.

[147] R. Wu *et al.*, "Long low-loss-litium niobate on insulator waveguides with sub-nanometer surface roughness," *Nanomaterials*, vol. 8, no. 11, 2018, doi: 10.3390/nano8110910.

[148] H. Hu, R. Ricken, W. Sohler, and R. B. Wehrspohn, "Lithium niobate ridge waveguides fabricated by wet etching," *IEEE Photonics Technol. Lett.*, vol. 19, no. 6, 2007, doi: 10.1109/LPT.2007.892886.

[149] L. Cai, Y. Wang, and H. Hu, "Low-loss waveguides in a single-crystal lithium niobate thin film," *Opt. Lett.*, vol. 40, no. 13, 2015, doi: 10.1364/ol.40.003013.

[150] D. Homoelle, S. Wielandy, A. L. Gaeta, N. F. Borrelli, and C. Smith, "Infrared photosensitivity in silica glasses exposed to femtosecond laser pulses," *Opt. Lett.*, vol. 24, no. 18, 1999, doi: 10.1364/ol.24.001311.

[151] L. Padberg *et al.*, "Characterisation of width-dependent diffusion dynamics in rubidium-exchanged KTP waveguides," *Opt. Express*, vol. 28, no. 17, p. 24353, 2020, doi: 10.1364/oe.397074.

[152] M. Minsky, "Microscopy apparatus," *US Pat. 3,013,467*, no. 3013467, 1961.

[153] K. Weber, "Device for Optically scanning the object in a microscope," US-patent 3518014, 1967.

[154] C. J. R. Sheppard and A. Choudhury, “Image formation in the scanning microscope,” *Opt. Acta (Lond).*, vol. 24, no. 10, 1977, doi: 10.1080/713819421.

[155] Ulrich Kubitschek, *Fluorescence Microscopy From Principles to Biological Applications*, 2nd ed. Wiley-VCH Verlag GmbH & Co. KGaA, Weinheim, 2017.

[156] T. Wilson, *Confocal Microscopy*. London: Academic Press, 1990.

[157] E. Wolf, “Light distribution near focus in an error-free diffraction image,” *Proc. R. Soc. London. Ser. A. Math. Phys. Sci.*, vol. 204, no. 1079, pp. 533–548, 1951, doi: 10.1098/rspa.1951.0010.

[158] M. Born and E. Wolf, “Principles of Optics: Electromagnetic theory of propagation, interference and diffraction of light.” Cambridge University Press, 1999.

[159] H. Beyer, *Handbuch der Mikroskopie*. Berlin: VEB Verlag Technik, 1989.

[160] Olympus-Corporation, “OLS4000 - Ultimate Measurement Performance (Brochure).” 2009.

[161] Z. H. Amber, B. Kirbus, L. M. Eng, and M. Rüsing, “Quantifying the coherent interaction length of second-harmonic microscopy in lithium niobate confined nanostructures,” *J. Appl. Phys.*, vol. 130, no. 13, 2021, doi: 10.1063/5.0058996.

[162] C. V. Raman, “A new radiation,” *Proc. Indian Acad. Sci. - Sect. A*, vol. 2, pp. 387–398, 1928.

[163] B. R. Masters, “C.V. Raman and the Raman Effect,” *Opt. Photonics News*, vol. 20, no. 3, p. 40, 2009.

[164] A. Smekal, “Zur Quantentheorie der Streuung und Dispersion,” *Naturwissenschaften*, vol. 16, no. 31, pp. 612–613, 1923.

[165] W. Demtröder, *Laserspektroskopie*, 4th ed. Heidelberg, Berlin: Springer, 2007.

[166] A. Anderson, “The Raman Effect, Vol. 1 Principles,” *Marcel Dekker, Inc., New York*, vol. 1, 1971, doi: 10.1002/ange.19730851418.

[167] H. Kuzmany, *Solid-State Spectroscopy*. Heidelberg, Berlin: Springer, 2009.

[168] F. Shimura, “Refractive indices of LiNb1-yTayO3 single crystals,” *J. Cryst. Growth*, vol. 42, no. C, 1977, doi: 10.1016/0022-0248(77)90250-0.

[169] D. Wieboldt and R. Heintz, “Fundamentals of Raman Polarization Microscopy! Application Note 52792.” Thermo Fisher Scientific, Madison, WI, 2016.

[170] P. Tonndorf *et al.*, “Photoluminescence emission and Raman response of monolayer MoS2, MoSe2, and WSe2,” *Opt. Express*, vol. 21, no. 4, 2013, doi: 10.1364/oe.21.004908.

[171] A. M. Weiner, *Ultrafast Optics*. Hoboken: John Wiley & Sons, Inc., 2009.

[172] B. Wilhelmi, W. Rudolph, E. Döpel, and W. Dietel, “Advantages and limits of light pulse compression inside and outside the laser cavity,” *Opt. Acta (Lond).*, vol. 32, no. 9–10, 1985, doi: 10.1080/713821850.

[173] A. Widhalm, C. Golla, N. Weber, P. Mackwitz, A. Zrenner, and C. Meier, “Electric-field-induced second harmonic generation in silicon dioxide,” *Opt. Express*, vol. 30, no. 4, 2022, doi: 10.1364/oe.443489.

[174] K. J. Spychala, P. Mackwitz, A. Widhalm, G. Berth, and A. Zrenner, “Spatially resolved light field analysis of the second-harmonic signal of χ(2)-materials in the tight focusing regime,” *J. Appl. Phys.*, vol. 127, no. 2, 2020, doi: 10.1063/1.5133476.

[175] I. J. Cooper, M. Roy, and C. J. R. Sheppard, “Focusing of pseudoradial polarized beams,” *Opt. Express*, vol. 13, no. 4, 2005.

[176] B. Hecht and L. Novotny, *Principles of Nano-Optics*. Cambridge University Press, 2006.

[177] O. Haeberlé, M. Ammar, H. Furukawa, K. Tenjimbayashi, and P. Török, “Point spread function of optical microscopes imaging through stratified media,” *Opt. Express*, vol. 11, no. 22, pp. 2964–2969, 2003.

[178] M. J. Woehl and J. C. Nasse, “Realistic modeling of the illumination point spread function in confocal scanning optical microscopy,” *J. Opt. Soc. Am. A*, vol. 27, no. 2, pp. 295–302, 2010.

[179] S. Cherifi-Hertel *et al.*, “Non-Ising and chiral ferroelectric domain walls revealed by nonlinear optical microscopy,” *Nat. Commun.*, vol. 8, 2017, doi: 10.1038/ncomms15768.

[180] J. Kaneshiro, S. Kawado, H. Yokota, Y. Uesu, and T. Fukui, “Three-dimensional observations of polar domain structures using a confocal second-harmonic generation interference microscope,” *J. Appl. Phys.*, vol. 104, no. 5, 2008, doi: 10.1063/1.2975218.

[181] M. Rüsing, J. Zhao, and S. Mookherjea, “Second harmonic microscopy of poled x-cut thin film lithium niobate: Understanding the contrast mechanism,” *J. Appl. Phys.*, vol. 126, no. 11, 2019, doi: 10.1063/1.5113727.

[182] X. Huang *et al.*, “Second-harmonic interference imaging of ferroelectric domains through a scanning microscope,” *J. Phys. D. Appl. Phys.*, vol. 50, no. 48, 2017, doi: 10.1088/1361-6463/aa9258.

[183] K. J. Spychala *et al.*, “Nonlinear focal mapping of ferroelectric domain walls in LiNbO3 : Analysis of the SHG microscopy contrast mechanism,” *J. Appl. Phys.*, vol. 128, no. 23, p. 234102, 2020, doi: 10.1063/5.0025284.

[184] S. A. Denev, T. T. A. Lummen, E. Barnes, A. Kumar, and V. Gopalan, “Probing ferroelectrics using optical second harmonic generation,” *J. Am. Ceram. Soc.*, vol. 94, no. 9, 2011, doi: 10.1111/j.1551-2916.2011.04740.x.

[185] G. Berth, V. Quiring, W. Sohler, and A. Zrenner, “Depth-resolved analysis of ferroelectric domain structures in Ti:PPLN waveguides by nonlinear confocal laser scanning microscopy,” in *Ferroelectrics*, 2007, vol. 352, no. 1 PART 2, doi: 10.1080/00150190701358159.

[186] M. Flörsheimer *et al.*, “Second-harmonic imaging of ferroelectric domains in LiNbO3 with micron resolution in lateral and axial directions,” *Appl. Phys. B Lasers Opt.*, vol. 67, no. 5, 1998, doi: 10.1007/s003400050552.

[187] M. Ayoub, J. Imbrock, and C. Denz, “Ferroelectric domain diagnostics near the phase transition by Čerenkov second-harmonic generation,” *Opt. Mater. Express*, vol. 7, no. 9, 2017, doi: 10.1364/ome.7.003448.

[188] T. Kämpfe *et al.*, “Optical three-dimensional profiling of charged domain walls in ferroelectrics by Cherenkov second-harmonic generation,” *Phys. Rev. B - Condens. Matter Mater. Phys.*, vol. 89, no. 3, 2014, doi: 10.1103/PhysRevB.89.035314.

[189] T. Kämpfe, P. Reichenbach, A. Haußmann, T. Woike, E. Soergel, and L. M. Eng, "Real-time three-dimensional profiling of ferroelectric domain walls," *Appl. Phys. Lett.*, vol. 107, no. 15, 2015, doi: 10.1063/1.4933171.

[190] R. Dorn, S. Quabis, and G. Leuchs, "Sharper focus for a radially polarized light beam," *Phys. Rev. Lett.*, vol. 91, no. 23, 2003, doi: 10.1103/PhysRevLett.91.233901.

[191] S. I. Bozhevolnyi et al., "Second-harmonic imaging of ferroelectric domain walls," *Appl. Phys. Lett.*, vol. 73, no. 13, 2011.

[192] A. S. Barker and R. Loudon, "Dielectric properties and optical phonons in LiNbO3," *Phys. Rev.*, vol. 158, no. 2, 1967, doi: 10.1103/PhysRev.158.433.

[193] M. D. Fontana and P. Bourson, "Microstructure and defects probed by Raman spectroscopy in lithium niobate crystals and devices," *Applied Physics Reviews*, vol. 2, no. 4. 2015, doi: 10.1063/1.4934203.

[194] R. Claus, L. Steffan, and E. Wlesendanger, "Directional Dispersion and Assignment of Optical Phonons in LiNbO3," *Zeitschrift fur Naturforsch. - Sect. A J. Phys. Sci.*, vol. 27, no. 8–9, 1972, doi: 10.1515/zna-1972-8-904.

[195] B. Mihailova, I. Savatinova, I. Savova, and L. Konstantinov, "Modeling of Raman spectra of H:LiNbO3," *Solid State Commun.*, vol. 116, no. 1, 2000, doi: 10.1016/S0038-1098(00)00275-1.

[196] S. Margueron *et al.*, "Resolved E-symmetry zone-centre phonons in LiTaO 3 and LiNbO 3," in *Journal of Applied Physics*, 2012, vol. 111, no. 10, doi: 10.1063/1.4716001.

[197] P. Hermet, M. Veithen, and P. Ghosez, "First-principles calculations of the nonlinear optical susceptibilities and Raman scattering spectra of lithium niobate," in *Journal of Physics Condensed Matter*, 2007, vol. 19, no. 45, doi: 10.1088/0953-8984/19/45/456202.

[198] Y. Y. Li, H. L. Chen, G. J. Chen, C. L. Kuo, P. H. Hsieh, and W. S. Hwang, "Investigation of the defect structure of congruent and Fe-Doped LiNbO3 powders synthesized by the combustion method," *Materials (Basel).*, vol. 10, no. 4, 2017, doi: 10.3390/ma10040380.

[199] M. Rüsing, "In Depth Raman Analysis of the Ferroelectrics KTiOPO4 and LiNbO3 — Role of Domain Boundaries and Defects," Universität Paderborn, Dissertation, 2018.

[200] S. Sanna, S. Neufeld, M. Rüsing, G. Berth, A. Zrenner, and W. G. Schmidt, "Raman scattering efficiency in LiTaO3 and LiNbO3 crystals," *Phys. Rev. B*, vol. 91, no. 22, 2015.

[201] G. H. Watson, "Polarized Raman spectra of ktioaso4 and isomorphic nonlinear-optical crystals," *J. Raman Spectrosc.*, vol. 22, no. 11, 1991, doi: 10.1002/jrs.1250221116.

[202] G. E. Kugel *et al.*, "The vibrational spectrum of a KTiOPO4 single crystal studied by raman and infrared reflectivity spectroscopy," *J. Phys. C Solid State Phys.*, vol. 21, no. 32, 1988, doi: 10.1088/0022-3719/21/32/011.

[203] I. Tordjman, R. Masse, and J. C. Guitel, "Structure cristalline du monophosphate KTiPO5," *Zeitschrift fur Krist. - New Cryst. Struct.*, vol. 139, no. 1–2, 1974, doi: 10.1524/zkri.1974.139.1-2.103.

[204] R. V. Pisarev, R. Farhi, P. Moch, and V. I. Voronkova, "Temperature dependence of Raman scattering and soft modes in TlTiOPO 4," *J. Phys. Condens. Matter*, vol. 2, no. 37, 1990, doi: 10.1088/0953-8984/2/37/001.

[205] M. Rüsing *et al.*, “Imaging of 180 ferroelectric domain walls in uniaxial ferroelectrics by confocal Raman spectroscopy: Unraveling the contrast mechanism,” *Phys. Rev. Mater.*, vol. 2, no. 10, pp. 1–16, 2018, doi: 10.1103/PhysRevMaterials.2.103801.

[206] G. Berth, W. Hahn, V. Wiedemeier, A. Zrenner, S. Sanna, and W. G. Schmidt, “Imaging of the ferroelectric domain structures by confocal raman spectroscopy,” in *Ferroelectrics*, 2011, vol. 420, no. 1, doi: 10.1080/00150193.2011.594774.

[207] M. D. Fontana, R. Hammoum, P. Bourson, S. Margueron, and V. Y. Shur, “Raman probe on PPLN microstructures,” in *Ferroelectrics*, 2008, vol. 373, no. 1 PART 1, doi: 10.1080/00150190802408598.

[208] R. Hammoum, M. D. Fontana, P. Bourson, and V. Y. Shur, “Characterization of PPLN-microstructures by means of Raman spectroscopy,” *Appl. Phys. A Mater. Sci. Process.*, vol. 91, no. 1, 2008, doi: 10.1007/s00339-007-4356-3.

[209] J. Brockmeier *et al.*, “Non-Invasive Visualization of Ferroelectric Domain Structures on the Non-Polar y-Surface of KTiOPO4 via Raman Imaging,” *Crystals*, vol. 11, no. 1086, pp. 1–12, 2021, doi: 10.3390/cryst11091086.

[210] J. Hellström, R. Clemens, V. Pasiskevicius, H. Karlsson, and F. Laurell, “Real-time and in situ monitoring of ferroelectric domains during periodic electric field poling of KTiOPO4,” *J. Appl. Phys.*, vol. 90, no. 3, 2001, doi: 10.1063/1.1382830.

[211] H. Karlsson, F. Laurell, and L. K. Cheng, “Periodic poling of RbTiOPO4 for quasi-phase matched blue light generation,” *Appl. Phys. Lett.*, vol. 74, no. 11, 1999, doi: 10.1063/1.123602.

[212] E. Fatuzzo and W. J. Merz, *Ferroelectricity*. Amsterdam: North-Holland, 1967.

[213] V. Y. Shur, A. R. Akhmatkhanov, and I. S. Baturin, “Micro- and nano-domain engineering in lithium niobate,” *Applied Physics Reviews*, vol. 2, no. 4. 2015, doi: 10.1063/1.4928591.

[214] C. Canalias and V. Pasiskevicius, “Mirrorless optical parametric oscillator,” *Nat. Photonics*, vol. 1, no. 8, 2007, doi: 10.1038/nphoton.2007.137.

[215] C. Canalias, V. Pasiskevicius, and F. Laurell, “Periodic poling of KTiOPO4: From micrometer to sub-micrometer domain gratings,” in *Ferroelectrics*, 2006, vol. 340, no. 1 PART 1, doi: 10.1080/00150190600888686.

[216] V. Gopalan, V. Dierolf, and D. A. Scrymgeour, “Defect-domain wall interactions in trigonal ferroelectrics,” *Annual Review of Materials Research*, vol. 37. 2007, doi: 10.1146/annurev.matsci.37.052506.084247.

[217] T. Jach, S. Kim, V. Gopalan, S. Durbin, and D. Bright, “Long-range strains and the effects of applied field at 180° ferroelectric domain walls in lithium niobate,” *Phys. Rev. B - Condens. Matter Mater. Phys.*, vol. 69, no. 6, 2004, doi: 10.1103/PhysRevB.69.064113.

[218] G. Stone, B. Knorr, V. Gopalan, and V. Dierolf, “Frequency shift of Raman modes due to an applied electric field and domain inversion in LiNbO3,” *Phys. Rev. B - Condens. Matter Mater. Phys.*, vol. 84, no. 13, 2011, doi: 10.1103/PhysRevB.84.134303.

[219] Y. Zhang, L. Guilbert, and P. Bourson, “Characterization of Ti: LiNbO3 waveguides by micro-raman and luminescence spectroscopy,” *Appl. Phys. B Lasers Opt.*, vol. 78, no. 3–4, 2004, doi: 10.1007/s00340-004-1402-0.

[220] V. Dierolf and C. Sandmann, “Inspection of periodically poled waveguide devices by confocal luminescence microscopy,” *Appl. Phys. B Lasers Opt.*, vol. 78, no. 3–4, 2004, doi: 10.1007/s00340-003-1377-2.

[221] G. Stone and V. Dierolf, “Influence of ferroelectric domain walls on the Raman scattering process in lithium tantalate and niobate,” *Opt. Lett.*, vol. 37, no. 6, 2012, doi: 10.1364/ol.37.001032.

[222] J. Brockmeier, “Local properties of PPKTP waveguide structures probed by Raman spectroscopy,” Universität Paderborn, Master thesis, 2018.

[223] J. Otte, “Analyse der elektrische Feldverteilung in KTP zur Domäneninversion,” Universität Paderborn, Bachelor thesis, 2020.

[224] C. Canalias, “Domain Engineering in KTiOPO4,” Royal Institute of Technology Stockholm, Stockholm, Sweden, Dissertation, 2005.

[225] M. Ghoohestani, S. J. Hashemifar, and A. Arab, “Linear and nonlinear optical properties of RbTiOPO4-KTiOPO4alloys studied from first principles,” *J. Appl. Phys.*, vol. 128, no. 12, 2020, doi: 10.1063/5.0022362.

[226] C. Eigner *et al.*, “Periodically poled ridge waveguides in KTP for second harmonic generation in the UV regime,” *Opt. Express*, vol. 26, no. 32925–32935, 2018.

[227] D. Sun *et al.*, “Microstructure and domain engineering of lithium niobate crystal films for integrated photonic applications,” *Light: Science and Applications*, vol. 9, no. 1. 2020, doi: 10.1038/s41377-020-00434-0.

[228] L. Duvillaret, S. Rialland, and J.-L. Coutaz, “Electro-optic sensors for electric field measurements II Choice of the crystals and complete optimization of their orientation,” *J. Opt. Soc. Am. B*, vol. 19, no. 11, 2002, doi: 10.1364/josab.19.002704.

[229] K.-H. Luo *et al.*, “Counter-propagating photon pair generation in a nonlinear waveguide,” *Opt. Express*, vol. 28, no. 3, 2020, doi: 10.1364/oe.378789.

[230] H. Hu, R. Ricken, and W. Sohler, “Large area, crystal-bonded LiNbO3 thin films and ridge waveguides of high refractive index contrast,” *Proc. Eur. Conf. Lasers Electro-Optics Eur. Quantum Electron. Conf.*, vol. 1, pp. 14–19, 2009.

[231] H. Han, L. Cai, and H. Hu, “Optical and structural properties of single-crystal lithium niobate thin film,” *Opt. Mater. (Amst).*, vol. 42, 2015, doi: 10.1016/j.optmat.2014.12.016.

[232] K. J. Spychala *et al.*, “Impact of carbon-ion implantation on the nonlinear optical susceptibility of LiNbO_3,” *Opt. Express*, vol. 25, no. 18, 2017, doi: 10.1364/oe.25.021444.

[233] M. L. Hu, L. J. Hu, and J. Y. Chang, “Polarization Switching of Pure and MgO-doped Lithium Niobate Crystals,” *Japanese J. Appl. Physics, Part 1 Regul. Pap. Short Notes Rev. Pap.*, vol. 42, no. 12, 2003, doi: 10.1143/jjap.42.7414.

[234] M. C. Wengler, B. Fassbender, E. Soergel, and K. Buse, “Impact of ultraviolet light on coercive field, poling dynamics and poling quality of various lithium niobate crystals from different sources,” *J. Appl. Phys.*, vol. 96, no. 5, 2004, doi: 10.1063/1.1776324.

List of Figures

List of Tables

Acknowledgements

At this point I would like to thank all those people who supported me during the work and contributed to the success of this work. I want to thank:

- First of all, I would like to thank Prof. Dr. Artur Zrenner for the support of this work and the assignment of this interesting topic.

- I would like to thank Prof. Dr. Christine Silberhorn for her work as a second supervisor, as well as for the good cooperation of the working groups within the scope of this work and its connected SFB/TRR 142 project B05.

- A special thanks to my adviser, Dr. Gerhard Berth, whose expertise I have benefited not only from the point of view of scientific work or experimental questions, but also humanly.

- For many very interesting discussions I would like to thank Alex Widhalm, Kai Spychala, Michael Rüsing and Julian Brockmeier from my working group and other institutions.

- A thank-you for the good working atmosphere and the quick help with all questions and problems applies to my colleagues from the working group "Optoelectronics and Spectroscopy of Nanostructures".

- A further thank you goes to the working group "Integrated Quantum Optics" by Prof. Dr. Silberhorn. I would particularly like to thank Christof Eigner and Laura Padberg for their informative discussion and the provision of the investigated samples.

- At this point, I would also like to thank my "Lektors", who helped me with their English skills.

- Last but not least, I thank my family and friends for their human and moral support.

Erklärung der Selbstständigkeit

Hiermit versichere ich, Peter Walter Martin Mackwitz, dass ich die vorgelegte Arbeit selbstständig verfasst und keine anderen, als die angegebenen Hilfsmittel verwendet habe. Alle Ausführungen, die anderen Werken wörtlich oder sinngemäß entnommen wurden, sind in jedem Falle unter Angabe der Quelle kenntlich gemacht. Die Arbeit ist noch nicht veröffentlicht oder in anderer Form an irgendeiner Stelle als Prüfungsleistung vorgelegt worden.

Paderborn, den 08.02.2023 _____